

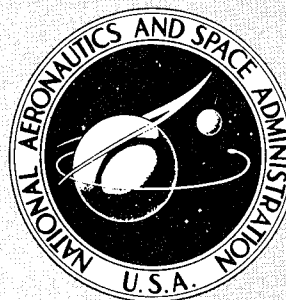
13808-  
13810

# AEROSPACE STRUCTURAL MATERIALS

**DISTRIBUTION STATEMENT A**

Approved for public release  
Distribution Unlimited

A conference held at  
LEWIS RESEARCH CENTER  
Cleveland, Ohio  
November 18-19, 1969



DEPARTMENT OF DEFENSE  
PLASTICS TECHNICAL EVALUATION CENTER  
PICATINNY ARSENAL, DOVER, N. J.

NATIONAL AERONAUTICS AND SPACE ADMINISTRATION

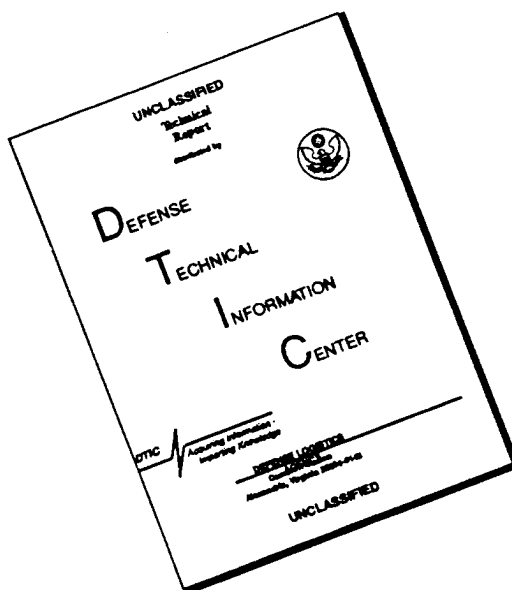
DTIC QUALITY INSPECTED 1

19960503 098

PLASTIC 13808

13810

# DISCLAIMER NOTICE



THIS DOCUMENT IS BEST QUALITY AVAILABLE. THE COPY FURNISHED TO DTIC CONTAINED A SIGNIFICANT NUMBER OF PAGES WHICH DO NOT REPRODUCE LEGIBLY.

# AEROSPACE STRUCTURAL MATERIALS

The proceedings of a conference held at  
the NASA Lewis Research Center on  
November 18-19, 1969



*Scientific and Technical Information Division*  
OFFICE OF TECHNOLOGY UTILIZATION  
NATIONAL AERONAUTICS AND SPACE ADMINISTRATION  
1970  
*Washington, D.C.*

For sale by the Clearinghouse for Federal Scientific and Technical Information  
Springfield, Virginia 22151 - Price \$3.00



## FOREWORD

As one of the keystones for our developing advanced power and propulsion technology and systems, the Lewis Research Center conducts investigations in the areas of aerospace structural materials. Because of the unique facilities at Lewis and our background in materials, we are involved in almost all aspects of materials research from the most fundamental to the most applied. The papers which comprise this conference represent a cross section of our entire effort and provide a sampling of our work in many areas with the emphasis upon highlights of new progress.

A series of papers concerned with fracture prevention and life prediction is followed by several papers on superalloys. They describe a number of different approaches taken to advance the technology of this important class of materials. Several papers similarly treat refractory metals. Fiber composite research and composite materials with metallic matrices and composites with nonmetallic matrices are described. New analytical methods of importance in materials research are discussed. Also included are descriptions of various environmental effects on material behavior and the protection systems being devised as a consequence of environmental effects.

## CONTENTS

	Page
FOREWORD . . . . .	iii
 <u>FRACTURE PREVENTION AND LIFE PREDICTION</u>	
1. FRACTURE MECHANICS CONCEPTS APPLIED TO AEROSPACE STRUCTURAL PROBLEMS	
John L. Shannon, Jr., and William F. Brown, Jr. . . . .	1
2. APPROACHES TO LIFE-PREDICTION PROBLEMS IN CREEP RUPTURE AND FATIGUE AT HIGH TEMPERATURES	
S. S. Manson . . . . .	19
3. THERMAL FATIGUE OF HIGH-TEMPERATURE MATERIALS	
David A. Spera . . . . .	43
4. PRESENT STATUS OF THE THEORETICAL CALCULATION OF DIFFUSION AND DIFFUSION-RELATED MECHANICAL PROPERTIES	
H. H. Grimes . . . . .	59
 <u>SUPERALLOYS FOR HIGH TEMPERATURES</u>	
5. NICKEL-BASE ALLOYS FOR AEROSPACE APPLICATIONS	
John C. Freche . . . . .	71
6. THERMOMECHANICAL PROCESSING OF THE NICKEL-BASE ALLOY U-700	
Charles P. Blankenship . . . . .	91
7. DEVELOPMENTS IN DISPERSION-STRENGTHENED MATERIALS	
Max Quatinetz and John W. Weeton . . . . .	101
8. SOLID-STATE WELDING OF DISPERSION-STRENGTHENED MATERIALS	
Thomas J. Moore . . . . .	119
 <u>REFRACTORY MATERIALS</u>	
9. RECENT DEVELOPMENTS IN CHROMIUM AND CHROMIUM ALLOYS	
William D. Klopp . . . . .	135

<b>10. CARBIDE STRENGTHENING OF TUNGSTEN AND MOLYBDENUM ALLOYS</b>	
Robert W. Hall, Peter L. Raffo, Walter R. Witzke, and William D. Klopp . . . . .	163
<b>11. MASS SPECTROMETRIC STUDIES OF THE VAPORIZATION OF REFRACTORY CARBIDES AND NITRIDES</b>	
Fred J. Kohl and Carl A. Stearns . . . . .	173
<b>FIBER COMPOSITES</b>	
<b>12. METAL-MATRIX FIBER COMPOSITES FOR HIGH TEMPERATURES</b>	
Robert A. Signorelli and John W. Weeton . . . . .	187
<b>13. HIGH-TEMPERATURE RESIN-MATRIX COMPOSITES</b>	
Tito T. Serafini . . . . .	207-13809
<b>14. DESIGN AND ANALYSIS OF FIBER COMPOSITE STRUCTURAL COMPONENTS</b>	
Christos C. Chamis . . . . .	217-13810
<b>ANALYSIS AND SPECIAL PREPARATION METHODS</b>	
<b>15. RADIATION-INDUCED PREPARATION OF PURE METALS FROM SOLUTION</b>	
Warren H. Philipp and Robert A. Lad . . . . .	229
<b>16. AN APPROACH TO A UNIVERSAL SPECTROCHEMICAL ANALYSIS</b>	
William A. Gordon . . . . .	239
<b>ENVIRONMENTAL EFFECTS AND PROTECTION</b>	
<b>17. HOT-SALT STRESS-CORROSION OF TITANIUM ALLOYS</b>	
Hugh R. Gray . . . . .	251
<b>18. SOME TENSILE AND ELECTRICAL RESISTANCE PROPERTIES OF PALLADIUM-HYDROGEN AND TITANIUM-HYDROGEN SYSTEMS</b>	
Robert J. Smith and Dumas A. Otterson . . . . .	269
<b>19. EFFECT OF ENVIRONMENT ON EROSION-CORROSION PROCESSES</b>	
Hubert B. Probst . . . . .	279
<b>20. OXIDATION OF WI-52, A COBALT-BASE SUPERALLOY</b>	
Carl E. Lowell . . . . .	295
<b>21. PROTECTIVE COATINGS FOR SUPERALLOYS</b>	
Salvatore J. Grisaffe . . . . .	305
<b>22. MATERIALS PROBLEMS IN AUTOMOTIVE EXHAUST REACTORS FOR POLLUTION CONTROL</b>	
Robert E. Oldrieve and Neal T. Saunders . . . . .	317

# 1. FRACTURE MECHANICS CONCEPTS APPLIED TO AEROSPACE STRUCTURAL PROBLEMS

John L. Shannon, Jr., and William F. Brown, Jr.

Structures can fail in two general ways: either by plastic deformation or by brittle fracture, the latter often catastrophic and the cause of extensive destruction. The study of catastrophic, brittle fracture has identified the following features common to all brittle failures: (1) fracture originates at a crack or crack-like flaw; (2) little, if any, gross plastic deformation attends the fracture; (3) failure occurs at a stress well below the yield strength; and (4) the tendency of material toward brittle fracture behavior is often not revealed by conventional tensile and impact tests.

Our research has been directed at two closely related problems: (1) the development of test methods for the qualitative evaluation of brittle crack propagation resistance (fracture toughness) that would be useful as a screening tool in alloy development, and (2) the development of a quantitative measure of fracture toughness which would be useful in design and proof testing.

Specimens containing cracks or very sharp notches to simulate cracks have been developed as a screening tool in evaluating relative fracture toughness. These specimens are included in the ASTM Method of Test for Sharp Notch Tension Testing of High Strength Sheet Material (ASTM E338-68). The influence of many factors on the crack toughness of alloys suitable for aerospace applications has been studied using these specimens. These factors include heat treatment, thermomechanical working, service environment, alloy purity, and certain geometrical variables.

Work at this laboratory on the engineering aspects of metal fracture has made possible the development of standardized methods for the quantitative measurement of brittle fracture resistance. These developments are now incorporated in an ASTM Proposed Method of Test for the Determination of Plane Strain Fracture Toughness and have been adopted by the SAE-AMS, MIL Handbook No. 5, and the British Standards. Specific use of the method is made in material selection, the calculation of working stresses, the development of rational proof testing procedures, and the establishment of realistic safety factors.

Structures can fail in two general ways: either by plastic deformation, such as occurs when someone bangs your automobile fender and it deforms and locks

against the wheel, or by brittle fracture which is frequently catastrophic and destroys not only the entire structure but often surrounding structures and people as well. The headlamp on that same damaged automobile fender also provides an example of catastrophic brittle fracture.

It is always a surprise when normally tough metals break in a catastrophic brittle manner. Figure 1-1 shows a high-speed photograph of the start of the brittle failure of a natural-gas line pipe (ref. 1). The several cracks you observe are of sinusoidal shape (characteristic of brittle fracture in line pipe) and form a fracture front which in this case is traveling at a measured speed of nearly 2000 feet per second (about the speed of a rifle bullet). The gas decompression wave is discernible by the fog-condensation resulting from expansive cooling of the escaping gas and is seen to be lagging the fracture front. The cracks, therefore, are propagating under the influence of full line pressure and could be expected to continue unimpeded until they reach some location where either the pressure is relieved or there is a discontinuity in the pipe such as at a joint or pump. Obviously, at the crack propagation speed cited here, a great length of pipe could be destroyed in a small time, liberating vast quantities of flammable gas possibly in a populated area.

Many examples of such brittle failures could be cited, including such diverse structures as storage vessels, suspension bridges, aircraft landing gears, and rocket motor cases. Few of these failures, however, are well documented in terms of failure stresses, fracture origin, service history, etc. One example (ref. 2), however, is well studied and illustrates common features of the brittle fracture problem. It is the solid propellant rocket motor case shown in figure 1-2.

This 260 inch diameter case failed in hydrotest and it can be seen that the analogy to the broken automobile headlamp is appropriate. This large structure was made from 3/4 inch thick, 230-ksi yield strength steel and failed at a stress less than one-half that of the design yield strength. The failure originated at a small crack-like defect in the heat-affected zone of a GTA repair weld. This triggering defect is shown in figure 1-3 and is about 0.1 inch wide and 1.4 inch long. This tiny flaw removed less than 0.02 percent of the load-carrying area of the motor case wall but cut the expected load-carrying capacity of the article in half. It did its damage by concentrating the stress in the vicinity of its boundaries and, unfortunately, the metal did not have a sufficient amount of toughness to relieve this stress concentration by plastic flow; consequently, the crack, once started, ran freely through the tank feeding on the elastic energy stored in the large structure.

This example illustrates features common to all brittle failures:

- (1) Fracture originates at crack or crack-like flaw.

(2) Little, if any, gross plastic deformation attends the fracture - all plastic flow is confined to the crack surfaces and there is no general yielding of the structure.

(3) Failure occurs at a stress well below the yield strength.

(4) And, as will be shown later, the material's tendency toward brittle fracture behavior is often not revealed by conventional tensile and impact tests.

The key to brittle fracture control lies in understanding the weakening effect of cracks in metals and those factors that influence this effect. To be useful in an engineering sense, this understanding must be translated into the types of tests and structural mechanics familiar to the metal producer and the designer.

About 10 years ago members of the NASA Lewis Research Center, researchers from the Navy, and certain representatives from industry joined, at the suggestion of the National Academy of Science and the Department of Defense, to form a special ASTM Committee to study the brittle-fracture problem. Their first job was to develop test methods that would permit a rational selection of steels and working stresses for the Polaris motor case and thereby put an end to a continuous series of failures which had by that time become a national emergency.

Since that time our fracture research has been directed at two closely related problems: (1) the development of test methods for the qualitative evaluation of brittle crack propagation resistance, or fracture toughness, that would be useful as a screening tool in alloy development and selection, and (2) the development of a quantitative measure of fracture toughness which would be useful in design and proof testing. The progress that has been made in these two areas is briefly reviewed in this paper and is based largely on the information and methods developed at NASA-Lewis.

## QUALITATIVE EVALUATION OF FRACTURE TOUGHNESS

Once the essential features of brittle fracture were recognized, it became obvious that any meaningful evaluation of fracture toughness would have to employ specimens containing cracks or crack-like flaws. This was a rather simple concept but was completely foreign to most metallurgists and designers who were not trained to think of structures and materials as inherently flawed.

Figure 1-4 shows two types of screening specimens containing such flaws. One contains a central fatigue crack, while the other contains very sharp machined notches intended to simulate cracks. These specimens were developed about 11 years ago (ref. 3), the cracked one at the Naval Research Laboratory and the sharp-notched one at NASA-Lewis. Using these specimens it became possible to

sort out alloy conditions with reference to their relative fracture toughness. For example, it was quickly found that alloy producers at that time consistently recommended heat treatments which, while producing high strength, frequently produced a metal condition greatly weakened by the presence of cracks. To illustrate this point, figure 1-5 shows the conventional tensile properties of a high strength stainless steel as a function of tempering temperature. Also shown is the strength of the sharp-notched specimen based on its breaking load divided by its cross-sectional area in the plane of the notches. If the very sharp notch did not weaken the material, the notch strength and yield strength would be about equal. However, we observe that in the recommended tempering temperature range, the yield strength is highest but the sharp notch strength is very low. Note also that the conventional elongation gives no clue to this brittle behavior. Considerably improved crack toughness is obtained if the alloy is tempered at temperatures above or below this brittle range. For example, if the tempering is carried out at 400° F, very little strength is sacrificed but a great improvement in toughness is realized.

New alloys such as the maraging steels, having greatly improved fracture toughness compared with our older steels, have been developed using this crack-strength or notch-strength approach.

Another important use for these types of tests is the selection of alloys for low temperature service. Frequently the combination of low temperature and cracks produces a serious loss in toughness which may not be revealed by conventional tests. Figure 1-6 shows the conventional tensile and Charpy-V impact properties of a commonly used low alloy steel as a function of test temperature down to -100° F. Such a steel might be used in aircraft where -65° F performance is frequently specified. There is nothing remarkable about the conventional property trends shown; in fact, only small changes are noted with varying temperature. Figure 1-7, on the other hand, shows results obtained using fatigue-cracked specimens. It is obvious that a pronounced embrittlement occurs below room temperature as revealed by the steeply falling curve for the crack strength. Alloys respond quite differently to the effects of low temperature, and tests of this nature show that aluminum alloys and some titanium alloys are far superior to the ferritic steels, such as 4335V, in their low temperature crack toughness.

Recently, there has been a great deal of interest in thermomechanical processing of certain alloys. These fabrication procedures often involve phase transformations during the application of work and can result in conditions having very high tensile strength. A classic example of strengthening by thermomechanical working is simply the cold rolling of the unstable austenitic stainless steel 301. During cold rolling this steel transforms from austenite to martensite, and during subsequent tensile testing additional transformation takes place. As indicated in figure

1-8, a very high yield strength at  $-320^{\circ}\text{F}$  can be produced by heavy cold reductions of 301 sheet (ref. 5). Note that up to 60-percent cold reduction, the elongations remain high and are equal in the longitudinal and transverse directions. However, a pronounced depression of the notch strength curve below the yield strength curve for the transverse direction indicates directional embrittlement not reflected in the conventional elongation measurement.

Studies like the preceding have taught us a great deal concerning the influence of various factors on the crack toughness of metallic alloys. Table 1-I summarizes some important generalizations derived from these investigations. Note that those factors which increase the conventional tensile or yield strengths reduce the crack toughness: namely, heat treatment, thermomechanical working, and low temperature. Notice, too, that the magnitude of this effect varies with the strengthening process and the alloy type. Thus, thermomechanical working can result in directional toughness reduction, the transverse direction frequently the least tough, as shown earlier for 301 sheet. Low temperature increases the conventional tensile and yield strengths and reduces the crack toughness to a degree which depends on the crystal structure of the metal. Thus the effect is most pronounced for the body-centered-cubic structure, least pronounced for the face-centered-cubic structure, with the close-packed-hexagonal structure intermediate between the two.

The converse to these observations is that those factors which tend to lower the strength generally also improve the toughness. One area where gains in toughness can be made with little or no loss in strength is that of increasing alloy purity. A now well-established example of this beneficial effect is the production of extra low interstitial element titanium alloys which have superior fracture toughness at cryogenic temperatures compared to their normal interstitial element counterparts (ref. 7).

Note that at the bottom of table 1-I thickness is listed as an embrittling factor. This effect, which can be a purely geometrical one (as opposed to a metallurgical thickness effect), leads to the second part of this discussion - namely, the quantitative measurement of fracture toughness.

## QUANTITATIVE MEASUREMENT OF FRACTURE TOUGHNESS

Figure 1-9 is a schematic illustration of the effect of thickness on the net fracture strength of a typical high strength steel. Also shown is a schematic representation of the fracture appearance as a function of thickness for the single-edge-crack-type specimen shown unbroken to the right. For these data, only the specimen thickness has been varied, the crack length and all other pertinent dimensions



have been kept the same. Note that the net fracture strength decreases to a constant value beyond a certain limiting thickness marked by the dashed vertical line.

Mixed mode fracture, characteristic of thinner gages, involves a considerable amount of plastic flow resulting in the development of rather sizable shear lips. These lips represent zones of ductile fracture along shear planes (as opposed to brittle fracture, which is the failure mechanism of the small flat areas between the shear lips).

As the specimen thickness is increased, the amount of plasticity accompanying fracture is reduced until at sufficient thickness the fracture surface is essentially flat. This development of embrittlement with increasing thickness is due to an increasing degree of constraint to plastic flow at the crack tip, and this effect reaches a limit designated as plane strain fracture. It is in this region where the amount of plastic flow accompanying fracture is sufficiently small that we can measure a quantitative value of fracture toughness.

Figure 1-10 illustrates the basic principle behind such a measure (ref. 9). Shown is a crack of length  $2a$  with rectangular and polar coordinates at one tip. Focusing attention on the conditions in the vicinity of the crack tip where fracture takes place, Dr. George Irwin (formerly of the Naval Research Laboratory and presently at Lehigh University) made use of mathematical relations developed by Westgaard and defined the plane strain elastic stress field in the vicinity of the crack tip by the expressions shown. These equations give the components of stress in the vicinity of the crack tip (the normal stresses  $\sigma_x$ ,  $\sigma_y$ , and  $\sigma_z$  and the shear stresses  $\tau_{xy}$ ,  $\tau_{xz}$ , and  $\tau_{yz}$ ) in terms of the polar coordinates  $r$  and  $\theta$  for the case where the crack grows by the normal separation of its surfaces, as opposed to a sliding motion. Each equation is an infinite series, but in the immediate vicinity of the crack tip, the first term dominates and these are shown. Notice that the complete elastic stress field in the vicinity of the crack tip can be approximated by a single scalar quantity  $K_I$ , which is designated the stress intensity factor and is proportional to the applied load and the geometry of the cracked body.

The basic assumption in elastic fracture mechanics is that when  $K_I$  reaches a critical value  $K_{Ic}$  failure occurs. Thus,  $K_{Ic}$  is the stress intensity necessary to cause fracture under plane strain conditions - it is commonly called the plane strain fracture toughness.

As far as the crack is concerned, any combination of body configuration and load distribution that produces a given value of  $K_I$  is equivalent to any other such combination. Thus  $K_{Ic}$ , the critical value, is independent of loading conditions and may be considered a material constant.

These concepts are similar to the older Griffith hypothesis for brittle fracture but are expressed in more useful engineering terms. We have  $K_I$  as the stress

intensity factor analogous to the stress in a tensile test, and  $K_{Ic}$  as a specific and useful engineering value of  $K_I$  relating to fracture resistance much like the yield strength relates to plastic flow resistance.

In principle, if the value of  $K_{Ic}$  is known from a laboratory test, we can, by a suitable stress analysis, calculate the load-carrying capacity of a part containing a crack of known size providing the bulk of the structure is sufficient to produce a plane strain failure. Figure 1-11 shows the possibility of doing this. The structures considered are simply panels of two widths containing cracks of various lengths  $2a$ . For this illustration a high strength steel at a yield strength level of 225 ksi and  $K_{Ic}$  of 35 ksi $\sqrt{\text{in.}}$  is considered. The curve through the data points was calculated from the equation shown using the  $K_{Ic}$  value of 35 ksi $\sqrt{\text{in.}}$  obtained from a small cracked-bend specimen. The data points were determined from laboratory tests on the cracked panels and the agreement between the curve and the points is satisfying indeed, proving the ability to calculate the cracked-panel strength for this brittle alloy from a single laboratory toughness determination. If the structure (panels) had not been sufficiently thick to support a plane strain failure, then the calculation of load-carrying capacity on the basis of  $K_{Ic}$  would have yielded a conservative result, and the data points would have plotted above the calculated curve.

At NASA-Lewis, major contributions to the development of test methods for measurement of  $K_{Ic}$  have been made. Analytical techniques and computer programs have been devised which permit calculation of stress intensity factors for a wide variety of specimen types. Specimen size requirements have been established which define the useful limits of linear elastic fracture mechanics in the measurement of fracture toughness of real materials. And necessary instrumentation has been developed for recording pertinent test quantities as well as the means for analyzing such records. All of these developments are now incorporated in an ASTM Test Method for Determination of Plane Strain Fracture Toughness which appears in Part 31 of the 1969 Book of ASTM Standards. This method has also been adopted by the Aerospace Materials Specifications Committee of the Society for Automotive Engineers, MIL Handbook-5, and the British Standards. It involves a great deal more sophistication both in instrumentation and analysis than previous standard mechanical tests, and it is the forerunner of what will be a series of modern test methods for the evaluation of fracture behavior.

We have shown by the example of figure 1-11 that the load-carrying capacity of a simple panel containing a crack of known size can be computed with the knowledge of  $K_{Ic}$  so long as the panel thickness is sufficient to provide a condition of plane strain. However, the designer seldom has so neat a job. Usually the stress distribution in the component is not completely known and the probable crack size

cannot be accurately assessed with state-of-the-art nondestructive testing techniques. The designer cannot, therefore, calculate his working stresses directly from  $K_{Ic}$  in these situations. However, he can use the fracture toughness concept to select materials, develop rational proof testing procedures, and help establish realistic safety factors. I want to avoid in this discussion the complexities involved in establishing proof testing procedures, but will comment briefly on the establishment of realistic safety factors.

Figure 1-12 shows schematically the effects of surface crack depth on two alloys - A, a very high strength steel, and B, a considerably lower strength material. The maximum operating stress (MOPS) in our hypothetical application is shown by the horizontal dashed line. For this example, a safety factor of 1.5 based on the yield strength to MOPS ratio is assumed. If the designer is guided by this value, he will choose alloy A which provides a safety factor of 1.9 and reject alloy B which provides a safety factor of only 1.3. Perhaps he will look at the elongation as well, and in this case he will find little difference. However, he could be in for a most unpleasant surprise if the structure contains even a very small flaw. For example, if a long surface crack only 0.1 inch deep were present, the structure made of the high strength alloy would fail at a stress below the MOPS but the lower strength material would provide a real margin of safety. This example graphically illustrates the need to examine conventional safety factors in light of performance in the presence of flaws. Generally speaking, it is more realistic from the standpoint of fracture safety to use a larger portion of the strength potential of a good low strength alloy than a relatively smaller proportion of the strength potential of a high strength alloy.

A good example of this philosophy is afforded by contrasting the ductile fracture of the subscale rocket motor case (ref. 10), shown in figure 1-13, with that of the wreckage of the 260 inch motor case, shown earlier in figure 1-2, which, as the reader recalls, broke like an eggshell. The subscale motor case (fig. 1-13) is 35 inches in diameter and made from 1 inch thick plate of HY-150 - a new, high toughness, 150 ksi yield strength steel. To simulate a crack, a large flaw was electric-discharge machined into the case's longitudinal weld. This flaw, which is shown in figure 1-14, is  $2\frac{1}{4}$  inches long by 0.8 inch deep and was sharpened by fatigue pressure cycling the vessel. The case was subsequently pressurized to burst at a membrane stress of 147 ksi - essentially at its yield strength.

The 260 inch diameter motor case was made of  $\frac{3}{4}$  inch thick, 250 grade maraging steel plate ( $F_{ty} = 230$  ksi) and failed catastrophically at 100 ksi. The failure originated at a flaw whose dimensions were only one-eighth as deep as that causing failure of the HY-150 case and at a stress which was significantly lower absolutely and in relation to the design yield strength. The brittle behavior of the

maraging steel motor case was due in large part to the welding method employed. All primary welds were made by the submerged arc process, which is a high heat-input welding technique that tends to embrittle maraging steels. Other large motor cases (156 in. diam) of the same air melted steel but gas tungsten arc welded were successfully fabricated and hydrotested. Present practice would employ vacuum melted steel and gas tungsten arc welding. A 260 inch diameter motor case fabricated of consumable electrode vacuum melted 200 grade maraging steel using gas tungsten arc welding was successfully hydrotested and has been fired twice.

This brief article was intended to impress the reader with the need to consider the materials resistance to brittle crack propagation in certain design situations and to apprise him of some of the progress in this area.

## REFERENCES

1. Duffy, A. R.: Full-Scale Studies. Presented at Symposium on Line Pipe Research, Pipeline Research Committee of American Gas Assoc., Dallas, Texas, Nov. 17-18, 1965.
2. Srawley, John E.; and Esgar, Jack B.: Investigation of Hydrotest Failure of Thiokol Chemical Corporation 260-Inch-Diameter SL-1 Motor Case. NASA TM X-1194, 1966.
3. ASTM Special Committee on Fracture Testing of High-Strength Metallic Materials: Fracture Testing of High-Strength Sheet Materials. ASTM Bull. no. 243, Jan. 1960, pp. 29-40.
4. Espey, G. B.; Jones, M. H.; and Brown, W. F., Jr.: The Sharp Edge Notch Tensile Strength of Several High-Strength Steel Sheet Alloys. Proc. ASTM, vol. 59, 1959, pp. 837-884.
5. Espey, G. B.; Repko, A. J.; and Brown, W. F., Jr.: Effect of Cold Rolling and Stress Relief on the Sharp Edge Notch Tensile Characteristics of Austenitic Stainless Steel Sheet Alloys. Proc. ASTM, vol. 59, 1959, pp. 816-836.
6. Espey, G. B.; Jones, M. H.; and Brown, W. F., Jr.: Factors Influencing Fracture Toughness of Sheet Alloys for Use in Lightweight Cryogenic Tankage. Symposium on Evaluation of Metallic Materials in Design for Low-Temperature Service. Spec. Tech. Publ. no. 302, ASTM, 1961, pp. 140-171.

7. Shannon, John L., Jr.; and Brown, W. F., Jr.: Effects of Several Production and Fabrication Variables on Sharp Notch Properties of 5Al-2.5Sn Titanium Alloy Sheet at Liquid Hydrogen Temperature. Proc. ASTM, vol. 63, 1963, pp. 809-829.
8. Brown, W. F., Jr.: and Srawley, J. E.: Plane Strain Crack Toughness Testing of High Strength Metallic Materials. Spec. Tech. Publ. no. 410, ASTM, 1967.
9. Irwin, G. R.: Analysis of Stresses and Strains Near the End of a Crack Traversing a Plate. J. Appl. Mech., vol. 24, no. 3, Sept. 1957, pp. 361-364.
10. Tiffany, C. F.; Masters, J. N.; and Regan, R. E.: A Study of Weldments and Pressure Vessels Made of HY-150 Steel Plates. Rep. D2-113433-1, Boeing Co. (NASA CR-72155), Jan. 1967.

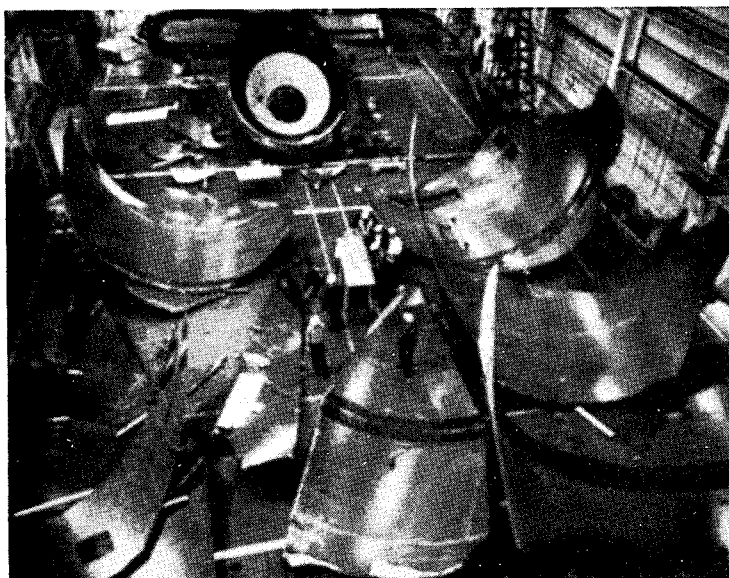
TABLE 1-I. - FACTORS INFLUENCING FRACTURE TOUGHNESS  
AND CONVENTIONAL STRENGTH

Factor	Effect on conventional strength	Probable effect on fracture toughness	Example references
Heat treatment	Increase	Reduction	4
Thermomechanical working	Increase	Reduction (transverse direction)	5
Low temperature	Increase bcc > cph > fcc	Reduction bcc > cph > fcc	6
Alloy purity	Little or none	Increase	7
Thickness	None	Reduction	8



CS-49369

Figure 1-1. - Brittle fracture of gas line pipe ( $\approx 4$  msec after initiation; ref. 1).



CS-44243

Figure 1-2. - Wreckage of 260-inch-diameter motor case (ref. 2).

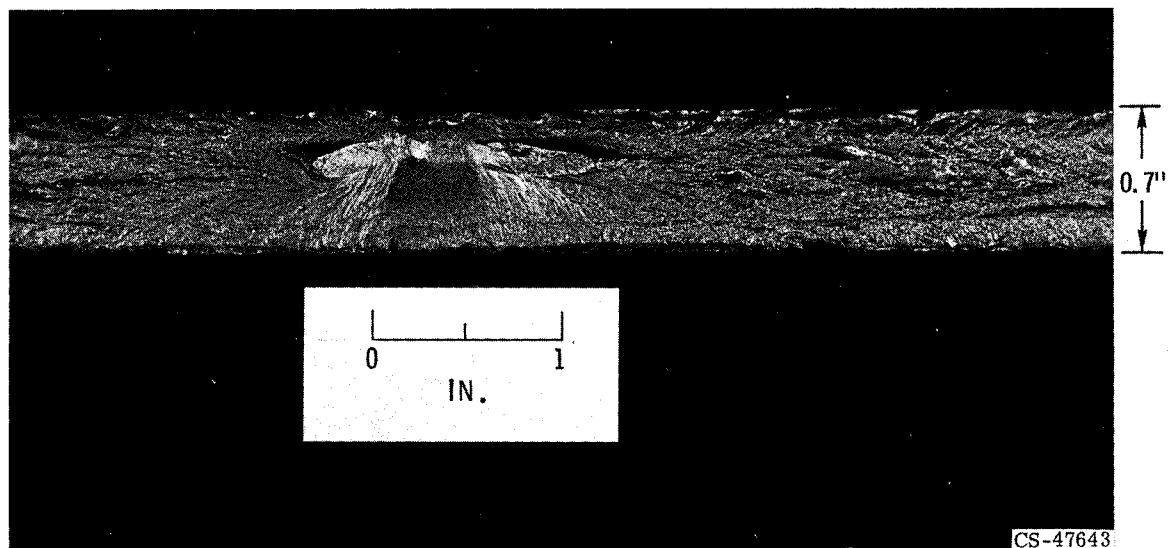


Figure 1-3. - Flaw at which fracture initiated (ref. 2).

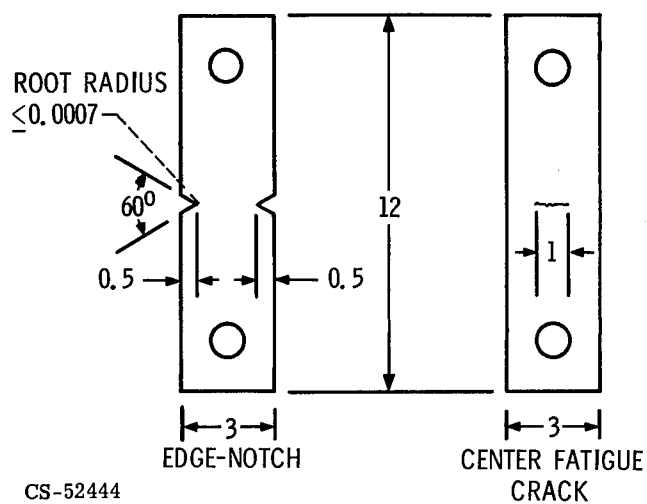


Figure 1-4. - ASTM specimens for sharp-notch testing of high-strength sheet materials (ref. 3).

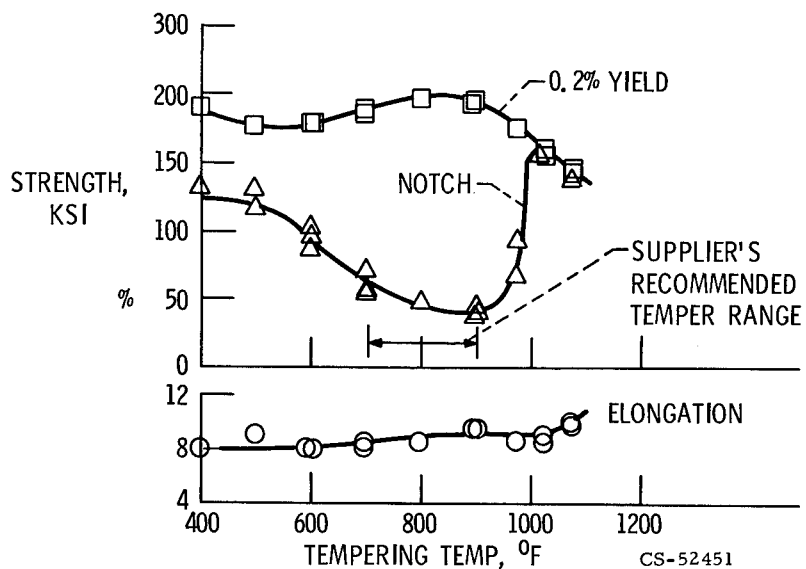


Figure 1-5. - Sharp notch and smooth tensile characteristics of 12 MoV stainless steel (ref. 4).

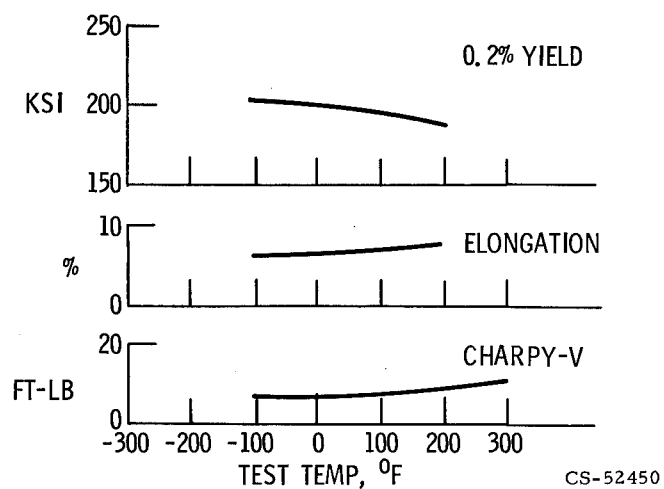


Figure 1-6. - Some conventional properties of SAE 4335V (400°F temper) at various temperatures.



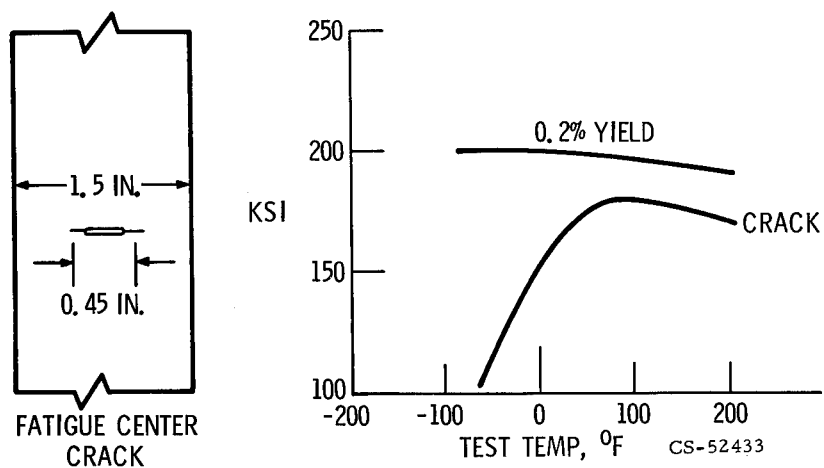


Figure 1-7. - Crack strength of SAE 4335V (0.125-in. sheet; 400° F temper) at various temperatures.

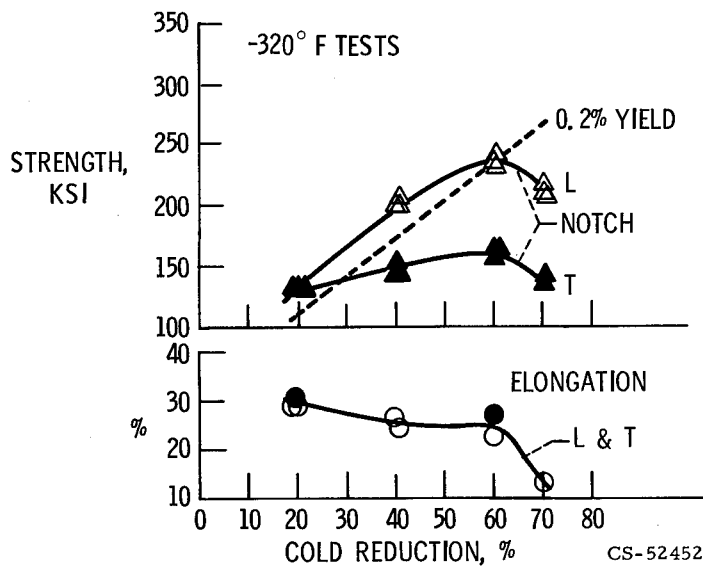


Figure 1-8. - Effect of thermomechanical working of AISI-301 sheet (ref. 5).

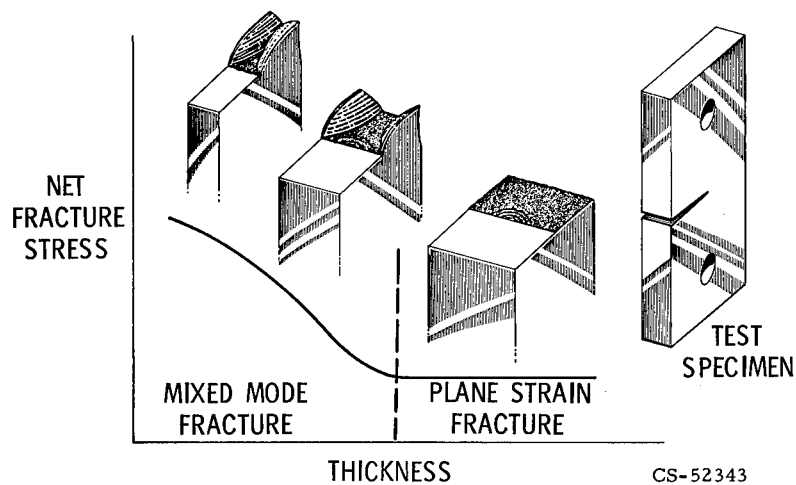


Figure 1-9. - Effect of thickness on fracture toughness.

$$\sigma_x = \frac{K_I}{(2\pi r)^{1/2}} \cos \frac{\theta}{2} \left( 1 - \sin \frac{\theta}{2} \sin \frac{3\theta}{2} \right) + \dots$$

$$\sigma_y = \frac{K_I}{(2\pi r)^{1/2}} \cos \frac{\theta}{2} \left( 1 + \sin \frac{\theta}{2} \sin \frac{3\theta}{2} \right) + \dots$$

$$\tau_{xy} = \frac{K_I}{(2\pi r)^{1/2}} \sin \frac{\theta}{2} \cos \frac{\theta}{2} \cos \frac{3\theta}{2} + \dots$$

$$\sigma_z = \nu(\sigma_x + \sigma_y); \tau_{xz} = \tau_{yz} = 0$$

$K_I$  IS THE STRESS INTENSITY FACTOR PROPORTIONAL TO LOAD AND CRACK LENGTH

$K_{Ic}$  IS THE STRESS INTENSITY NECESSARY TO CAUSE FRACTURE UNDER PLANE STRAIN CONDITIONS

CS-44238

Figure 1-10. - Plane strain elastic stress field in vicinity of crack tip (ref. 9).

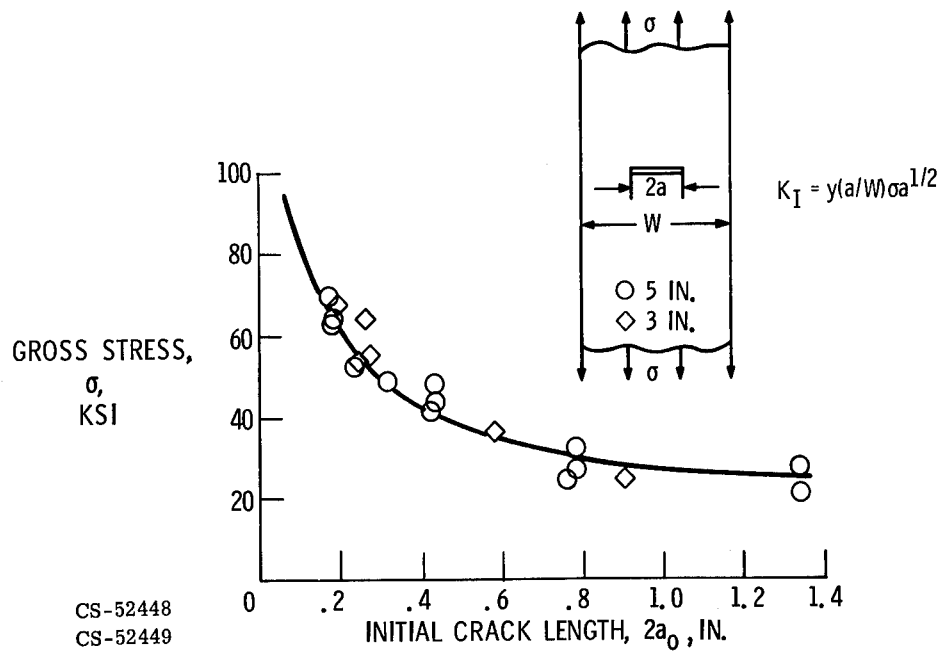


Figure 1-11. - Fracture stress as function of crack length for high strength steel ( $F_{ty} = 225$  ksi;  $K_{Ic} = \text{ksi}\sqrt{\text{in.}}$ )

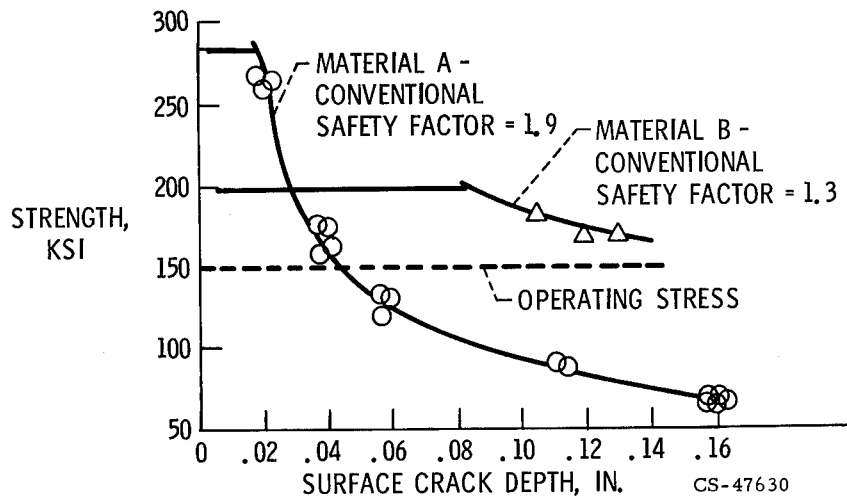
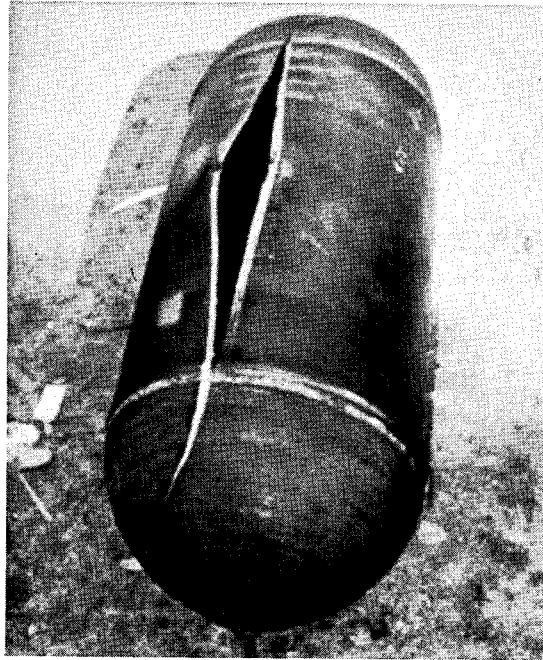
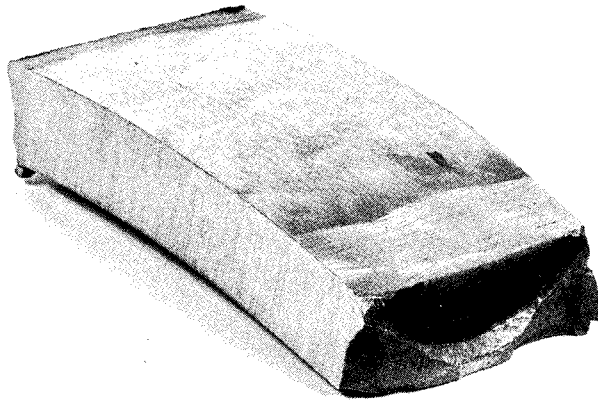


Figure 1-12. - Importance of considering materials flaws or cracks in design.



CS-52445

Figure 1-13. - Ductile failure of subscale motor case  
(ref. 10).



C-66-4578  
CS-52446

Figure 1-14. - Flaw in longitudinal weld of subscale motor case  
(ref. 10).



## 2. APPROACHES TO LIFE-PREDICTION PROBLEMS IN CREEP RUPTURE AND FATIGUE AT HIGH TEMPERATURES

S. S. Manson

Life prediction procedures are discussed for two types of design problems encountered in high-temperature approaches such as in the jet propulsion engine and in nuclear power generation equipment. The first prediction method relates to the estimation of life of components that must endure for longer periods than can reasonably be duplicated in real time in the laboratory, for example, 20 to 30 years. The approach relies on a generalization of the concept of time-temperature parameters in which higher temperature is substituted for longer time in generating the data from which the extrapolations are made. The new approach does not, however, favor any one of the standard parameters now in use. Rather, by introducing a station-function procedure, the method applies an optimization procedure for seeking out the most pertinent parameter whether or not it is among those in common use. This new method will yield more accurate results in cases where present approaches yield dangerously unconservative results. The second prediction method relates to the estimation of fatigue life at high temperature, wherein the complexity of loading and the wide range of service conditions makes impractical the direct simulation of service in preliminary laboratory tests. Treating the high-temperature fatigue process as a combination of the individual effects of fatigue damage and creep damage makes it possible to analyze a wide variety of complex conditions within the framework of a single analytical procedure rather than devising separate procedures for each type of loading. The fatigue component of damage is estimated from the universal slopes equation for treating fatigue of materials at temperatures below the creep range. The creep-damage component is estimated from a new but simply conducted "cyclic creep" test on the material. In cases where such a test cannot be conducted, conventional creep-rupture test results can be used, but the estimates so obtained must be viewed with less confidence. Study of several materials has shown that reasonably accurate predictions can be made of frequency and temperature effects by this procedure. The method also serves as a framework around which to treat thermal stress problems wherein complex variations of temperature, stress, and strain are involved.

In a sense, most engineering analyses are life predictions. Engineers use the measured properties on simple specimens, compute the local stresses in the struc-

tures of interest, and from the basic properties and local loadings determine whether the structure will survive, and for how long. But there are several types of life-prediction problems that are more difficult to harness. They relate either to the generation of the basic material data or to the determination of how a material behaves under complex loadings not easily duplicated in the laboratory for the multi-fold conditions encountered in service. It is the purpose of this paper to treat two such cases, one in each category. These problems are identified in figure 2-1.

The first problem relates to the estimation of very long-time properties of materials without actually conducting the test in real time. Creep-rupture material properties are required for durations too long to be directly duplicated in the laboratory. In jet engine applications such times may be of the order of 10 000 hours; for nuclear powerplants or stationary turbines the times involved may be 100 000 to 200 000 hours. To conduct the tests directly would require times approaching 20 years, an obvious impracticality. Some means must therefore be sought to extrapolate shorter time data to obtain at least an estimate of the required long-time properties.

A second problem relates to the determination of the high-temperature fatigue properties of materials. These properties depend on stress, temperature, and frequency, and progressive changes in each of these variables occur during the life of a component. Some means must therefore be found to use the results determined from a few selected laboratory tests to make the multifold predictions required for a large range of conditions encountered during the service life of a component.

In outlining the recent contributions made at this laboratory on these two illustrative applications, we shall present only the highlights; details may be found in the references cited at the end of the paper.

## CORRELATION AND EXTRAPOLATION OF CREEP-RUPTURE DATA

### Requirements

Conventional creep-rupture tests are conducted by applying a steady load to a simple specimen at high temperature and by noting the time history of the elongation (creep) and the time at which the specimen finally fractures into two distinct pieces (creep-rupture time). Tests of short duration are rather easily conducted, but as noted, it is in the long-time tests that the time factor becomes burdensome, and must somehow be bypassed.

One of the approaches used to condense the time factor is the time-temperature parameter. In this procedure higher temperature is, in essence, substituted for long time. The concept is well accepted in applications involving chemical reactions. It is known, for example, that such reactions are accelerated by increasing temperature, the rate for many reactions roughly doubling for each increase of about 20 F°. Thus, if the rate is required at a low temperature where the time involved in the reaction is very long, tests could be conducted at several higher temperatures at shorter times, note made of the progressive increase of the rate with increasing temperatures, and the rate at the requisite low temperature computed from a knowledge of the rate-temperature characteristic.

The metallurgical problem in the creep and rupture process is a complex one and is not as readily defined as the simple chemical process noted above. But in general higher temperature does accelerate the process, and suitable tests at higher temperature can indeed be helpful in estimating long lives. Tactically, the procedure involves the introduction of an analytical expression involving both time and temperature, usually referred to as a time-temperature parameter. This parameter provides the information as to how much of a temperature increase is needed to bring the time required for the test to within a practical level.

One of the first time-temperature parameters suggested for this application came from Larson and Miller at the General Electric Company in 1952 (ref. 1). It had the form  $(T + 460)(20 + \log t)$ , where  $T$  is the temperature in °F, and  $t$  is the rupture time in hours. Another simple parametric form that has been used (ref. 2) is in the form  $\log t + mT$ , where  $m$  is a material constant. For the cobalt base alloy L-605, we have found, for example, that the data can best be correlated by a parameter in the form  $\log t + 0.0108 T$ , as shown in figure 2-2. The data are generated by running creep tests at temperatures and stresses which result in relatively short rupture times. Plots such as shown in this figure are constructed from the known stresses, temperatures, and rupture times. Extrapolations to higher rupture times are then made by the use of the master curve. The two selected variables, stress and temperature, are used in conjunction with the curve to determine the third variable, rupture time.

The time-temperature parameter approach is a reasonable one for many materials. But uniformity of agreement has not been achieved among competent investigators as to what form the time-temperature parameter should have. The Larson-Miller parameter is but one of many suggested parameters; there are numerous others that have been proposed. At Lewis we have been active in this field, and several forms have originated out of our research. One such form that we have favored is



$$\frac{T - T_a}{\log t - \log t_a}$$

where  $T_a$  and  $\log t_a$  are material constants (ref. 3). Numerous other forms are also possible, each proposed by its author as a result of experience with specific materials.

The truth of the matter is that different materials do yield better to treatment by different parameters. What we really need is a single form that embraces all the common forms as special cases, so that agreement can be achieved among those favoring the different forms. In addition, mathematical techniques are needed for handling the equations that arise when material constants are optimized. For example, the least squares equations that arise when a given set of experimental data are used to optimize the constants  $T_a$  and  $\log t_a$  in the preceding parameters are badly ill-conditioned. This means that special techniques are needed to solve the equations, and, even with these techniques, it is difficult to distinguish a good solution from a bad one, especially when there is any degree of scatter in the data. Finally, a method is needed in which the procedure can be standardized so that as few elements as possible of subjective judgment can enter to destroy the objectivity of the final evaluation.

### Decoupled Station-Function Parameter

Within the past year we have arrived at a parametric approach which comes quite close to satisfying these major requirements. Discussion of all the details of the procedure, as well as the reasons why these procedures overcome the basic problems, is somewhat beyond the scope of this paper, but a brief outline of the method will be instructive. Further details can be found in reference 4.

We start by assuming the functional form of the relation among stress, temperature, and rupture time.

$$f(\log t) + p(T) = g(\log \sigma) \quad (1)$$

where  $f$ ,  $p$ , and  $g$  are functions of rupture time, temperature, and stress, respectively. For convenience, we express the  $f$  and  $g$  functions in terms of the logarithms of their respective independent variables. The functions  $f$ ,  $p$ , and  $g$  are not, at this point, known; but it is obvious that the commonly used time-temperature parameters are consistent with the form of equation (1). For the case of the

Larson-Miller parameter, for example, where the relation is  $(T + 460)(20 + \log t) = P(\log \sigma)$ , the form of equation (1) can be obtained by taking logarithms of both sides, producing

$$\log(20 + \log t) + \log(T + 460) = \log P(\log \sigma)$$

Thus, in this case

$$f(\log t) = \log(20 + \log t)$$

$$P(T) = \log(T + 460)$$

$$g(\log \sigma) = \log P(\log \sigma)$$

The parameter  $\log t + mT$  is immediately in the form of equation (1) wherein  $f(\log t) = \log t$ ,  $p(T) = mT$ , and  $g(\sigma)$  is defined by the master curve such as shown in figure 2-2 for the alloy L-605. In a similar way, it can be demonstrated that other commonly used time-temperature parameters are satisfied by a form of equation (1); the difference among parameters being that each parameter has a different time, temperature, and stress function. Thus, for a given set of data, if we can optimize the  $f$ ,  $p$ , and  $g$  functions, we will automatically have determined the best parameter. No commitment need be made in advance as to the form of the  $f$ ,  $p$ , and  $g$  functions, which is another way of saying that we do not commit ourselves as to the form of the parameter, letting the data themselves choose the optimum form.

The problem is how to go about finding the best form of the  $f$ ,  $p$ , and  $g$  functions for a given set of data. The basic approach is indicated in figure 2-3, which shows the conventional isothermal creep-rupture curves for a typical alloy Astroloy. The time, temperature, and stress domains of interest are divided into an arbitrary number of intervals (usually equally spaced, although this is not a necessary requirement). At each nodal point between intervals, called a station, the value of the function is identified by a suitable symbol. For example, in figure 2-3 we have divided the time range from 10 to 1000 hours by five station functions  $f_1, f_2, \dots, f_5$  at  $\log t = 1, 1.5, \dots, 3.0$ . The stress range of interest between 10 and 100 ksi is represented by six station functions  $g_1, g_2, \dots, g_6$  at  $\log \sigma = 1, 1.2, \dots, 2.0$ , where  $\sigma$  is given in ksi) and the five temperatures for which data are presented are assigned station function values  $p_1, p_2, \dots, p_5$ . At this point, all the values  $f_1, \dots, f_5, g_1, \dots, g_6$ , and  $p_1, \dots, p_5$  have unknown numerical magnitudes. The method of

analysis is to determine these magnitudes so that plots can be made of each of the functions at the discrete stations designated. Thus, the aim of the analysis is to obtain numerical representation of each of the functions, without making any commitment whatever as to the analytical description of the functions. For this reason we call the method a minimum-commitment, station-function analysis.

To determine the numerical values of the functions, we must now introduce the experimental data. The analysis will be shown only for point A, but of course many data points are usually available, all of which are treated in the same way. What we wish to do now is to translate the information associated with point A into a form analogous to equation (1):

$$f(\log t_A) + p(T_A) = g(\log \sigma_A)$$

However, since point A does not lie on one of the chosen time stations, the value of  $f_A$  must be determined in terms of the  $f$  values at the adjacent stations. Lagrangian interpolation formulas (ref. 5) can be used, resulting in

$$f(2.082) = 0.069 f_2 + 0.973 f_3 + 0.096 f_4 \quad (2)$$

For the temperature function no interpolation is required since point A lies on one of the station temperatures

$$p(1700) = p_4 \quad (3)$$

For the stress function, interpolation is again needed

$$g(1.462) = -0.108 g_2 + 0.903 g_3 + 0.205 g_4 \quad (4)$$

Substituting into equation (1) such that

$$f(2.082) + p(1700) = g(1.462) \quad (5)$$

leads to

$$-0.069 f_2 + 0.973 f_3 + 0.096 f_4 + p_4 = -0.108 g_2 + 0.903 g_3 + 0.205 g_4 \quad (6)$$

Obviously, a similar equation can be written for each experimental data point

available, and the system of equations so written can then be solved for all the unknowns. For reasons discussed in reference 4, three of the unknowns can be assigned arbitrary values. The remaining number of unknowns is usually much lower than the number of equations that can be written, and the best solution is obtained by application of least-squares procedures. It is for the following reasons that the method has advantages over other methods that have been used:

(1) Since no assumption is made as to the form of the  $f$ ,  $p$ , and  $g$  functions, the method seeks out the best functions dictated by the data. In contrast, other methods of applying time-temperature parameters work in reverse: A given type of function is assumed, and the analysis seeks out the best member of that class of function as the answer. But the class of function may not be the best that can be found.

(2) All the equations in the form of equation (6) are linear in all the unknowns, and can be solved by direct procedures. In contrast, other existing methods are formulated to result in nonlinear equations, and trial and error procedures are often needed to obtain a solution. The process is sometimes very inefficient.

(3) Each equation of the set contains very few of the unknowns. For example, equation (6) contains three  $f$  values, one  $p$  value, and three  $g$  values, which is typical of all the equations derived from individual data points. This makes for a well-conditioned set of equations which cause no significant figure problems in solution. In contrast, other methods generate equation sets in which all the unknowns appear in each equation. Significant-figure problems are common and can only be handled by very special techniques, often with difficulty.

(4) Since each data point generates its own equation, raw data can be used directly, and no fairing of data is required of the analyst. The resulting analysis is completely objective; no subjective influences are introduced by the analyst, and all analysts get essentially the same answer from a given set of data. In contrast, some of the other methods of analysis depend on faired data, and different analysts obtain different answers depending on their subjective decisions in fairing the data.

Thus, this method has considerable potential merit over other methods that are in current use for correlating data. When the solution is obtained by the least-squares solution of the resulting system of equations analogous to equation (6), the numerical functions so determined constitute the best functions that can be obtained that are consistent with the basic assumption in equation (1) and that correlate the data within the experimental range. For extrapolation, one more step is needed. The  $p$  and  $g$  functions will usually cover the complete temperature and stress range of interest, or at least this can be assumed by including suitable tests that can be conducted in short times. The  $f$  function, however, will be defined only up to the longest time for which experimental results are available. To predict longer lives, the  $f$  function must be extrapolated. In our approach we have used two pro-

cedures: the polynomial representation and the recurrence-relation representation of the  $f$  curve. Details are discussed in reference 4; in the examples to be discussed here both methods give approximately the same results. More research is needed, however, to settle on a standardized procedure.

The final form of the station-function representation is as shown in figure 2-4. In figure 2-4 the computed value of each station function is plotted against its corresponding independent variable, the total solution being represented by three curves. To get the value of one variable when the other two are specified, equation (1) is applied in connection with the three curves. For example, when the stress and temperature are specified, the  $g$  and  $p$  values are determined from the proper curves in figure 2-4. Equation (1) is then applied to determine  $f(\log t)$ , and the rupture time is read from the curve of  $f$  against  $\log t$  in figure 2-4. Alternatively, since equation (1) is in the simple form wherein the sum of two functions is equal to a third function, a nomogram can readily be constructed to relate the three functions. Such a nomogram is shown in figure 2-5. The scale for each function depends, of course, on the relation between that function and its independent variable, that is, on the corresponding curve in figure 2-4. A straight line joining any two points on two of the station function lines intersects the third line at the unknown value of the third variable. Such nomograms, which have not found common usage in representation of creep-rupture data, are very convenient and compact; they are also easily constructed when the station function approach is used, even when no analytical expressions are used to represent the functions.

## Examples

To determine whether the method is capable of finding the correct solution when the correlation functions are indeed representable by one of the commonly used parameters, the computations shown in figure 2-6 were made. The data in this figure were generated by selecting the time-temperature parameter  $(T + 460)(20 + \log t)$  together with a suitable master curve. The points in the rupture-time range from 10 to 1000 hours ( $\log t$  from 1 to 3) are the presumed experimental "data." Using these "data" together with the station-function analysis just described, the  $f$ ,  $p$ , and  $g$  functions were determined, and the predictions were made as shown by the lines in the figure. These lines agree extremely well with the "data" points in the experimental range as well as in the extrapolated time range from 1000 to 100 000 hours ( $\log t = 3$  to 5). The same good agreement between "data" and computations by the station function method was obtained when "data" were generated using other common time-temperature parameters. Thus, if data do indeed fit any

of the standard time-temperature parameters, the station-function procedure will produce the same extrapolations as the correct time-temperature parameter would have predicted. The station-function approach is as accurate as the correct time-temperature parameter, but the correct time-temperature parameter is much harder to find because so many different forms must first be studied.

On the other hand, there are materials for which the commonly used time-temperature parameters are not well suited for long-time extrapolation. Glen and Johnson (ref. 6) have discussed silicon-carbon steel in this connection. They attempted to predict 100 000-hour strength values from short-time data and concluded that all commonly used time-temperature parameters produced unconservative predictions. That is, the stress levels that were predicted by the time-temperature parameters as supportable by the material for 100 000 hours were not indeed safe levels. Glen and Johnson did not show their analyses which led to their choice of particular time-temperature parameters, and it is possible that more sophisticated choices of parameters might have reduced the pessimistic appearance of the applicability of time-temperature parameters. Nevertheless, it is true that in the manner applied by Glen and Johnson the conventional time-temperature parameters produced unconservative predictions. The question might then appropriately be asked whether the station-function approach would be any better.

The analysis of Glen and Johnson's data by the station-function approach is shown in figure 2-7 where, also, a comparison is made with the corresponding predictions based on the Larson-Miller parameter. To make the predictions, data up to 6000-hour duration were used for the station-function analysis and for the construction of a Larson-Miller master curve. Extrapolations were then made for rupture times up to 100 000 hours. The dashed curves show the analysis on the basis of the Larson-Miller parameter, the continuous lines the station-function analysis.

It is seen in figure 2-7 that the station function lines do conform better to the data both in the time range up to 6000 hours and in the range beyond this value than do the Larson-Miller lines. The largest differences between the two types of extrapolation occur at 100 000 hours. These are shown for the 840<sup>0</sup> F temperature in figure 2-8. The figure shows that according to the Larson-Miller parameter the allowable stress is 12.9 ksi and according to the station function analysis the allowable stress is only 8.4 ksi. Glen and Johnson estimated 10.3 ksi. Looking at it another way, if the designer had selected a stress value of 12.9 ksi intending the life to be 100 000 hours, then the allowable life might be as low as 34 700 hours if the station-function extrapolations were correct. Figure 2-7 does show a tendency of the long-time data to fall lower than the dashed line extrapolations. And, of course, Glen and Johnson's main point was that predictions such as those shown

by the dashed lines would be dangerously unconservative. So at least in this case, the station-function approach provides the conservatism sought by the designer within the framework of totally analytical and objective procedures. Of course, much more experience is needed to establish how well the station function procedure performs with other materials. But up to this point our experience has been encouraging.

## HIGH TEMPERATURE FATIGUE

The second aspect of life prediction to be discussed is associated with high-temperature fatigue. Analytical computation rather than direct test is desirable because the actual life may be too long to be practically duplicated in test, or, because of their severity, operating conditions are too difficult to duplicate in test, or because the design variables and operating conditions are so diverse that it is impractical to attempt to simulate them all.

The processes involved in high-temperature fatigue are extremely complex, and our approach is not intended to predict behavior from first principles only. Rather, we have attempted to devise procedures for computing fatigue behavior under complex conditions from a few well-chosen tests conducted under carefully controlled, simple conditions. This section summarizes the present state of our analytical approach.

### Basis

We must regard high-temperature fatigue as the simultaneous occurrence of two effects.

- (1) "Pure fatigue," in which the principal governing variables are the reversals of stresses and strains without regard for the time of their application
- (2) "Creep-effect," in which the time of application of each loading is as important as the loading itself

Each of these factors requires individual treatment before combining their cumulative effect.

### Pure Fatigue

It is very difficult to conduct a high-temperature fatigue experiment without introducing a creep effect. Therefore, to estimate what the fatigue life would be at elevated temperature if there were no creep effect, we can examine the factors that

govern fatigue at room temperature where, for most metals, there is no creep effect. These factors are expressed by the universal slopes equation developed at Lewis several years ago (ref. 7).

$$\Delta\epsilon = \frac{3.5 \sigma_u}{E} N_f^{-0.12} + D^{0.6} N_f^{-0.6} \quad (7)$$

where  $\Delta\epsilon$  is the total strain range to which the material is subjected,  $D$  is the ductility of the material and is related to the reduction of area  $RA$  in the tensile test by the equation  $D = -\ln(1 - RA)$ ,  $\sigma_u$  is the ultimate tensile strength of the material, and  $E$  the elastic modulus.

Thus, if we assume that in the absence of a creep effect the material behavior is also governed by equation (7), all we need to know is the strain range and the tensile properties normally obtained in a conventional tensile test. Of course the tensile test for use in equation (7) must be conducted at the high temperature of interest for which the pure fatigue behavior is to be computed.

### Creep Effect

Several different creep-rupture curves have been used by us to determine the creep effect. One is the conventional uniaxial creep-rupture curve, which is similar to those which were discussed in the first part of this paper. In general, however, this curve tends to overestimate the creep-rupture effect and produces life estimates which are lower than those obtainable experimentally. This is probably due, in part, to the fact that in a monotonically loaded creep test the area progressively decreases, whereas in a cyclically loaded test alternate tension and compression maintain an approximately constant cross-sectional area. Thus, the calculations of cyclic creep life based on the conventional creep curve tend to give a lower bound on life.

We have also used a creep-rupture test of a notched specimen having a stress-concentration factor of 2 to 4 for estimates of cyclic creep life (ref. 8). The notch produces constraint of plastic flow at its root, and, for most materials, when the stresses are computed on the basis of the minimum section of the notched test specimen, the material is found to be notch-strengthening. That is, for a given nominal stress at the minimum section, a notched specimen generally gives a longer life in creep rupture than a smooth specimen at the same stress level. In general, for materials which are notched-strengthened, the creep-rupture curve of the notched material tends to give an upper bound on life when used in fatigue analysis. However, the use of a notched specimen introduces complexities in material behavior associated



with stress state and stress gradient so that the results of such tests must be viewed with care.

The two conventional types of creep-rupture curves described give estimates of upper and lower bounds on life for a particular material; but these bounds may differ appreciably, and we are left with considerable uncertainty regarding a more definitive estimate of life. In order to narrow down the estimate and also to avoid the extraneous complexities introduced by the use of a notched specimen, we have introduced (ref. 9) what we call a cyclic creep-rupture test as shown in figure 2-9. To conduct such a test we use a smooth specimen, and periodically reverse the load so that on the average the mean strain is zero. This method simulates what happens in practice in reversed strain-cycling situations. At the start of the test the specimen is loaded in tension, and the condition of the material in figure 2-9 is at point A. The material is then allowed to creep until it reaches a predetermined strain (we have used strain range values between 1 and 4 percent with relatively little difference in final result). When this strain is reached (point B), the stress is reversed to compression of equal magnitude (point C). It is then allowed to creep in compression until it reaches a negative creep strain of equal magnitude (point D). The load is again reversed, and the process repeated until rupture occurs. Because of the large creep strains used in the test, the fatigue damage in such a test is usually low, but, if necessary, it can be subtracted using equation (7) together with the observed number of cycles sustained, as indicated in reference 9. Thus, the test emphasizes the creep-rupture effect under conditions closely simulating service conditions in which cycling occurs about a mean strain of approximately zero. Figure 2-10 shows the results of such tests for 316 stainless steel. The conventional creep-rupture curve for the material at 1300° F is shown together with the cyclic creep-rupture curve. In plotting the cyclic creep-rupture curve only the tensile loading times are summed. The point of view is taken that in this particular test only the tensile periods produce creep damage. The purpose of the compressive loading is to maintain a zero mean strain and to carry out the stress alternation that might influence microstructural changes. Under some circumstances the compressive loading might also involve creep damage; this matter is further discussed in reference 9. Even neglecting the time spent in compression, it is seen in figure 2-10 that the creep-rupture time under cyclic loading is much higher than under static loading, and can be on the order of a factor of 10. The difference between the static and cyclic creep-rupture curves depends on the material. Other materials do not show as large a difference as that shown for the 316 stainless steel in figure 2-10.

## Cumulative Effect of Creep and Fatigue Damage

Once the appropriate tensile properties and creep-rupture curves are determined for all the temperatures of interest, the analysis can be made on the basis of a simple linear damage rule, as shown in figure 2-11. To obtain the creep damage, we simply add up the time fractions. The numerator in each fraction is the time the specimen resides at a given stress level; the denominator is the appropriate creep-rupture time for that stress level. There are some technicalities that have to be observed in determining the creep-rupture effects, but the details can be obtained from reference 9.

To obtain the fatigue damage, we simply take the ratio of the number of applied cycles to the number of cycles to failure computed by equation (7) using the tensile properties at the temperature of interest.

Combining the creep-damage relation with the fatigue-damage relation yields an equation which permits solution for the number of cycles to failure. Although the approach is subject to some criticism, its merits in terms of simplicity, relative ease of basic data generation, and generality in terms of the ability to treat the many variables that enter into high-temperature fatigue problems, all point to the potential promise of the method.

## Examples

One of the applications of the method is the study of the frequency effect; that is, how is fatigue life affected by frequency? In the past this effect has been studied empirically, and a power-law relation between life and frequency has been observed in some cases. But why some materials are so sensitive to frequency, while others are not, has not been explained. Nor has there ever been an explanation for the breakdown in this power-law relation beyond a certain frequency.

Figure 2-12 shows the results of calculations by this method for the cobalt-base alloy L-605. To identify the important component of damage in each frequency range, the creep and fatigue components are shown as dashed lines, plotted on logarithmic coordinates, and their sum is shown as the continuous line. It is seen that a nearly straight line results within the frequency range from  $10^{-3}$  to  $10^{-1}$  hertz where the creep effect predominates over the fatigue effect. Such a straight line implies a power-law relation between life and frequency, as has typically been observed for many materials. However, the curve levels off in the frequency range from  $10^{-1}$  to 1 hertz where both creep and fatigue effects are of comparable magnitude. At

frequencies higher than 1 hertz the fatigue effect predominates, and the curve would be expected to become nearly horizontal. The experimental results agree reasonably well with the calculations over the entire range of frequencies shown.

On the other hand the 316 stainless-steel alloy strain cycled at 1300° F exhibited very little change in cyclic life as the frequency was varied over the same range.

The explanation for this divergent behavior between the two alloys lies in their metallurgy, which in turn affects the stresses that develop as the frequency of strain cycling is varied. The L-605 alloy is subject to the precipitation of a Laves phase which is accentuated by the longer exposure times associated with lower frequencies. The precipitate hardens the material, so that, if the strain range is maintained constant, the stress necessary to maintain this strain range progressively increases as the hardening occurs. This hardening is reflected in figure 2-13 which shows the stresses necessary to maintain a strain range of 0.9 percent at a temperature of 1180° F. The figure shows the stress after 10 cycles of loading and after 100 cycles of loading for each of several frequencies ranging from 1 to  $10^{-3}$  hertz. The stress can increase by as much as 30 percent as the frequency is lowered. Since creep-rupture life is sensitive to stress, the life decreases appreciably due to the increase in stress as the frequency is reduced. Also, the exposure time for a single cycle is increased as the frequency is reduced, thus further reducing the cyclic life at the lower frequencies. The total effect of increasing stress as well as exposure time at low frequency is to reduce life drastically, as was already shown in figure 2-12.

The 316 stainless steel shows a different characteristic. No new precipitates are involved because of cycling and high temperature exposure. Instead of hardening as the frequency is reduced, the material softens, as shown in figure 2-14. Here the data are for 1300° F and a strain range of 1.25 percent. Thus, there is a counter-acting effect of stress and exposure time as the frequency is changed. Lowering the frequency increases the exposure time per cycle of loading, but this exposure is at a lower stress. Hence, the creep-rupture damage per cycle remains essentially the same regardless of frequency. The net effect is that very little change in cyclic life occurs as the frequency is varied over a large range.

Thus, by the use of the creep-fatigue damage analysis we get not only reasonably good predictions of life as frequency is varied, but also a physical explanation of this behavior, which is very desirable in extending concepts to other materials and ranges of conditions.

As a final example we show in figure 2-15 the effect on cyclic life for the alloy L-605 as the temperature is varied from 70 to 1400° F. Here the strain range is maintained constant at 0.9 percent, and the frequency is held constant at 0.33 hertz. The calculated cyclic lives are shown as dashed lines for the separate fatigue and creep-damage components. The result of summing the two components is shown as

the continuous line. Below approximately  $1000^{\circ}$  F the creep effect is very small (i.e., the cycles to failure if life were governed by creep alone would be very high). This small creep damage should be expected because of the sensitivity of creep-rupture life to temperature. Cyclic life below  $1000^{\circ}$  F should then be governed largely by the fatigue effect (eq. (7)). Above  $1000^{\circ}$  F, however, the creep effect predominates, and a strong dependency of life on temperature is indicated. Good agreement is seen between the computations and the experimental results.

## CONCLUDING REMARKS

An attempt has been made to outline the usefulness of two new approaches that have recently been developed at Lewis Research Center for treating various aspects of high-temperature material life predictions. The illustrative examples have indicated the basic procedures involved, and the results that can be expected. However, it should be emphasized that our experience with the procedures involved is still quite limited in both types of problems discussed. We recognize that these procedures have been idealized and highly simplified for ease of explanation and we have chosen for illustration problems that readily yielded to application of the proposed techniques. However, material behavior at high temperature is very complex, and we fully expect that the procedures discussed will require modification to handle various complexities as they are encountered. Thus we must emphasize that this paper is merely a status report of a framework for analysis of several important high-temperature materials problems. The body to this framework is yet to be fashioned on the basis of future experience.

## REFERENCES

1. Larson, F. R.; and Miller, James: A Time-Temperature Relationship for Rupture and Creep Stresses. Trans. ASME, vol. 74, no. 5, July 1952, pp. 765-775.
2. Manson, S. S.; and Succop, G.: Stress-Rupture Properties of Inconel 700 and Correlation on the Basis of Several Time-Temperature Parameters. Symposium on Metallic Materials for Service at Temperatures Above 1600 F. Spec. Tech. Publ. No. 174, ASTM, 1956, pp. 40-46.
3. Manson, S. S.; and Haferd, A. M.: A Linear Time-Temperature Relation for Extrapolation of Creep and Stress-Rupture Data. NACA TN 2890, 1953.

4. Manson, S. S.: Time-Temperature Parameters - A Re-Evaluation and Some New Approaches, to be published by The American Society for Metals.
5. Milne, William E.: Numerical Calculus. Princeton Univ. Press, 1949, p. 83.
6. Glen, J.; and Johnson, R. F.: Some Aspects Concerning the Extrapolation of Rupture Data. BISRA - The Inter-Group Laboratories of the British Steel Corp., London, England.
7. Manson, S. S.: Fatigue: A Complex Subject - Some Simple Approximations. Exper. Mech., vol. 5, no. 7, July 1965, pp. 193-226.
8. Spera, David A.: The Calculation of Elevated-Temperature Cyclic Life Considering Low-Cycle Fatigue and Creep. NASA TN D-5317, 1969.
9. Manson, S. S.; Halford, G. R.; and Spera, D. A.: The Role of Creep in High-Temperature Low-Cycle Fatigue. A. E. Johnson Memorial Volume, Nat. Eng. Lab., Glasgow, Scotland, 1970.

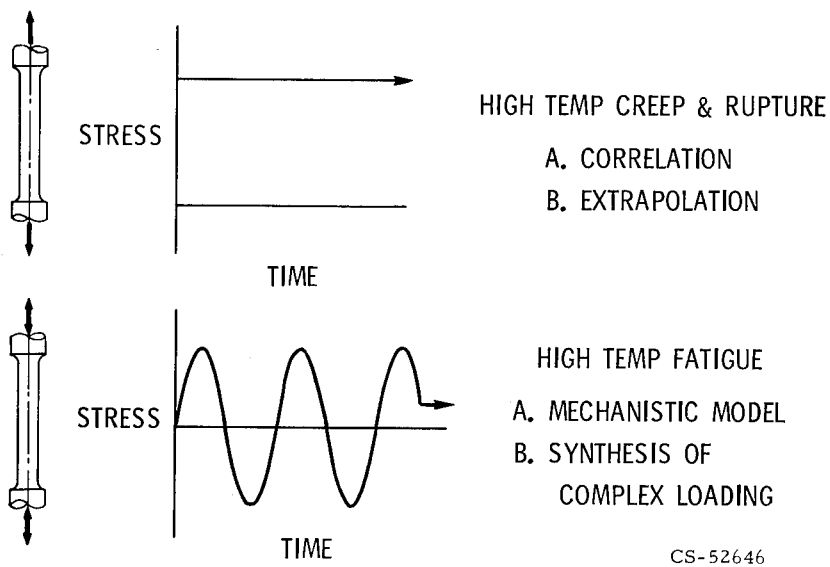


Figure 2-1. - Selected problems in life prediction.

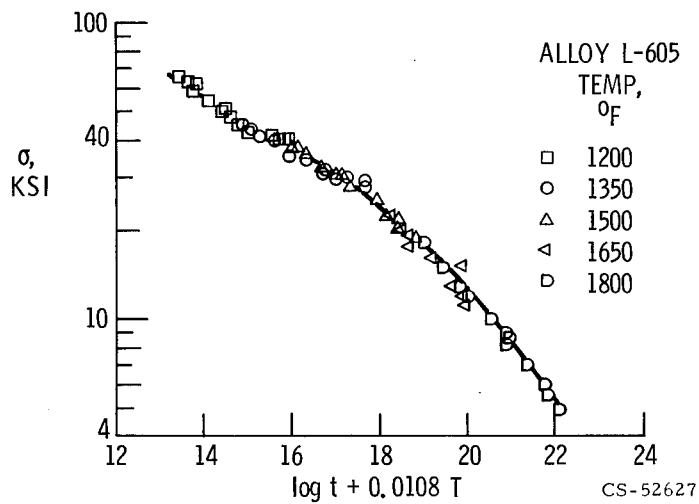


Figure 2-2. - Master curve for use in extrapolation by time-temperature parameter.

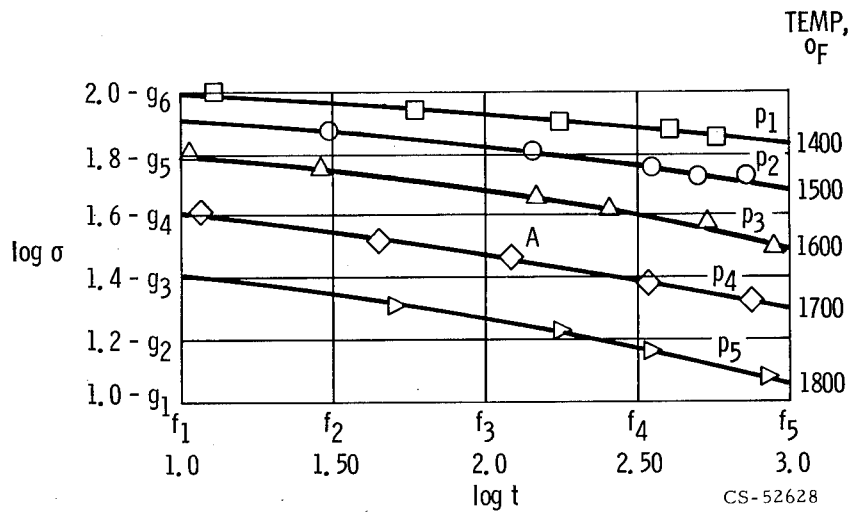


Figure 2-3. - Station function approach.

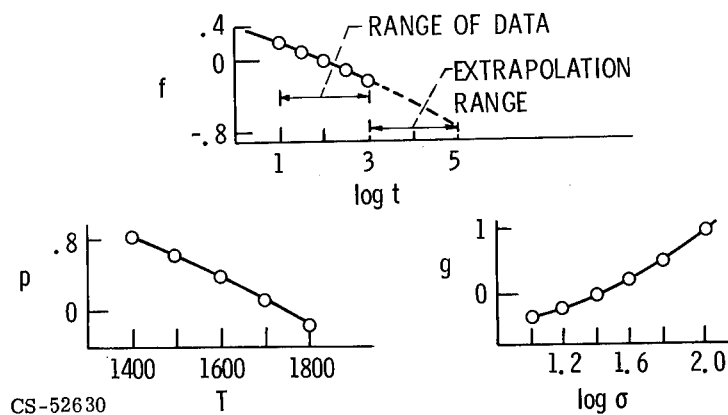


Figure 2-4. - Station functions for Astroloy.

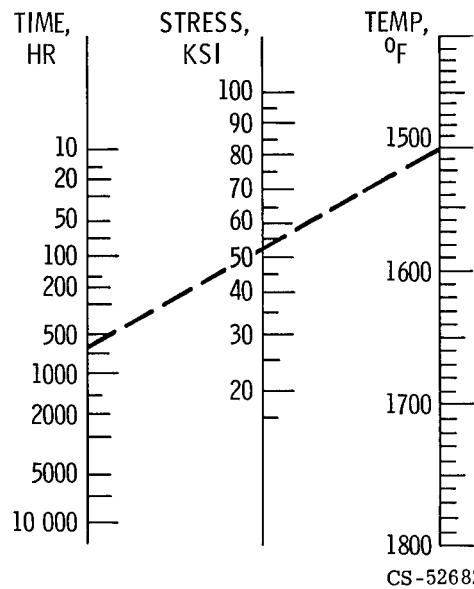


Figure 2-5. - Nomogram for creep-rupture of Astroloy.

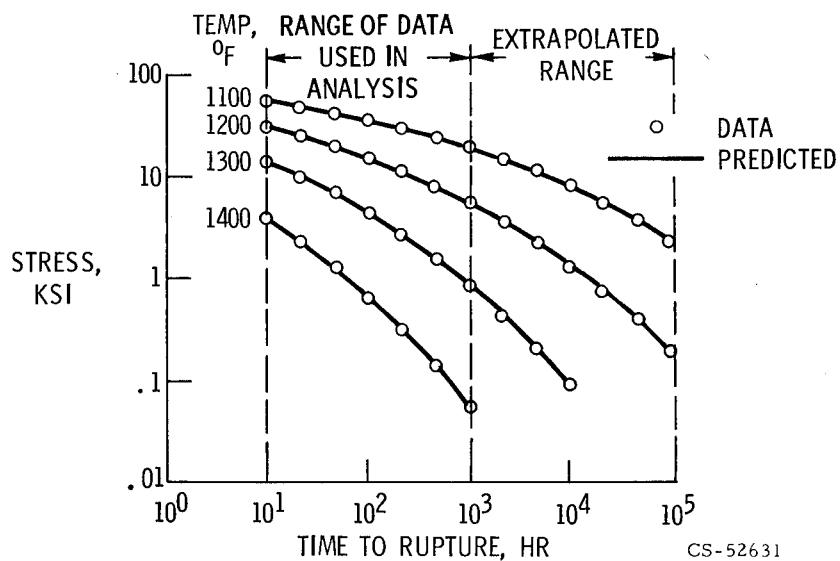


Figure 2-6. - Station function representation of data conforming to parameter  $(20 + \log t)(T + 460)$ .



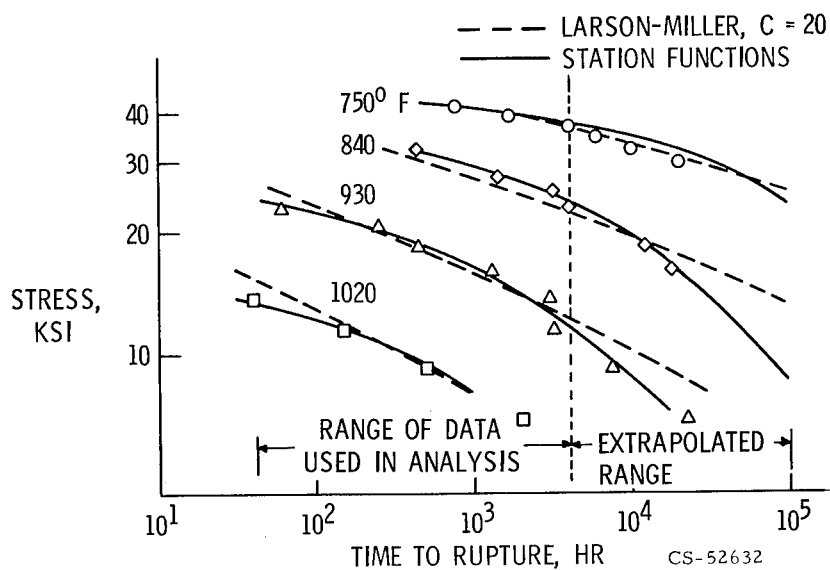


Figure 2-7. - Analysis of silicon-carbon steel. (Data from Glen and Johnson (1967).)

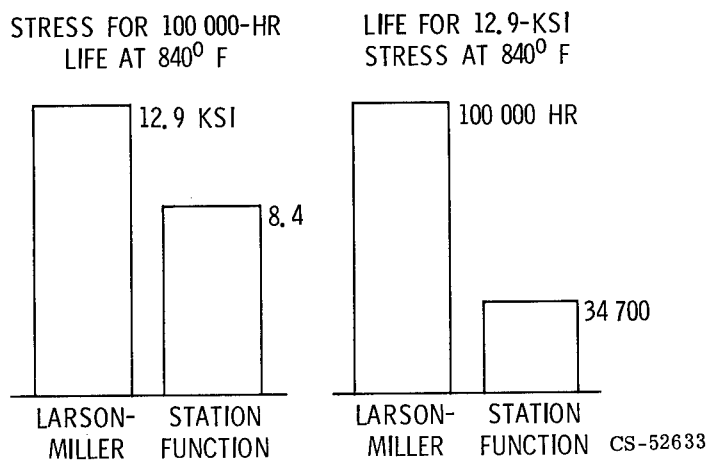


Figure 2-8. - Possible danger of unconservative prediction methods.

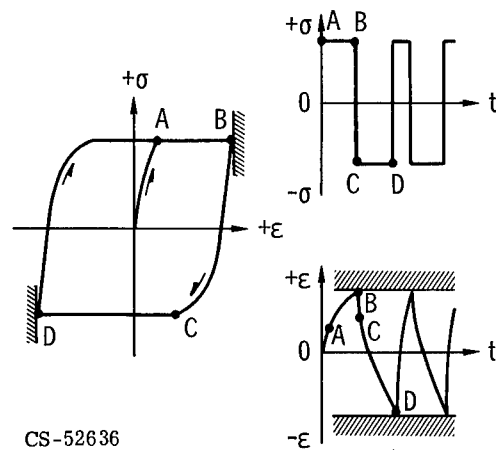


Figure 2-9. - Cyclic creep-rupture test.

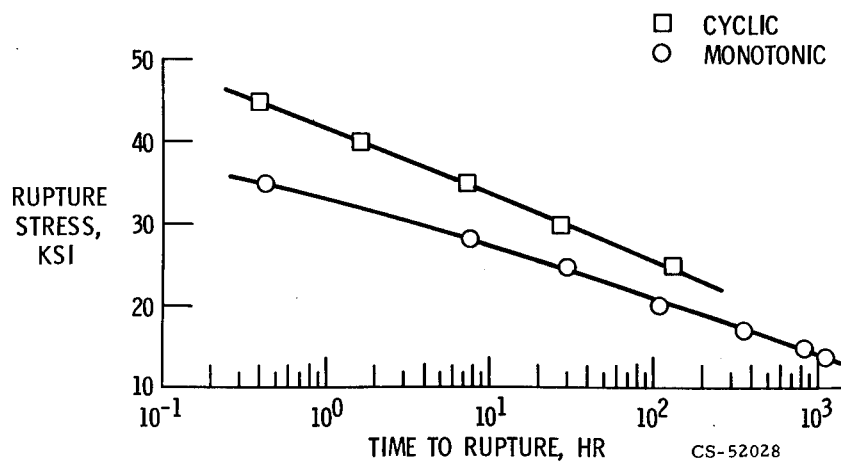
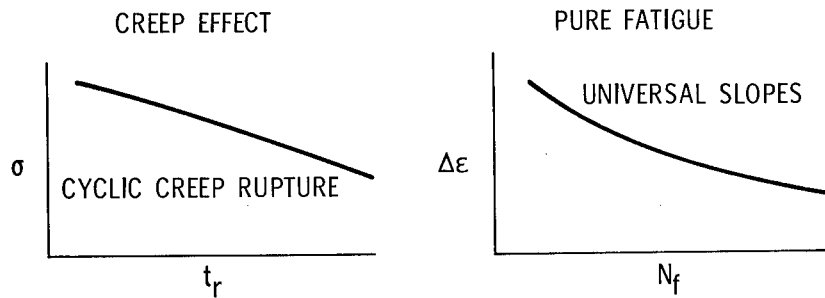


Figure 2-10. - Creep-rupture curves. Alloy, 316 stainless steel; fully annealed; temperature, 1300° F.

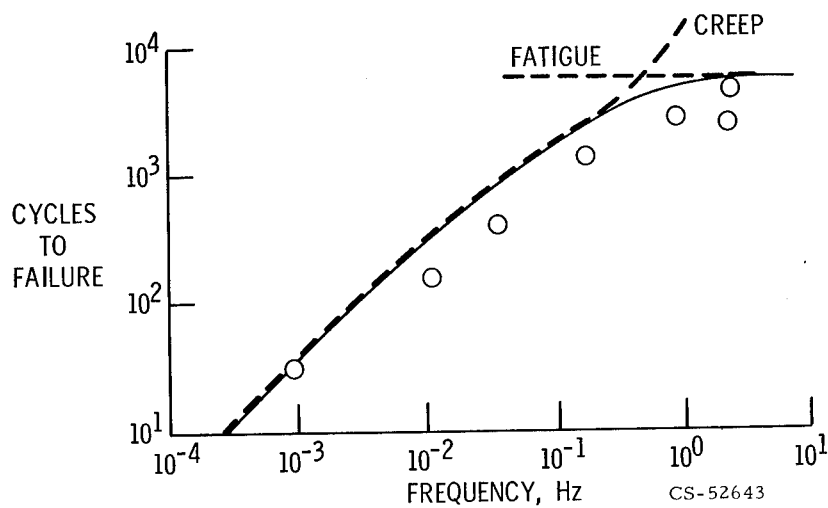


$$\sum (\text{CREEP DAMAGE}) + \sum (\text{FATIGUE DAMAGE}) = 1$$

$$\sum \frac{t}{t_r} + \sum \frac{n}{N_f} = 1$$

CS-52637

Figure 2-11. - Damage analysis by combined effects of creep and fatigue.



CS-52643

Figure 2-12. - Creep-fatigue results for cobalt-base alloy L-605.  
Temperature, 1180° F; total strain range, 0.9 percent.

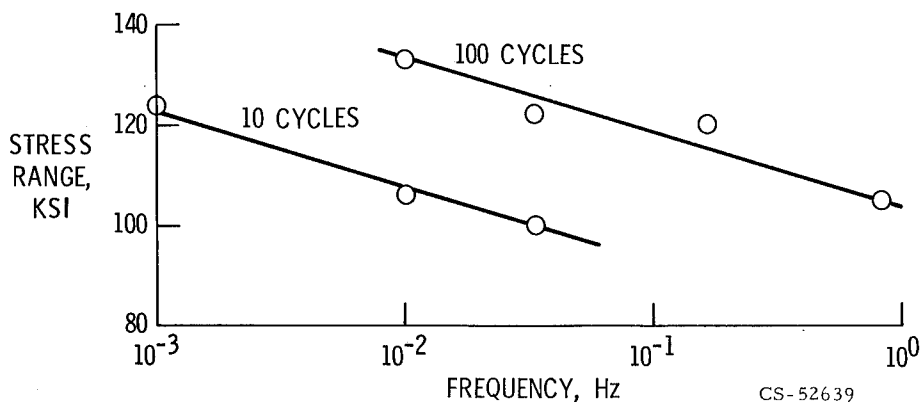


Figure 2-13. - Effect of frequency on cyclically induced stress. Cobalt-base alloy L-605; temperature, 1180° F; total strain range, 0.9 percent.

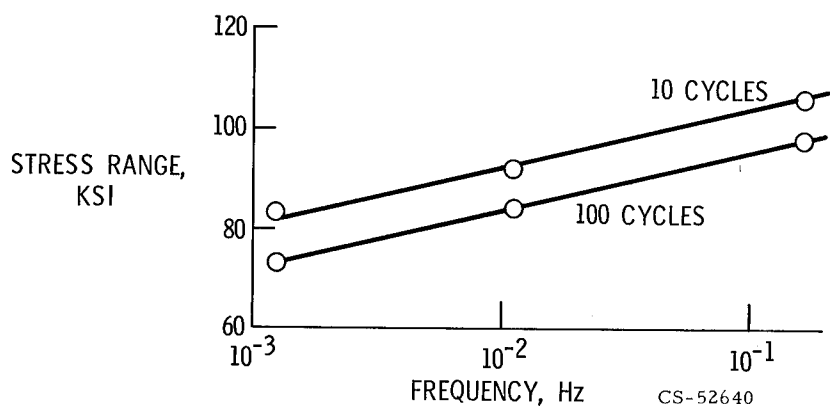


Figure 2-14. - Effect of frequency on cyclically induced stress. Alloy, 316 stainless steel; temperature, 1300° F; total strain range, 1.25 percent.

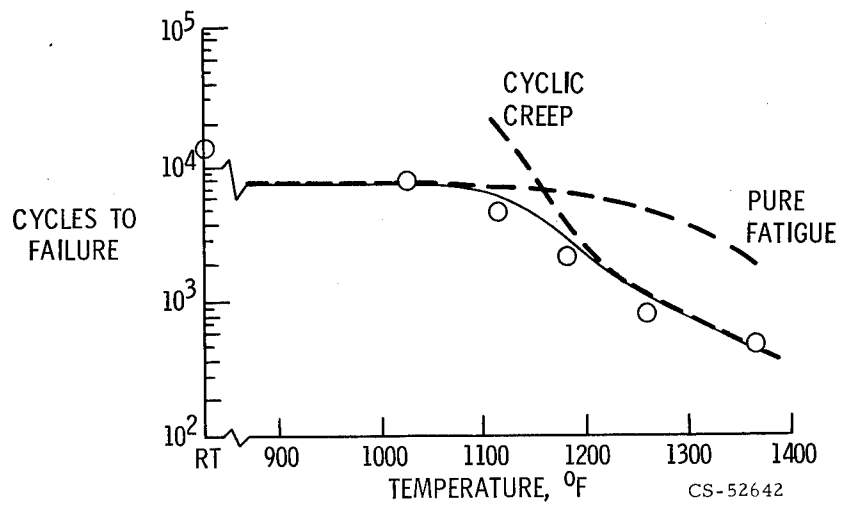


Figure 2-15. - Creep-fatigue results for cobalt-base alloy L-605. Total strain range, 0.9 percent; frequency, 0.33 hertz.

### 3. THERMAL FATIGUE OF HIGH-TEMPERATURE MATERIALS

David A. Spera

Thermal fatigue is a possible mode of failure in almost any high-temperature component. In aircraft gas turbines, thermal fatigue of blades, vanes, and disks can become the dominant failure mechanism as operating temperatures are increased, service times are lengthened, and temperature transients become more severe. This paper describes thermal-fatigue research conducted to develop a method for predicting the thermal-fatigue life of high-temperature components. Three test programs being used to evaluate the life prediction method are discussed.

The first test program consists of producing comparative thermal-fatigue data on a wide variety of nickel- and cobalt-base alloys. Fluidized beds are used for rapid heating and cooling of simple wedge-shaped specimens. The thermal-fatigue resistance of each alloy is calculated from measured transient temperatures by means of a theory which considers both low-cycle fatigue and cyclic creep. Observed and predicted cycles to crack initiation are shown to compare favorably for IN-100.

In the second test program simulated cooled turbine blades are thermally cycled in a high-velocity burner facility while under tensile load to simulate centrifugal stress. The blade specimens were cast from IN-100 and B-1900 alloys and are tested in the coated and uncoated conditions. Thermal-fatigue data produced in this program are used to evaluate the life prediction method when the complexities of airfoil shape, internal cooling, stress concentration, mean stress, and coating are introduced.

The third test program utilizes a plasma-jet heat source and sheet specimens to produce thermal fatigue in a controlled atmosphere, including an oxygen-free environment. The objective of this program is to clarify the interaction between thermal fatigue, oxidation, and the alloying effect of coatings.

Thermal fatigue is a potential mode of failure in almost any heat engine or piece of high-temperature machinery. Thermal fatigue is defined as the initiation and propagation of cracks in a material caused primarily by alternate heating and cooling. This heating and cooling almost always gives rise to a nonuniform distribution of temperature which in turn causes cyclic thermal stress. This thermal stress of course leads to thermal-fatigue cracking. Thermal fatigue can (and quite often does) occur in gas and steam turbine blades, diesel engine pistons, railroad loco-

motive wheels, die-casting machinery, electric lamps, and the heat exchanger of a house furnace. The thermal-fatigue problem of greatest concern to us is the initiation of cracks in aircraft gas turbine blades. Modern gas turbines are running at hotter and hotter temperatures in the search for increased efficiency, thrust, and economy. Service times are also being lengthened. These are just the circumstances which tend to make thermal fatigue dominant as a mode of failure. Figure 3-1 shows what thermal fatigue can do to a gas turbine blade. (This figure shows four views of the same blade, photographed at different times under different conditions of light and orientations.) After 55 hours of operation in a stationary research engine, small cracks appeared perpendicular to the sharp leading edge of this blade. After 175 hours of operation, these cracks propagated to a considerable length. The cracks opened by 278 hours, and finally, after 306 hours of operation, they caused the loss of the top half of the blade.

Our goal is to develop an ability to predict when thermal-fatigue cracks will start and how fast they will propagate under service (rather than laboratory) conditions. To do this, the thermal-fatigue research program outlined in figure 3-2 was instituted. Of course, we want to start with the simplest possible material tests and end with an assessment of component performance for the most complex turbine blades or other components which may be found. The simple material tests are as follows:

- (1) Tensile tests in which a bar specimen is broken into two pieces quickly
- (2) Creep tests in which the material is subjected to a lower load and must sustain that load for a long period of time at high temperature
- (3) Mechanical-fatigue tests (or low-cycle fatigue tests) in which a bar or tube specimen of the material is held at a constant temperature and a known history of stress or strain is applied until the material breaks

All three of these test types are isothermal. The life prediction theory, which Mr. Manson described in the previous paper (see also refs. 1 to 3), was developed on mechanical-fatigue tests and uses material properties obtained from the first two types of tests. We are developing prediction methods (represented by the large arrows in fig. 3-2) to tie together material tests, simple thermal-fatigue tests, complex rig tests, and engine component performance. The simple fluidized-bed thermal-fatigue test is described in some detail later. Its general features are a specimen with a sharp edge and a bulky center, to promote non-uniform heating and cooling, and fluidized beds which add and take away heat very rapidly. This testing under closely controlled laboratory conditions and without combustion produces exactly the same kind of thermal-fatigue cracks as are found in turbine blades. Our theory has been partially checked out with these simple thermal-fatigue tests, and we feel we are ready to proceed to much

more complicated rig tests. Here the specimens are no longer simple prisms but contain all the complexities of an actual turbine blade: airfoil shape, camber, internal and external cooling passages, external gas flow, rapid heating and cooling, and even simulated centrifugal stress. Thus, if it can be proven that our thermal-fatigue theory applies to these complicated rig specimens, we feel we will be on the way to predicting actual component performance.

The following four topics are considered in this report:

- (1) The application of life prediction theory to thermal-fatigue tests
- (2) A description of fluidized-bed thermal-fatigue testing
- (3) A description of rig testing
- (4) A brief discussion of tests instituted to determine the effect of oxidation on thermal-fatigue life

## LIFE PREDICTION METHOD

As shown in figure 3-3, when predicting thermal-fatigue life there are a series of computations which must be made. Initially, only the environment is known, and in a gas turbine engine this environment consists of the temperature and mass flow of the gases passing over the blades. We want to end the computations with an estimate of the number of cycles to crack initiation. To do this, the changing metal temperatures resulting from the environment must first be computed using the conductivity and specific heat of the alloy in question. Knowing the metal temperatures, which of course are cyclic, we compute cyclic strains using thermal expansion coefficients. When the strains are known, the cyclic thermal stresses can be calculated. This is generally the most difficult step. Here we utilize the elastic modulus of the material, its yield strength, and its creep rate. These first three steps - the computation of cyclic temperature, strain, and stress - are the most difficult parts of applying thermal-fatigue theory to an actual component. Unlike mechanical-fatigue testing at a constant temperature in a laboratory, these three items cannot be measured directly. Therefore, of necessity, life calculations can contain errors not only in fatigue theory but also in stress analysis. Knowing temperature, strain, and stress, we can calculate the cycles to crack initiation using exactly the theory described by Mr. Manson in the previous paper. This theory utilizes the ductility (ability to deform in a tensile test), tensile strength (ability to carry load for a short time), and creep-rupture strength (ability to carry load for an extended time) of the material. Thus, when our simple theory is applied to a realistic situation, we have the opportunity to evaluate the effect of a large number of thermal and mechanical properties on cyclic life.



## FLUIDIZED-BED THERMAL-FATIGUE TESTING

One of the simplest thermal-fatigue tests which we have used employs fluidized beds for rapid heating and cooling. A diagram of a fluidized-bed thermal-fatigue facility is shown in figure 3-4. A facility of this type is being operated by IIT Research Institute under contract to NASA. The beds are used in pairs - the one on the left is for heating and the other is for cooling. The beds themselves are composed of ceramic particles contained in circular retorts and supported on perforated plates. Air is pumped through the perforated plates and passes upward through the particles causing them to separate from one another. The beds develop a churning action which is similar to that of a rapidly boiling fluid. This is the origin of the name "fluidized bed." In the hot bed, heating rods of the globar type surround the retort and heat it by radiation. These electric resistance heaters and the high heat capacity of the beds are responsible for the main advantage of the fluidized-bed system for thermal-fatigue testing - high heat-transfer rates without combustion. A minimum of operator attention is required. In the cooling bed, a cooling jacket surrounds the retort instead of the heating rods. Otherwise, the two beds are the same. It is relatively easy to maintain the beds at fixed temperature levels.

The fluidized-bed specimens are simple wedges in which cracks form perpendicular to the sharp edges which heat and cool much more rapidly than the thicker center section. These cracks have all the important metallurgical factors seen in cracks in gas turbine blades. Specimens are tested in groups. Multiple specimen testing easily compares the thermal-fatigue resistance of one alloy with another, one alloy condition with another, or one coating with another. We have tested as many as 36 specimens (2 groups of 18 each) at one time. The transfer mechanism lifts a group of specimens up from the heating bed, moves it laterally to a position over the cooling bed, and then plunges it into the lower temperature bed.

The results of these tests can be plotted as the average cycles to crack initiation against the heating time - that is, the amount of time the specimens are in the hotter fluidized bed. This is done in figure 3-5. In these cycles, the hot bed was held at 1900° F while the cooling bed was at 600° F. The thermal-fatigue resistance of one alloy can be compared with another without making any analysis at all. There are no theoretical lines on this plot. The lowest resistance to thermal fatigue shown in the figure is that of a typical nickel-base alloy. A cobalt-base alloy has higher resistance, while the highest resistance of these three alloys is that of a recently developed alloy, NASA TAZ 8A, which also has a nickel base. This type of comparative plot raises certain questions:

Why does TAZ 8A last as much as 80 times as long as another nickel-base alloy?

Does the cobalt-base alloy really experience an increase in life as heating times increase above 3 minutes? If so, why does it?

These are the kinds of questions our theory should be able to answer and thereby guide the development of new alloys with high resistance to thermal-fatigue cracks. Our goal is not only to provide comparative thermal-fatigue data (which we will be doing for about 28 different alloys or alloy conditions) but also to explain why an alloy behaves as it does and what might be done to improve it.

Figure 3-6 shows the application of our life prediction theory to the data for IN-100, a well-known nickel-base alloy. Again, the average number of cycles for crack initiation is plotted against the heating time per cycle. There are two theoretical lines plotted in this figure - one for fatigue and one for cyclic creep. As explained by Mr. Manson, we are accounting for both failure modes in computing life. Fatigue life, as mentioned previously, is based primarily on the range of strain experienced by the material. Creep life, on the other hand, is based on the combination of stress, temperature, and time which the material sees. Our theory indicates that at heating times in excess of 2 minutes, cyclic creep is the dominate failure mode and the correlation between theoretical and experimental lives is good. Had we run tests at shorter times, say 1 minute of heating, failure would have been dominated by fatigue rather than by cyclic creep. The dashed line shows a linear interaction between lives as calculated independently for each mode. We are now in the process of making this same analysis for the rest of the alloys being tested under this comprehensive program.

One of the conclusions we are examining is that cyclic creep is generally dominant, particularly when temperatures are very high and cycle times are long. However, some data are shown for which our theory indicates that both fatigue and cyclic creep caused failure (figs. 3-7 and 3-8). These are some of the earliest fluidized-bed thermal-fatigue data. They were generated at the National Gas Turbine Establishment in England about 10 years ago using the nickel-base alloy Nimonic 90. In figure 3-7, the average number of cycles to crack initiation is plotted against the heating time. In this case, cyclic creep is indicated as the dominant failure mode for most of the tests except for very short heating times. When heating times are shorter than 0.3 minute, creep is no longer the dominant failure mechanism. Instead, conventional fatigue occurs, based on the range of strain. In figure 3-8, maximum temperature in the cycle is the variable quantity but the same general pattern is seen. Temperature cycling here was done between room temperature and the variable maximum temperature. Creep was calculated

to be the dominant failure mode at maximum temperatures of 1500° F and above. But at more moderate temperatures, below 1500° F, fatigue is apparently the mode of failure. So, one of the conclusions which I think can be drawn is that under very high temperature service, such as in a gas turbine blade, cyclic creep is probably the dominant mode of failure; however, during more moderate temperature service and for very short periods of time, such as might be seen in die casting machinery or injection molds, fatigue could be the dominant failure mode. The theory is general enough to cover these widely differing cases.

### AIRFOIL THERMAL-FATIGUE TESTING

Application of theory to very simple fluidized-bed specimens and tests has been very encouraging for us, and we have gone on to apply this theory to much more complicated specimens as shown by figure 3-9. We are now using specimens which represent a turbine blade but in a nonrotating test rig. We have the airfoil shape, internal cooling passages running the length of the specimen, and some with surface holes and slots which allow the formation of a film of air to protect the leading and trailing edges, which are usually the critical parts of the blade. Platforms have been added to the top and bottom of the specimen so that we might apply a simulated centrifugal stress. Figures 3-10 and 3-11 show the rig in which these specimens are being tested. Figure 3-10 is a general view showing the tensile machine which can apply up to 20 000 pounds of load to the turbine blade specimen. On the left is the nozzle from a high velocity burner, which is capable of producing a 2800° F gas stream at a velocity of the speed of sound, and on the right are the exhaust ducts. Figure 3-11 is a closeup view showing the heating nozzle, the specimen in the center (fixed between platens which apply load), and a cooling nozzle to the rear. The entire tensile machine can be rotated about one of the rear corners in such a way that when rotated forward the blade specimen is in front of the heating nozzle, and when rotated to the rear it is removed from the hot gas stream and can be cooled. Thus, the distinctive feature of this rig is that very rapid heating and cooling can be applied to airfoil turbine blade specimens, and at the same time an axial load can be applied to simulate centrifugal stress. As was mentioned, this is a new program we are just now conducting, and we hope in the near future to show a correlation between thermal-fatigue theory and experimental results for the lives of these very complicated turbine blade specimens.

## OXIDATION AND THERMAL FATIGUE

One of the things we, and of course quite a few other investigators, have noticed is the presence of oxidation in thermal-fatigue cracks (see fig. 3-12). This structure is very typical of thermal-fatigue cracks. Such cracks generally occur along grain boundaries and contain oxides, as shown by the light gray areas, right out to the tip of the crack as well as in the pitted area where the crack started. And of course the question of which came first arises: Did the crack propagate through oxidation-weakened grain boundaries, or did the oxidation occur once the crack had opened the grain boundaries to the outside air? The answer is important when we try to extend thermal-fatigue life. For example, we know that if a coating, the right coating, is put on a metal we can extend its thermal-fatigue life as shown in figure 3-13. This is a simple wedge-type specimen tested in front of the same burner shown in figures 3-10 and 3-11. In this case, the cycles are 1 hour at 1900° F followed by a rapid cool to 100° F for a few minutes and then back up to 1900° F. The alloy is IN-100, a typical nickel-base alloy. In the uncoated condition, 30 cycles (or 30 hr) of operation were sufficient to cause cracking. But with a NASA aluminide coating applied to the specimen, we were able to extend the life by more than a factor of 10. On the other hand, we know that if the wrong coating is put on an alloy it can cause the surface to develop mechanical properties which increase the rate of thermal-fatigue cracking rather than decrease it even though oxygen is excluded. So what we have to know is the tradeoff between the exclusion of oxygen and the changing of mechanical properties.

To find the answer, we must be able to conduct thermal-fatigue tests in a controlled atmosphere where we can exclude oxygen at will, add coatings, or take coatings away. We are investigating several different techniques for doing this, and we are finding it relatively difficult to exclude oxygen completely. Figure 3-14, which shows one of the techniques we are pursuing, is a schematic drawing of a thermal-fatigue facility in which a plasma jet is used as a heat source. The entire test is done in a controlled atmosphere. In a plasma gun, which is the heart of this facility, argon gas is passed through a circular spark discharge and in effect electrical energy is transferred to the gas. The atoms of gas become ionized (they develop a very high velocity and a very high temperature) and thus form the plasma jet. Specimens are simple squares of sheet metal which may have a notch to concentrate stress. These are fastened to the periphery of a slowly rotating disk. A specimen passes through the plasma jet in about 1 second and the heat flux is high enough so that the temperature of the specimen can be raised to about 2000° F in the vicinity of the notch. This localized heating promotes the nonuniform temperature and thermal stress required to get thermal fatigue cracking and we can do it in a

controlled atmosphere, with or without oxygen, at will. Again, this plasma-jet facility is an experimental rig. We will be conducting further tests and have data to report in the future.

## SUMMARY

We started with a theory developed on simple isothermal tests in a mechanical fatigue testing machine where we knew the temperature, the stress, and the strain history. We are now trying to apply this theory to much more complicated thermal fatigue tests where just about everything must be calculated. We have some data on the fluidized-bed tests which indicate our theory will apply just as well to thermal fatigue. We are trying to increase the amount of our data and increase the complexity of the specimens we have tested; for example, we are using burner rig specimens that closely simulate turbine blades. Finally, we are trying to include the effects of oxidation into this theory. Aircraft gas turbine blades have been emphasized in this paper because they are the basic components we are interested in and for which we have some tangible data. However, the theory is general enough so that it can be applied to a wide variety of components.

## REFERENCES

1. Spera, David A.: A Linear Creep Damage Theory for the Thermal Fatigue of Materials. Ph.D. Thesis, Univ. Wisconsin, 1968.
2. Spera, David A.: The Calculation of Elevated-Temperature Cyclic Life Considering Low-Cycle Fatigue and Creep. NASA TN D-5317, 1969.
3. Spera, David A.: Calculation of Thermal-Fatigue Life Based on Accumulated Creep Damage. NASA TN D-5489, 1969.

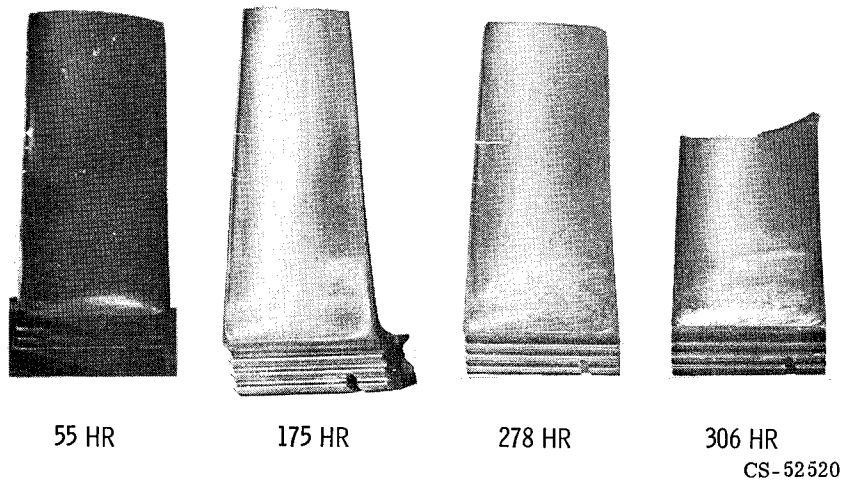


Figure 3-1. - Thermal fatigue failure in gas turbine blade.

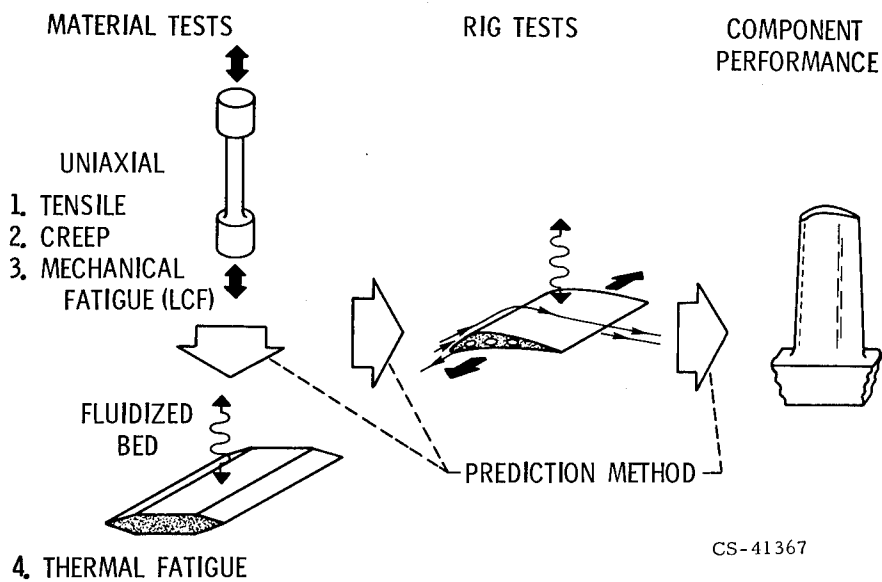
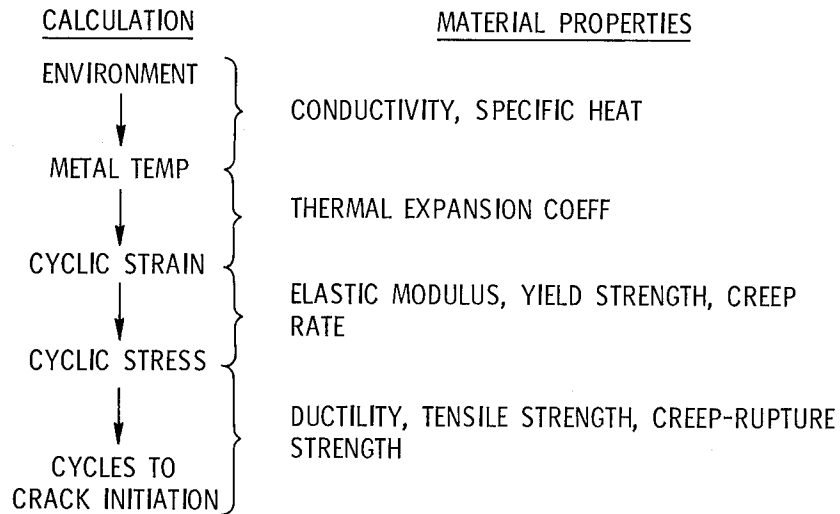
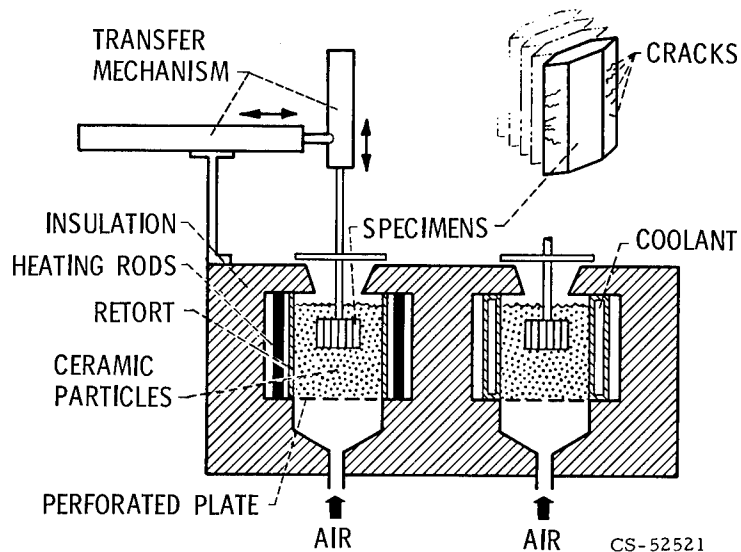


Figure 3-2. - Thermal-fatigue program.



CS-52514

Figure 3-3. - Prediction of thermal-fatigue life.



CS-52521

Figure 3-4. - Fluidized-bed thermal-fatigue facility.

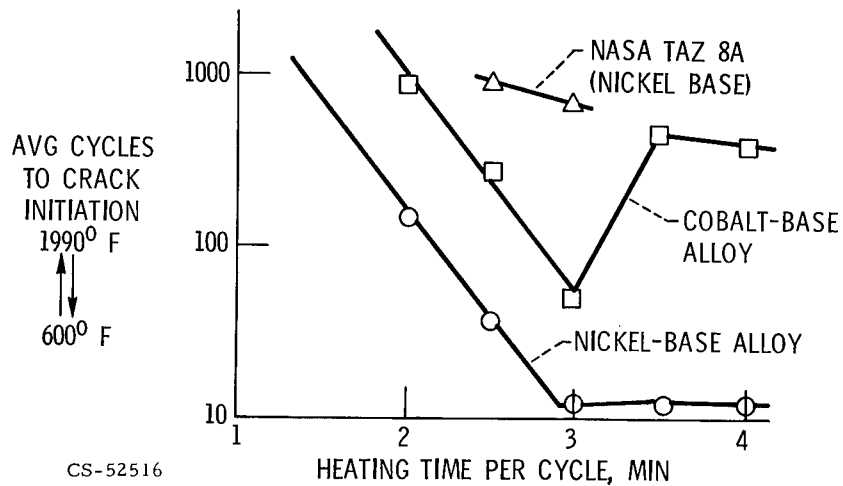


Figure 3-5. - Thermal-fatigue resistance of several alloys (IIT Research Institute, 1969).

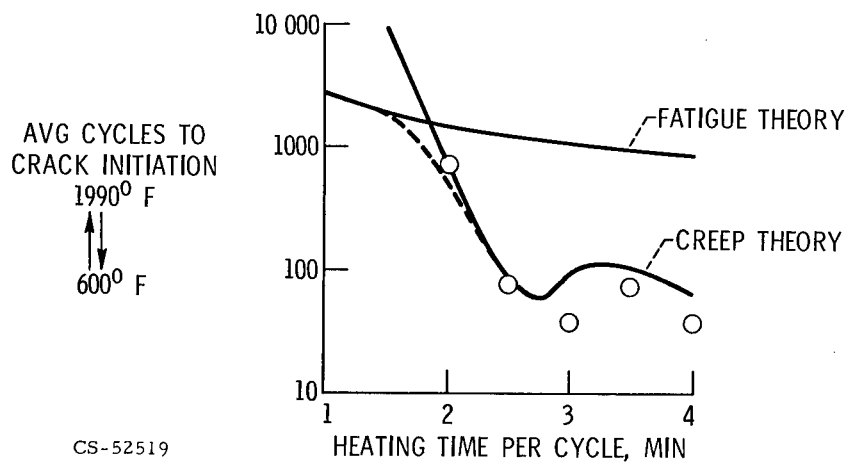


Figure 3-6. - Effect of heating time on thermal-fatigue life for IN-100 (IIT Research Institute, 1969).



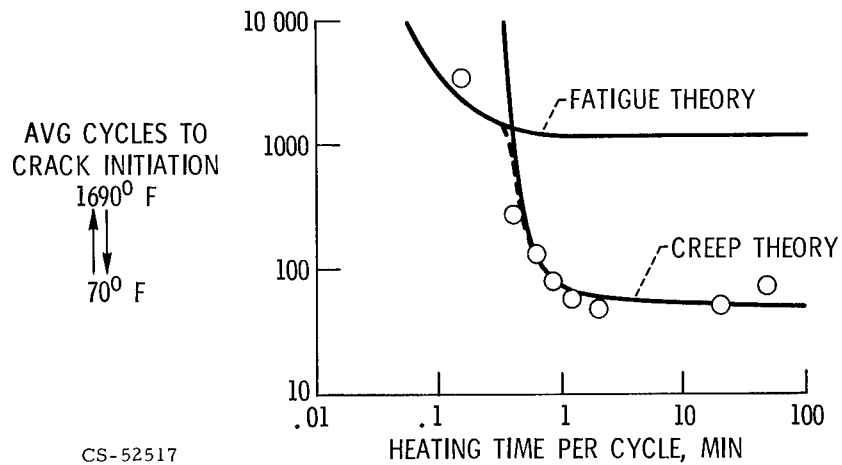


Figure 3-7. - Effect of heating time on thermal-fatigue life for Nimonic 90 (National Gas Turbine Establishment, 1959).

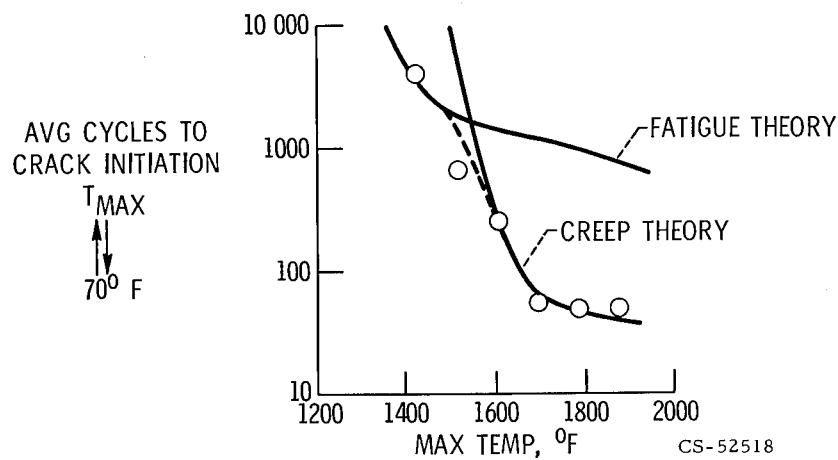


Figure 3-8. - Effect of maximum temperature on thermal-fatigue life for Nimonic 90 (National Gas Turbine Establishment, 1959).

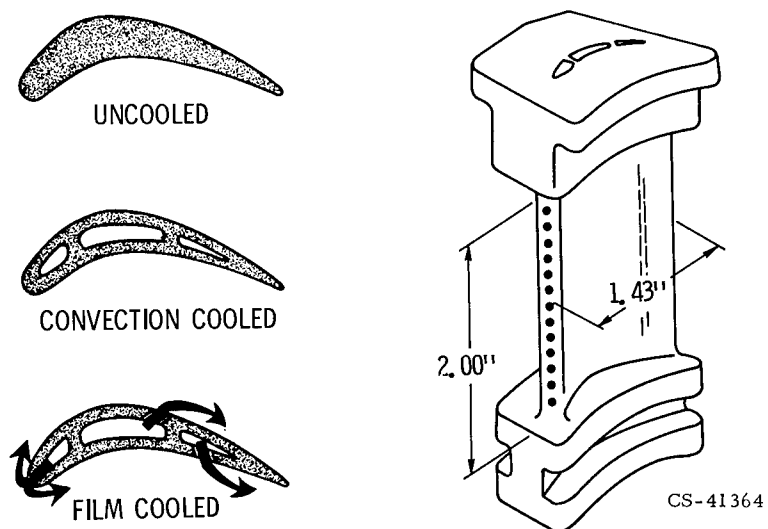


Figure 3-9. - Airfoil thermal-fatigue specimens.

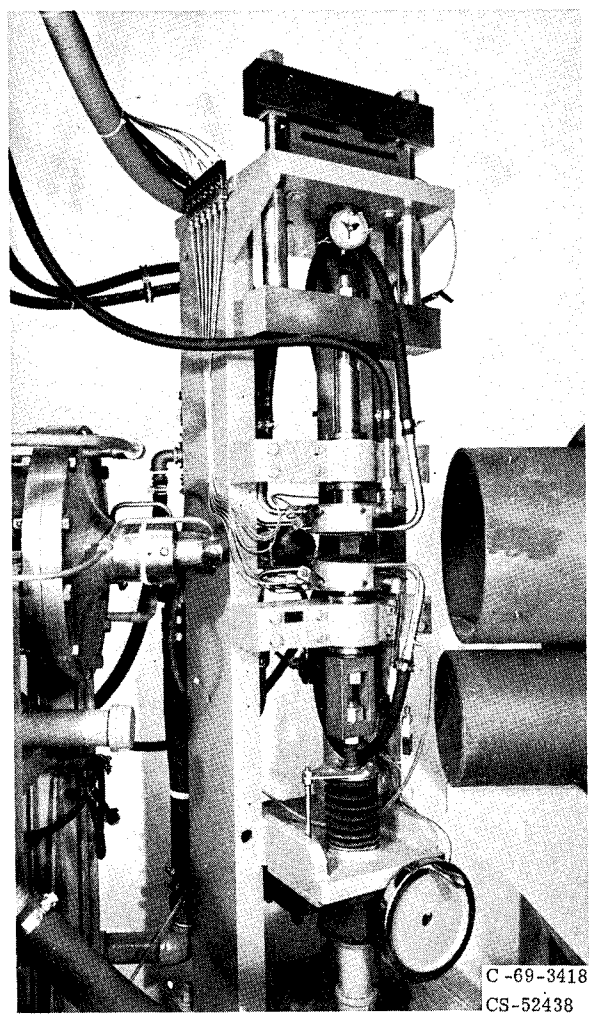


Figure 3-10. - Airfoil thermal-fatigue facility.

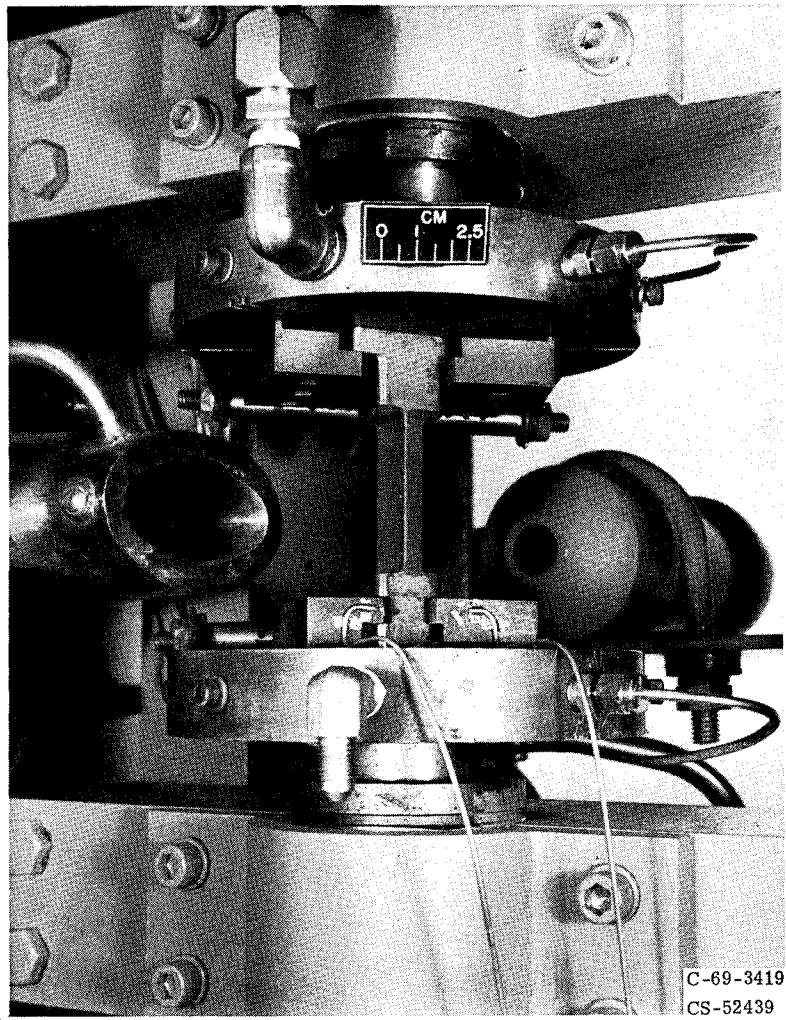


Figure 3-11. - Section of airfoil thermal-fatigue facility showing heating nozzle, specimen, and cooling nozzle.

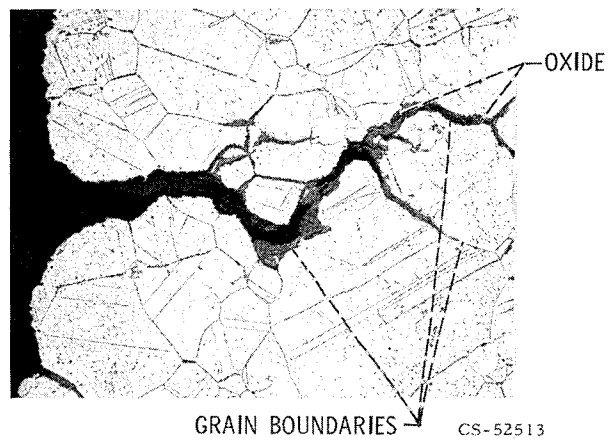


Figure 3-12. - Typical thermal-fatigue crack. X100.

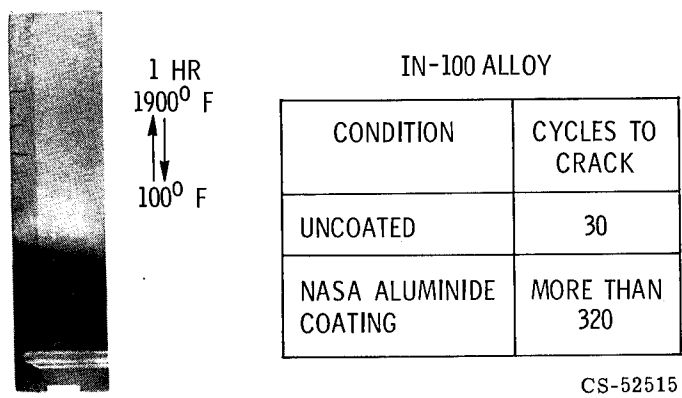


Figure 3-13. - Effect of coating on thermal-fatigue life.

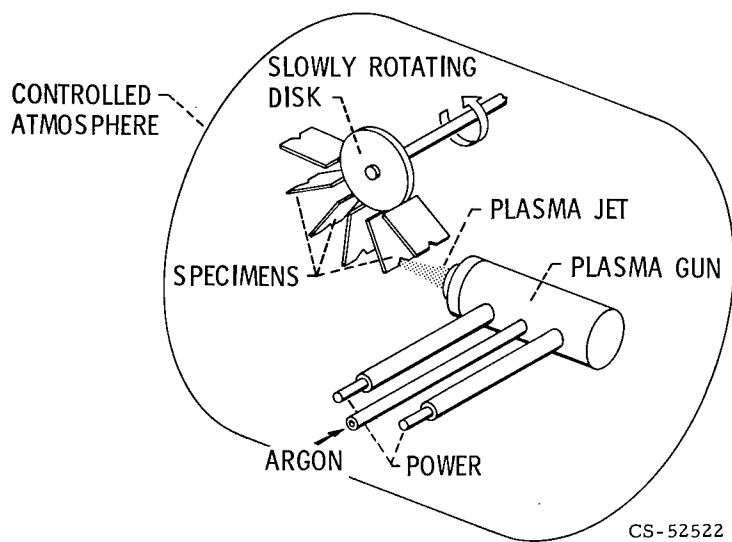


Figure 3-14. - Plasma jet thermal-fatigue facility.



#### 4. PRESENT STATUS OF THE THEORETICAL CALCULATION OF DIFFUSION AND DIFFUSION-RELATED MECHANICAL PROPERTIES

H. H. Grimes

A long range goal of the material scientist is to be able to understand the mechanical behavior of solids in terms of fundamental physical processes. With such knowledge, he can then predict their behavior under various use conditions and possibly even find new ways to improve their properties. Using the properties of steady-state creep and diffusion as examples, a discussion of the degree of success one can now attain in predicting behavior is presented. A comparison of the empirical and theoretical approach in the prediction of creep behavior is given to illustrate the value of the mechanistic approach. The dependencies of creep rate on temperature, stress, and diffusion are discussed. Solid-state diffusion is treated in greater detail based primarily on Lewis studies. The problems in determining the various parameters in the equation for the diffusion coefficient are discussed. The effect of strain on diffusion is treated briefly, and experimental techniques to evaluate these effects are described. Typical results of some of these experiments are shown. Finally, the use of interatomic potential energy functions in the calculation of the various energy and volume terms in the vacancy diffusion equation is discussed and results are shown for these computer methods applied to the computation of migration energies.

In the aerospace field, we often place extreme demands on materials. We subject them to temperatures ranging from near absolute zero to several thousand degrees, stress them to near or beyond their yield points, and place them into the hostile environments of radiation and reactive atmospheres or liquids. At the same time, we require of them reliability and constancy of properties well beyond those needed for ordinary applications.

To provide materials suitable for these applications, it is often necessary to optimize the properties of existing materials or possibly even to design new materials with the desired properties. This may require study of solid behavior at the fundamental level, to learn why solids have the properties they do and how they can be modified.

In these two rather typical equations, the constants  $A$ ,  $B$ ,  $Q$ ,  $\alpha$ , and  $n$  are adjustable parameters, determined by experiment for each material tested. What is learned about these parameters for one material does not help to predict the behavior of another material. However, some insight into the mechanism of creep can be gained from these empirical relations. For example, from the temperature dependence it appears that there is an activated rate process involved; that is, some energy barrier exists to the creep motion. Furthermore, if the constant  $Q$  is evaluated from the slope of the log of the creep rate against reciprocal temperature, the energy obtained in many cases compares remarkably well with the activation energy for bulk diffusion in that material. In table 4-I are listed the activation energies for creep and for self-diffusion in nine metals for which these data were available. The difference between these energies is only about 0.1 electron volt, or less, in most cases. However, there are real exceptions. The larger differences found for tin, iron, and possibly lead suggest that the temperature dependence of creep may not always be as straightforward as is shown in equation (1). In fact, if the process of creep is considered to depend on the movement of dislocations whose motions are impeded by jogs or steps on the dislocations, high-temperature creep results as a process of overcoming these jog barriers by diffusive motions of the atoms near the jogs. Based on this reasoning, Barrett and Nix (ref. 2), starting with some earlier ideas of Mott, derived the following equation for creep rate:

$$\dot{\epsilon} = 2\pi D \beta \left(\frac{b}{a}\right)^3 \rho_s \sinh\left(\frac{\sigma b^2 \lambda}{2kT}\right) \quad (3)$$

Several important differences between this equation and equations (1) and (2) can be noted. First, the temperature dependence is somewhat more complex, entering in several parameters, not just in the bulk diffusion coefficient, and this may indicate why the energies for creep and diffusion will not necessarily agree in all materials. Also seen clearly in this equation is the dependence of creep on diffusion and on stress.

The second noticeable difference is that this equation is written entirely in terms of known, or easily understood, constants. And this, of course, is the strength of the mechanistic approach. The constant  $\beta$  is the number of atoms per unit cell,  $b$  Burgers vector,  $a$  the lattice parameter, and  $k$  the Boltzmann constant; all are well known. The other constants, the density of mobile screw dislocations  $\rho_s$ , the average spacing between jogs in the dislocation  $\lambda$ , and, of course, the diffusion coefficient  $D$ , are not as easy to evaluate. Either experiment, special calculation techniques, or possibly even additional insights or relations must be

There are, of course, many aspects of solid behavior involved in such a study. This paper treats those aspects of the basic materials research program at Lewis that deal with solid-state diffusion. Diffusion is important because many high-temperature physical and mechanical properties involve the flow of matter which results from the migration of individual atoms in the solid. Typical mechanical properties include creep, stress rupture, fatigue, and, in some cases, even fracture itself. Also discussed is a representative diffusion-related property, steady-state creep which, in addition to setting the diffusion work into a practical perspective, further illustrates the value and the extent of the application of the basic approach in the study of materials behavior.

Learning the atomic level mechanisms that underlie the behavior of a material can often lead to new and significant developments in the field. This results from the greater informational value of relations which are derived from first principles. These relations often permit the properties of a material to be determined from a very basic knowledge of the solid; for example, from its structure, or from the knowledge of the bonding forces between its atoms. This is not to suggest that the correlational approaches which certainly have been largely responsible for the present state of material science should be abandoned. We do believe though that the mechanistic approach is now coming of age and will offer new insights into the problems of materials design - maybe just the insights needed to make the important breakthroughs.

## STEADY-STATE CREEP

To illustrate the basic approach as applied to creep, first consider, for comparison purposes, two familiar empirical relations found for the creep rate. Equation (1) shows the creep rate written as a function of temperature at constant applied stress

$$\dot{\epsilon}_{\sigma} = A e^{-Q/kT} \quad (1)$$

This is a relation observed by several early workers in the field. There is a simple exponential dependence on temperature. Equation (2) gives the stress dependence of the creep rate at constant temperature found by Garofalo in 1960 (ref. 1).

$$\dot{\epsilon}_T = B \sinh(\alpha\sigma)^n \quad (2)$$



used to evaluate them. The constants  $\rho_s$  and  $\lambda$  have been evaluated in a few specific cases. For stainless steel, aluminum, and Al-3Mg,  $\rho_s$  has been determined from etch-pit considerations, and  $\lambda$  has been estimated from the shear modulus. These constants were then used to predict the creep rate at various stress levels.

Figure 4-1 shows creep-rate data for austenitic stainless steel taken at a constant temperature of 704° C. In the figure the fit of the empirical equation of Garofalo (eq. (2)) is compared with the fit of the equation based on the jogged screw dislocation theory (eq. (3)) in which no arbitrary adjustment of parameters was made except to slightly correct  $\rho_s$  to match the creep-rate data at one stress level. The theoretical equation is seen to fit the data at least as well as the empirical one. But, considering that the theoretical equation was based almost entirely on first principle constants, the agreement with actual creep data here is somewhat more gratifying.

Now in this particular example, the experimental value for the known diffusion coefficient was used. Since the measurement of diffusion is generally difficult and time consuming, it would be of great advantage to find other ways to estimate diffusion rates. The remainder of this paper discusses methods to do this.

## DIFFUSION

As with creep, what is required is a return to first principles: to write an expression for the diffusion coefficient based on atomic mechanisms, in terms of well-known, or easily determined constants. This is somewhat easier for diffusion because it is a more fundamental process than creep and is therefore more tractable theoretically.

Now, based partly on some of our earlier theoretical work, it can be shown that the diffusion coefficient (e.g., for a vacancy mechanism) is given by the following equation:

$$D = f\gamma a^2 \nu e^{\frac{S}{k}} e^{-\frac{E_f}{kT}} e^{-\frac{E_m}{kT}} e^{\frac{P\Delta V_f}{kT}} e^{\frac{P\Delta V_m}{kT}} \quad (4)$$

This equation differs from the familiar  $D = D_0 e^{-Q/kT}$  in two ways. First, it is written to include the effects of elastic strain on diffusion, and, second, it is explicit enough that if all the parameters can be evaluated,  $D$  can be determined without recourse to experiments. The parameters include a correlation factor  $f$  which can be calculated from the geometry. It gives the extent to which the diffusion jumps are nonrandom. The parameter  $\gamma$  is a structure constant known from the crystal geometry,  $a$  again is the lattice parameter,  $\nu$  is a simple function of

the atom vibration frequency in the solid, and  $S$  is the vibrational entropy and can be estimated from  $\nu$ . These parameters are all either well known or can be easily determined from other well-known parameters.

The temperature dependence of diffusion enters in the exponential factors which include the energy and volume terms: the vacancy formation energy  $E_f$ , the migration energy  $E_m$ , and the crystal volume changes due to vacancy formation and migration  $\Delta V_f$  and  $\Delta V_m$ . These terms, of course, add together to  $Q$ , the measured activation energy for diffusion. In general, these terms are not easy to evaluate: they require special techniques and this is where the real problem of predicting diffusion rates is.

Several aspects of this problem have been studied at Lewis. The theory has been extended to include effects of strain on diffusion, both for elastic strains (ref. 3) and for systems which the straining results in permanent deformation or cold working. Indications are that plastic deformation leads to an enhancement of diffusion, due to the more rapid diffusion down new dislocations or subboundaries produced by the deformation. This effect will, of course, be noticed more at lower diffusion temperatures. However, since this does not directly affect the factors in equation (4), further discussion will be reserved for another time.

For homogeneous elastic straining, our theory shows the main effect of strain to be a change in the height of the energy barrier that must be overcome in the diffusion jump. Equation (4) gives the dependence for the case of a uniform volume strain. This would be the situation, for example, in a system under hydrostatic pressure. In most cases, that is, for small strains, these last two factors will become 1.

But, for large hydrostatic pressures, the effect may not be small. In the case of hydrostatic compression, the vacancy diffusion rate decreases in systems under high pressures since the activation energy is increased by the  $P\Delta V$  terms. The magnitude of the effect can be measured experimentally; figure 4-2 shows Nachtrieb's results for lead at 301° C (ref. 4). Note that equation (4) predicts the correct functional dependence on pressure. Notice also that for this metal an order of magnitude change in the diffusion coefficient results from a pressure of about 8000 atmospheres.

Experimental techniques have been developed at Lewis which enable us to measure the vacancy formation volume and also to independently measure the volume change due to the atom migrating. These techniques involve the successive heating, rapid quenching, and then controlled annealing of fine wire samples, all done at pressures to about 10 000 atmospheres. The electrical resistivity of the wire is measured, and this is related to the vacancy concentration.

Figure 4-3 shows the data used to determine the formation volume, or volume

of the vacancy. The metal studied was gold (ref. 5). The vacancy volume is obtained from the slope of the semilog plot of quenched-in resistance against pressure. Here it is assumed that the resistance difference before and after quenching is due entirely to the additional vacancies created at the high quench temperature. The value found for the vacancy formation volume is 0.52, about one-half of the atomic volume. This indicates that as the vacancy is formed the atoms surrounding it relax inwards so that the total volume change of the crystal is only one-half of an atom volume per vacancy. In a similar way we could also measure the change in the crystal volume as the atom diffuses. This is done by annealing out the quenched-in vacancies at high pressures and again measuring the resistance changes.

These experiments give a detailed understanding of the role of elastic strains on diffusion. Such results are very useful in pressure forming and hydrostatic extrusion processes.

## COMPUTER TECHNIQUES

These measured volumes and energies are additionally valuable to measure the success of our computational methods for predicting diffusion. This, our most recent approach, consists of writing computer programs to calculate these volume and energy terms directly from simple crystal properties.

Briefly, the technique is this: Determine first, if it is not already known, the energy of interaction between two isolated atoms of the material as a function of their separation. This pair potential energy function can be expressed in terms of well-known properties of the solid. The following is an example of one such function, the familiar Morse equation:

$$\phi_{ij} = \mathcal{D} \left[ e^{-2\alpha(r_{ij}-r_0)} - 2e^{-\alpha(r_{ij}-r_0)} \right] \quad (5)$$

It gives the energy of attraction or repulsion between two isolated atoms separated a distance  $r_{ij}$  in terms of three constants. These constants are the pair dissociation energy  $\mathcal{D}$ , the equilibrium separation  $r_0$ , and a material constant  $\alpha$ . These constants can be determined from the measured dissociation energy, the lattice parameter, and the compressibility.

Now, using this potential energy function, the total energy of a hypothetical crystal containing several thousand atoms and a vacancy is next computed by summing up all the pairwise interactions. This may involve several hundred thousand

interactions; hence, the need for the computer. This is done for several configurations as the diffusing atom is moved through the crystal. Of course, the atoms near to the diffusing atom also move to accommodate it. The maximum energy difference from the equilibrium energy as the lattice configuration is progressively changed is the height of the diffusion barrier shown in figure 4-4; that is, the energy of migration  $E_m$ . Typical results of such calculations for several face-centered cubic and body-centered cubic metals are shown in table 4-II.

The first two columns give the experimental values of  $E_m$ , or in some cases  $Q - E_f$ , which equals  $E_m$ ; the last column shows both our and Wynblatt's (ref. 6) computed values. Since these results are for a wide variety of metals, and considering the simplicity of the calculations involved, the overall results are encouragingly good. Gold and perhaps platinum, however, show poor agreement. In these cases, the Morse function clearly does not represent the interatomic forces as well. In fact, other evidence indicates that these metals cannot be correctly described by a central force law. Currently being considered is a more sophisticated potential energy function which should be a more realistic description of nontransition metals. This new function is the so-called pseudopotential (ref. 7). It includes electronic interactions which are generally neglected or incorrectly treated in the simpler functions, so it is closer to the physical picture of the interatomic forces in solids. Regardless of the potential energy function used, however, the general technique is the same.

The energy to form a defect can also be determined in a way similar to that used to calculate the migration energy. Here the energy computed for a crystal containing the defect is compared to the energy of a perfect crystal, the difference being the formation energy.

The rearrangement, or the relaxation, of the atoms around the vacancy as it is formed has also been calculated (ref. 8). From this, the formation volume can be estimated.

## CONCLUDING REMARKS

The big advantage of a computational approach is its versatility. In principle, calculations can treat more complex structures, such as dislocations, to perhaps more precisely evaluate  $\rho_s$  and  $\lambda$  in equation (3). There is, at present, at least one laboratory tackling the problem of calculating dislocation properties using pair potentials.

However, a few words of caution are appropriate. While it is certainly true that the calculations can, in principle, be set up for more complicated systems,

only simpler systems and properties have been considered, to date, because of computing costs and the limitations of computer memories. Where this is not a problem, a second major difficulty may prevail. This is the choice of the proper potential energy function. The failure of the simpler functions for certain metals has been mentioned. Similar problems can be expected with the application of these methods to other systems, to alloys, or to covalent or ionic solids. Additional work with other potential functions, such as the pseudopotential, is clearly needed.

Nevertheless, some success has been achieved with our beginning efforts. The overall mechanistic approach, especially with the computer techniques, is a powerful one, and one which, we believe, will lead to an increasing contribution of the basic scientist towards the understanding of materials behavior.

## REFERENCES

1. Garofalo, F.: Resistance to Creep Deformation and Fracture in Metals and Alloys. Properties of Crystalline Solids. Spec. Tech. Publ. No. 283, ASTM, 1961, pp. 82-98.
2. Barrett, C. R.; and Nix, W. D.: A Model for Steady State Creep Based on the Motion of Jogged Screw Dislocations. Acta Met., vol. 13, no. 12, Dec. 1965, pp. 1247-1258.
3. Girifalco, L. A.; and Grimes, H. H.: Effect of Static Strains on Diffusion. Phys. Rev., vol. 121, no. 4, Feb. 15, 1961, pp. 982-991.
4. Nachtrieb, N. H.: Self-Diffusion in Liquids and Crystalline Solids. Isotopes in Research. Vol. 20 of Proceedings of the Second United Nations International Conference on the Peaceful Uses of Atomic Energy. United Nations, 1958, pp. 104-107.
5. Grimes, Hubert H.: Vacancy Formation in Gold Under High Pressure. J. Phys. Chem. Solids, vol. 26, 1965, pp. 509-516.
6. Wynblatt, P.: Calculation of the Vacancy Migration Energy in Cubic Crystals. J. Phys. Chem. Solids, vol. 29, 1968, pp. 215-224.
7. Harrison, Walter A.: Pseudopotentials in the Theory of Metals. W. A. Benjamin, Inc., 1966.
8. Grimes, H. H.; and Rice, J. H.: Vacancy Relaxations in b.c.c. Crystals. J. Phys. Chem. Solids, vol. 29, 1968, pp. 1481-1484.

TABLE 4-I. - ACTIVATION ENERGY FOR  
CREEP AND DIFFUSION

Metal	Activation energy, Q, eV		Difference, eV
	Creep	Diffusion	
Al	1.55	1.43	0.1
Au	2.05	1.95	.1
Cd	.91	.80	.1
In	.72	.78	.1
Mg	1.26	1.39	.1
Ni	2.8	2.9	.1
Pb	.93	1.12	.2
$\gamma$ -Fe	3.2	3.0	-.2
$\alpha$ -Fe	3.2	2.6	-.6
Sn	.91	0.26 to 0.46	-0.65 to -0.45

TABLE 4-II. - VACANCY  
MIGRATION ENERGY

Metal	Migration energy, kcal/mole		
	Experimental		Calculated, $E_m$
	$E_m$	$Q - E_f$	
Cu	24.8	-----	20.8
Ag	19.2	-----	23.8
Au	19.4	-----	39.5
Al	15.0	-----	15.2
Pt	33.5	-----	56.5
Ni	23 to 35	-----	28.0
Pb	-----	15.0	17.5
W	-----	57.0	52.1
Mo	-----	30.0	31.0
Na	-----	.70	.58

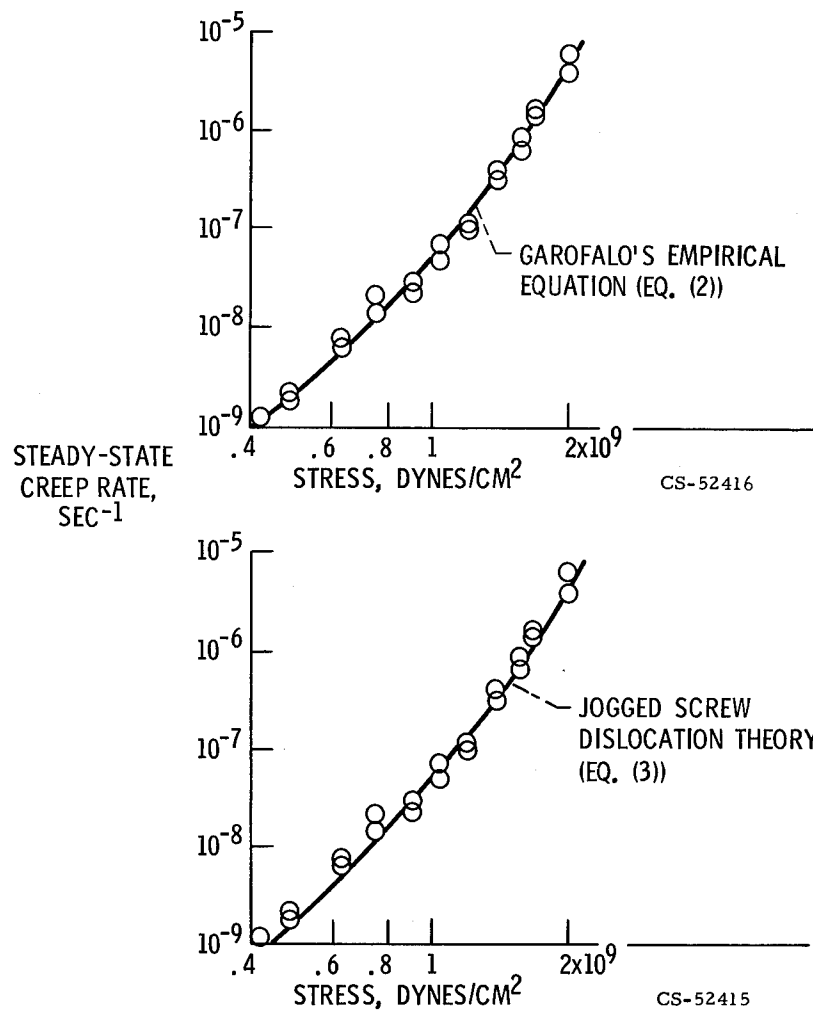


Figure 4-1. - Fit of empirical and theoretical equations to creep data.  
Austenitic stainless steel at 704° C.

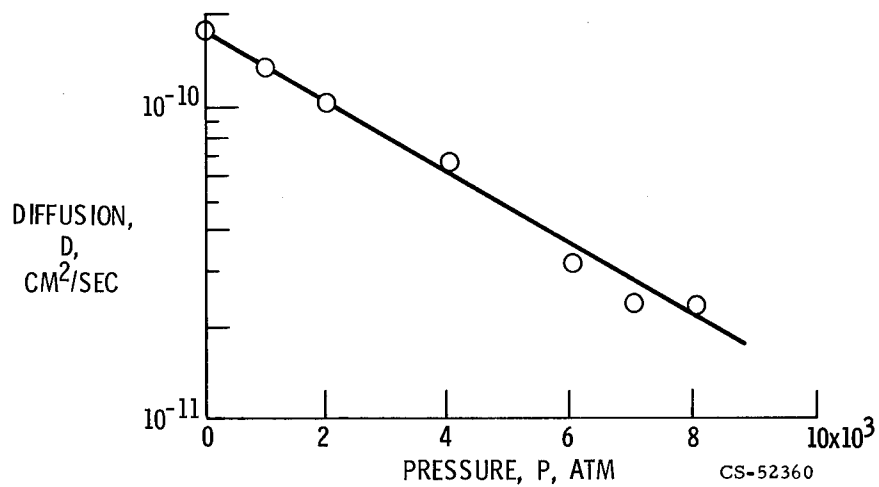


Figure 4-2. - Self-diffusion in lead at 301° C as function of pressure.

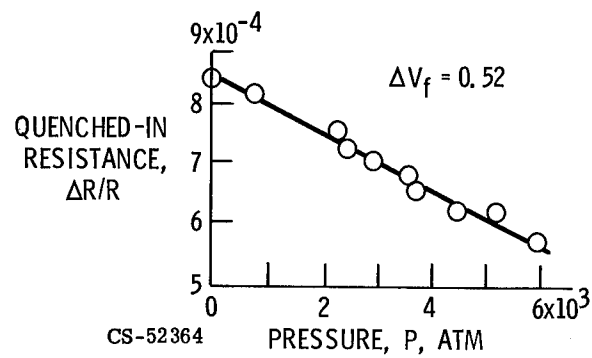


Figure 4-3. - Determination of vacancy formation volume for gold at 600° C.

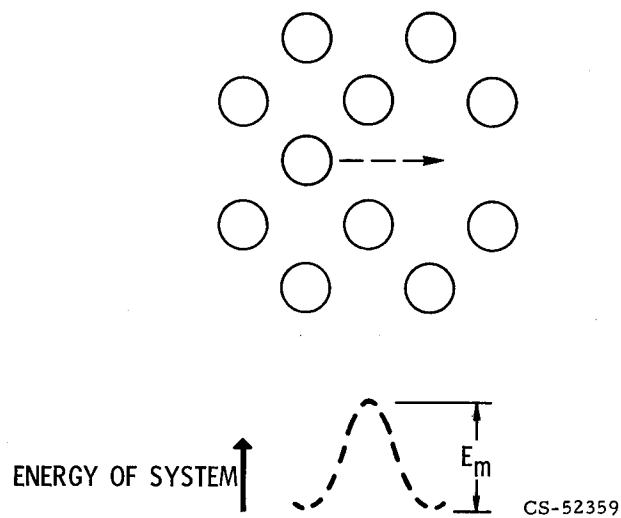


Figure 4-4. - Calculation of migration energy.





## 5. NICKEL-BASE ALLOYS FOR AEROSPACE APPLICATIONS

John C. Freche

Alloying techniques together with directional solidification were applied to achieve a nickel-base alloy for potential application to the first-stage turbine stator vanes of advanced gas turbine engines. Prealloyed powder techniques were used to improve the properties of the NASA TAZ-8A alloy and alloy 713C for potential application to turbine and compressor disks and the latter stage compressor blades of such engines.

By limiting the number of alloying constituents and making tungsten the primary alloying constituent, a nickel-base alloy designated WAZ-20 was developed which has an incipient melting temperature of 2375° F, about 150° F higher than conventional highly alloyed cast nickel-base alloys. Its tensile strength at 2200° F is 20 000 psi. Substantial increases in intermediate-temperature tensile strength and generally increased ductility and stress-rupture life were obtained with the alloy in the directional polycrystalline form as compared to the random polycrystalline form. It does not appear to be subject to formation of embrittling phases and has significantly higher impact strength than available cast nickel-base alloys.

Prealloyed powder products of TAZ-8A and alloy 713C were made by inert-gas atomization and extruded into bar stock. Tensile strength of the powder products was substantially greater than that of their cast counterparts up to 1400° F. In the 1800° to 2000° F range, the powder products exhibited superplasticity. It was possible to take advantage of this superplastic behavior to deform the prealloyed powder products into any desired shape. Simultaneous application of pressure and temperatures above the incipient melting point suggests a means of achieving the coarseness of microstructure needed to improve high-temperature strength of prealloyed powder products.

Cast and wrought nickel-base alloys are the workhorse materials for the "hot components" of gas turbine engines, and will probably continue to be for some time to come. There are a number of reasons for this. The major reasons are that such alloys have high strength in the temperature range up to 2000° F; they have generally good oxidation resistance, although coatings are certainly required for high-temperature application; and, finally, a vast backlog of experience has been accumulated by industry in casting, working, and repairing nickel-base alloys. The latter aspects are particularly important to the reliability and economic use of these materials in gas turbine engines.

Figure 5-1 shows a schematic diagram of a jet engine. The "hot components" of the engine that are discussed in this paper are the first stage turbine stator vanes, the first stage turbine disk, and the latter compressor stages, both disks and blades. In advanced engine designs, the first stage turbine stator vanes can reach metal temperatures of 2000° to 2200° F. Despite internal cooling applied to the first stage turbine rotor blades, considerable heat is conducted to the disk, so that the maximum disk metal temperatures can be 1200° to 1400° F. Considerable heat is generated in compressing the air, so that the latter compressor stages reach metal temperatures of 1000° to 1200° F. It therefore becomes an important objective of superalloy research to improve the properties of nickel-base alloys to meet the ever more severe material requirements imposed by advanced engine designs.

Over the past 8 or 9 years, we have conducted a program at the NASA Lewis Research Center which is intended to extend the capability of both nickel- and cobalt-base alloys. This program is being implemented by in-house research as well as by NASA supported contracts. The property improvements sought include increased use-temperature, increased strength, and improved oxidation resistance, to mention a few.

Figure 5-2 illustrates chronologically some of the advances we have made with nickel-base alloys. Shown on a plot of temperature against time are the 15-ksi isostress lines for several NASA alloys, beginning with TAZ-8 in 1961 (ref. 1). In 1965, a superior oxidation resistant alloy, TAZ-8A, was achieved, but at a considerable trade-off in strength (ref. 2). In 1967, alloy VI-A was developed at TRW, Inc. under NASA sponsorship (ref. 3). This alloy represents one of the strongest high-temperature nickel-base alloys available today. For purposes of comparison, the 15-ksi isostress lines for two, strong, commonly used nickel-base alloys, alloy 713C and IN-100 are included (ref. 4).

It is apparent from figure 5-1 that each of the hot engine components referred to previously functions in its own particular temperature regime. Alloy design should therefore be tailored to meet the specific requirements of each application. This paper deals with recent work done at Lewis to provide improved nickel-base materials for potential application to the first stage turbine stator vanes, the first stage turbine disk, and the latter stage compressor disks and blades of advanced engines. This work is described in greater detail in references 5 and 6, respectively.

The temperature requirements of the first stage turbine stator vanes represent the highest end of the temperature spectrum for nickel alloys. Alloying techniques together with conventional casting and controlled solidification were used to achieve an entirely new alloy formulation with substantial increases in material capability over currently used alloys for this application. For the other applications, the first stage turbine disk and the latter compressor stage components, which incidentally

represent the lower end of the temperature spectrum for nickel-base materials, prealloyed powder techniques were employed to upgrade the capability of two existing alloy compositions, alloy 713C and TAZ-8A.

## ALLOY FOR STATOR VANE APPLICATION

The major requirements that a material must meet in order to be used as a first stage turbine stator vane in advanced engine designs are as follows:

- (1) Use-temperature above 2000° F
- (2) High incipient melting point
- (3) Microstructural stability
- (4) Good impact resistance
- (5) Oxidation resistance

Most important, we must extend the use-temperature capability above 2000° F, since this is about the maximum temperature at which present nickel-base alloys can be used under reasonably high stresses. Coincident with this requirement is the need to increase the incipient melting temperature over the level found in currently used alloys so as to avoid the possibility of vane failure from localized overheating. Local hotspots as much as 150° F higher than the average vane metal temperature can occur as a result of uneven combustion gas profiles. A third requirement is microstructural stability in the sense of avoiding the formation of possible embrittling phases during longtime exposure to elevated temperatures. Fourth, good impact resistance is needed to prevent possible foreign object damage. Finally, good oxidation resistance is needed. However, with regard to this requirement, it should be noted that all nickel and cobalt alloys must be coated to operate satisfactorily for long times at high temperatures in an engine environment.

In order to achieve the first two objectives, we felt that a radical departure from current nickel-base alloy formulations was needed. Nickel-base alloys in use today are metallurgically very complex and can contain as many as 10 or more alloying constituents. Generally speaking, the larger the number of alloying constituents, the more the melting point of the resulting alloy is depressed. Therefore, we considered it mandatory to drastically reduce the number of alloying constituents. Second, we decided to make the principal alloying constituent one that would tend to raise rather than lower the alloy melting point.

Examination of existing phase diagrams indicated that only a few elements can be added to nickel which will increase the melting point of the resulting alloy. The most effective additive in this respect is tungsten. Figure 5-3 illustrates a portion of the nickel-tungsten phase diagram taken from reference 7. It is apparent that an

addition of 35 weight percent tungsten to nickel will increase the melting point of the resulting alloy by approximately 100° F over that of unalloyed nickel. Also, marked differences in atomic diameter between tungsten and nickel serve to introduce strain to the lattice when these two elements are combined, thus enhancing alloy strength. Tungsten was therefore chosen as the principal alloying constituent. The nominal composition in weight percent of our alloy, designated WAZ-20, is as follows:

W	Al	Zr	C	Ni
17 to 20	6 to 7	1.4 to 1.6	0.10 to 0.20	Balance

Besides tungsten, the other alloying constituents were limited to aluminum, zirconium, and carbon. Aluminum was added to form the Ni<sub>3</sub>Al intermetallic compound phase, or as it is better known, the  $\gamma'$  phase, which is the principal strengthening phase in nickel-base alloys to about 2000° F. Above this temperature, this phase tends to lose its effectiveness as a strengthener. Aluminum also contributes to alloy oxidation resistance, and its low density serves to offset the high density of tungsten. The measured density of the alloy is between 0.323 and 0.329 pound per cubic inch, which is somewhat higher than conventional, highly alloyed, nickel-base alloys. However, this is not too serious from the standpoint of adding to engine weight since the turbine stator vane is not a rotating component. Zirconium and carbon were added to provide stable-grain-boundary carbides so as to prevent grain-boundary sliding at high temperatures and thereby enhance high-temperature creep-rupture strength. The amounts of each of these elements which comprise the final composition were determined experimentally to give an alloy with good high-temperature properties but at the same time ensure the ability to achieve reproducible, sound castings with a minimum of segregation. Further modifications of this composition may be possible, which could result in an alloy with reduced density. This aspect is currently under investigation.

The degree to which we have succeeded in meeting the requirements for a first stage turbine stator vane material will now be discussed.

Table 5-I shows the incipient melting points (i. e., the temperature at which some of the minor phases present in an alloy will melt) of WAZ-20 along with those of representative current superalloys. The incipient melting point of WAZ-20 is 2375° F, approximately 100° to 165° F higher than conventional, highly alloyed, nickel-base materials being used today. This is, of course, an obvious advantage in overcoming the potential problem of localized hotspots in gas turbine stator vane materials. Also shown in the table are the incipient melting temperatures of two representative cobalt-base alloys. Because cobalt has a higher melting point than

nickel, cobalt-base alloys generally have higher incipient melting temperatures than nickel-base alloys. This is one reason why they are often used as stator vanes in engines. Their potential for this application is also under investigation at Lewis. Nevertheless, it is apparent that the incipient melting temperature of WAZ-20 is as high or higher than those of current cobalt-base alloys.

The increased melting point of WAZ-20 is further reflected in its high-temperature strength. Figure 5-4 shows a comparison of the 2200° F ultimate tensile strength of WAZ-20 with those of representative nickel-base materials. At this temperature WAZ-20 has an ultimate tensile strength of 20 ksi, about two to three times that of conventional, highly alloyed, nickel-base alloys such as B-1900 and the TAZ-8 series. It is interesting that it also shows a substantial strength advantage over TD-nickel, which is normally superior to cast nickel-base alloys in this temperature range and is therefore also a competitor for first stage turbine stator vane applications.

We have also applied directional solidification techniques, as originally pioneered by Pratt & Whitney, to WAZ-20 and found that further improvements in properties can be realized. Figure 5-5 shows the macrostructure of conventionally cast and directionally solidified tensile bars of WAZ-20. In the directionally solidified bar, the grains are aligned parallel to the stressed axis, whereas a randomly oriented grain structure exists in the conventionally cast bars. Since superalloys usually fail intergranularly at high temperatures, it might be expected that improved high-temperature strength and ductility could be achieved by eliminating grain boundaries transverse to the major stress axis. This was true for WAZ-20 and is illustrated in figures 5-6 and 5-7.

The tensile properties of WAZ-20 in the random and directional polycrystalline form are compared over a range of temperatures in figure 5-6. The ultimate tensile strength is increased by about 20 percent by directional solidification up to 1600° F. At this temperature the increase is from 90 to 110 ksi. Elongation is improved over the entire temperature range, with the maximum increases occurring at room temperature and at the high end of the temperature scale.

The 15-ksi rupture life of WAZ-20 in the random and directional polycrystalline form is compared over a range of temperatures in figure 5-7. Stress-rupture life is increased by a factor of about 2. For example, at 1900° F, life is increased from approximately 100 to 200 hours. Or, for any given life, use-temperature is increased about 50° F. Thus, for 100-hour life, use-temperature is raised from 1900° to about 1950° F.

For stator vane applications it is important to consider other alloy properties as well as strength and high melting point. One of the more important is microstructural stability. As engine design requirements become more severe, super-

alloys used for the turbine components are required to operate for many thousands of hours. Much of this time is accumulated at intermediate temperatures of the order of 1400<sup>0</sup> to 1600<sup>0</sup> F. Recently, it has been observed that a number of nickel-base alloys became subject to the formation of embrittling phases, such as the sigma phase, upon long exposure at intermediate temperatures. Figure 5-8 shows a typical example of sigma phase formation in a commonly used nickel-base alloy, IN-100, after it was exposed for 500 hours to a temperature of 1550<sup>0</sup> F. The effect of sigma phase, which is evidenced by the needlelike precipitate, is to drastically reduce stress-rupture life and ductility. Compositional modifications can be made which will permit use of IN-100 for long periods of time without sigma phase formation. Although we would not expect sigma phase to form in WAZ-20 from a consideration of phase diagrams, we nevertheless exposed samples of the alloy for 1000 hours at 1600<sup>0</sup> F and examined them metallographically. Figure 5-9 shows the microstructure of random polycrystalline WAZ-20 at two magnifications after such exposure. There is no evidence of the formation of any acicular embrittling phase.

To further check whether the alloy was embrittled, we conducted Charpy impact tests with notched specimens of WAZ-20 in both the as-cast and aged conditions. The results are shown in figure 5-10 and compared with representative superalloys. The directional polycrystalline form of the alloy has higher impact resistance than the random polycrystalline form, as might be expected from previous comparisons of ductility. Note that the alloy after aging shows increased, rather than reduced, impact resistance compared to the as-cast condition. This tends to substantiate the earlier conclusions that it is not subject to the formation of embrittling phases, at least after 1000 hours exposure at 1600<sup>0</sup> F. These impact resistance values are substantially higher than for typical cast nickel- or cobalt-base alloys.

Finally, despite the fact that WAZ-20 does not contain chromium, it has reasonably good oxidation resistance. Although oxidation tests were not run with this alloy, the long rupture lives obtained in stress-rupture tests in air at high temperatures substantiate that the alloy has considerable oxidation resistance. In any case, a suitable coating will be required if the alloy is to function for long periods of time at high temperatures in an engine environment, which is true of even the best oxidation-resistant superalloys.

The advantages and disadvantages of WAZ-20 for application to the first stage turbine stator vanes of advanced engines can be summarized as follows:

- (1) It has approximately a 150<sup>0</sup> F higher incipient melting point than currently used alloys.
- (2) Its strength is substantially greater at 2200<sup>0</sup> F than currently used materials.

(3) It appears to be microstructurally stable.

(4) It has substantially higher impact strength than typical cast nickel- and cobalt-base alloys.

(5) It is amenable to directional solidification in that substantially improved ductility, impact strength, and rupture strength can be achieved when these techniques are applied to the alloy.

A potential disadvantage lies in its somewhat higher density, 0.323 against about 0.300 to 0.310 pound per cubic inch for more conventional, highly alloyed, nickel-base materials. However, further modifications of the alloy appear possible, which would result in reduced density.

## ALLOYS FOR DISK APPLICATION

A second experimental approach was applied to achieve advances in the intermediate-temperature ( $\sim 1000^{\circ}$  to  $1400^{\circ}$  F) strength of nickel-base alloys for potential application to first stage turbine disks and latter stage compressor components. This involved the use of prealloyed powder techniques to make both alloy 713C and NASA TAZ-8A. It should be emphasized that the use of the prealloyed powder technique need not necessarily be limited to improving alloy properties in the intermediate-temperature regime. As will be pointed out later, there is potential for significant improvements at high temperatures as well.

Figure 5-11 schematically illustrates the steps involved in making an alloy from prealloyed powders. The desired composition is first vacuum melted to ensure low oxygen content. Next, the melt is poured, and inert gas jets atomize the molten metal into small droplets which solidify into powders. These powders are then compacted by hot pressing or extrusion, or both. Finally, the compacted powders can be subjected to heat treatments to achieve required properties. It is important throughout this process to keep oxygen content low so as to avoid the formation of tightly adherent oxide films on the powders and thereby facilitate powder compaction. Two major advantages accrue from making an alloy in this way because of the rapid solidification rates of the atomized metal droplets: the grain size of the product is very small, of the order of microns, much smaller than in typical cast materials; also, the microconstituents are finer and more uniform than in cast materials. This, in turn, gives a better, more homogeneous distribution of the strengthening phases throughout the powder compact and should result in better properties.

Figure 5-12 provides a comparison of the tensile properties of TAZ-8A in the as-extruded powder form and in the as-cast condition over a range of temperatures. Both ultimate tensile strength and percent elongation are plotted against tempera-



ture. Room-temperature ultimate tensile strength almost doubled (from 128 to 228 ksi). This advantage in strength over the as-cast condition is maintained up to 1200° F. Above approximately 1500° F the powder product shows decreasing strength compared to its cast counterpart. This need not concern us for the particular engine components under consideration, which all function below 1400° F. Elongation increased with increasing temperature. At 1800° F the TAZ-8A powder product was superplastic. Similar behavior was observed with the alloy 713C powder product.

The advantages of the prealloyed powder method in obtaining improvements in intermediate-temperature strength are further shown in figure 5-13. Here the 1200° F, 105-ksi rupture properties of the prealloyed powder products for both alloys are compared to that of a conventional, wrought, nickel-base alloy, Inconel 718. The latter is used in some engines for compressor disk and blade applications. It has 100-hour life at this test condition. The heat-treated, extruded powder product of TAZ-8A had almost 1000 hours of life at this temperature. The alloy 713C powder product also had substantially higher life (about 600 hr) than conventional wrought Inconel 718. After a high-temperature solution treatment, the powder products of both alloys were given a three-step aging treatment to enhance intermediate-temperature properties (ref. 6). Comparison with a conventional wrought alloy is tenable only if the powder products can be worked. This is indeed the case, as will be discussed shortly.

Before describing the workability of the prealloyed powder products, however, it is pertinent to mention that the improvement in intermediate-temperature strength obtained with the prealloyed powder products is probably largely due to the fine grain size and retained work from the extrusion process. At high temperatures, however, the fine grain size contributes to the superplasticity phenomenon mentioned earlier. For example, because the grain boundaries are weak at high temperature, and the grain size is so small in the as-extruded powder product, the resulting large grain-boundary network area acts in a detrimental manner insofar as strength of the powder product is concerned. As a matter of fact, the powder products stretch in a manner analogous to taffy at very low applied loads at high temperatures. This is illustrated physically in figure 5-14. Shown is a TAZ-8A specimen both before and after testing at 1900° F for 4.1 hours at a stress of 1 ksi. A long (over 600 percent) neck-free elongation typical of superplastic behavior was obtained.

We have utilized this superplasticity to form the material, as shown in figure 5-15. On the left is a 5/8-inch round of as-extruded TAZ-8A powder product. This was reduced in height 75 percent without edge cracking by upsetting at 2000° F. It is important to note that merely heating the as-extruded powder product to

2200° F and then applying conventional high-strain-rate forging practice simply shattered the material.

The significance of being able to harness the superplasticity phenomenon is that it permits the prealloyed powder product to be readily formed into any required shape. This is illustrated even more dramatically in figure 5-16. By hot pressing at 2000° F under low applied loads, we were able to form the TAZ-8A extruded powder product into a simple blade shape using cast TAZ-8A dies. This serves to illustrate the potential inherent in this process. It is possible to take highly alloyed compositions which were designed to be used as cast materials and by applying the prealloyed powder process transform them into readily workable alloys.

The prealloyed powder process need not be confined to the improvement of alloys for use in the intermediate-temperature range if superplasticity can be eliminated and the alloy's resistance to deformation at high temperatures restored once the alloy has been formed into a desired shape. Various heat-treating techniques are under investigation to accomplish this. It is intended by heat treatment to grow grains comparable in size to those found in cast alloys. This will reduce the grain-boundary surface area. Since grain boundaries are relatively weak compared to the matrix at high temperatures, the resultant effect should be to increase the high-temperature strength. Unfortunately, growing grains to the desired size is not so simple in highly alloyed, complex nickel-base systems. We have found that it is necessary to expose the alloys to very high temperatures to do this, temperatures that actually exceed the incipient melting temperature. As a result, minor phase melting occurs, and regions of weakness are introduced to the alloy. To overcome this problem we are currently investigating the joint application of high temperature and pressure so as to press together the metal as it is heated and fill in any voids resulting from minor phase melting. This approach holds considerable promise, although we have not yet been able to achieve strengths equivalent to those of the as-cast alloys at high temperatures with prealloyed powder products.

To summarize, the advantages of the prealloyed powder approach, both immediate and potential, are as follows: The immediate advantages are

- (1) Existing compositions when made in this fashion have substantial strength advantages over their cast counterparts to intermediate temperatures of about 1500° F.

- (2) Cast alloys, unworkable by conventional techniques, can be transformed into workable materials thereby making them amenable to applications such as turbine disks, compressor disks, and blades.

Potential advantages are

- (1) Increased high-temperature strength can be expected with existing alloys

because of the finer distribution of the strengthening phases inherent in the pre-alloyed powder process if suitable heat-treating methods can be developed.

(2) Again, because of the finer distribution of the microconstituents and the corresponding lack of segregation of these constituents, new alloys can be designed or tailored to contain higher alloy content than is possible using casting techniques. This, in turn, should contribute to the development of alloys with still greater strength.

## REFERENCES

1. Freche, John C.; Waters, William J.; and Riley, Thomas J.: A New Series of Advanced-Temperature Nickel Base Alloys. High Temperature Materials - II. G. M. Ault, W. F. Barclay, and H. P. Munger, eds., Interscience Publ., 1963, pp. 215-228.
2. Waters, William J.; and Freche, John C.: Investigation of Columbium-Modified NASA TAZ-8 Superalloy. NASA TN D-3597, 1966. (Also "A High Strength Nickel-Base Alloy With Improved Oxidation Resistance up to 2200° F." J. Eng. Power, vol. 90, no. 1, 1968, pp. 1-10.)
3. Collins, H. E.: Development of High Temperature Nickel-Base Alloys for Jet Engine Turbine Bucket Applications. Rep. TRW-ER-7162, TRW, Inc. (NASA CR-54507), June 20, 1967.
4. Anon.: High Temperature, High Strength Nickel Base Alloys. Rev. ed., International Nickel Co., Inc., 1964.
5. Waters, William J.; and Freche, John C.: A Nickel Base Alloy, WAZ-20, With Improved Strength in the 2000° to 2200° F Range. NASA TN D-5352, 1969.
6. Freche, John C.; Waters, William J.; and Ashbrook, Richard L.: Evaluation of Two Nickel-Base Alloys, Alloy 713 C and NASA TAZ-8A, Produced by Extrusion of Prealloyed Powders. NASA TN D-5248, 1969.
7. Hansen, Max; and Anderko, Kurt: Constitution of Binary Alloys. Second ed., McGraw-Hill Book Co., Inc., 1958, p. 1058.

TABLE 5-I. - INCIPIENT MELTING  
TEMPERATURES OF SUPERALLOYS

Alloy	Incipient melting temperature, °F
Nickel base	
WAZ-20	2375
VI-A	2275
B-1900	2220
MAR-M200	2220
IN-100	2210
Cobalt base	
WI-52	2375
MAR-M302	2260

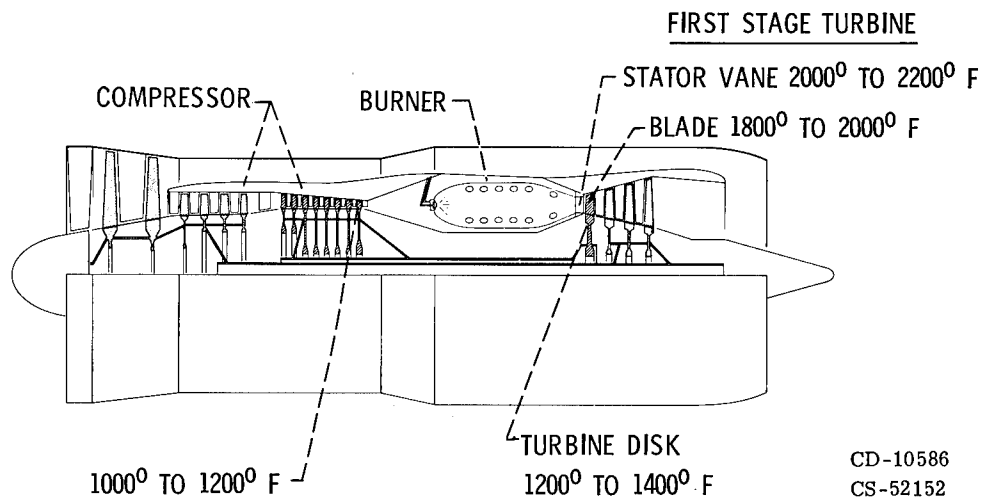


Figure 5-1. - Schematic diagram of jet engine.

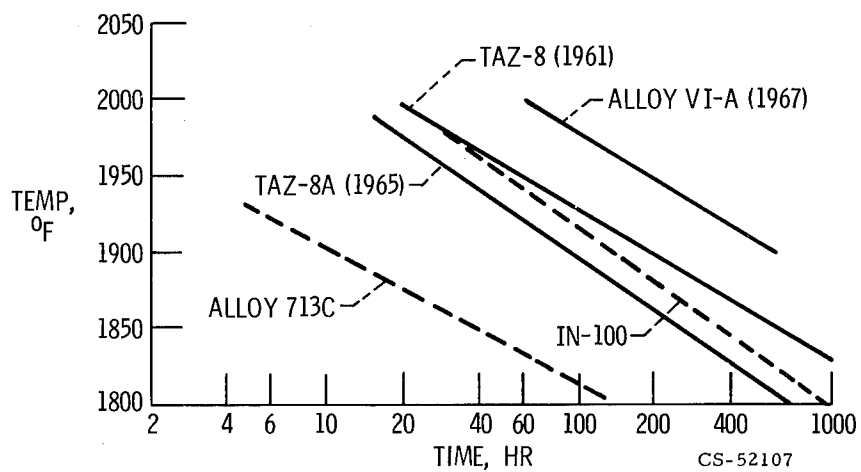


Figure 5-2. - Progress in superalloys. Stress, 15 ksi.

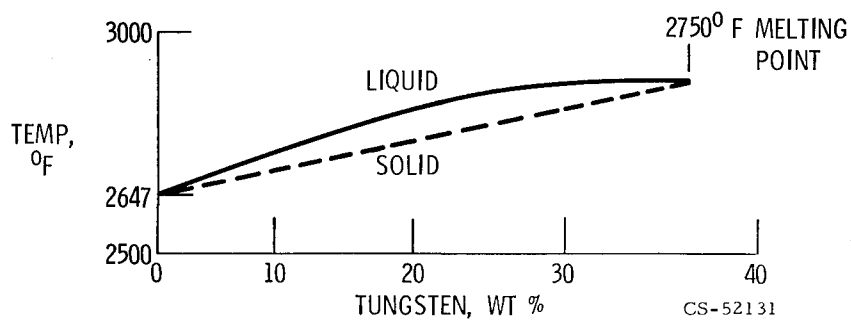


Figure 5-3. - Portion of nickel-tungsten phase diagram.

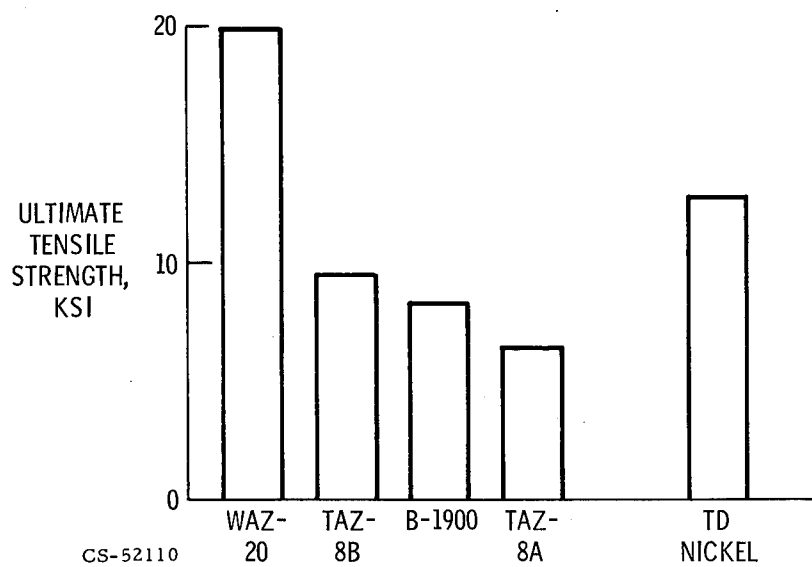


Figure 5-4. - Strength of nickel-base alloys at 2200°F.

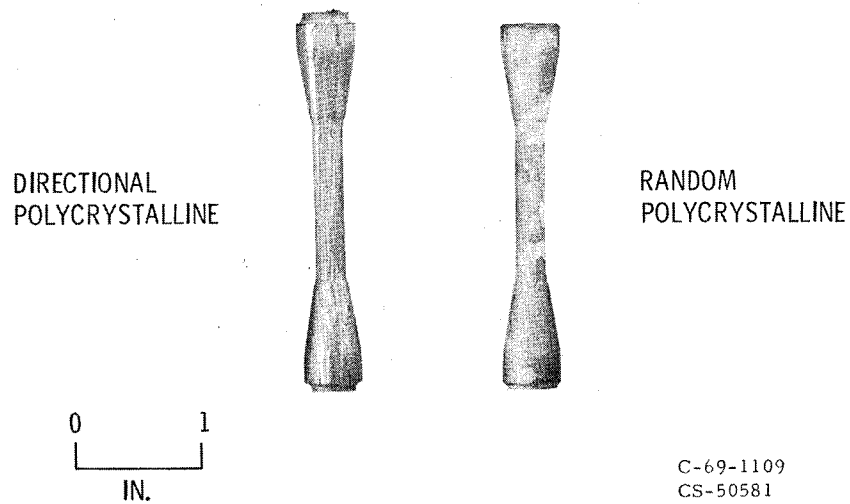


Figure 5-5. - Two cast forms of WAZ-20. Surface etched.

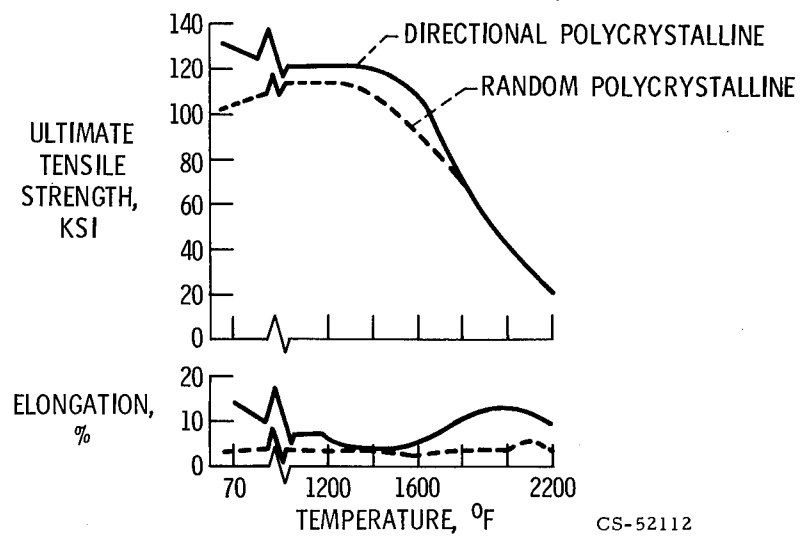


Figure 5-6. - Effect of directional solidification on tensile properties of WAZ-20.

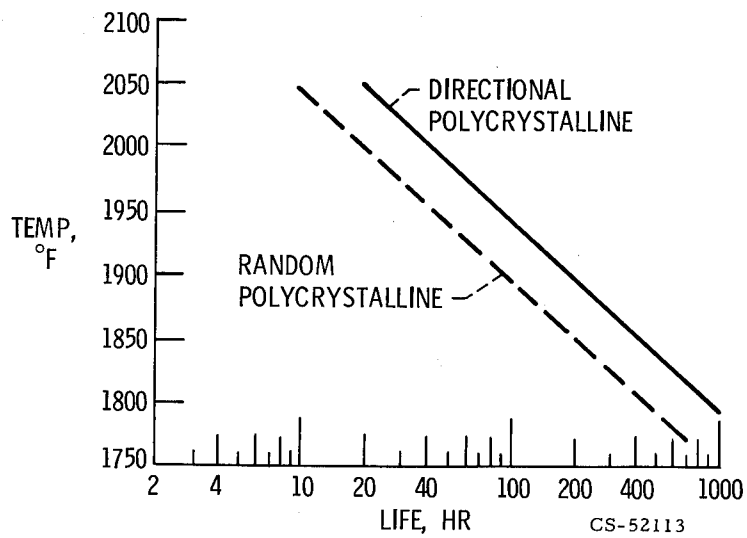


Figure 5-7. - Effect of directional solidification on rupture properties of WAZ-20. Stress, 15 ksi.

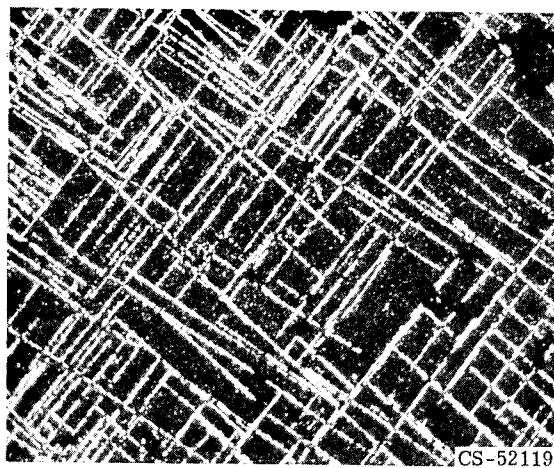


Figure 5-8. - Typical sigma phase formation. Coarse-grained IN-100 exposed 500 hours at 1550° F. X750.



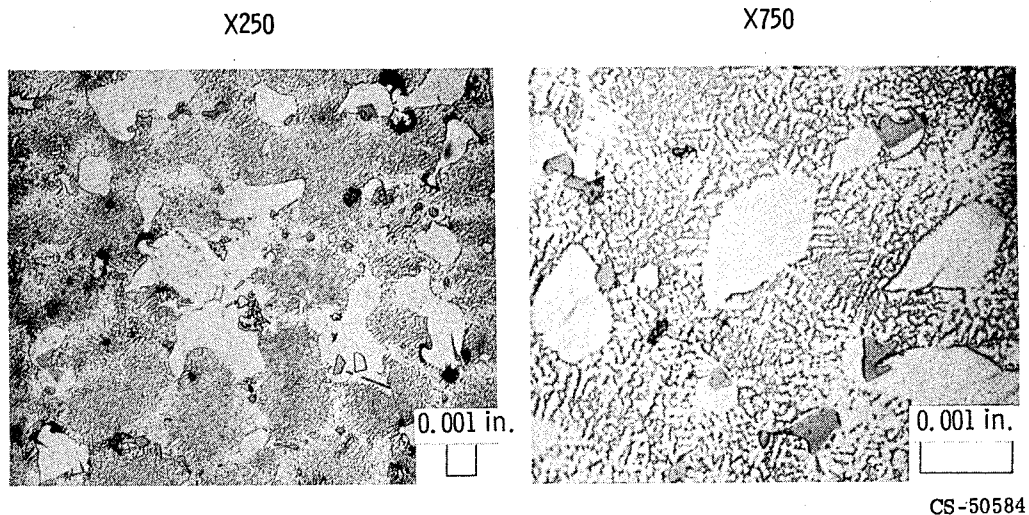


Figure 5-9. - Absence of sigma phase in WAZ-20 exposed 1000 hours at 1600° F.

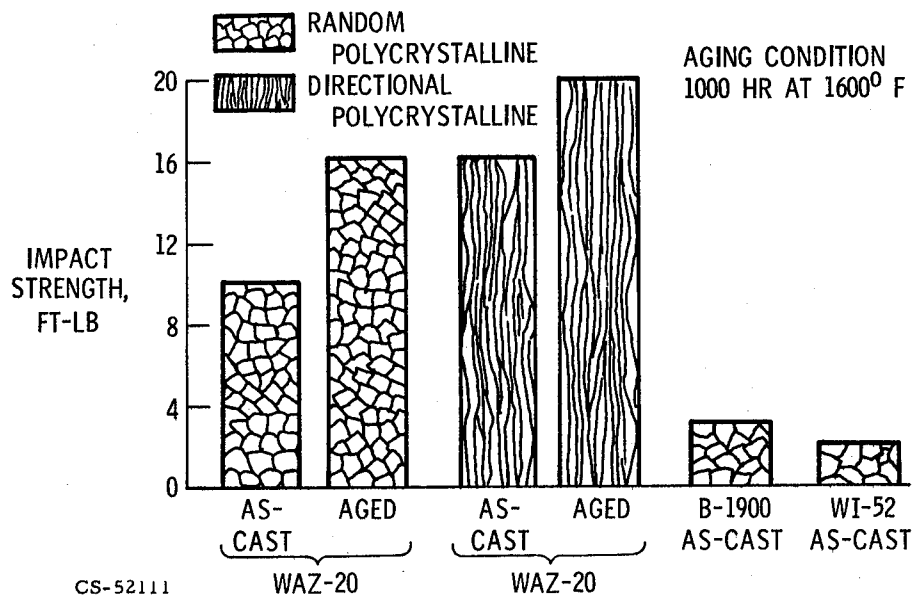


Figure 5-10. - Notched impact strengths of cast superalloys.

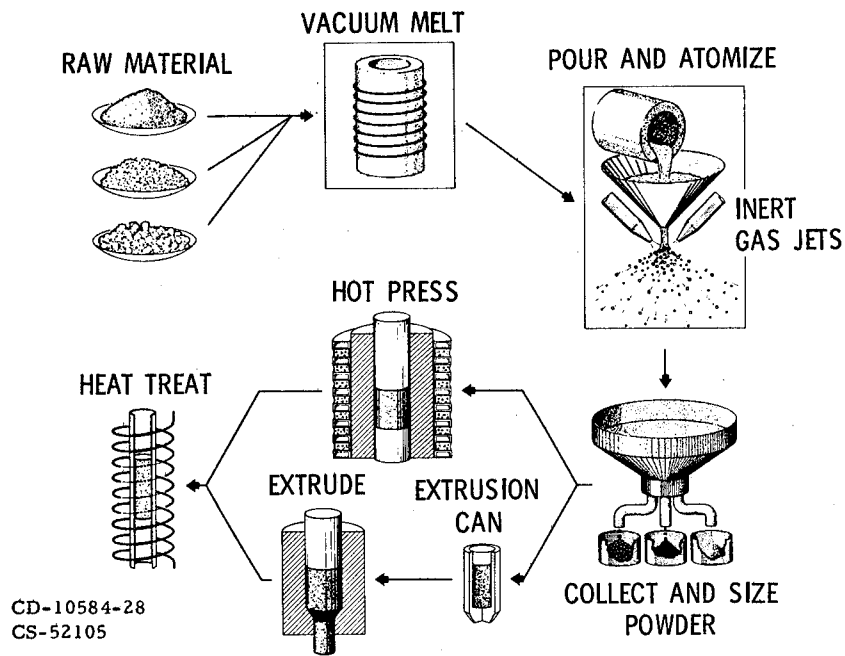


Figure 5-11. - Prealloyed powder processing.

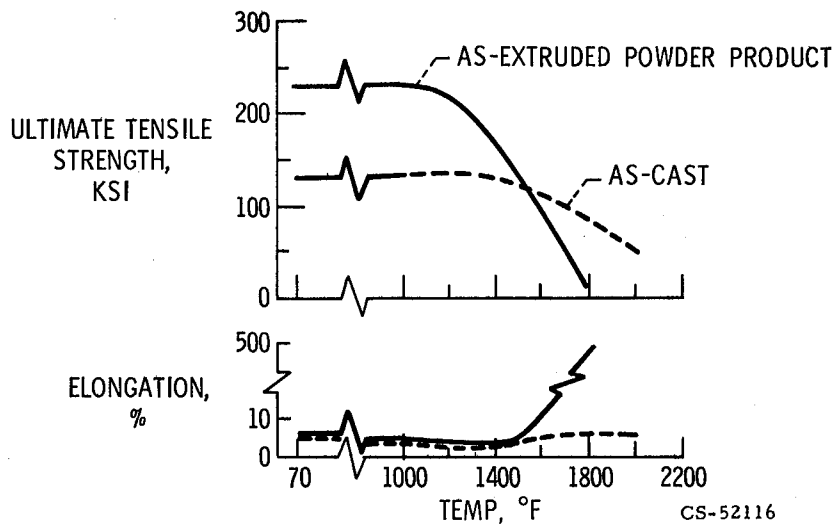


Figure 5-12. - Improvements in tensile properties of TAZ-8A.

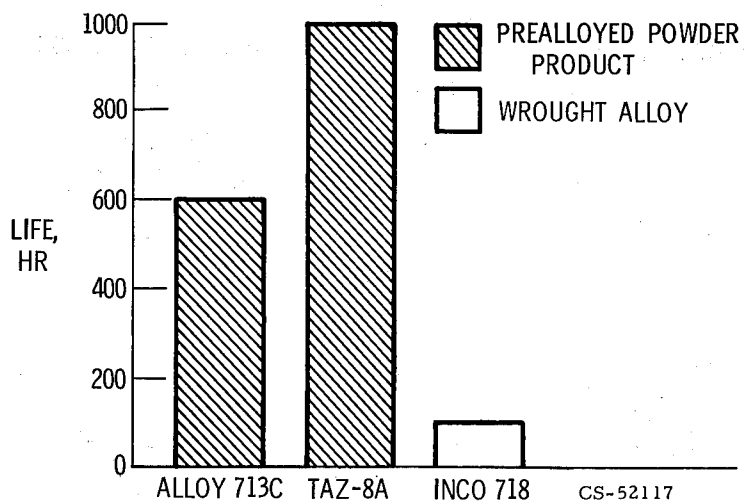


Figure 5-13. - Improvement in intermediate-temperature stress-rupture life. Stress, 105 ksi; temperature, 1200° F.

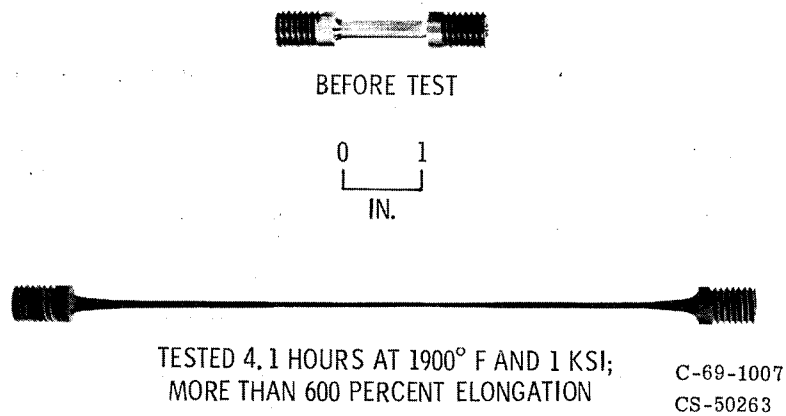
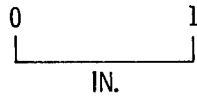


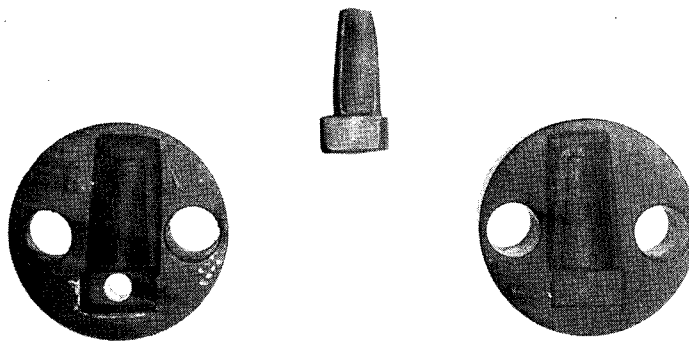
Figure 5-14. - Superplasticity in as-extruded TAZ-8A powder product.



C-69-598  
CS-50264

Figure 5-15. - TAZ-8A extruded powder product after upsetting at 2000° F.

TAZ-8A BLADE HOT  
PRESSED AT 2000° F



CAST TAZ-8A DIES USED

C-69-3280  
CS-52106

Figure 5-16. - Formability of TAZ-8A prealloyed powder product.



## 6. THERMOMECHANICAL PROCESSING OF THE NICKEL-BASE ALLOY U-700

Charles P. Blankenship

The potential of improving the strength of the nickel-base alloy U-700 by thermomechanical processing (TMP) was investigated. Strengthening by TMP consists of extensive strain hardening by mechanical deformation in conjunction with a precipitation hardening reaction. The U-700 alloy was cold worked either in the solution treated condition or after the  $\gamma'$  and carbide precipitation steps in the conventional heat-treating schedule for this alloy. Cold working was accomplished by hydrostatic extrusion at reductions in area of 20, 35, and 50 percent. Aging after cold working followed the conventional heat-treating schedule.

At temperatures of 1000° to 1200° F, the yield strength of the alloy after TMP was as much as 100 ksi greater than the yield strength after conventional heat treatment. TMP also improved the 1200° F stress-rupture life. At a stress of 120 ksi, the rupture life of the TMP samples exceeded 1500 hours. Conventionally heat-treated samples lasted about 400 hours in a similar test. The best combination of tensile and stress-rupture properties was obtained with 20 percent cold work in the TMP schedules.

Special processing techniques that have shown potential for improving the mechanical properties of nickel-base alloys include the powder metallurgy approach (ref. 1), directional solidification (ref. 2), and thermomechanical processing (refs. 3 to 5). Thermomechanical processing (TMP) consists of the application of combined mechanical working and heat treatment. The purpose of TMP is to provide extensive strain hardening of the alloy in conjunction with a precipitation hardening reaction. Precipitation can take place either during or after mechanical working. Both of these effects contribute to the strength of the alloy.

The purpose of this study was to evaluate the response of a high-strength, commercially available, nickel-base alloy to TMP. Alloy U-700, a precipitation hardening alloy with good high-temperature strength, was selected for this study. The alloy was cold worked at two different steps in the conventional heat-treating schedule. Cold working was accomplished by hydrostatic extrusion. Mechanical properties at temperatures from 1000° to 1400° F and the stress-rupture life at 1200° F were used in evaluating the response of this alloy to TMP.

## EXPERIMENTAL PROCEDURE

### Conventional Heat Treatment

The conventional heat treatment used for alloy U-700 is designated STA for solution treat and age. It consists of a 2150<sup>0</sup> F solution treatment for 4 hours, aging at 1950<sup>0</sup> F to allow for primary  $\gamma'$  precipitation, aging at 1550<sup>0</sup> F for grain-boundary carbide precipitation, and a final aging at 1400<sup>0</sup> F. The composition in weight percent of the alloy used in this study is as follows:

Co	Cr	Mo	Al	Ti	C	Zr	B	Ni
15	15	4	4	3	0.13	0.04	0.02	Balance

### Thermomechanical Processing

The TMP schedule used in this study is outlined in table 6-I. For reference, the STA schedule is included. As shown, TMP was accomplished by cold working the alloy at different steps in the STA schedule.

TMP schedule A consisted of cold working the alloy in the solution treated condition. Subsequent aging was done at the lower temperatures (1550<sup>0</sup> and 1400<sup>0</sup> F), since the alloy would recrystallize at the temperature required for primary  $\gamma'$  precipitation. Recrystallization would eliminate any strength improvement from strain hardening. An undesirable feature of this approach was that cold work usually causes intragranular carbide precipitation in this type of alloy upon subsequent heat treatment. Intragranular carbide precipitation might decrease the amount of grain-boundary carbides present. Grain-boundary carbides are important for balanced high-temperature properties (ref. 6).

In TMP schedule B, the alloy was cold worked after the primary  $\gamma'$  and grain-boundary carbide precipitation heat treatments. After cold working, the samples were given the final 1400<sup>0</sup> F aging treatment.

Cold working levels for both TMP schedules A and B were 20, 35, and 50 percent reductions in area. Cold working was accomplished by the hydrostatic extrusion process described in the following section.

It should be emphasized that no attempt was made to determine an optimum TMP schedule for U-700. The schedules used are somewhat arbitrary and represent one approach of applying TMP techniques to alloys of this type.

## Hydrostatic Extrusion

Cold working was accomplished by the hydrostatic extrusion process illustrated in figure 6-1. As shown, the billet is surrounded by a fluid pressurized by a carbide piston. The piston does not touch the billet. Extrusion of the billet results from the pressure differential across the die. Deformation forces much greater than those found in conventional cold-working processes can be developed by hydrostatic extrusion. For example, fluid pressures can be as high as 400 ksi. A more complete description of the hydrostatic extrusion process and potential applications is given in references 7 and 8.

Alloy U-700 is difficult to cold work even in the solution treated condition. By using the hydrostatic extrusion process, at least a 50 percent reduction in area could be obtained in one step. The U-700 billets used in this study were machined from commercial bar stock to a diameter of 0.72 inch. A lead coating ( $\sim 0.0005$  in. thick) was used for billet lubrication, and the pressurizing fluid was castor oil. Extrusion pressures were about 230 ksi for 50 percent cold work; 160 ksi for 35 percent cold work; and 100 ksi for 20 percent cold work. For the same level of cold work, there was no appreciable difference in the extrusion pressure required for samples processed according to TMP schedule A or schedule B.

## Process Evaluation

The effect of TMP on the structure of alloy U-700 was examined by both optical and electron microscopy. However, no attempt was made to correlate mechanical properties to the microstructure or to the morphology of the phases present.

Mechanical properties were evaluated by conventional tensile tests at temperatures from  $1000^{\circ}$  to  $1400^{\circ}$  F. Samples conforming to ASTM designation E8-61T were tested in an Instron machine at a crosshead speed of 0.05 inch per minute to fracture. Similar type specimens were tested in stress-rupture at a temperature of  $1200^{\circ}$  F and a stress of 120 ksi. For comparison, all tests included samples in the STA condition.

## RESULTS AND DISCUSSION

### Effect of TMP on Microstructure

The microstructure of U-700 in the STA condition and after TMP is shown in figure 6-2. In the STA condition, the structure consists of a duplex grain size with



primary  $\gamma'$  precipitation within the grains. TMP schedule A resulted in elongation of the grains in the direction of working and heavy deformation bands within the grains. The deformation bands represent areas of massive dislocations. Primary  $\gamma'$  precipitation is not present in the structure. After processing according to TMP schedule B, the grains are elongated in the direction of cold work with no evidence of deformation bands. Primary  $\gamma'$  precipitation is similar to that found in the STA condition.

Electron photomicrographs of the STA and TMP structures are shown in figure 6-3. In the STA condition, the structure exhibits discontinuous carbide precipitation at the grain boundaries and the cube-shaped, primary  $\gamma'$  within the grains. After TMP according to schedule A, the structure shows discontinuous carbide precipitation along the grain boundaries, carbide precipitation within the grains, but no evidence of primary  $\gamma'$ . The intragranular carbides precipitated along the deformation bands shown in figure 6-2. The TMP schedule B structure is very similar to the structure observed in the STA condition.

### Effect of TMP on Tensile Properties

For the same level of cold work, there was no appreciable difference in the high-temperature tensile properties of the alloy processed either by TMP schedule A or schedule B. However, the amount of cold work had a pronounced effect, as shown in figures 6-4 and 6-5. In figure 6-4, the yield strength data for TMP schedules A and B are shown in two banded regions representing different levels of cold work. As shown, the higher levels of cold work (35 and 50 percent) resulted in yield strengths about twice that of the alloy in the STA condition up to 1200° F. The rapid decrease in strength as the temperature approached 1400° F suggests loss of strain hardening by recovery and possibly some overaging. In comparison, 20 percent cold work gave about a 50 percent increase in yield strength over the alloy in the STA condition up to 1400° F.

The tensile strength data for TMP schedules A and B are shown in a similar manner in figure 6-5. Compared to the alloy in the STA condition, the increase in tensile strength by TMP was not as great as the improvement in yield strength. Cold working 20 percent (schedule A or B) gave about a 25 percent increase in tensile strength up to 1400° F. The higher levels of cold work resulted in about a 40 percent strength increase at 1000° to 1200° F.

Thermomechanical processing reduced the tensile ductility, as illustrated in figure 6-6 for the 1200° F tests. In the STA condition, the alloy exhibits about

20 percent elongation. Both TMP schedules A and B resulted in tensile elongation of 5 to 10 percent.

### Effect of TMP on Stress-Rupture Life

The improvement in stress-rupture life obtained by TMP is shown in figure 6-7. Under the test conditions of 1200° F and 120 ksi, the alloy in the STA condition had a life of about 400 hours. In comparison, TMP of the alloy more than tripled the stress-rupture life, as shown for 20 percent cold work in schedules A and B. These tests are still in progress. With increasing amounts of cold work in schedules A and B, the improvement in stress-rupture life decreased. The ductility, as measured by the total elongation in the stress-rupture test, was about 4 percent for the alloy in the STA and TMP conditions (for the tests completed).

### SUMMARY OF RESULTS

The response of the precipitation hardening, nickel-base alloy U-700 to thermomechanical processing (TMP) was evaluated. Mechanical properties were compared to those of the alloy after conventional heat treatment (STA). The results are as follows:

1. At a temperature of 1200° F and a stress of 120 ksi, the stress-rupture life of the alloy after TMP (20 percent cold work) exceeded 1500 hours. Conventionally heat-treated samples (STA) lasted about 400 hours under similar test conditions.
2. With 20 percent cold work in the TMP schedules, the yield strength was about 50 percent greater than that of the alloy in the STA conditions at temperatures from 1000° to 1400° F. Greater amounts of cold work (35 and 50 percent) gave a 100 percent improvement in yield strength at 1000° to 1200° F.
3. In the STA condition, the alloy exhibited about 20 percent elongation in the tensile tests. TMP samples exhibited from 5 to 10 percent elongation.
4. The best combination of tensile and stress-rupture properties was obtained with 20 percent cold work in the TMP schedules.

## REFERENCES

1. Freche, John C.; Waters, William J.; and Ashbrook, Richard L.: Evaluation of Two Nickel-Base Alloys, Alloy 713C and NASA TAZ-8A, Produced By Extrusion of Prealloyed Powders. NASA TN D-5248, 1969.
2. Freche, John C.; Waters, William J.; and Ashbrook, Richard L.: Application of Directional Solidification to a NASA Nickel-Base Alloy (TAZ-8B). NASA TN D-4390, 1968.
3. Sokolkov, Ye. N.; Gaydukov, M. G.; and Petrova, S. N.: Features of the Initial Stage of Creep In An Alloy of the Nimonic Type After High-Temperature Thermomechanical Treatment. Phys. Metals Metallography, vol. 19, no. 1, 1965, pp. 91-94.
4. Slunder, C. J.; and Hall, A. M.: Thermal and Mechanical Treatments for Nickel and Selected Nickel-Base Alloys and Their Effect on Mechanical Properties. Rep. RSIC, Battelle Memorial Inst. (NASA TM X-53443), Apr. 20, 1966.
5. Richmond, F. M.: Increasing Strength of Gas Turbine Alloys by Cold Work Prior to Aging. J. Eng. Power, vol. 89, no. 1, Jan. 1967, pp. 61-66.
6. Sullivan, C. P.; and Donachie, M. J., Jr.: Some Effects of Microstructure on the Mechanical Properties of Nickel-Base Superalloys. ASM Metals Eng. Quart., vol. 7, no. 1, Feb. 1967, pp. 36-45.
7. Pugh, H. L. D.: Application of High Pressure to the Forming of Brittle Metals. Metal Deformation Processing. Vol. 3: Survey Conducted as Part of the Metalworking Process and Equipment Program (MPEP). Rep. DMIC-243, vol. 3, Battelle Memorial Inst., June 10, 1967, pp. 19-47. (Available from DDC as AD-827761.)
8. Gelles, S. H.: Hydrostatic Forming - A Survey. J. Metals, vol. 19, no. 9, Sept. 1967, pp. 35-46.

TABLE 6-I. - THERMOMECHANICAL PROCESSING SCHEDULE FOR U-700

Conventional heat-treatment (STA)	Thermomechanical processing (TMP)	
	Schedule A	Schedule B
Solution treat at 2150° F for 4 hours	Solution treat at 2150° F for 4 hours	Solution treat at 2150° F for 4 hours
$\gamma'$ precipitation	-----	$\gamma'$ precipitation
-----	Cold work (20, 35, and 50 percent reduction in area)	-----
Carbide precipitation	Carbide precipitation	Carbide precipitation
-----	-----	Cold work (20, 35, and 50 percent reduction in area)
Final age	Final age	Final age

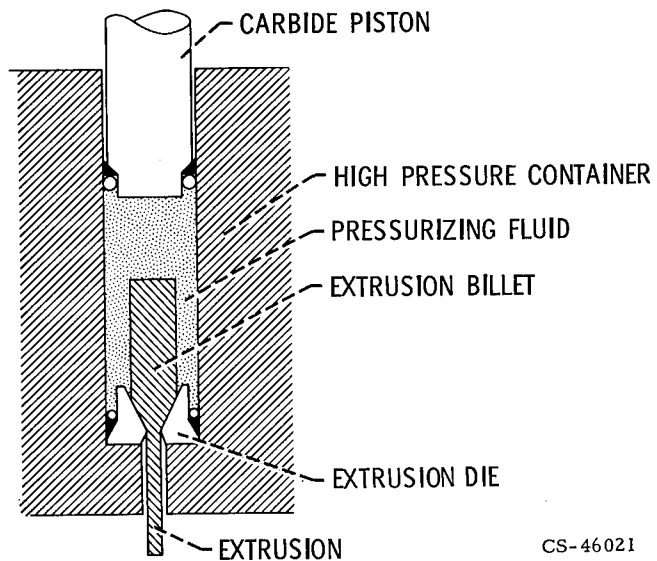


Figure 6-1. - Schematic diagram of hydrostatic extrusion.

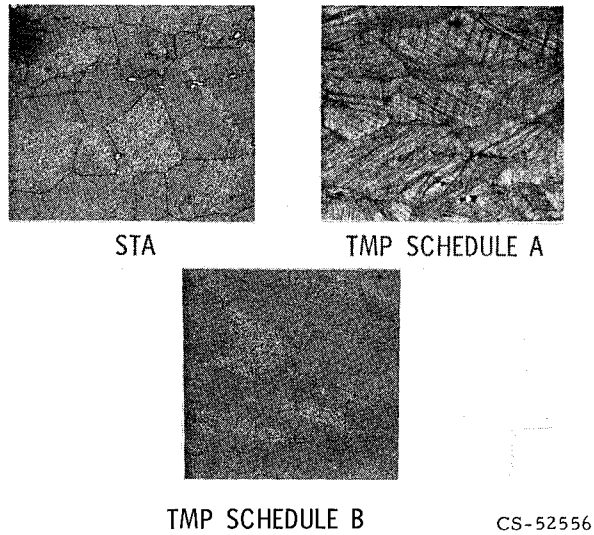


Figure 6-2. - Effect of thermomechanical processing  
on microstructure of U-700. X250.

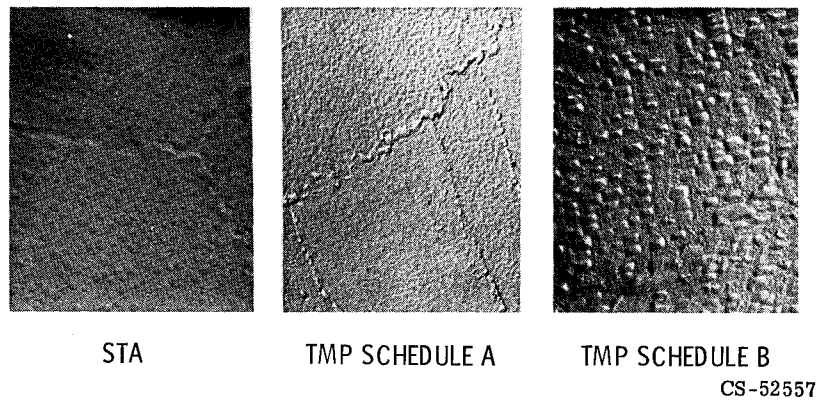


Figure 6-3. - Effect of thermomechanical processing on microstructure of  
U-700. X10 000.

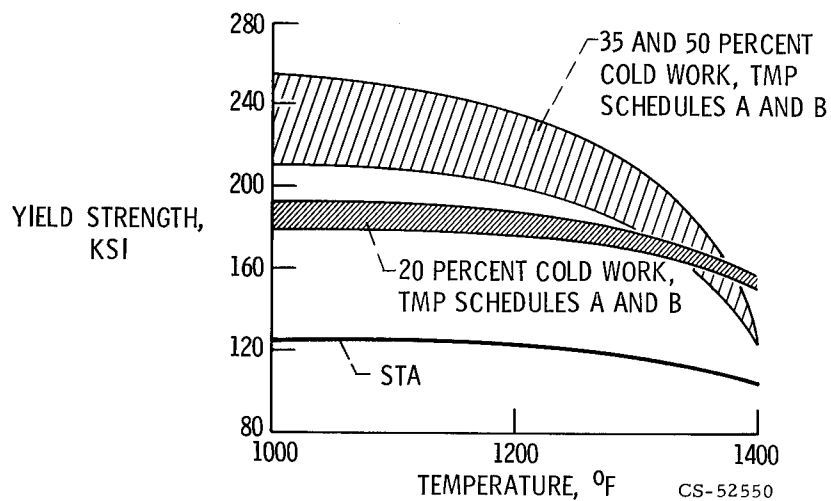


Figure 6-4. - Improvement in yield strength of U-700 by thermomechanical processing.

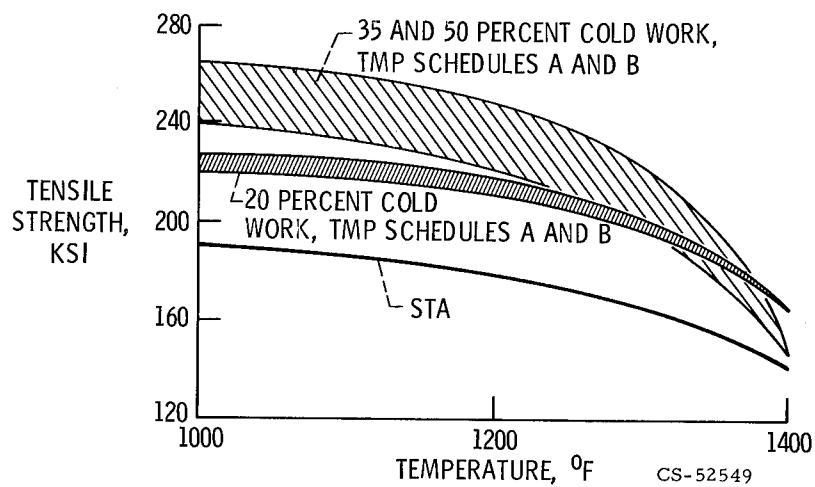


Figure 6-5. - Improvement in tensile strength of U-700 by thermomechanical processing.

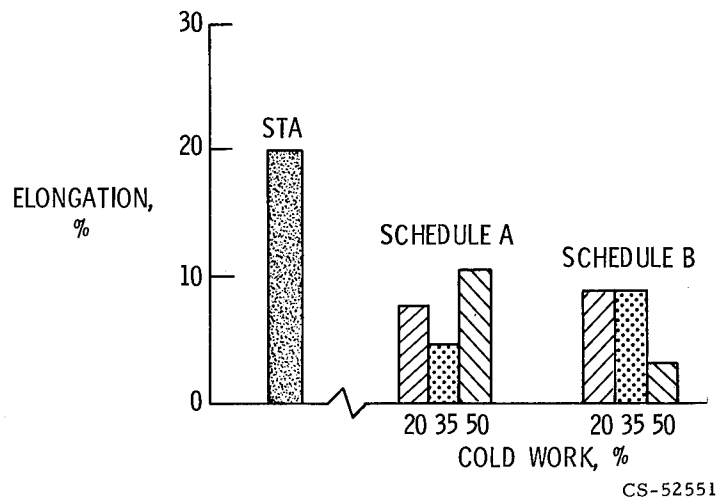


Figure 6-6. - Reduction in tensile ductility of U-700 by thermo-mechanical processing. Temperature, 1200° F.

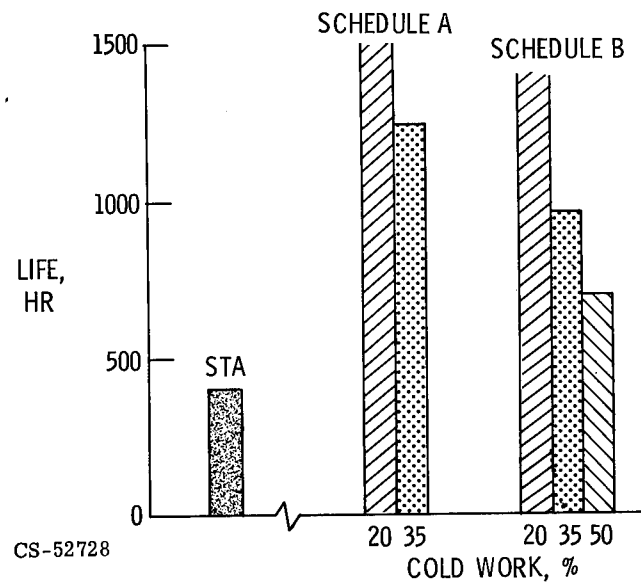


Figure 6-7. - Improvement in stress-rupture life of U-700 by thermomechanical processing. Temperature, 1200° F; stress, 120 ksi.

## 7. DEVELOPMENTS IN DISPERSION-STRENGTHENED MATERIALS

Max Quatinetz and John W. Weeton

Dispersion-strengthened products, comparable in strength to the best commercial products (prepared by chemical approaches) were produced by thermomechanical processing of comminuted and blended composites; Ni-4 ThO<sub>2</sub> and Ni-0.5 Zr-4 ThO<sub>2</sub> composites were prepared. The products were cold pressed, sintered, hot rolled, and subjected to 7, 14, or 21 cold-roll - anneal cycles. A number of the sheet materials produced were stronger in 2000° F tensile and stress-rupture properties than a processed reference powder and the best available dispersion-strengthened commercial nickel sheet product. While the strength of the dispersion products generally increased as the number of cold-roll - anneal cycles increased, changes in composition and processing were shown to affect the response of the materials to the working process. The mechanical comminution approach is applicable to complex alloys and could yield composite materials which combine the advantages of alloy properties with dispersion strength.

### BACKGROUND

The number of mechanisms by which the high-temperature strength of metals may be improved is relatively limited. Dispersion strengthening is a method used for improving the high-temperature strength of materials. In metals, dispersion strengthening has the potential for increasing the use temperature about 200° to 400° F above that achievable by conventional alloying. The strengthened materials can then be used for relatively high stressed hot components of an engine or for other applications requiring durability at high temperature. This paper will consider the status, problems, and potential of dispersion strengthening and also cover some recent work carried out at the NASA Lewis Research Center on the use of a mechanical grinding and blending approach to produce dispersion strengthened materials.

Dispersion strengthening is accomplished by distributing nonreactive particles, such as stable refractory oxides or other stable high-melting-point com-



pounds throughout a metallic matrix. The dispersion-strengthening process was discovered about 20 years ago by a Swiss professor, R. Irmann, while processing aluminum powder. He found that aluminum with a fine aluminum oxide distribution had greater strength at higher percentages of the melting point than conventional aluminum alloys (ref. 1). Efforts were then made by others to apply dispersion strengthening methods to other metals with higher melting points such as copper, nickel, and cobalt in order to attain higher use temperatures. This was difficult to do because in these cases the normal oxides formed by the metal matrices are unstable and other stable dispersoids have to be added in order to achieve the desired effect. The most successful results have been accomplished using thorium oxide in nickel and nickel-chromium matrices.

### Comparison of Alloy and Dispersion Properties

Some idea of the high-temperature strength advantage that can be gained by using dispersions can be obtained from the first two figures. Figure 7-1 compares the 1000-hour stress-rupture properties of a nickel alloy with dispersion-strengthened nickel at various fractions of the melting point of the base material. It can be noted from the figure that the alloy has higher strength at low temperatures; however, the strength falls off rapidly to a low value at temperatures which are generally below 0.7 of the melting point. The dispersion-strengthened nickel has greater strength at elevated temperatures generally usable up to 0.9 of the melting point.

Figure 7-2 is a comparison of the 100-hour stress-rupture properties of Hastelloy X and with dispersion-strengthened nickel-chromium from 1300° to 2300° F. If a line is drawn at the 10-ksi stress level across the two curves, it can be seen that the Hastelloy X can sustain a stress load of 10 ksi for 100 hours at 1600° F and that the Ni-20Cr-2ThO<sub>2</sub> can sustain the same load for the same time at 2000° F. Thus, in this case the dispersion-strengthened material has a use-temperature advantage of 400° F over the conventional alloy.

The reason for the difference in behavior of the dispersion-strengthened materials and that of other alloys is shown in the next two figures.

Figure 7-3(a) is a microstructure of a high-temperature alloy in its strongest condition with a precipitate produced by conventional heat treating and aging. As the temperature increases, the particles coarsen and dissolve, and the alloy loses its strength. A microstructure of the same alloy after heating to 2175° F is shown in figure 7-3(b). Coarsening of the particles, solutioning, and loss of strength in superalloys usually starts below 2000° F.

Figure 7-4 shows a microstructure of a dispersion-strengthened Ni-Zr-ThO<sub>2</sub> alloy produced at NASA Lewis (NAS-CAB refers to the NASA comminution and blend process). The product is a ground, cleaned, and sintered composite with extremely fine particles of thorium oxide. The average particle size of the oxide is about 300 Å and many of the particles are as small as 50 Å. The composite has been heated to 2400° F without dissolving or agglomerating the particles. The strength is developed in this type of composite by thermomechanical working during processing and the dispersoids help to retain the strength in the product at high temperatures.

Some potential applications for dispersion-strengthened materials because of their superior high-temperature properties can be seen in figure 7-5. Here we see the 1000-hour stress-rupture strength of a nickel alloy (Udimet 700) and dispersion-strengthened nickel shown with the proposed design stress criteria for turbine vanes and blades at temperatures from 1600° to 2400° F. The dispersion-strengthened nickel is more suitable than the alloy for application to vanes over a wide temperature range.

One objective of current work is to apply the dispersion-strengthening process to alloys. By combining the low- and intermediate-temperature strengths of alloys with the high-temperature strength achievable by dispersion strengthening, materials with better low, intermediate, and high-temperature strength may be obtained so that design criteria for blades as well as other highly stressed high-temperature engine and space vehicle components may be more easily met. The thoria dispersed cobalt data point shown in figure 7-5 is for an experimental dispersion strengthened Co-Ni-Cr-ThO<sub>2</sub> alloy produced by the Fansteel Metallurgical Corporation under an Air Force Contract. This is not yet a commercial product but does show the potential of dispersion-strengthening alloys.

## Requirements and Methods of Manufacture of Dispersion-Strengthening Alloys

Till now, all blends for commercial dispersion-strengthened materials have been prepared by chemical methods. At NASA Lewis the bulk of the effort in the dispersion-strengthening field has been concerned with mechanical comminution and blending. This approach could be readily applied to many materials, including simple and complex alloys. Before describing some of the results of this work as applied to the production of nickel plus thoria sheet material, some of the requirements and methods of manufacture of dispersion-strengthened materials will be considered.

Some of the requirements that must be met in order to achieve strength in

dispersion-strengthened materials are as follows: First we must produce a blend with an ultrafine dispersoid. The dispersoid must be stable in the matrix at high temperatures, have an interparticle spacing of less than 2 microns, be ultrafine with an average particle size preferably below 500 Å, and have a uniform distribution. The material must be produced free of detrimental impurities and generally must be thermomechanically worked in a controlled manner during processing in order to develop its strength.

Blends may be prepared by chemical, physical, or mechanical methods. A chemical precipitation approach to dispersion-strengthened material is shown in figure 7-6. In this method a soluble nickel salt, a base, and a colloidal thoria slurry are run simultaneously into a common reaction vessel. By heating and reducing the gel obtained, thoria particles coated with nickel are produced. The particles are consolidated by cold pressing and sintering into billets or slabs. Final densification and working may be done by various combinations of methods such as extrusion, swaging, or rolling to produce bar or sheet material. Work of this nature started by Dupont led to the production of commercially available dispersion-strengthened thoria-dispersed Ni-ThO<sub>2</sub> bar and sheet and thoria-dispersed NiCr-ThO<sub>2</sub> sheet. These products are currently available from the Fansteel Metallurgical Corporation, which has recently taken over the dispersion-strengthened materials production from Dupont.

Figure 7-7 illustrates a mechanical approach to dispersion-strengthened material production. Here, the dispersion is prepared by grinding and blending. The NASA-Lewis has made a number of contributions which have permitted the production of dispersion-strengthened materials with good properties by this method. By using suitable additives (ref. 2) in the grinding media in conventional as well as special attritor ball mills, we have been able to grind most metallic and ceramic materials to an average particle size below 300 Å.

Some of the powders produced are radioactive or toxic or burn spontaneously in air so methods for safe handling of the powders had to be developed, and many of the processing steps are carried out in dry boxes under inert atmosphere (ref. 3).

Because the powders produced have large amounts of reactive surface, they tend to have large amounts of detrimental impurities that aggravate the agglomeration of the fine oxide which is added during processing. The problem of cleaning and densifying the blend without oxide agglomeration has been solved by cleaning partially densified thin compacts with gaseous hydrogen and by raising the furnace temperature in a controlled stepwise fashion. In this way it was possible to reduce the impurities, particularly matrix oxide, to a low level (ref. 4). The effect of this cleaning approach is shown in figure 7-8. Here, we see the microstructures of a Ni-5Al<sub>2</sub>O<sub>3</sub> composite sample (prepared at NASA-Lewis) cleaned in a conventional

manner and one cleaned with the new method. After heating at 2560° F for 35 hours, the conventionally cleaned sample shows large agglomerated oxide particles while the sample cleaned by the new method retains fine discrete particles. The magnification of the samples in both photomicrographs was 10 000.

## SCOPE OF NASA INVESTIGATION OF MECHANICAL APPROACH TO DISPERSION-STRENGTHENED MATERIALS

The objective of the current investigation to be described was to determine whether dispersion-strengthened products comparable in strength to commercial chemically produced materials could be made by thermomechanical processing of comminuted and blended composites. Another objective was to vary the powder composition and processing to determine whether such changes would influence the response of the material to the thermomechanical working treatments. Some of the blends processed and the processing steps are

Blends processed:

- (1) Ni-4ThO<sub>2</sub>
- (2) Ni-4ThO<sub>2</sub>-0.5Zr
- (3) Ni-4ThO<sub>2</sub>
- (4) Ni-3ThO<sub>2</sub> (commercial powder)

Processing steps:

- (1) Preparation of blends - Attritor grind in heptane
- (2) Densification - Cold press and sinter
- (3) Thermomechanical work - Hot roll; cold roll with intermediate anneals

The first three are NASA produced blends consisting of Ni-4ThO<sub>2</sub>, Ni-4ThO<sub>2</sub> with the addition of 0.5-percent Zr, and Ni-4ThO<sub>2</sub> prepared from NiO-4ThO<sub>2</sub> the NiO being selectively reduced to nickel during the processing. The processing steps (1) and (2) consisted of attritor grinding in heptane and densification by cold pressing and sintering. The thermomechanical work (step (3)) consisted of two hot-roll reductions of 30 percent each at 2000° F and 7, 14, or 21 cold-roll reductions of 10 percent each with intermediate 30-minute anneals at 2200° F in hydrogen. The Ni-3ThO<sub>2</sub> material was a chemically produced commercial powder. This powder was densified and thermomechanically worked at NASA-Lewis in the same manner as the NASA produced blends and was used as a reference material for comparing results obtained from the tests. Test data consist mainly of results of 2000° F tensile and stress-rupture tests. Microstructures of some of the products were examined. More complete details of the investigation can be found in reference 5.

## RESULTS OF 2000° F TENSILE STRENGTH TESTS

### Reference Materials

Figure 7-9 shows the 2000° F tensile strength of the Ni-3ThO<sub>2</sub> reference material after 7, 14, and 21 cold-roll - anneal cycles. The strength increases with increasing amounts of thermomechanical working and ranges from 9000 psi at 7 passes to 16 000 psi at 21 passes.

Commercial thoria dispersed Ni-2ThO<sub>2</sub> sheet material purchased earlier from Dupont and tested in the as-received condition had tensile-strength properties ranging from 9000 to 12 000 psi at 2000° F. The current Fansteel brochure lists available commercial thoria-dispersed nickel sheet with 2000° F tensile strength of 14 000 psi.

### NASA Materials

Ni-4ThO<sub>2</sub>. - Figure 7-10 shows the 2000° F tensile strength of dispersion-strengthened Ni-4ThO<sub>2</sub> sheet produced from a blend prepared by grinding nickel and thoria directly in heptane. The results are compared with the reference material at 7, 14, and 21 cold-roll - anneal cycles. As in the case of the reference material, we see an increase in strength with increased amounts of working; however, the slope of the curve is greater. Although the tensile strength properties at 7 and 14 passes are below the reference material, the results at 21 passes are above. The tensile strength ranges from 6000 to 20 000 psi with increasing amounts of thermomechanical work (from 7 to 21 cold-roll - anneal cycles).

Ni-4ThO<sub>2</sub> Prepared From NiO-ThO<sub>2</sub>. - The 2000° F tensile strength data for Ni-4ThO<sub>2</sub> sheet prepared from NiO-ThO<sub>2</sub> are compared with the reference material at 7, 14, and 21 cold-roll - anneal cycles in figure 7-11. These are the best results obtained in the investigation. An increase in strength with increasing amounts of working is apparent. The slope of the curve obtained is roughly the same as for the reference material, but the curve is at a much higher stress level. Whereas the tensile strength of the reference material ranges as noted previously (from 9000 to 16 000 psi), the NASA materials results run from 19 000 to 26 000 psi.

Ni-0.5Zr-4ThO<sub>2</sub>. - The 2000° F tensile strength data are shown in figure 7-12. Here the best results ranging from 16 000 to 22 000 psi were obtained using seven cold-roll - anneal cycles. The strength then decreases with increasing amount of thermomechanical working. While the results at 7 and 14 passes are above those of the reference materials, the results at 21 passes are slightly below. This is a

significant result since less working (i. e., 7 rather than 21 passes) is required to get the maximum properties. The zirconium may improve the properties of the material by providing solid solution strength, by acting as an oxygen getter, thus helping to clean the matrix by reducing matrix oxides, and by assisting in bonding the matrix to the oxide.

## 2000° F STRESS-RUPTURE PROPERTIES

The stress-rupture properties are compared with the reference materials in figures 7-13 and 7-14. In figure 7-13 the time to failure at a stress of 10 000 psi is shown. While the life of the reference materials runs from 5 to 150 hours, the life of the NASA materials run from 300 to 500 hours. Thus, there is a 2 to 3 time advantage in rupture time over similar materials.

In figure 7-14 the data are plotted in the more conventional manner, that is, with stress against rupture time. This figure shows that the strengths of the NASA materials are generally better than the reference materials. For a 100-hour life there is a 2000-psi increase in stress (from 9000 to 11 000 psi) as compared with the reference materials.

Materials with better tensile strength properties have been obtained since these tests were run and may yield even better stress-rupture properties than those described. These materials have yet to be evaluated in stress rupture.

## MICROSTRUCTURES

Microstructures of some of the NASA materials were studied using a number of electron microscopy techniques. Figure 7-15 shows replica electron microstructures of sheet material after rolling and tensile testing produced from Ni-Zr-ThO<sub>2</sub>, NiO-ThO<sub>2</sub>, and Ni-ThO<sub>2</sub>. The 2000° F tensile strengths of these materials were 22 000, 26 000, and 7000 psi, respectively. While dense fine oxide particles can be seen in the microstructure of the strongest specimens (fig. 7-15(a) and (b)), a large area devoid of fine particles and with some large oxide particles may be seen in the microstructure of the weak material (fig. 7-15(c)). Although it is difficult to draw any conclusions from these replicas, the strengths noted may be related in part to the fine oxide particle structure observed in the stronger materials.

In figure 7-16 a replica of Ni-Zr-ThO<sub>2</sub> sheet at a magnification of 11 000 is shown next to an extraction microstructure at a magnification of 46 000. Since

in the extraction microstructure the matrix is dissolved away, the technique reveals that the fine oxide particle structure is real. An estimate of the interparticle spacing based on the extraction microstructure is approximately 0.5 micron.

Another technique used to examine the Ni-Zr-ThO<sub>2</sub> is thin-film electron microscopy. In figure 7-17 a thin film microstructure of the Ni-Zr-ThO<sub>2</sub> may be compared with the reference material at a magnification of 48 000. The microstructures show that a higher density of particles is present in the NASA material.

More work will be required to fully define the structures and understand the significance of the differences observed.

## CONCLUSIONS

Dispersion strengthening provides a means of meeting needs where materials with good strength at high temperature are necessary. Products are available which can meet the design criteria for a number of applications. Work is going on in the field to better define the strengthening mechanisms involved and to tap more of the potential of the method. The conclusions to be drawn as a result of the Lewis investigation are encouraging. The study has shown that dispersion-strengthened nickel sheet materials can be made by a mechanical approach with properties comparable to those obtained with products made by chemical methods. Also, the response of the NASA comminuted and blended materials to thermomechanical working was shown to be affected by the composition of the product and the nature of the processing.

The mechanical approach may be useful as a tool because it can be readily applied to dispersion strengthen other materials, including simple and complex alloys. By dispersion strengthening alloys we can hopefully obtain materials with better low, intermediate, and high-temperature strength and thus achieve proposed design stress criteria for turbine blades and other highly stressed high-temperature engine and space vehicle components.

## REFERENCES

1. Irrmann, R.: On a New Sintered Aluminum Product with High Strength at Elevated Temperatures. *Leichtmetall*, vol. 3, 1950, pp. 21-25.
2. Quatinetz, Max; Schafer, Robert J.; and Smeal, Charles R.: The Production of Submicron Metal Powder by Ball Milling with Grinding Aids. NASA TN D-879, 1962.

3. Viles, F. J., Jr.; Chamberlain, R. I.; and Boyler, G. W., Jr.: Survey and Analysis of Health Hazards Resulting from Ultrafine Metal and Metal Oxide Powders at the NASA Lewis Research Center, Cleveland, Ohio. (NASA Cr-72492), Mar. 15, 1966.
4. Weeton, John W.; and Quatinetz, Max: Cleaning and Stabilization of Dispersion Strengthened Materials. Presented at the AIME Conference on Oxide Dispersion Strengthening, Bolton Landing, N.Y., June 27-29, 1966.
5. Quatinetz, Max; and Weeton, John W.: Dispersion-Strengthened Nickel Produced from Ultrafine Comminuted Powders. NASA TN D-5421, 1969.



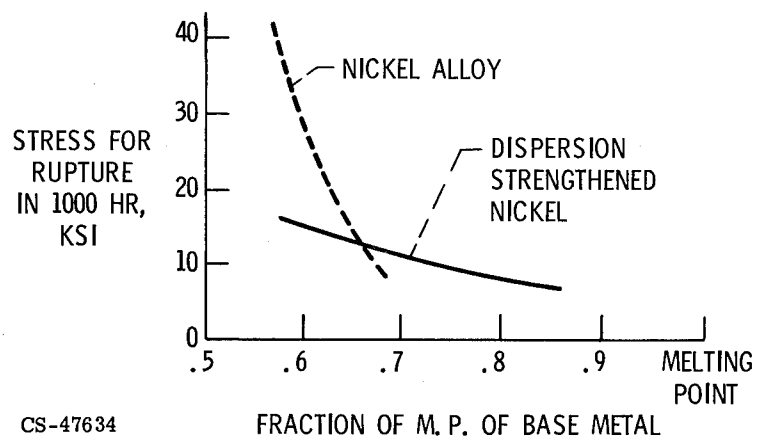


Figure 7-1. - Strength retention in metals with dispersoids.

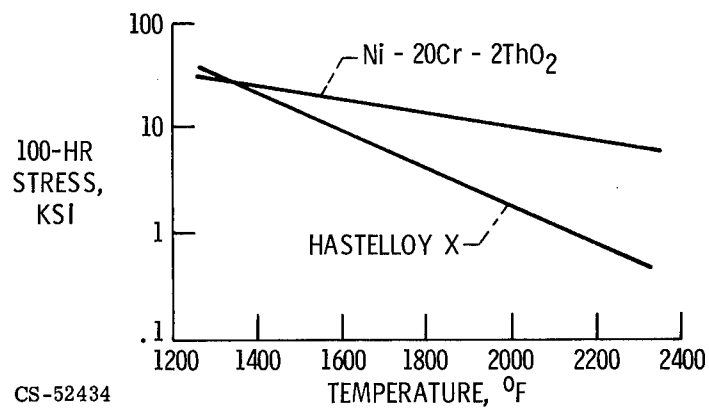
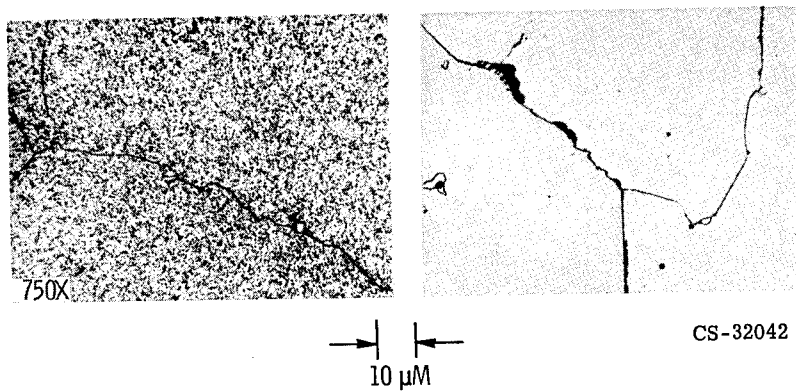


Figure 7-2. - Comparison of stress-rupture properties of nickel base alloy and nickel-chromium alloy.



(a) Strongest condition. (b) After heating to 2175<sup>o</sup> F.

Figure 7-3. - Microstructure of high temperature alloy.

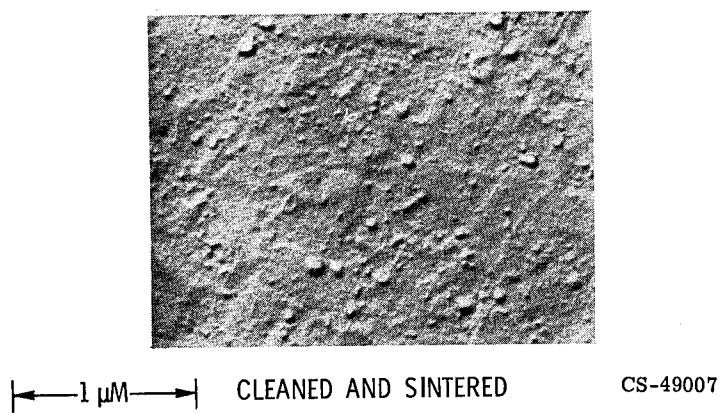


Figure 7-4. - NASA dispersion-strengthened alloy. NAS CAB sheet Ni-0.5Zr-4ThO<sub>2</sub>. X48 000.

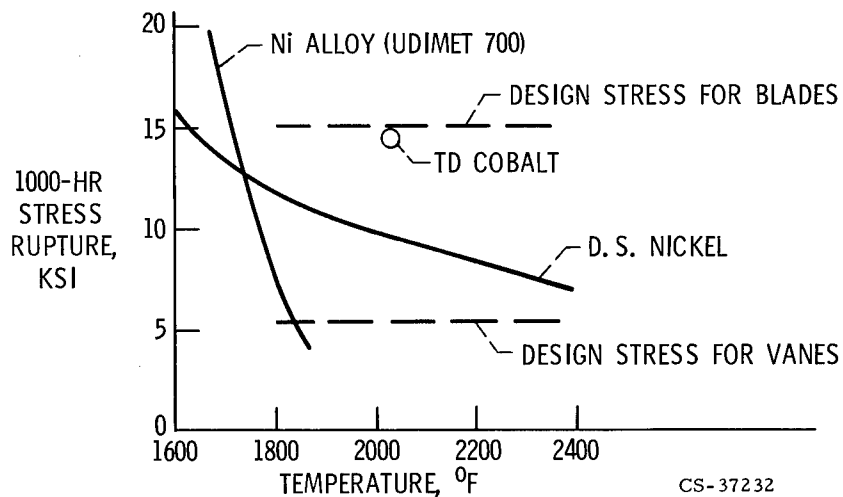


Figure 7-5. - Strength of dispersion-strengthened superalloy.

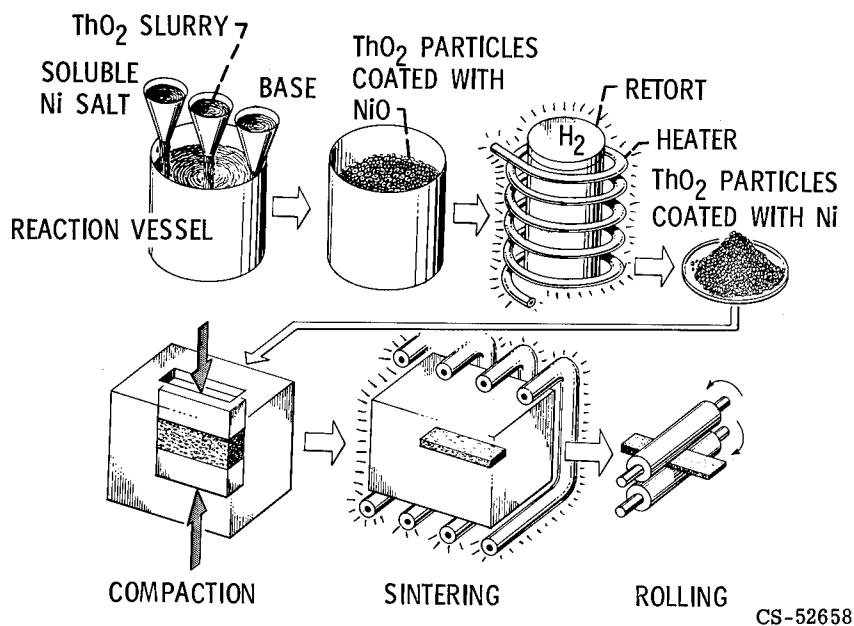


Figure 7-6. - Chemical precipitation approach to dispersion strengthening materials.

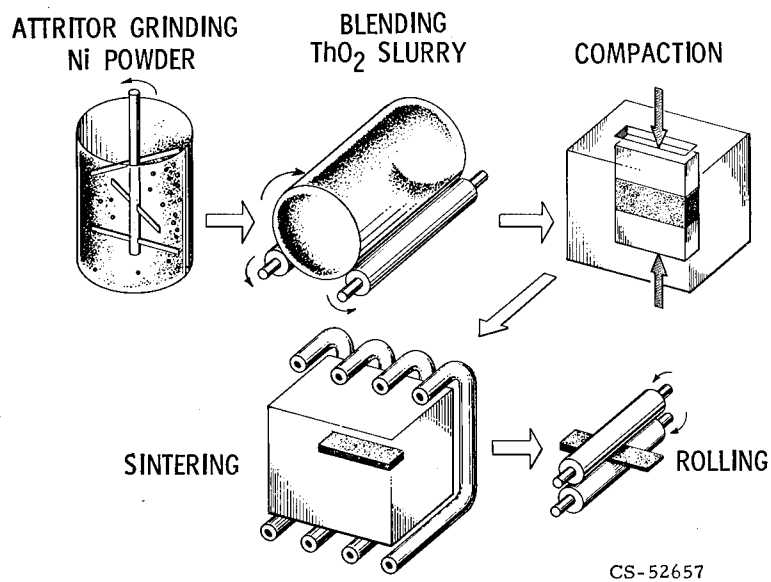


Figure 7-7. - Mechanical approach to dispersion strengthening materials.

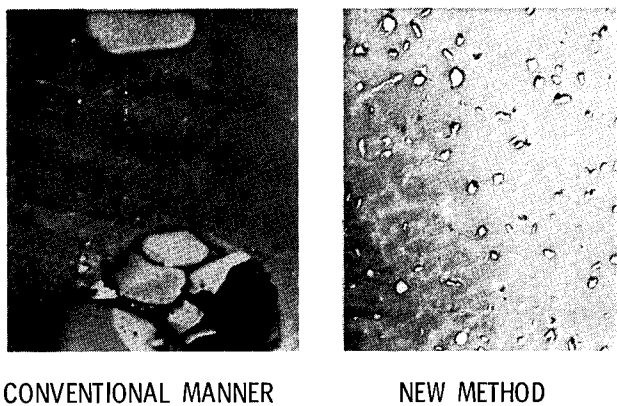


Figure 7-8. - Microstructure of cleaned and annealed Ni-5Al<sub>2</sub>O<sub>3</sub> composite. Heat treatment, 35 hours at 2560° F. X10 000.

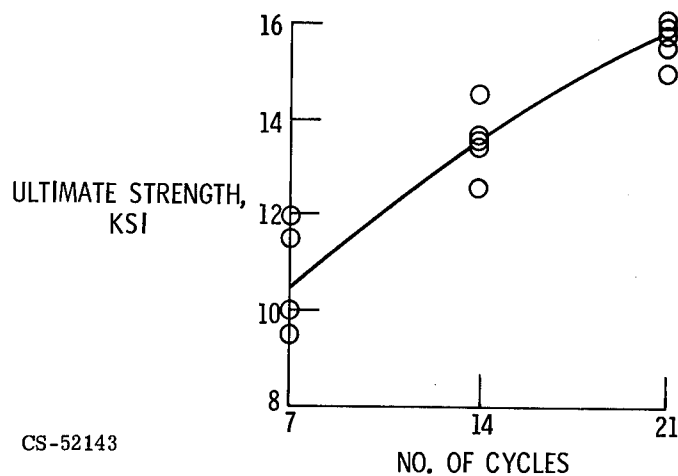


Figure 7-9. - Tensile strength as function of cold-roll - anneal cycles for nickel sheet (Ni-3ThO<sub>2</sub> reference sheet.) Temperature, 2000° F.

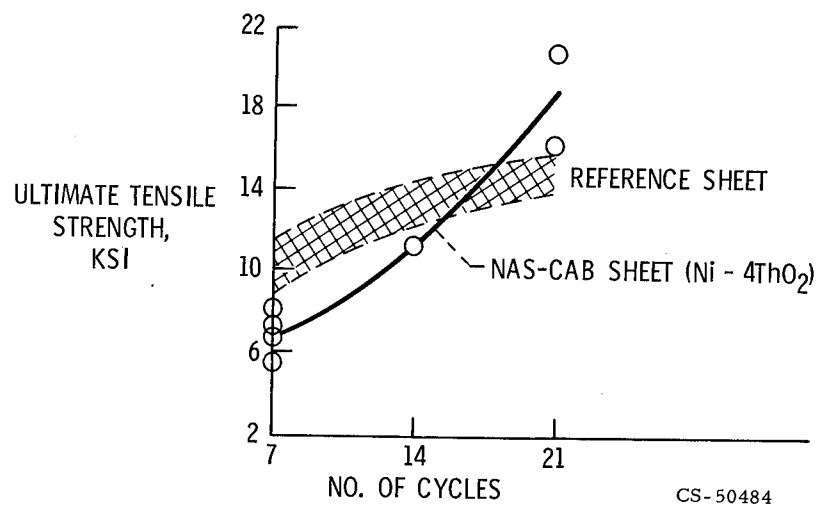


Figure 7-10. - Tensile strength as function of cold-roll - anneal cycles for dispersion-strengthened Ni-4ThO<sub>2</sub> sheet. Temperature, 2000° F.

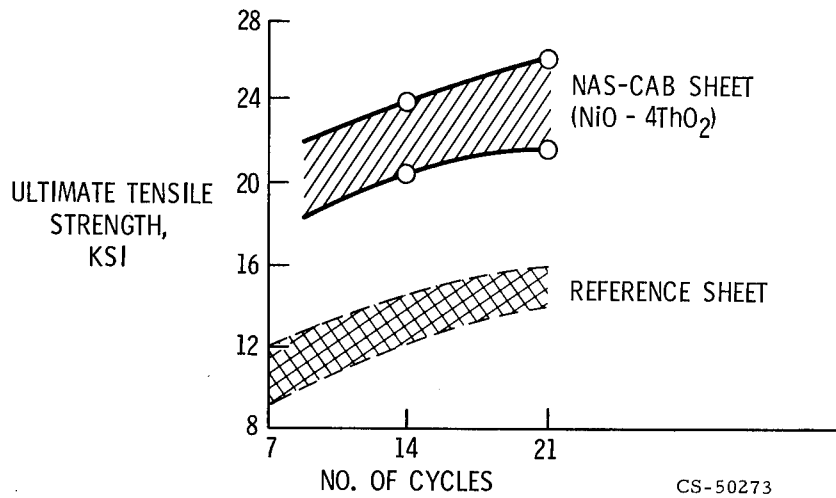


Figure 7-11. - Tensile strength as function of cold-roll - anneal cycles for dispersion-strengthened NiO-4ThO<sub>2</sub> sheet. Temperature, 2000° F.

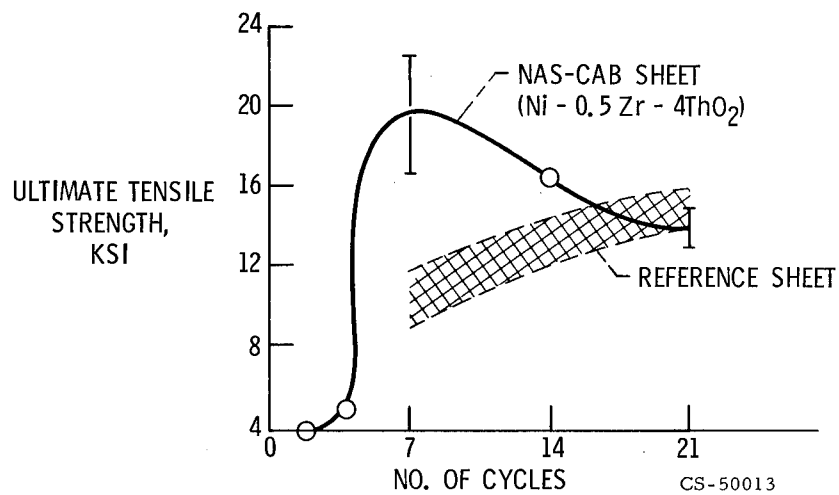


Figure 7-12. - Tensile strength as function of cold-roll - anneal cycles for dispersion-strengthened Ni-0.5Zr-4ThO<sub>2</sub> sheet.

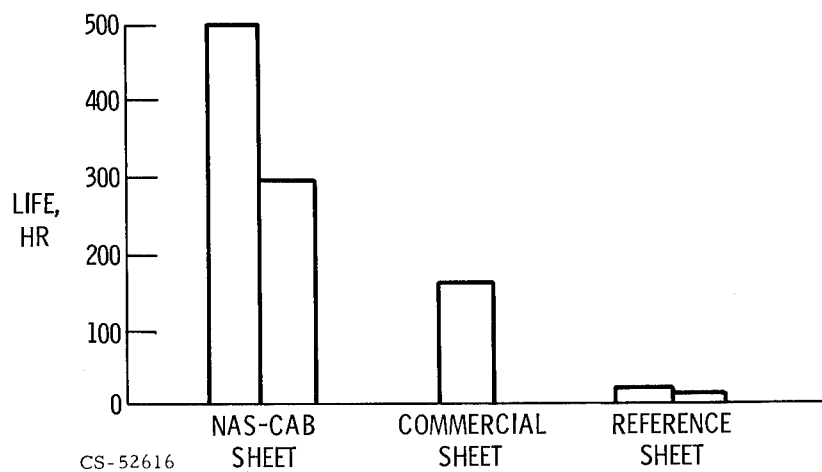


Figure 7-13. - Stress-rupture properties of dispersion-strengthened nickel sheet. Stress, 10 000 psi; temperature, 2000° F.

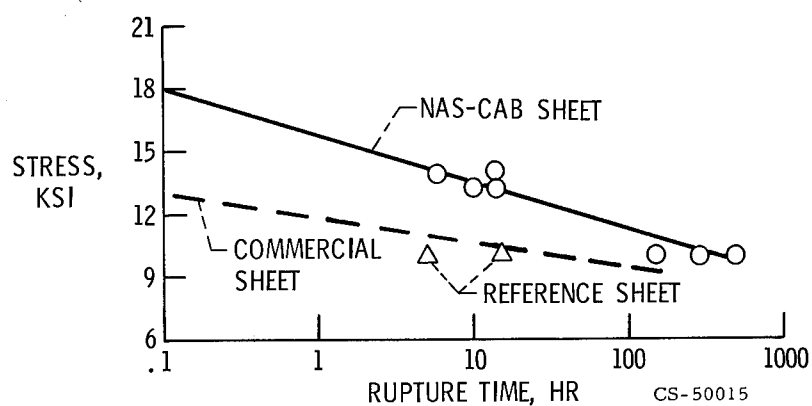
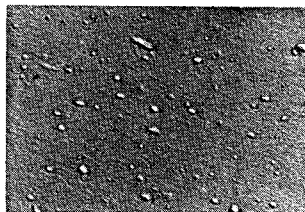
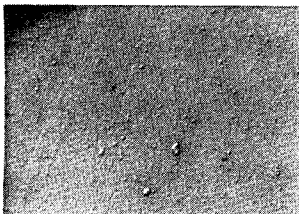


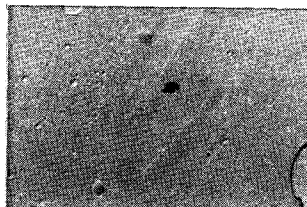
Figure 7-14. - Stress-rupture properties of dispersion-strengthened nickel sheet. Temperature, 2000° F.



Ni - 0.5 Zr - 4ThO<sub>2</sub>



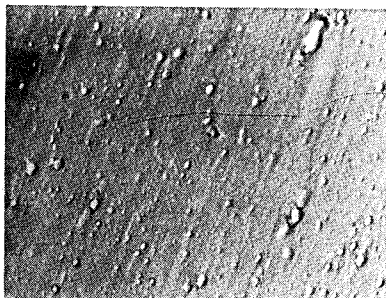
NiO - 4ThO<sub>2</sub> (HEPTANE)



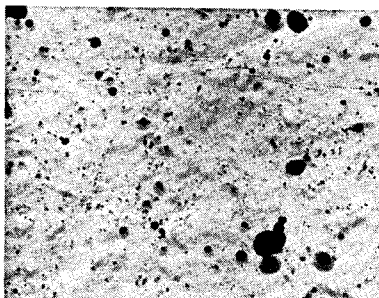
Ni - 4ThO<sub>2</sub>

CS-52137

Figure 7-15. - Microstructure of NAS-CAB Ni-ThO<sub>2</sub> sheet. X11 000.



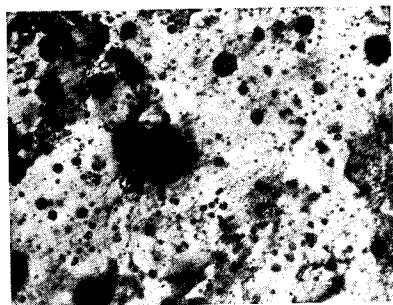
REPLICATION  
X11 000



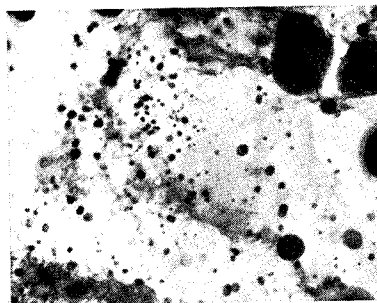
EXTRACTION  
X46 000 CS-42455

Figure 7-16. - Electron micrograph of NAS-CAB sheet (Ni-0.5Zr-4ThO<sub>2</sub>).





NAS-CAB SHEET  
Ni - 0.5 Zr - 4ThO<sub>2</sub>



REFERENCE SHEET  
Ni - 3ThO<sub>2</sub> CS-42456

Figure 7-17. - Thin-film micrographs of dispersion-strengthened nickel sheet. X48 000.

## 8. SOLID-STATE WELDING OF DISPERSION-STRENGTHENED MATERIALS

Thomas J. Moore

The potential of two solid-state welding processes was evaluated for joining the dispersion-strengthened materials thoriated nickel (TD-Ni) and thoriated nickel + 20-percent chromium (TD-NiCr). Butt joints in sheet material were made by hot isostatic pressure (HIP) welding and by magnetic force upset (MFU) welding. HIP welding was accomplished with two different sets of parameters: 1500° F at 30 ksi for 3 hours, and 2000° F at 20 ksi for 2 hours. Only microdeformation occurred at the weldment. In the MFU welding process, the faying surfaces were resistance heated, with welding accomplished by upsetting of the joint. Joint upset was generated by a forging blow from an electromagnet. Welding required about 1/10 second.

Joint efficiencies (defined as percent of parent material strength) of the butt weldments were determined in 2000° F tensile tests. Under these conditions, TD-NiCr HIP welds were 100 percent efficient. HIP welds in TD-Ni exhibited about 90-percent efficiency. TD-Ni joints made by the MFU welding process were about 80 percent efficient. MFU welds in TD-NiCr were 56 percent efficient. In comparison, conventional fusion welding techniques have produced joint efficiencies of only about 40 to 50 percent when applied to TD-Ni and TD-NiCr.

Dispersion-strengthened materials, such as thoriated nickel (TD-Ni) and thoriated nickel + 20-percent chromium (TD-NiCr), are of major interest for structural applications because of their strength in the temperature range 1900° to 2200° F. When conventional fusion welding processes are applied to these materials, however, joint efficiencies (percent of parent material strength) of only 40 to 50 percent are obtained at elevated temperatures (ref. 1). Fusion welding destroys the fine thoria dispersion and the strengthening effects produced by thermomechanical processing. If all fusion welding processes were eliminated because of low weld strength, perhaps 95 percent of commercial welding processes would be removed from consideration.

In previous work for development of suitable welding processes for TD-Ni and TD-NiCr sheet, Yount (ref. 2) has indicated that brazing shows great promise. Solid-state resistance welding also shows promise in that thoria agglomeration is avoided. Unfortunately, the lap joints that Yount used in evaluating the strength of

brazed and solid-state welded joints tended to rotate during testing. Because of the bending stresses and peeling action that take place due to joint rotation, accurate determination of joint strength and joint efficiency at 2000<sup>0</sup> F was not possible. Yount (ref. 2) and Metcalfe (ref. 3) have both found that it is relatively easy to obtain nearly 100-percent weld joint efficiency at room temperature, but the 2000<sup>0</sup> F joint efficiency is only about 50 percent for brazed lap joints and solid-state welded lap joints.

In this study, the potential of two solid-state welding processes was evaluated for joining TD-Ni and TD-NiCr sheet. The processes were hot isostatic pressure (HIP) welding and magnetic force upset (MFU) welding. HIP welding is accomplished with only microdeformation. In MFU welding, macrodeformation is produced at the joint. Butt welds made by both processes were evaluated on the basis of tensile joint efficiency at 2000<sup>0</sup> F. Results of metallographic studies of the weldments are included.

## MATERIALS

Both commercial sheet materials used in this study, TD-Ni and TD-NiCr, contain a very fine 2-volume-percent dispersion of thoria in a metal matrix that has been strengthened by thermomechanical processing. Chemical analysis of the sheet materials is presented in table 8-I.

Tensile strengths of these sheet materials at 2000<sup>0</sup> F are presented in table 8-II. Duplicate tests of flat sheet specimens were run on as-received 1/8-inch TD-Ni and heat-treated 1/8-inch TD-NiCr sheet materials parallel to the principal rolling direction. The TD-NiCr sheet was slightly stronger than TD-Ni sheet (14.6 against 13.2 ksi), but the ductility of the TD-NiCr sheet was much less than that of the TD-Ni sheet. Percent elongation of 17 percent for the 1/8-inch TD-Ni sheet was higher than would normally be expected (5 to 8 percent is more common). Because the 1/4-inch sheet was in short supply, single tests were run using bars with a 0.160-inch-diameter reduced section for tests parallel and normal to the principal rolling direction. The 1/4-inch sheet had somewhat directional properties: 14.1 ksi (parallel), 11.9 ksi (transverse), and less than 1 percent elongation in both directions.

## SOLID-STATE WELDING PROCESSES

Materials can be joined by solid-state welding methods that simply involve

bringing clean surfaces into intimate contact. Two families of solid-state welding processes are

(1) Relatively long weld-time processes that involve achievement of the required intimate contact by microdeformation. HIP welding is an example of this type of welding process.

(2) Welding processes that employ macrodeformation at the faying surfaces in order to obtain the intimate contact of virgin materials that produces a weld. The MFU welding process employs this concept.

The HIP and MFU welding procedures used in this study are described in the following sections.

### Hot Isostatic Pressure Welding

HIP welding involves a simple concept, as shown in figure 8-1. The type-304 stainless steel can was fabricated using 1/8-inch-thick sheet for the sides and 0.035-inch sheet for the ends. The can was cleaned by using a light acid etch followed by a distilled water rinse.

Outgassing heat treatments were applied to the TD-Ni ( $2200^{\circ}\text{F}$  for 1/2 hr in vacuum) and TD-NiCr ( $2000^{\circ}\text{F}$  for 10 min in vacuum) sheet materials as the first step in specimen preparation. The outgassing step was included because Metcalfe (ref. 3) has indicated that residual gas ( $\text{CO}$ ,  $\text{CO}_2$ ,  $\text{H}_2\text{O}$ ) content may impair weldability. During machining of the welding specimens, a 16 rms surface finish was produced on the faying surfaces. The machined specimens were ultrasonically cleaned in Freon and a detergent, followed by a distilled water rinse. After the cleaned specimens were placed in the can, the lid was welded to the can by using the gas tungsten-arc process in an argon-filled welding chamber. The can then was evacuated and sealed in an electron beam welding chamber after a 1/2-hour hold time at  $600^{\circ}\text{F}$  and  $2 \times 10^{-5}$  torr. Next the sealed can (fig. 8-2) containing two 1/8-inch by 1-inch by  $1\frac{1}{2}$ -inch TD-Ni specimens used to make a 1/8-inch by 1-inch by 3-inch weldment was placed into a cold-wall autoclave. One of the two sets of HIP-welding parameters (temperature, pressure, and time) shown in figure 8-1 was applied. During the HIP-welding cycle, the 0.035-inch ends of the can collapsed and forced the faying surfaces into intimate contact. Then, the entire can was squeezed against the welding specimens. During the 2- or 3-hour HIP-welding cycle used in this study, the TD-Ni and TD-NiCr specimens were welded to the can. But no macrodeformation was produced in the welding specimens because pressure was equal in all directions. The appearance of the can before and after exposure to the HIP-welding cycle is shown in figure 8-2. After HIP welding, the cans were

removed by machining. Postweld heat treatment, where applied, was accomplished after the stainless-steel can was removed.

In commercial applications, the HIP welding process may not find wide acceptance because it is expensive and difficult to apply. The expense results from the time-consuming steps that are required to produce an HIP weld. Also, there are technical problems associated with the use of a canning material and its subsequent removal. More conventional hot-press welding processes that produce only micro-deformation may find much wider acceptance.

### Magnetic Force Upset Welding

MFU welding is a solid-state resistance welding process in which specimens are welded in about 1/10 second. The MFU welding process is shown schematically in figure 8-3. Prior to welding, the faying surfaces were wiped with acetone. Copper grips (RWMA Class III) were used to hold the welding specimens in the secondary of a welding transformer. Air pressure was used to bring the faying surfaces into contact. Welding variables included joint design, phase shift control of welding and magnet current, welding current, magnet pressure, and number of cycles.

During the MFU welding process, a pulse of magnetic force is applied during each half-cycle of welding current. Synchronous timing and sequencing controls (ref. 4) were available to initiate and stop the current to the welding transformer and to the electromagnet transformer. Independent phase shift control of the welding transformer current and the electromagnet transformer current permitted precise synchronization of welding current and magnetic force. All pressure and current density calculations were made on the initial parent material cross section.

Specimens 1/8 inch by 3/4 inch by  $1\frac{9}{16}$  inches were butt welded to make weldments 1/8 inch by 3/4 inch by about 3 inches long. A decrease in length of about 0.10 inch took place during MFU welding when upset material was produced at the joint. The upset material was subsequently removed in the machining of tensile specimens.

## WELD EVALUATION PROCEDURES

### Metallography

Metallographic examination of the HIP and MFU butt welds was made to study weld microstructure. Samples were examined in the as-welded and heat-treated conditions.

## Tensile Tests

Two types of tensile specimens were used for 2000<sup>0</sup> F tests. The first type, a sheet tensile specimen (fig. 8-4(a)) was used to test 1/8-inch TD-Ni and 1/8-inch TD-NiCr sheet and weldments. For tests of weldments, the weld joint was located at midlength. In all cases, the tensile load was applied parallel to the principal rolling direction. Three tensile specimen thicknesses were used, as shown in figure 8-4(a). For the HIP weldment in TD-Ni, about 0.027 inch of TD-Ni material was removed from each major surface in order to minimize surface contamination caused by interdiffusion with the stainless-steel can. Little TD-Ni material was removed from the major surfaces of the MFU weldment, except for the upset material at the joint. For the MFU weldment in TD-NiCr, however, it was necessary to reduce the thickness from 1/8 to about 0.090 inch in order to remove surface imperfections at the weld joint.

Small button-head bars (fig. 8-4(b)) were machined from the 1/4-inch TD-NiCr sheet because this material was in short supply. Tests were made in two directions, parallel and normal to the principal rolling direction. For HIP weldments, the joint was located at midlength. Since the diameter at the reduced section is 0.160 inch, the surface of the reduced section was about 0.045 inch below the TD-NiCr weld specimen - can interface.

The specimens were held at 2000<sup>0</sup> F for 5 minutes prior to the application of load. Tensile testing was conducted in air at a crosshead speed of 0.05 inch per minute.

## THORIATED-NICKEL WELDING RESULTS

Typical microstructures for HIP and MFU butt welds in 1/8-inch TD-Ni sheet are shown in figure 8-5. These photomicrographs do not show the ThO<sub>2</sub> particles because of the extreme fineness of the particles. The parent material is recrystallized as received from the manufacturer. But new recrystallized grains were formed at the bond line of the HIP welds that were made at both 1500<sup>0</sup> and 2000<sup>0</sup> F. No new recrystallized grains were observed at the MFU weld, but extensive plastic flow is evident in the low-magnification, half cross section (X25). The type of microstructures that were developed during welding were quite stable. Postwelding heat treatment at 2300<sup>0</sup> F for 1 hour in hydrogen produced no visible effect.

Tensile test data at 2000<sup>0</sup> F are shown in table 8-III for HIP weldments and table 8-IV for MFU weldments. The bar chart in figure 8-6 shows the best test results for HIP (specimen 1) and for MFU (specimen 4) weldments in comparison with

the TD-Ni parent material data from table 8-II. The HIP weld is 92 percent efficient, and the MFU weld is 79 percent efficient. The parent material elongation of 17 percent is well above more normal parent material ductility of 5 to 8 percent. The HIP weldment, however, shows practically no ductility; the MFU weldment gave 2-percent elongation. Figure 8-7 shows the square-edge fracture and smooth fracture surface for the HIP weldment and the irregular fracture for the MFU weldment.

Further examination of the data in table 8-III reveals that 1500° F HIP weldments were somewhat weaker after heat treating (2300° F for 1 hr in hydrogen) than those tested in the as-welded condition. More work is necessary to evaluate the effects of heat treatment on mechanical properties. The heat-treated 2000° F weldment (88 percent efficient) was nearly as strong as the as-welded 1500° F weldment (92 percent efficient).

MFU welded joints in TD-Ni varied from 40- to 79-percent joint efficiency depending on the welding parameters that were used (table 8-IV). One variable that was shown to have an effect on joint efficiency is peak magnetic force. In figure 8-8, the plot for specimens 1, 2, and 3 (from table 8-IV) shows that joint efficiency increases with increasing peak magnetic pressure. Also note in table 8-IV that the strongest joints show 2- or 3-percent elongation. At lower magnet pressure, localized overheating may have occurred at the interface. Overheating might have caused ThO<sub>2</sub> agglomeration or even some localized melting. Additional studies are required to relate these factors to the welding parameters.

## THORIATED-NICKEL-CHROMIUM WELDING RESULTS

Typical HIP and MFU butt welds in TD-NiCr sheet are shown in figure 8-9. The parent material is recrystallized as received from the manufacturer. For the HIP weld in 1/4-inch sheet, the as-welded structure shown is for a weld joint normal to the principal rolling direction. The HIP weld in 1/4-inch sheet that was made parallel to the principal rolling direction was identical in appearance. For joints of both orientations, no recrystallized grains were present at the joint. Diffusion across the bond line has eliminated all evidence of the joint. In the MFU weld shown in figure 8-9, gross plastic deformation has taken place. Grain flow at the joint tends to become parallel to the bond line. And the grains in the plastically deformed region tend to be very fine. Heat treatments at 2300° F for 1 hour and 2400° F for 1 hour in vacuum produced little effect on the microstructure.

Tensile data for 2000° F tests of HIP and MFU butt welds in TD-NiCr sheet are shown in tables 8-V and 8-VI. A bar chart showing the best results for both welding processes in comparison with parent material data from table 8-II is shown in fig-

ure 8-10. Joint efficiency for the HIP weld is 100 percent because fracture took place away from the weld joint. The parent material was weakened, however, due to exposure to the HIP-welding cycle in the type-304 stainless-steel can. Interdiffusion between the can and the TD-NiCr apparently produced a weakening effect. The MFU weldment in 1/8-inch sheet was only 56 percent efficient (fig. 8-10). Evidently, the effects of the extensive plastic deformation produced a weakening effect at the joint. As can be seen in figure 8-10, practically no ductility was obtained for both the parent metal and the weldments. This lack of ductility must be taken into account when TD-NiCr is considered for structural applications at elevated temperatures. Thinner sheet than was used in this study may offer some measure of ductility and thus be of more promise.

Table 8-V shows that HIP butt welds with the joints both normal and parallel to the principal rolling direction were 100 percent efficient. This illustrates the highly beneficial effects of microdeformation welding processes. Little difference in joint efficiency (49 to 56 percent) was noted for the six MFU weldments in TD-NiCr (table 8-VI).

## SUMMARY OF RESULTS

The applicability of two solid-state welding processes, hot isostatic pressure (HIP) welding and magnetic force upset (MFU) welding, for joining thoriaated nickel (TD-Ni) and thoriaated nickel chromium (TD-NiCr) was investigated. Butt welds were produced in sheet materials, and 2000<sup>0</sup> F tensile strength was determined. Joint efficiency (percent of parent material strength) at 2000<sup>0</sup> F and metallographic examination of the weldments were used in the evaluation. The results are as follows:

1. Solid-state welding methods offer great potential for producing weldments in dispersion-strengthened materials with high joint efficiency at elevated temperatures.
2. HIP-welded joints in TD-NiCr were 100 percent efficient. Diffusion across the bond line eliminated all evidence of the joint.
3. HIP welds in TD-Ni with about 90-percent efficiency were obtained even though a band of recrystallized grains was present at the joint.
4. MFU welds in TD-NiCr were only about 55 percent efficient. The TD-NiCr material was apparently weakened by the extensive plastic deformation at the joint.
5. MFU welds in TD-Ni were about 80 percent efficient and gave about 2-percent elongation.



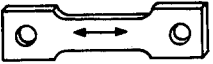
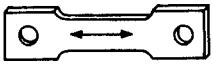
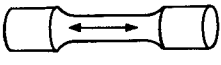
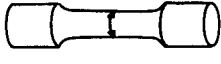
## REFERENCES

1. Redden, Thomas K.; and Barker, James F.: Making TD-Nickel Parts. Metal Progr., vol. 87, no. 1, Jan. 1965, pp. 107-113.
2. Yount, R. E.: Joining Techniques for Thoria Dispersion Strengthened Materials. SAMPE Proceedings. Vol. 14. Western Periodicals Co., 1968, p. II-2B-1.
3. Metcalfe, A. G.: Diffusion Bonding of Dispersion Strengthened Nickel Alloys. Oxide Dispersion Strengthening. George S. Ansell, Thomas D. Cooper, and Fritz V. Lenel, eds., Gordon and Breach Science Publ., 1968, pp. 783-812.
4. Phillips, Arthur L., ed.: Welding Handbook. Section 2. Fifth ed., American Welding Soc., 1964.

TABLE 8-I. - CHEMICAL ANALYSIS OF THORIATED-  
NICKEL AND THORIATED-NICKEL-CHROMIUM  
SHEET MATERIALS

Element	TD-Ni sheet, 1/8 inch thick	TD-NiCr sheet	
		1/8 Inch thick	1/4 Inch thick
	Heat number		
	1596	3089	1862-2
	Mill analysis, weight percent		
C	0.0017	0.0278	0.04
Ti	<0.001	-----	----
Fe	<0.01	-----	----
Cr	<0.01	19.87	21.39
Co	<0.01	0.030	-----
Cu	0.003	0.001	-----
S	0.0016	0.0066	0.0061
N	-----	0.002	0.0005
Ni	Balance	Balance	Balance
ThO <sub>2</sub>	2.2	2.1	2.5

TABLE 8-II. - TENSILE STRENGTHS OF THORIATED-NICKEL AND  
THORIATED-NICKEL-CHROMIUM SHEET AT 2000° F

Material	Specimen type and orientation <sup>a</sup>	Condition	Tensile strength, ksi	Percent elongation
1/8-Inch TD-Ni		As received	13.3 13.1	17 17
1/8-Inch TD-NiCr		Heat treated at 2300° F for 1 hour in vacuum	14.5 14.7	<1 <1
1/4-Inch TD-NiCr		As received	14.1	<1
		As received	11.9	<1

<sup>a</sup>Arrows indicate principal rolling direction.

TABLE 8-III. - HOT ISOSTATIC PRESSURE WELDING PARAMETERS  
AND TENSILE DATA FOR BUTT WELDS IN 1/8-INCH  
THORIATED-NICKEL SHEET

[Percent elongation, <1.]

Specimen	Welding parameters			2000° F Tensile data <sup>a</sup>	
	Temperature, °F	Helium pressure, ksi	Time, hr	Postwelding heat treatment <sup>b</sup>	Tensile strength, ksi
1	1500	30.0	3	None	12.1
2	1500	30.0	3	} 2300° F for 1 hour in hydrogen	10.5
3	1500	30.0	3		9.8
4	2000	20.0	2		11.6

<sup>a</sup>All fractures at weld joint.

<sup>b</sup>Postwelding heat treatments applied after can material was removed by machining.

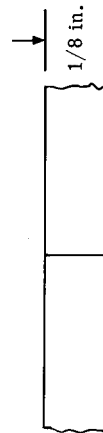
TABLE 8-IV. - MAGNETIC FORCE UPSET WELDING PARAMETERS FOR TENSILE DATA  
FOR BUTT WELDS IN 1/8-INCH THORIATED-NICKEL SHEET

[Static air pressure, 23.5 ksi; postwelding heat treatment, 2300° F for 1 hr in hydrogen.]

Specimen	Welding parameters					2000° F Tensile data <sup>a</sup>		
	Joint design <sup>b</sup>	Number of cycles	Phase shift control, percent		Welding current density, 2 peak A/in.	Peak magnet pressure, ksi	Tensile strength, ksi	Percent elongation
			Welding current	Magnet current				
1	S	8	60	100	6.6×10 <sup>5</sup>	15.2	8.3	1
2	S	8	↓	↓	6.6	28.8	9.8	3
3	S	8	↓	↓	6.6	40.8	10.1	2
4	B	5	↓	40	6.4	27.2	10.4	2
5	↓	4	↓	40	6.2	18.4	5.3	1
6	↓	3	↓	40	6.2	18.4	6.0	<1
7	↓	3	65	40	6.6	18.4	8.6	1

<sup>a</sup>All fractures at weld joint.

<sup>b</sup>S: Square butt joint



B: Beveled butt joint

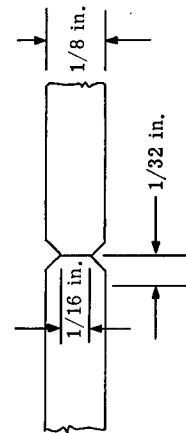


TABLE 8-V. - HOT ISOSTATIC PRESSURE

WELDING PARAMETERS AND TENSILE

DATA FOR BUTT WELDS IN 1/4-INCH

THORIATED-NICKEL-CHROMIUM

# SHEET

[Welding parameters: temperature, 2000° F; helium pressure, 20 ksi; time, 2 hr. Postwelding heat treatment, none; percent elongation, <1.]

Specimen	2000° F Tensile data <sup>a</sup>	
	Tensile strength, ksi	Joint orientation <sup>b</sup>
1	13.3	
2	8.8	

<sup>a</sup>Both fractures near specimen shoulders, away from weld joint.

<sup>b</sup>Arrows indicate principal rolling direction.

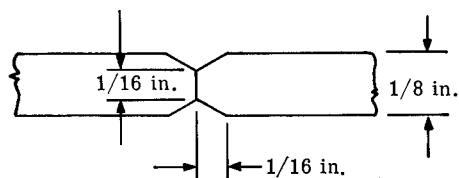
TABLE 8-VI. - MAGNETIC FORCE UPSET WELDING PARAMETERS AND  
TENSILE DATA FOR BUTT WELDS IN 1/8-INCH  
THORIATED-NICKEL-CHROMIUM SHEET

[Welding parameters: phase shift control of magnet current, 100 percent;  
peak magnet pressure, 36.0 ksi; static air pressure, 23.5 ksi.  
Percent elongation, <1.]

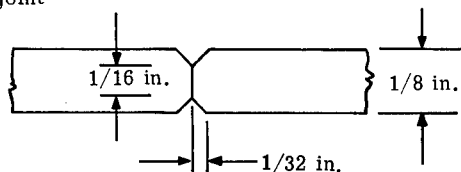
Specimen	Welding parameters				2000° F Tensile data <sup>a</sup>	
	Joint <sup>b</sup> design	Number of cycles	Phase shift control of welding current, percent	Welding current density, peak A/in. <sup>2</sup>	Postwelding heat treatment	Tensile strength, ksi
1	B-1	4	40	$4.2 \times 10^5$	} 2300° F for 1 hr in vacuum	8.2
2	B-2	6	34	3.8		7.7
3	B-1	5	↓	3.6	} 2400° F for 1 hr in vacuum	7.9
4	B-1	6		4.1		7.2
5	B-2	6		3.7		7.5
6	B-2	13	26	2.9		7.3

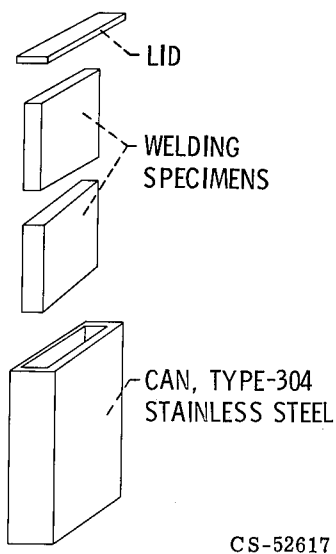
<sup>a</sup>All fractures at weld joint.

<sup>b</sup>B-1: Beveled butt joint



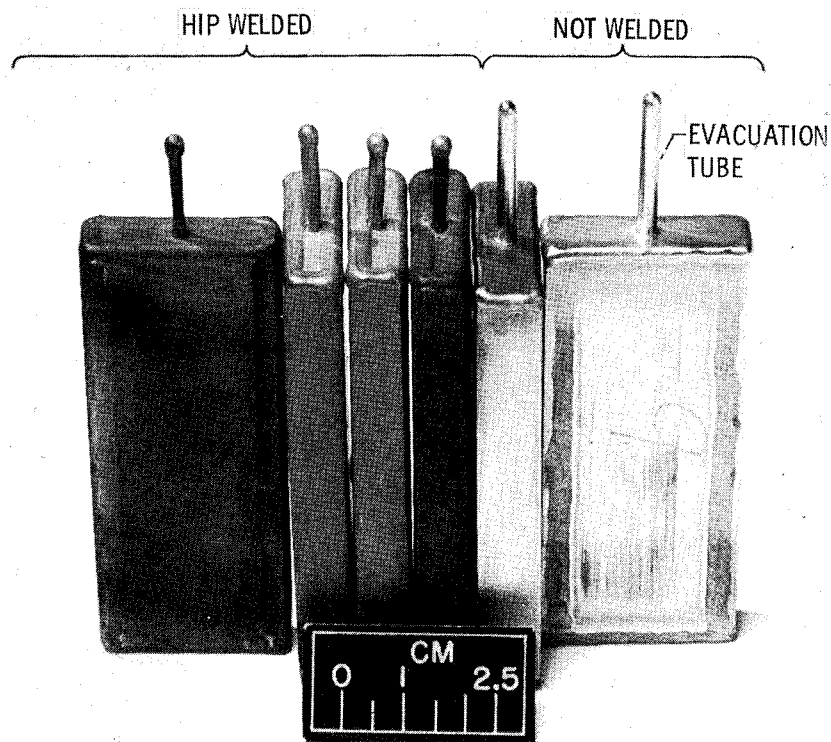
B-2: Beveled butt joint





CS-52617

Figure 8-1. - Hot isostatic pressure (HIP) welding.  
Features: microdeformation, long weld-time, overall heating. Parameters for this study: 1500° F at 30 ksi (helium) for 3 hours; 2000° F at 20 ksi (helium) for 2 hours.



C-69-1986

Figure 8-2. - Sealed cans containing thoriated-nickel samples, before and after exposure to hot isostatic pressure welding cycle.

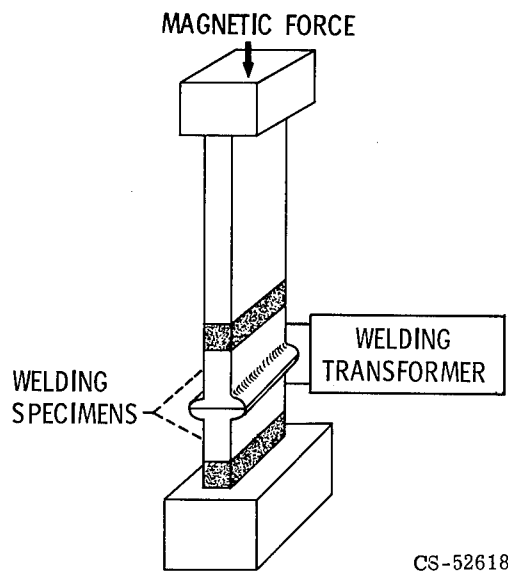
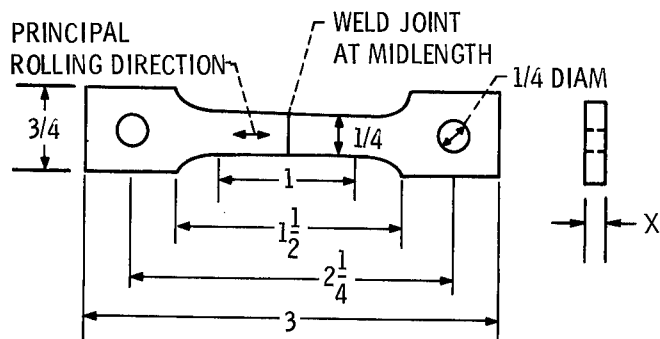
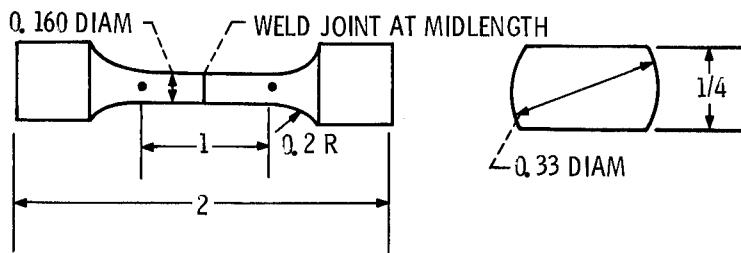


Figure 8-3. - Magnetic force upset (MFU) welding. Features: macrodeformation, short weld-time, local heating. Typical parameters: weld time, 1/10 sec; weld current,  $7 \times 10^5$  amperes per square inch; magnet pressure, 30 ksi.



PROCESS	MATERIAL, 1/8-IN. -THICK SHEET OF -	SPECIMEN THICKNESS, X, IN.
HIP	TD-Ni	0.070
MFU	TD-Ni	.115
MFU	TD-NiCr	.090

(a) Sheet tensile specimens.



(b) Bar tensile specimen, 1/4-inch TD-NiCr sheet.

Figure 8-4. - Tensile specimens. (All dimensions are in inches.)

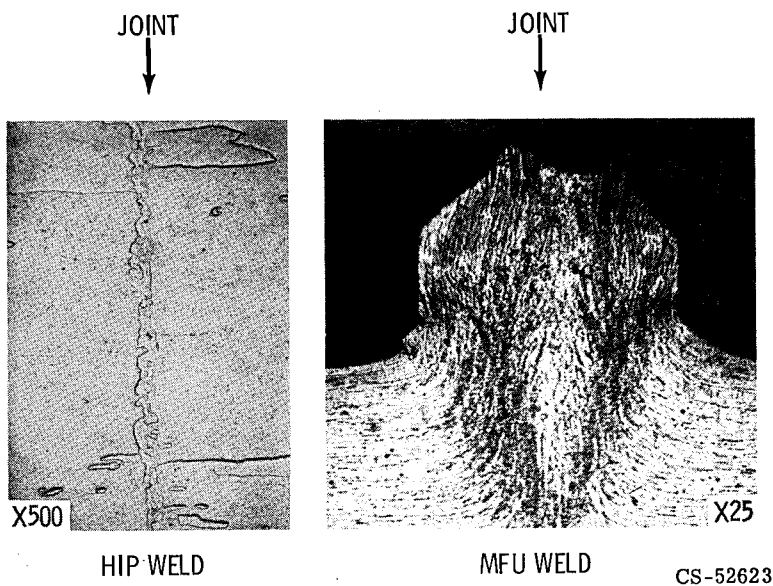


Figure 8-5. - Hot isostatic pressure (HIP) and magnetic force upset (MFU) butt welds in 1/8-inch thoria-nickel sheet. Heat treated at 2300° F for 1 hour in hydrogen.

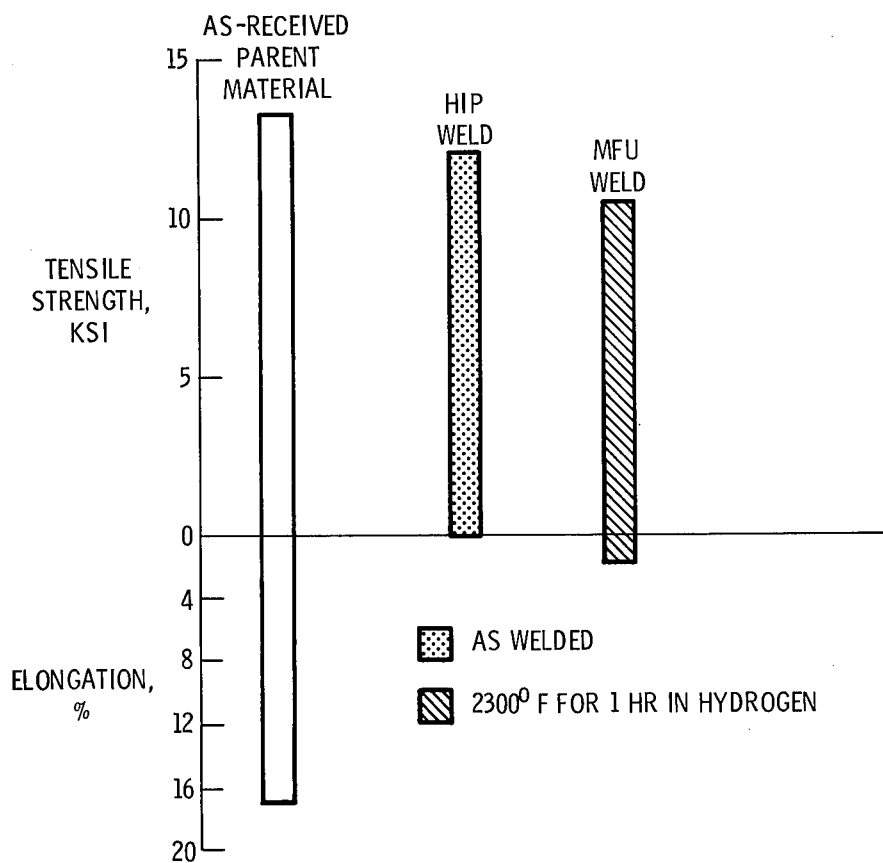


Figure 8-6. - Tensile properties of butt welds in 1/8-inch thoria-nickel sheet. Temperature, 2000° F.

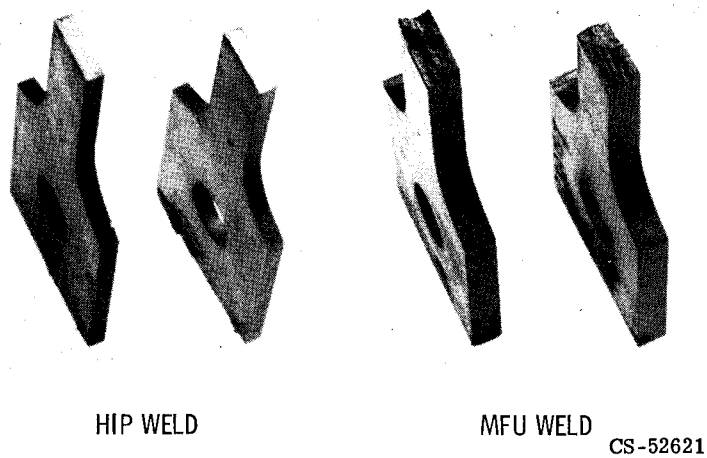


Figure 8-7. - Fracture at hot isostatic pressure (HIP) and magnetic force upset (MFU) weld joints in thoriated-nickel sheet in 2000° F tensile tests.

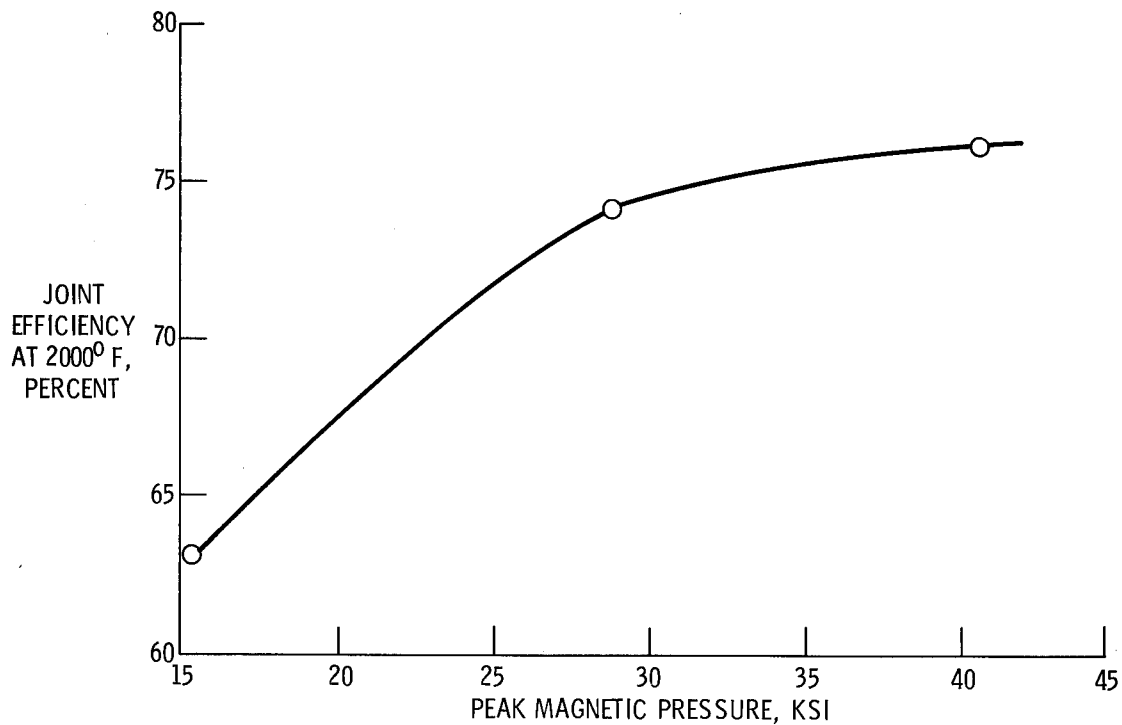


Figure 8-8. - Effect of peak magnetic pressure on 2000° F joint efficiency of magnetic force upset (MFU) weldments in 1/8-inch thoriated-nickel sheet. Square butt joint design; number of weld cycles, 8; welding current density,  $6.6 \times 10^5$  peak amperes per square inch; static air pressure, 23.5 ksi; decrease in length of weldment, 0.12 to 0.13 inch; phase shift control: welding current, 60 percent; magnetic force current, 100 percent.



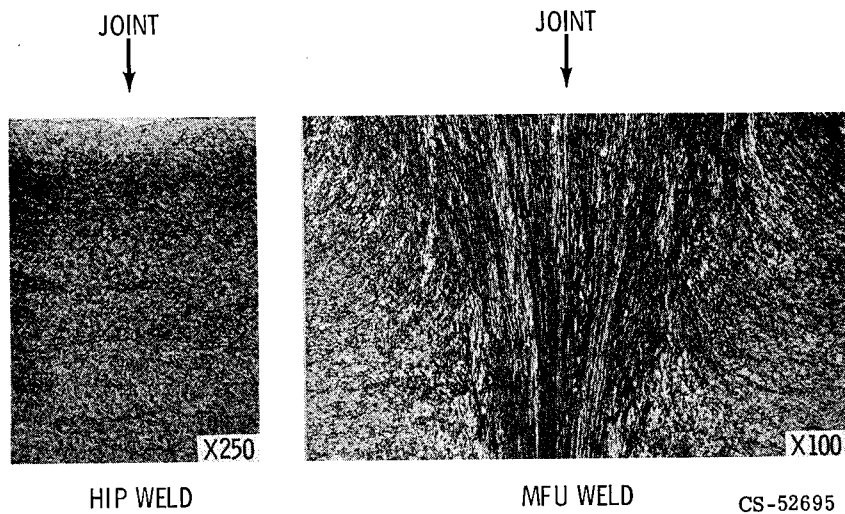


Figure 8-9. - Butt welds in thoriaated-nickel-chromium sheet: hot isostatic pressure (HIP) weld in 1/4-inch sheet, as welded; magnetic force upset (MFU) weld in 1/8-inch sheet, heat treated at 2300° F for 1 hour in vacuum.

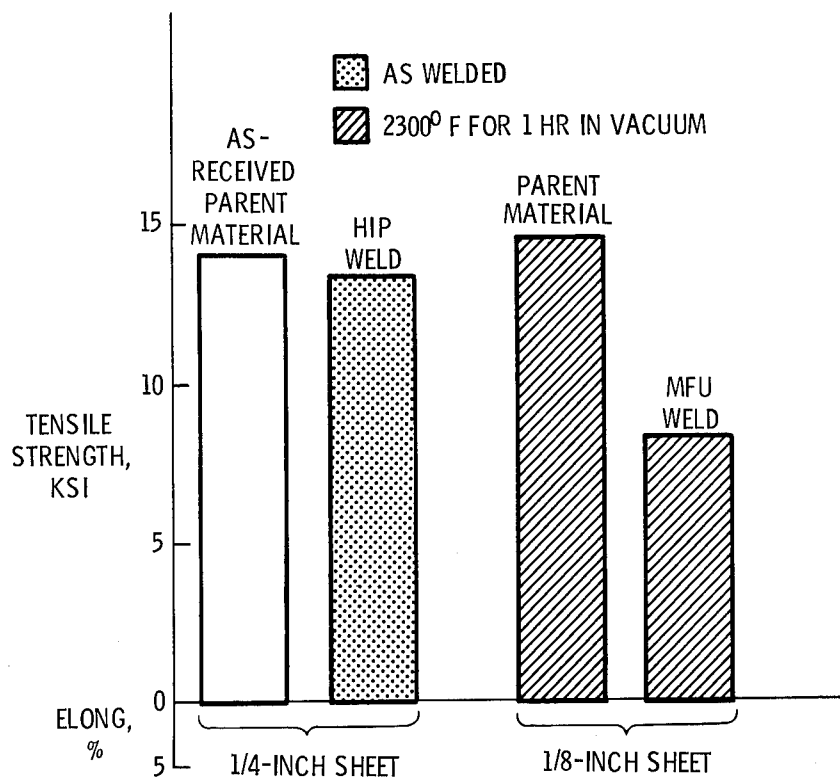


Figure 8-10. - Tensile properties of butt welds in thoriaated-nickel-chromium sheet. Temperature, 2000° F.

## 9. RECENT DEVELOPMENTS IN CHROMIUM AND CHROMIUM ALLOYS\*

William D. Klopp

Recent developments in chromium pertinent to its potential use in advanced jet engines are reviewed. Although chromium has a strength-to-density advantage over nickel, its inherent brittleness and further embrittlement by nitrogen during high-temperature exposure are serious limitations to its use. Twelve chromium alloys are currently under development, the strongest showing a potential 150° F (83 K) service temperature advantage over nickel-base superalloys. However, a better balance between solution strengthening and precipitate strengthening must be achieved in order to improve the low temperature ductility of these alloys. Improved coatings for protection against nitrogen embrittlement must be developed.

Chromium-base alloys are currently of considerable interest as potential turbine bucket and stator vane materials for advanced jet engines. The advantages of chromium over current nickel-base superalloys are well known and include higher melting point, higher elastic modulus, and lower density. The disadvantages of chromium are equally well known, being primarily the transition from ductile to brittle behavior, usually above room temperature, a characteristic shared with its sister elements molybdenum and tungsten, and the further embrittlement resulting from nitrogen contamination during high-temperature air exposure.

Historically, chromium as an alloy base has been of interest for slightly more than two decades, dating back to the work of Parke and Bens in the middle 1940's (ref. 1). These early studies were hampered by the unavailability of chromium metal of good purity, the only available grade at that time being electrolytic chromium of questionable quality.

The extensive studies on chromium in Australia initiated in 1946 (ref. 2) and the development of the iodide process for the production of high-purity chromium in the early 1950's (ref. 3) provided major impetus to the development of chromium-base alloys. Concurrently, nitrogen was identified as the major embrittling impurity in chromium (ref. 4).

---

\*Also published as NASA Technical Memorandum X-1867.

The 1955 Conference on Ductile Chromium and Its Alloy (ref. 5) represents a milestone in the development of usable chromium-base materials. At this meeting, the effects of purity on ductility and the results of early alloying studies on strength (refs. 6 and 7) were reported.

From 1955 to 1959, chromium research continued through a number of largely unrelated projects. The only identifiable continuing effort during this time period was that jointly conducted by the Aeronautical Research Laboratories and the Defence Standards Laboratory, both of the Research and Development Branch of the Australian Department of Supply.

In 1959, the beneficial effects of yttrium on the oxidation-embrittlement resistance of chromium were reported by Collins and coworkers from the General Electric Company (refs. 8 and 9). This discovery and the development of ductile Cr-MgO alloys by Scruggs and coworkers at the Bendix Corporation (ref. 10) marked the initiation of a second period of alloy development which is still continuing. The early Bendix alloy, Cr-6MgO-0.5Ti, was designated Chrome-30 (ref. 11). Development of Cr-MgO alloys has continued under sponsorship of the Air Force and the Bureau of Naval Weapons, culminating in the recent development of the Chrome-90S alloy (ref. 12).

Alloy development at the General Electric Company was conducted under partial Air Force sponsorship and resulted in the development of the C-207 alloy, Cr-7.5W-0.8Zr-0.2Ti-0.1C-0.15Y, reported by Clark and Chang in 1966 (ref. 13). Development of these alloys combining both carbide strengthening and solid solution strengthening has continued since 1965 under NASA sponsorship.

The Australian efforts resulted in the development of Cr-2Ta-0.5Si-0.1Ti, designated as Alloy E, in the early 1960's (ref. 14). Modified alloys, designated as H and J, were reported subsequently (refs. 15 and 16), with the major portions of this extensive and valuable program terminating in 1965.

This paper reviews the reasons for our continuing interest in chromium alloys, the pertinent physical metallurgy of chromium including the general effects of alloying, and the status of chromium alloys currently under development. Suggested areas for future research are also discussed. For a more detailed review of chromium technology up to 1966, the reader is referred to the comprehensive report by Maykuth and Gilbert (ref. 17). The articles by Sims (ref. 18), Wain and Johnstone (ref. 15), and Rogers and Brown (ref. 19), and the recently revised book by Sully (ref. 20) also provide excellent background information.

## METHODS FOR OBTAINING HIGHER OPERATING TEMPERATURES IN JET ENGINES

Much of the current interest in chromium alloys is motivated by their potential for use in advanced aircraft engines. Therefore, before reviewing the properties of chromium, it is appropriate to consider briefly the status of competitive materials and methods for obtaining higher operating temperatures.

The stress-to-density ratios for rupture in 1000 hours are shown in figure 9-1 for typical nickel-base superalloys. The horizontal bands indicate the stress levels typical of rotating turbine buckets and stator vanes in many modern engines. The current cast alloys, such as IN-100 and the NASA-TRW VI-A alloy, offer an operating temperature advantage of about 100° F over wrought alloys, such as U-700.

Currently, turbine inlet temperatures above the temperature capabilities of nickel-base alloys are being achieved by cooling the nickel components with air bled from the aft section of the compressor. This involves a penalty in terms of a slight loss of expensive compressor air and increased engine complexity. It would be more desirable to use a high-temperature material which did not require cooling.

Several potential materials for achieving higher operating temperatures are being studied. In addition to chromium, these include improved nickel alloys, single-crystal alloys, thoria-dispersed nickel and cobalt alloys, fiber-reinforced alloys, and at much higher temperatures, columbium and tantalum alloys. All these materials are currently receiving attention and are competitive with chromium as potential high-temperature engine materials.

Table 9-I lists the major properties of interest for both chromium and nickel. Chromium has the open, body-centered-cubic structure and thus is expected to have higher self-diffusion rates and lower creep strength at the same homologous temperature as nickel, which has the close-packed, face-centered-cubic structure. However, the open structure of chromium is more than compensated for by its higher melting point, higher elastic modulus, and lower density, which combine to give chromium a significant strength-to-density advantage over nickel. Chromium has a lower coefficient of thermal expansion than nickel, making chromium more resistant to thermal fatigue during cyclic heating.

The major disadvantages of chromium are its almost complete lack of ductility below the ductile-brittle transition temperature, which for unalloyed recrystallized chromium of commercial purity is around 300° F, and the further severe embrittlement which results from nitrogen contamination during high-temperature air exposure. In contrast, nickel exhibits good ductility and toughness to subzero temperatures.

The high vapor pressure of chromium is of some concern during melting and during vacuum heating, such as for use in space applications, but has not been shown to be deleterious during normal air heating.

## GENERAL ALLOYING EFFECTS ON STRENGTH AND DUCTILITY

In order to present an adequate picture of the present status of chromium alloy development, it is necessary to assess as best as possible the effects of individual alloying elements of interest on the pertinent properties of chromium. These properties, for the purposes of this review, include high-temperature strength, particularly creep strength, low-temperature ductility, and oxidation-nitridation resistance.

The effects of solid solution alloying on the high-temperature strength of chromium are presented in figure 9-2 (refs. 14 and 21 to 26). To construct this figure it has been necessary to draw from a number of separate investigations, most of which differed significantly in the manner of alloy preparation and also in the reporting of strength in terms of tensile or creep results. For this reason, it was chosen to report the strengthening effects as a ratio of the tensile or creep strength to that of unalloyed chromium under similar conditions.

It is seen from figure 9-2 that substitutional solutes can increase the high-temperature strength of chromium threefold to fourfold. The highest specific strengthening rates are achieved on alloying with the Group VA elements, Ta, Nb, and V. Tantalum, and probably also columbium, lose their strengthening effectiveness at low alloying levels because of restricted solubilities in chromium, both of which are in the range of 0.5 to 1 atomic percent in the temperature range of interest. Vanadium also appears to become less effective at alloying levels above 1 atomic percent, although it is completely soluble in chromium. Of the Group VIA solutes, tungsten is a more effective strengthener than molybdenum and both are more effective than rhenium from Group VIIA. These three elements have more extended solubilities in chromium than do tantalum and columbium, but alloys containing 4 atomic percent or more of these elements are difficult to fabricate. Zirconium, the lone representative of Group IVA for which data were available, is seen to be weakening.

The relative strengthening rates of solutes within Group VA and within Groups VIA and VIIA follow qualitatively the well-known principles of solution strengthening which relate strengthening effectiveness to differences in atomic size and elastic modulus. The most effective strengtheners in these two groups, tantalum and tungsten, have the largest size differences and the largest elastic moduli differences

with chromium. An additional unknown factor, probably related to the position of the solute in the periodic table, is needed to correlate the strengthening effects of solutes from different periodic groups.

Unfortunately, most solution strengthening solutes have a deleterious effect on the low-temperature ductility of chromium (refs. 21, 25, 27 to 31). (Exceptions are Fe, Co, Re, and Ru, which at large alloying concentrations promote improved ductility through the "rhenium ductilizing effect" (ref. 32).) Representative data on the effects of these elements on the ductile-brittle transition temperature of chromium are shown in figure 9-3. These data, taken from the study of Carlson et al. (ref. 30), illustrate the changes in ductile-brittle transition temperature on alloying with columbium, tantalum, molybdenum, and tungsten. The increases in ductile-brittle transition temperatures on alloying with these four elements may be considered typical of the effects of alloying with solution strengthening elements. Although molybdenum had little effect in this study, other work (refs. 25 and 29) indicates it to be almost as embrittling as tungsten. It is thus apparent that although considerable strengthening can be achieved in chromium by alloying with substitutional solutes, such strengthening is only achieved at the cost of a significant increase in the ductile-brittle transition temperature.

The low transition temperature of  $-50^{\circ}\text{F}$  for unalloyed chromium was observed in Carlson's study because of the slow bending rate used. It is of interest to note that minor solution softening effects were observed at alloying levels of about 0.05 atomic percent.

Limited data on the effects of precipitate strengthening with carbides, borides, and nitrides are presented in figure 9-4 (refs. 15, 23 to 26, and 33 to 38). In this case, as for solid solution strengthening, it is necessary to present the results as strength ratios to unalloyed chromium in order to compare results obtained by different investigators at different temperatures. For all precipitate alloys, the interpolated or extrapolated strengths for rupture in 100 hours were used.

Among the carbides, it is seen that least strengthening is obtained from  $\text{ZrC}$ , while much higher strength increments are obtained from  $\text{CbC}$  and from  $\text{TaC}$ . This difference is related to the low solubility for zirconium in chromium, which prevents refinement of the carbides through solutioning and results in the retention of coarse carbides which are less strengthening (ref. 38).

The most effective precipitate strengthener for which data are available is  $\text{TaB}_2$ , which produces almost a fivefold increase in the creep strength of chromium. Columbium boride and other mixed borides are also known to be effective creep strengtheners for chromium from the recent work of Clark (ref. 25).

Titanium nitride is seen to be a moderate strengthener for chromium and also promotes a low ductile-brittle transition temperature.

The strength of a precipitate-strengthened or dispersion-strengthened material is related to the particle spacing, according to Orowan (ref. 39), Ansell (ref. 40), and others, by

$$\sigma = \sigma_o + \frac{C}{\lambda} \quad (1)$$

where

$\sigma$  yield strength or creep strength

$\sigma_o$  matrix strength

$C$  constant including Burgers vector and matrix shear modulus

$\lambda$  interparticle spacing

Westmacott et al. (ref. 41) have shown by planar analysis that  $\lambda$  is directly proportional to the particle diameter  $d$  and inversely proportional to the square root of the volume fraction of dispersed phase  $f$ , so that equation (1) can be written as

$$\sigma = \sigma_o + C' \frac{f^{1/2}}{d} \quad (2)$$

Thus, decreasing the particle size at a constant volume fraction or increasing the volume fraction at a constant particle size tends to increase the strength contribution from the second phase. Recent data on tungsten and W-Re strengthened by HfC (ref. 42) tend to confirm the validity of equation (2). Ryan (ref. 36) has also shown that the creep strength of chromium strengthened by TaC is decreased by increasing the TaC particle size. Considerable work, however, remains to be done on chromium in order to identify the most strengthening precipitate and determine the optimum volume fraction and particle size.

It is most significant to note that precipitate strengthening does not increase the ductile-brittle transition temperature to the extent that solution strengthening does. As indicated in figure 9-4, the range of transition temperatures is equal to, or less than, that of unalloyed chromium. The work of Ryan, in fact, indicated that the carbides of most of the Group IVA and VA elements reduced the transition temperatures to significantly below that of unalloyed recrystallized chromium. These results are in accord with the recent theories of Hahn and Rosenfield (ref. 43) and others (ref. 44) regarding the ductilizing of Group VIA metals by finely dispersed second phases.

Thus, strength improvements in chromium comparable to those achieved by solution strengthening can be obtained by proper dispersion strengthening without a concurrent increase in the ductile-brittle transition temperature.

The question of particle size stability must be considered when developing alloys whose strength is dependent on the maintenance of a fine particle size. Recent work on the coarsening of a precipitated phase in a binary system has shown that the coarsening rate is cubic with respect to time and is proportional to both the diffusivity and the soluble concentration of the slower-diffusing component (ref. 45). It may thus be estimated that for ternary systems, such as carbides of the Group IVA and VA elements in a Group VIA matrix, the coarsening kinetics should also be cubic and should be proportional to the diffusivities and soluble concentrations of the Group IVA or VA element. In order to examine the coarsening rates of carbides in chromium on this basis, cubic coarsening rates were estimated from the data of Ryan (ref. 36) (the experimental coarsening curves were approximately parabolic at 2372° and 2552° F and logarithmic at 2192° F) and are compared with carbide coarsening rates in molybdenum (ref. 46) and tungsten (ref. 42) in figure 9-5. The similarity of the coarsening rates and of the temperature dependency on a homologous temperature basis suggests that the diffusivity of the carbide forming element, which would have a temperature dependence similar to that for self-diffusion of the solvent metal, is rate-controlling. More importantly, however, Ryan's data indicate that CbC and TaC precipitates in chromium should be able to maintain particle sizes of several tenths of a micron for times greater than 1000 hours in the temperature range of 2000° to 2200° F. Good creep strength should also be maintained in this time-temperature range.

## EFFECTS OF NITROGEN ON DUCTILITY

It is now well-known that nitrogen has a particularly deleterious effect on the ductility of chromium. This effect poses a serious obstacle to the development of useful chromium alloys, since the oxide scale which forms during high-temperature air exposure is usually sufficiently porous that nitrogen can saturate and embrittle the surface of the underlying substrate.

Part of the reason for the rather unusual sensitivity of chromium to nitrogen as opposed to oxygen lies in the relatively high solubility of nitrogen in chromium at elevated temperatures. As shown in figure 9-6, carbon has a fairly high solubility in all three Group VIA metals, up to about 1 atomic percent (refs. 47 and 48). In contrast, oxygen solubility is low, less than 0.05 atomic percent in all three metals



(refs. 49 to 51), possibly reflecting the larger diameter of the interstitially dissolved oxygen ion. Nitrogen solubility, however, ranges from less than 0.01 atomic percent in tungsten to 1 atomic percent in chromium (refs. 49 and 52 to 56). Thus, at high temperatures, chromium can dissolve about 100 times as much nitrogen as oxygen. This high solubility, plus the fact that the nitride tends to precipitate as an acicular intragranular phase rather than as a spheroidal or intergranular phase like the carbide and oxide, makes nitrogen more deleterious than oxygen in chromium.

The effects of nitrogen on the ductility of chromium have been the subject of several recent investigations (refs. 4 and 57 to 60). The data plotted in figure 9-7 are illustrative of the results. When dilute chromium-nitrogen alloys are slow-cooled, the nitride can coalesce into large particles which increase the ductile-brittle transition temperature by only about 100° F at the 0.1 atomic percent nitrogen level. However, as the cooling rate increases, the effectiveness of nitrogen in increasing the ductile-brittle transition temperature also increases. Although it was originally postulated that this increased effect was a result of nitrogen retained in supersaturated solution, the effect is now attributed to a decrease in size of the nitride precipitate, possibly through increased coherency strains between the precipitate and the chromium matrix (ref. 61). Gilbert and Klein (ref. 62) have recently shown that dissolved nitrogen, which can be retained in solution only by rapid quenching of thin sections, has little effect on the transition temperature of chromium. It may also be noted in figure 9-7 that the "unalloyed" iodide chromium of Cairns and Grant also exhibited an effect of quenching rate on ductile-brittle transition temperature, suggesting that high-purity chromium is quite sensitive to trace impurities.

The effects of alloying on the oxidation behavior of chromium has been the subject of several recent studies (refs. 15, 22, 25, 38, and 63 to 70). The results of these studies, however, have usually been expressed in terms of alloying effects on oxidation weight gain. As shown by Abrahamson and Grant (ref. 65), the oxidation weight gains cannot be related to nitrogen absorption nor presumably to the property of most interest, ductile-brittle transition temperature.

Some of the recent results of Clark (ref. 25) are directly pertinent in that the ductile-brittle transition temperatures (15° bend at 0.05 in./min) were measured as a function of both alloying and oxidation. These results are shown in figure 9-8. Although unalloyed chromium is not shown here, it has a bend transition temperature (90° bend at 1 in./min) of about 300° F in the annealed condition and 1000° F after air exposure for 100 hours at 2100° F (unpublished work, J. R. Stephens, NASA). The addition of 0.1 atomic percent yttrium is beneficial in reducing the transition temperature of chromium both in the annealed condition and after oxidation at 1500°

and 2100<sup>0</sup> F for 100 hours. This effect is shared by most of the other rare earths, notably lanthanum, and is apparently related both to gettering of interstitials from solution in chromium (ref. 71) and to promoting formation of a tightly adherent oxide scale which substantially reduces ingress of nitrogen to the substrate (ref. 64). Similar but more complex alloys, such as Cr-Y-Hf-Th, have been shown (refs. 22 and 25) to be even more resistant to oxidation-nitridation than Cr-Y and may be useful as claddings for a high-strength substrate. Yttrium, however, is slightly detrimental to high-temperature strength and, more unfortunately, is not so effective in reducing oxidation embrittlement of carbide-strengthened chromium alloys. Chromium-yttrium alloys with TiC, NbC, and TaC are seen in figure 9-8 to be particularly embrittled by high-temperature air exposure, while alloys with ZrC and HfC are not so prone to oxidation-embrittlement.

It is apparent that nitrogen embrittlement during high-temperature air exposure poses a major problem to the development of chromium alloys. This problem does not appear amenable to solution by alloying, such as with yttrium. Protective coatings, clads, or special surface alloying techniques must be developed if chromium alloys are to be useful at high temperatures in air.

## CURRENT CHROMIUM ALLOYS

A total of 12 chromium alloys can be classified as recently developed or currently under development. These include five from the United States, three from Australia, and four from the Soviet Union. Compositions (where known) and developing organizations are given in table 9-II.

The strength and ductility properties of the five United States alloys are summarized in figure 9-9 (refs. 12, 13, and 25). This group can be divided into two subgroups. Two alloys, designated C-207 and CI-41, are produced by induction melting and combine solution strengthening by tungsten or molybdenum with precipitate strengthening by carbides. These two alloys also contain small amounts of yttrium or yttrium plus lanthanum for scavenging and slightly improved oxidation resistance. Both alloys have good strength in the 2000<sup>0</sup> to 2100<sup>0</sup> F range, with the CI-41 alloy exhibiting about a 75<sup>0</sup> F service temperature advantage over C-207. Both alloys have moderately high ductile-brittle transition temperatures, particularly in impact, probably resulting from alloying with tungsten and molybdenum. Both alloys have been produced as 100-pound induction-melted ingots. The CI-41 alloy has been fabricated to rod, plate, and sheet for use as a substrate for protective coatings development and for other special property evaluations (ref. 72).

The three alloys designated Chrome-30, Chrome-90, and Chrome-90S are produced by powder metallurgy techniques, the principal alloy addition in each being MgO. The Chrome-30 alloy, developed in 1962, also contains 0.5 percent titanium, while later alloys also contain other elements for improved high-temperature strength and oxidation resistance. The main advantage of these alloys is the improved low-temperature ductility and high-temperature oxidation resistance imparted by MgO. As seen in figure 9-9, the Chrome-30 and Chrome-90 alloys exhibit tensile ductility at room temperature, but have low strength at elevated temperatures. The Chrome-90S alloy has improved high-temperature strength, but at the expense of a substantial increase in the ductile-brittle transition temperature. This class of alloys may be useful in low-strength applications such as stator vanes.

Three alloys, designated as E, H, and J, have been developed under the auspices of the Australian Department of Supply. All have similar compositions based on Cr-2Ta-0.5Si, with E and H also containing 0.1 percent Ti and 0.5 percent rare-earth elements, respectively. The mechanical properties of alloy E have been studied rather extensively (refs. 15 and 73), but very little property data are available on alloys H and J. The high-temperature rupture strength of alloy E is shown in figure 9-10 and is seen to be slightly lower than that of C-207 and CI-41. Both strength and ductility of alloy E are affected by annealing treatments, the ductility tending to increase and the rupture strength tending to decrease with increasing annealing temperature. In the as-extruded condition, alloy E has a bend transition temperature of about 200° F, but annealing at 2300° F reduces the transition temperature to -100° F. Alloy H has better ductility retention after high-temperature air exposure than alloy E through the substitution of rare-earth elements for titanium.

Advanced rig testing has been performed on all three of the Australian chromium alloys. Turbine buckets forged of alloys E and H withstood 9 hours of running at 1875° F in a rotating rig turbine wheel (ref. 74). The test was terminated when the combustor failed and pieces from the combustor caused two of the six chromium alloy buckets to fail at the root. Although the chromium alloy buckets showed considerably less creep extension than did the cobalt HS31 alloy buckets, the mode of failure indicates that the chromium buckets were brittle in impact at the root temperature. Clearly, chromium alloys must be ductile in impact at the minimum operating temperature in order to be used safely.

Several alloy J blades were also evaluated in a "cascade rig," which involved stationary heating to 2000° F for 25 hours in a sonic velocity gas stream (ref. 16). The major result from this test was the observation that the oxide scale was more adherent and the depth of nitrogen contamination was considerably less after heating in the sonic velocity gas stream than after comparable heating in static air. Thus,

static air exposure tests on chromium alloys may give inaccurate results (see also ref. 75).

The limited strength and ductility data available for Soviet alloys are summarized in figure 9-11 (refs. 76 and 77). The BX-3 alloy is apparently stronger than C-207 and CI-41, but is produced only in the cast condition and has poor ductility. The weaker BX-2, BX-2I, and BX-4 alloys are fabricable and have "good" low-temperature ductility. Compositions and status of development for these alloys are unknown.

The trade-off between high-temperature strength and low-temperature ductility for chromium alloys under development is indicated in figure 9-12. The data are seen to fall into two groupings, one comprised of the melted alloys, and the second comprised of the powder metallurgy alloys. The melted alloys have higher 2000° F rupture strengths than do the powder metallurgy alloys. It is also obvious that the major trend within each grouping is for the ductile-brittle transition temperature to increase substantially as the high-temperature strength is increased. This is a result of reliance on solid solution strengthening for the major portion of the strength of these alloys. It is apparent that other means for strengthening, such as precipitate strengthening or dispersion strengthening, must be more effectively utilized in order to develop chromium alloys with a more usable combination of low-temperature ductility and high-temperature strength.

The extrapolated long-time strengths of current chromium alloys are compared with those of nickel and columbium alloys on a density-compensated basis in figure 9-13. In the stress range of interest for turbine buckets, alloy E offers a 25° F advantage over the strongest current nickel alloys, while C-207 and CI-41 offer temperature advantages of about 75° and 150° F, respectively. A columbium alloy such as B-88 would offer a temperature advantage of about 500° F, pending solution of the difficult oxidation protection problem.

Although protective coatings for chromium have been under study for several years, progress has been slow. The current status of some potential coatings for chromium is summarized in figure 9-14 (refs. 78 and 79). Claddings of Ni-Cr-Al have been evaluated, but are embrittling to the chromium substrate because of metallic interdiffusion. Aluminide coatings are protective from oxidation, but aluminum itself diffuses into chromium rapidly and is embrittling. In contrast, silicide coatings are not in themselves embrittling to the substrate. Although  $\text{CrSi}_2$  is unable to form a protective oxide scale because of the refractoriness of  $\text{Cr}_2\text{O}_3$ , modification of the silicide with elements such as iron allows the formation of a vitreous and more protective silicate scale which substantially reduces embrittlement of the substrate. This type of coating is potentially quite attractive although the brittleness of the silicide is of some concern.

## AREAS FOR FUTURE WORK

It is possible at this time to identify the most critical problems associated with the development of useful chromium alloys and to suggest some profitable avenues for future work.

The most critical current problems in the development of chromium are, in order of importance, (1) the protection of chromium from nitridation-embrittlement; (2) improvement in the intrinsic impact ductility of chromium alloys at low temperatures; and (3) further improvement in the high-temperature strength of chromium.

The protection of chromium from embrittlement through nitrogen contamination during high-temperature air exposure appears to require the development of a protective coating. Although alloying with yttrium and/or other rare earths improves the resistance of unalloyed chromium, the effectiveness of these additions is practically eliminated by further alloying for high-temperature strength. Types of surface coatings which might prove useful include chromium compounds, particularly modified silicides, ductile claddings, and surface diffusion layers. Future work should include all three of these approaches. Silicides should be modified with elements such as iron, vanadium, molybdenum, and rhenium which form low-melting oxides and thus might be expected to help form a more vitreous silicate scale. Cladding candidates should include compatible alloys, such as Cr-Y-Th-Hf, which have good oxidation resistance and ductility retention. On a practical basis, it may be difficult to completely clad such a complex shape as a turbine bucket. Surface alloying to introduce protective elements at the surface through diffusion should be studied. Elements such as yttrium, thorium, and hafnium could be deposited by pack cementation or "metallizing" to produce an oxidation-resistant surface. Any such protection method must be ultimately capable of protecting the substrate from embrittlement for times of the order of hundreds to thousands of hours in the temperature range 2000° to 2200° F.

In the evaluation of protection methods, the effects of air velocity must be considered, since it has been demonstrated that oxidation and embrittlement are different in static and high velocity air.

Improvements in the intrinsic impact ductility of chromium at low temperatures will require modifications in alloying approaches for high-temperature strength. The reliance on solution strengthening should be decreased in favor of precipitate or dispersion strengthening, since solution strengthening involves a rather severe penalty in terms of increased ductile-brittle transition temperature while the latter may actually improve the low-temperature ductility.

Although the strength levels achieved in current chromium alloys are compet-

itive with advanced nickel alloys, further improvements appear possible. Specifically, further alloying studies should be directed towards precipitate-strengthened alloys. The optimum strengthening compound should be identified and the optimum amount of this compound should be determined. Stabilities with respect to solutioning and coarsening should be evaluated, and further alloying to improve the stability at fine particle sizes should be studied. Prime candidates for particle strengthening are the carbides and borides of columbium and tantalum.

Dispersion strengthening with inert particles has not been effective to date but refinement in particle sizes should be beneficial. The potential of forming fine oxide particles in situ through low-pressure oxidation of suitable binary alloys also appears to offer possibilities.

## CONCLUSIONS

The following conclusions are drawn from this review of recent developments in chromium alloys:

1. The development of chromium alloys is continuing at a moderate pace. Although several attractive alloy compositions have been identified, no truly usable alloy has yet been developed. In the sense of becoming commercially acceptable, chromium alloy development is still at an early stage.
2. The major deterrent to the use of chromium alloys in jet engines and other intermediate-temperature applications is embrittlement from nitrogen contamination resulting from air exposure in the 2000<sup>0</sup> F temperature range. Protective coatings such as those based on silicides or rare earths must be developed to eliminate this problem.
3. The ductile-brittle transition temperature of high-strength chromium alloys must be lowered as much as possible. This reduction will require a balance between solution strengthening, which tends to increase the transition temperature, and precipitate or dispersion strengthening, which tends to reduce the transition temperature.
4. The strength levels of currently available chromium alloys appear adequate for service in advanced jet engines in the 2000<sup>0</sup> to 2200<sup>0</sup> F temperature range, pending a solution to the embrittlement problem. Additional strengthening should be obtainable from optimized precipitate strengthening.

## REFERENCES

1. Parke, Robert M.; and Bens, Frederick P.: Chromium-Base Alloys. Symposium on Materials for Gas Turbines. ASTM, 1946, pp. 80-98.
2. Wain, H. L.: Research on Chromium in Australia. Ductile Chromium and its Alloys. ASM, 1957, pp. 27-57.
3. Runck, R. J.; Fearnside, T. E.; Blocher, J. M.; and Campbell, I. E.: Properties of High-Purity Iodide Chromium. Ductile Chromium and its Alloys. ASM, 1957, pp. 129-137.
4. Wain, H. L.; Henderson, F.; and Johnstone, S. T. M.: A Study of the Room-Temperature Ductility of Chromium. J. Inst. Metals, vol. 83, 1954-55, pp. 133-142.
5. Anon.: Ductile Chromium and its Alloys. ASM, 1957.
6. Maykuth, D. J.; and Jaffee, R. I.: Influence of Chromium Metal Purity on the Properties of Chromium Alloys. Ductile Chromium and its Alloys. ASM, 1957, pp. 229-246.
7. Maykuth, D. J.; and Jaffee, R. I.: The Mechanical Properties of Swaged Iodide-Base Chromium and Chromium Alloys. Ductile Chromium and its Alloys. ASM, 1957, pp. 247-254.
8. Collins, J. F.; Calkins, V. P.; and McGurty, J. A.: Applications of Rare Earths to Ferrous and Non-Ferrous Alloys. Presented at ASM-AEC Symposium on Rare Earths and Related Metals, Chicago, 1959.
9. Fox, James E.; and McGurty, James A.: Chromium and Chromium-Base Alloys. Refractory Metals and Alloys. Interscience Publ., 1961, pp. 207-218.
10. Scruggs, David M.: Modified Chromium for Unprotected Structures. ARS. J., vol. 31, no. 11, Nov. 1961, pp. 1527-1533.
11. Reed, G. C.: Recent Developments in Chromium-Magnesia Composites Possessing Room-Temperature Ductility. Presented at AIME Meeting, Dallas, Texas, Feb. 24-28, 1963.
12. Watkins, Robert V.: Optimization and Evaluation of Chromium Composites. Final Rep., Bendix Corp., Feb. 1968. (Available from DDC as AD-829417.)
13. Clark, J. W.; and Chang, W. H.: New Chromium Alloys. Presented at AIME Meeting, New York, N. Y., Feb. 27-Mar. 3, 1966.
14. Greenaway, H. T.: Creep Testing of Chromium-Base Alloys. Rep. ARL/MET-55, Aeronautical Research Labs., Melbourne, Oct. 1964.

15. Wain, H. L.; and Johnstone, S. T. M.: Chromium Alloy Development in Australia. High Temperature Refractory Metals. Part 2. R. W. Fountain, Joseph Maltz and L. S. Richardson, eds., Gordon and Breach Science Publ., 1966, pp. 286-308.
16. Holt, G. G.; and Greenaway, H. T.: Cascade Rig Testing of Chromium Alloy Guide Vanes. Rep. ARL/MET. 43, ARL/M.E.277, Aeronautical Research Lab., Australia, July 1966.
17. Maykuth, D. J.; and Gilbert, A.: Chromium and Chromium Alloys. Rep. DMIC-234, Battelle Memorial Inst., Oct. 1, 1966. (Available from DDC as AD-810530.)
18. Sims, Chester T.: The Case for Chromium. J. Metals, vol. 15, no. 2, Feb. 1963, pp. 127-132.
19. Rogers, J. A.; and Brown, A. R. G.: The Development of Chromium-Base Alloys for Use at High Temperatures. Metals Mater., vol. 1, no. 8, Aug. 1967, pp. 246-258.
20. Sully, A. H.; and Brandes, E. A.: Chromium. Second ed., Plenum Press, 1967.
21. Cairns, R. R., Jr.; and Grant, N. J.: Mechanical Properties of a Chromium-1 Per Cent Columbium Alloy. Proc. ASTM, vol. 63, 1963, pp. 566-577.
22. Wukusick, Carl S.: Research on Chromium-Base Alloys Exhibiting High-Temperature Strength, Low-Temperature Ductility, and Oxidation Resistance. General Electric Co. (ASD-TDR-63-493), June 1963.
23. Wilms, G. R.; and Rea, T. W.: The Tensile Creep Properties of Some Extruded Chromium Alloys. J. Less-Common Metals, vol. 6, no. 3, Mar. 1964, pp. 184-200.
24. Wilms, G. R.; and Rea, T. W.: Continued Tensile Creep Studies on Extruded Chromium Alloys. J. Less-Common Metals, vol. 7, no. 4, Oct. 1964, pp. 296-315.
25. Clark, J. W.: Development of High-Temperature Chromium Alloys. General Electric Co. (NASA CR-92691), June 30, 1967.
26. Pugh, J. W.: The Tensile and Stress-Rupture Properties of Chromium. Trans. ASM, vol. 50, 1958, pp. 1072-1080.



27. Johnstone, S. T. M.; Henderson, F.; and Wain, H. L.: Some Properties of Chromium and Chromium-Tungsten Alloys. II. Fabrication and Ductility. J. Inst. Metals, vol. 89, 1960-1961, pp. 101-104.
28. Abrahamson, Ernest P., II; and Grant, Nicholas J.: Transition Temperatures of Chromium and Chromium-Base Alloys. High Temperature Materials. John Wiley & Sons, Inc., 1959, pp. 229-242.
29. Abrahamson, E. P., II; and Grant, N. J.: Brittle to Ductile Transition Temperatures of Binary Chromium-Base Alloys. Trans. ASM, vol. 50, 1958, pp. 705-721.
30. Carlson, O. N.; Sherwood, L. L.; and Schmidt, F. A.: The Effect of Low Percentage Alloying Additions on the Ductility of Iodide Chromium. J. Less-Common Metals, vol. 6, no. 6, June 1964, pp. 439-450.
31. Sherwood, L. L.; and Schmidt, F. A.; and Carlson, O. N.: The Effect of Composition, Crystalline Condition and Thermal History on the Bend Transition Temperature of Chromium Alloys. Trans. ASM, vol. 58, 1965, pp. 403-410.
32. Klopp, William D.: Review of Ductilizing of Group VIa Elements by Rhenium and Other Solutes. NASA TN D-4955, 1968.
33. Sims, C. T.; and Clark, J. W.: Carbide-Strengthened Chromium Alloys. Trans. AIME, vol. 230, no. 5, Aug. 1964, pp. 1168-1181.
34. Wilms, G. R.: The Tensile Properties of Some Extruded Chromium Alloys Between 800° and 1000° C. J. Less-Common Metals, vol. 6, no. 3, Mar. 1964, pp. 169-183.
35. Ryan, N. E.; and Wilms, G. R.: The Effect of a Tantalum Carbide Dispersion on the High-Temperature Properties of Chromium. J. Less-Common Metals, vol. 6, no. 3, Mar. 1964, pp. 201-206.
36. Ryan, N. E.: The Formation, Stability and Influence on Carbide Dispersions in Chromium. J. Less-Common Metals, vol. 11, no. 4, Oct. 1966, pp. 221-248.
37. Ryan, N. E.; and Johnstone, S. T. M.: The Properties of a Chromium-Titanium-Nitrogen Alloy. J. Less-Common Metals, vol. 8, no. 3, Mar. 1965, pp. 159-164.
38. Chang, Winston H.: Influence of Heat Treatment on Microstructure and Properties of Columbium-Base and Chromium-Base Alloys. General Electric Co. (ASD-TDR-62-211, Pt. IV, DDC No. AD-482519), Feb. 1966.

39. Orowan, E.: Classification and Nomenclature of Internal Stresses. Symposium on Internal Stresses in Metals and Alloys. Inst. of Metals, 1948, p. 451.
40. Ansell, G. S.: The Mechanism of Dispersion Strengthening: A Review. Oxide Dispersion Strengthening. George S. Ansell, Thomas D. Cooper and Fritz V. Lenel, eds., Gordon and Breach Science Publ. 1968, pp. 61-141.
41. Westmacott, K. H.; Fountain, C. W.; and Stirton, R. J.: On the Spacing of Dispersed Obstacles. Acta Met., vol. 14, no. 11, Nov. 1966, pp. 1628-1629.
42. Klopp, William D.; and Witzke, Walter R.: Mechanical Properties of Arc-Melted Tungsten-Rhenium-Hafnium-Carbon Alloys. NASA TN D-5349, 1969.
43. Hahn, G. T.; and Rosenfield, A. R.: Effects of Second-Phase Particles on Ductility. Battelle Memorial Inst. (AFML-TR-65-409, DDC No. AD-480038), Jan. 1966.
44. Conrad, H.: Guiding Principles for Lowering the Ductile-to-Brittle Transition Temperature in the BCC Metals. High Temperature Refractory Metals, Part 2. R. W. Fountain, Joseph Maltz and L. S. Richardson, eds., Gordon and Breach Science Publ., 1966, pp. 113-128.
45. Ardell, A. J.: Further Applications of the Theory of Particle Coarsening. Acta Met., vol. 15, no. 11, Nov. 1967, pp. 1772-1775.
46. Raffo, Peter L.: Exploratory Study of Mechanical Properties and Heat Treatment of Molybdenum-Hafnium-Carbon Alloys. NASA TN D-5025, 1969.
47. Smith, W. H.: Solid Solubility of Carbon in Chromium. J. Metals, vol. 9, no. 1, Jan. 1957, pp. 47-49.
48. Gebhardt, Erich; Fromm, Eckehard; and Roy, Upendra: Die Löslichkeit von Kohlenstoff in Molybdän, Wolfram und Rhenium. Z. Metallk., vol. 57, no. 10, 1966, pp. 732-736.
49. Caplan, D.; Fraser, M. J.; and Burr, A. A.: Solubility of Nitrogen and Oxygen in Solid Chromium. Ductile Chromium and its Alloy. ASM, 1957, pp. 196-215.
50. Few, W. E.; and Manning, G. K.: Solubility of Carbon and Oxygen in Molybdenum. Trans. AIME, vol. 194, 1952, pp. 271-274.
51. Allen, B. C.; Maykuth, D. J.; and Jaffee, R. I.: The Recrystallization and Ductile-Brittle Transition Behavior of Tungsten. Effect of Impurities on Polycrystals Prepared from Single Crystals. J. Inst. Metals, vol. 90, 1961-62, pp. 120-128.

52. Klein, Mark J.; and Clauer, A. H.: Nitrogen-Induced Internal Friction in Chromium. *Trans. AIME*, vol. 233, no. 9, Sept. 1965, pp. 1771-1777.
53. Seybolt, A. U.; and Oriani, R. A.: Pressure-Temperature-Composition Relations in the Cr-N Terminal Solid Solution. *Trans. AIME*, vol. 26, May 1956, pp. 556-562.
54. Fromm, E.; and Jehn, H.: Hochtemperatur-Löslichkeit von Stickstoff in Molybdän. *J. Less-Common Metals*, vol. 14, no. 4, Apr. 1968, pp. 474-475.
55. Hansen, Max: Constitution of Binary Alloys. Second ed., McGraw-Hill Book Co., Inc., 1958.
56. Fromm, E.; and Jehn, H.: Zur Hochtemperaturlöslichkeit von Stickstoff in Wolfram. *J. Less-Common Metals*, vol. 17, no. 1, Jan. 1969, pp. 124-126.
57. Cairns, Raymond E., Jr.; and Grant, Nicholas J.: The Effects of Carbon, Nitrogen, Oxygen, and Sulfur on the Ductile-Brittle Fracture Temperature of Chromium. *Trans. AIME*, vol. 230, no. 5, Aug. 1964, pp. 1150-1159.
58. Allen, B. C.; Maykuth, D. J.; and Jaffee, R. I.: The Effect of Impurities and Structure on the Tensile Transition Temperature of Chromium. *Trans. AIME*, vol. 227, no. 3, June 1963, pp. 724-732.
59. Solie, K. E.; and Carlson, O. N.: The Effect of Nitrogen on the Brittle-Ductile Transition of Chromium. *Trans. AIME*, vol. 230, no. 3, Apr. 1964, pp. 480-485.
60. Maykuth, D. J.; Klopp, W. D.; Jaffee, R. I.; and Goodwin, H. B.: A Metallurgical Evaluation of Iodide Chromium. *J. Electrochem. Soc.*, vol. 102, June 1955, pp. 316-331.
61. Weaver, C. W.: Precipitation in Dilute Chromium-Nitrogen Alloys. *Acta Met.*, vol. 10, no. 12, Dec. 1962, pp. 1151-1160.
62. Gilbert, A.; and Klein, M. J.: The Effect of Cooling Rate on the Ductile-Brittle Bend-Transition Temperature of Chromium Wire. *Acta Met.*, vol. 14, no. 4, Apr. 1966, pp. 541-543.
63. Fox, J. E.: Chromium-Base Alloy Development. Rep. APEX-680, General Electric Co., Apr. 1962.
64. Hagel, William C.: Factors Controlling the High-Temperature Oxidation of Chromium. *Trans. ASM*, vol. 56, 1963, pp. 583-599.
65. Abrahamson, Ernest P., II; and Grant, Nicholas J.: Oxidation Resistance of Binary Chromium-Base Alloys. *High Temperature Materials*. John Wiley & Sons, Inc., 1959, pp. 501-509.

66. Widmer, R.; Yukawa, T.; and Grant, N. J.: Oxidation Behavior of Chromium-Base Alloys at Temperatures Between 1800<sup>0</sup> and 2200<sup>0</sup> F. *Refractory Metals and Alloys*. Interscience Publ., 1961, pp. 183-205.
67. Tedmon, C. S., Jr.: The High-Temperature Oxidation of Ductile Cr-Re Alloys. *J. Electrochem. Soc.*, vol. 113, no. 8, Aug. 1966, pp. 769-773.
68. Seybolt, A. U.: High Temperature Oxidation of Chromium Containing Y<sub>2</sub>O<sub>3</sub>. *Corrosion Sci.*, vol. 6, no. 6, June 1966, pp. 263-269.
69. Tedmon, C. S., Jr.: The High-Temperature Oxidation of Ductile Cr-Ru Alloys. *J. Less-Common Metals*, vol. 10, no. 5, May 1966, pp. 301-311.
70. Tedmon, C. S., Jr.: The Effect of Oxide Volatilization on the Oxidation Kinetics of Cr and Fe-Cr Alloys. *J. Electrochem. Soc.*, vol. 113, no. 8, Aug. 1966, pp. 766-768.
71. Henderson, F.; Johnstone, S. T. M.; and Wain, H. L.: The Effect of Nitride-Formers Upon the Ductile-Brittle Transition in Chromium. *J. Inst. Metals*, vol. 92, 1963-64, pp. 111-117.
72. Slaughter, E. R.; Hughes, J. R.; and Moore, W. F.: Small Quantity Production of Complex Chromium Alloy Sheet. NASA CR-72545, 1968.
73. Northwood, J. E.; Shaw, M. B.; and Smith, R. S.: An Evaluation of a Chromium-Base Alloy for High-Temperature Service. *J. Less-Common Metals*, vol. 14, no. 2, Feb. 1968, pp. 157-166.
74. Ellery, A. R.; and Finlay, A. S.: First Running of Uncooled Chromium Alloy Blades Above 1000<sup>0</sup> C in a Rig Turbine. Rep. ARL/MET. 35, ARL/M. E. 273, Aeronautical Research Lab., Australia, Feb. 1966.
75. Wilms, G. R.; and Rea, T. W.: Scaling of Chromium in a Hot Gas Stream. *J. Less-Common Metals*, vol. 3, 1961, pp. 234-238.
76. Panasyak, I. O.: Chromium Alloys. (Russian) *Constructional Materials Encyclopedia of Modern Engineering*, vol. 3, 1965, pp. 423-424.
77. Anon.: Chromium Alloys. Brochure from Aviaexport, Moscow.
78. Grisaffe, S. J.; and Oldrieve, R. E.: Protective Coatings for Chromium Alloys. Paper presented at WESTEC Conference, Los Angeles, Calif., Mar. 10-14, 1969. (NASA TM X-52503.)
79. Stephens, Joseph R.; and Klopp, William D.: Exploratory Study of Silicide, Aluminide, and Boride Coatings for Nitridation-Oxidation Protection of Chromium Alloys. NASA TN D-5157, 1969.

TABLE 9-I. - PROPERTIES OF CHROMIUM AND NICKEL

	Chromium	Nickel
Structure	Body-centered cubic	Face-centered cubic
Melting point, °F	3410	2650
Modulus, psi	$36 \times 10^6$	$30 \times 10^6$
Density, lb/in. <sup>3</sup>	0.26	0.322
Coefficient of thermal expansion, F <sup>-1</sup>	$3.4 \times 10^{-6}$	$7.4 \times 10^{-6}$
Low-temperature ductility	Poor	Good
Oxidation resistance	Embrittles in air	Fair
Vapor pressure at 2000° F, mm Hg	$2 \times 10^{-5}$	$2 \times 10^{-6}$

TABLE 9-II. - CHROMIUM ALLOYS UNDER DEVELOPMENT

Country	Designation	Composition, wt. %	Organization
United States	C-207	Cr-7.5W-0.8Zr-0.2Ti-0.1C-0.15Y	General Electric (USAF)
	CI-41	Cr-7.1Mo-2Ta-0.09C-0.1(Y+La)	General Electric (NASA)
	Chrome-30	Cr-6MgO-0.5Ti	Bendix (Navy)
	Chrome-90	Cr-3MgO-2.5V-0.5Si	Bendix (Navy)
	Chrome-90S	Cr-3MgO-2.5V-1Si-0.5Ti-2Ta-0.5C	Bendix (Navy)
Australia	Alloy E	Cr-2Ta-0.5Si-0.1Ti	Dept. of Supply
	Alloy H	Cr-2Ta-0.5Si-0.5 rare earth	Dept. of Supply
	Alloy J	Cr-2Ta-0.5Si	Dept. of Supply
Soviet Union	BX-2	Unknown	-----
	BX-2I	BX-2 plus Y	-----
	BX-3	Unknown	-----
	BX-4	Unknown	-----

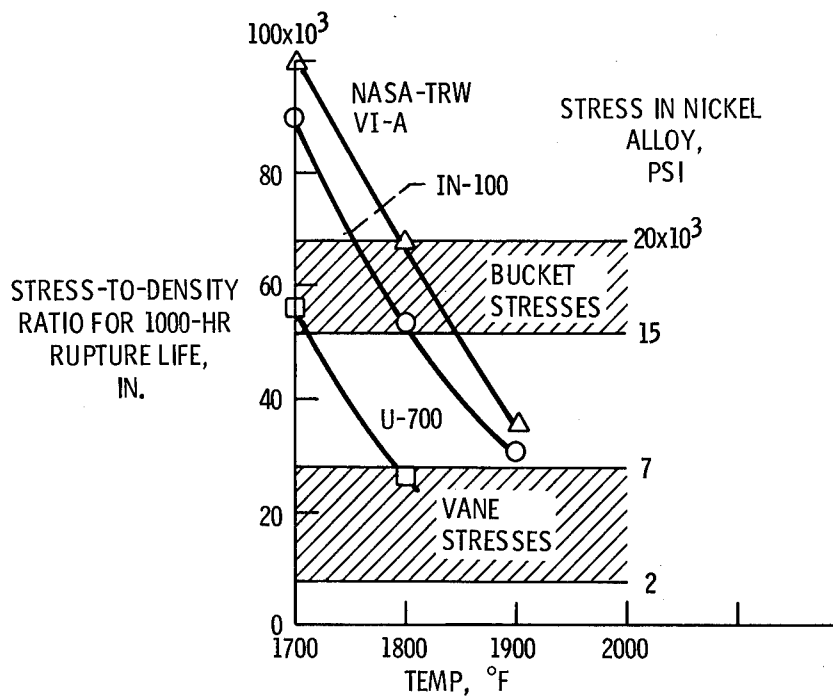


Figure 9-1. - Current status of materials for turbine components.

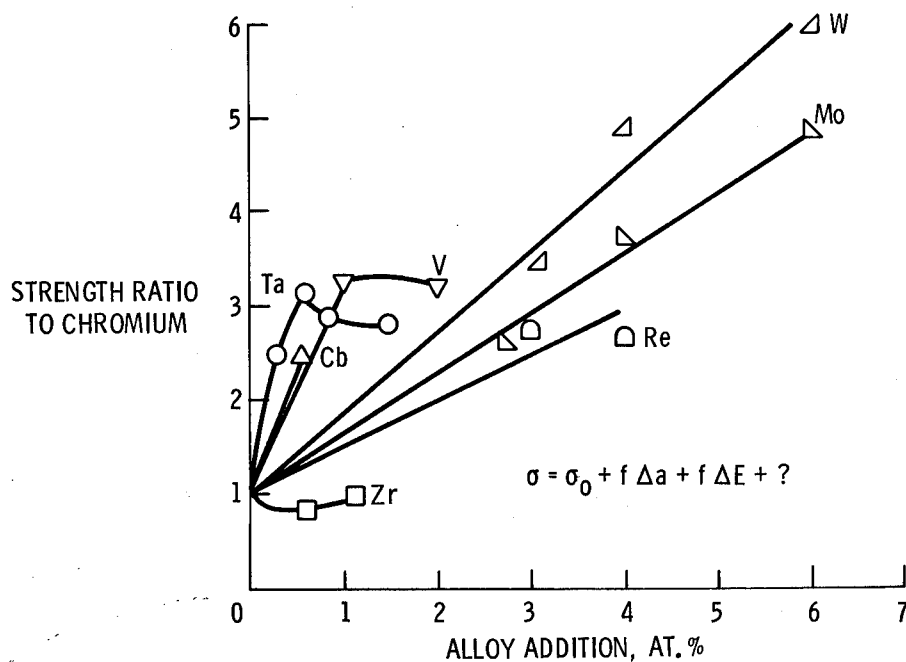


Figure 9-2. - Effects of substitutional solutes on strength of chromium (1800° to 2400° F).

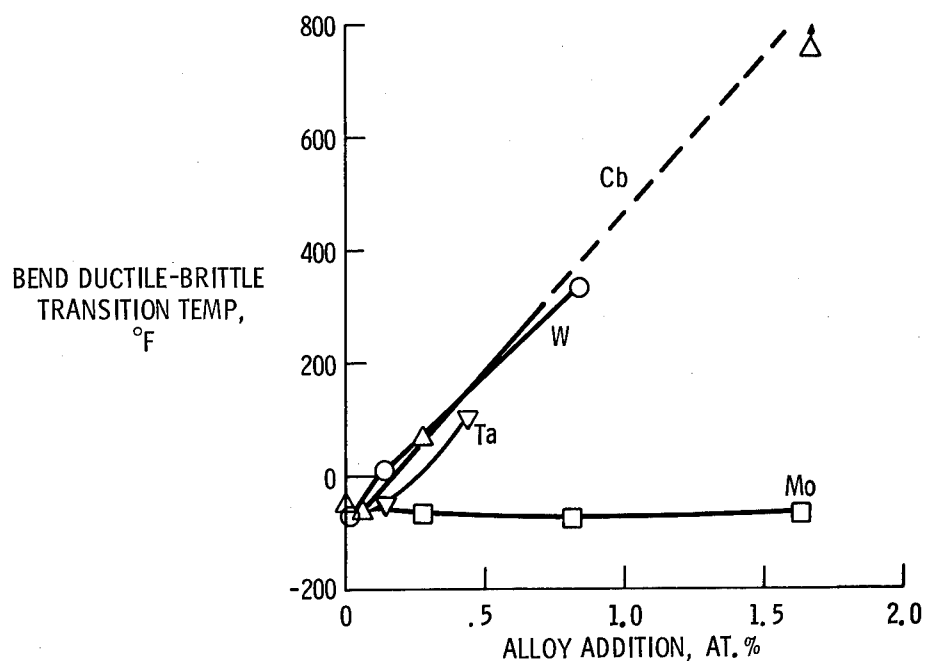


Figure 9-3. - Effects of substitutional solutes on ductile-brittle transition temperature of chromium.

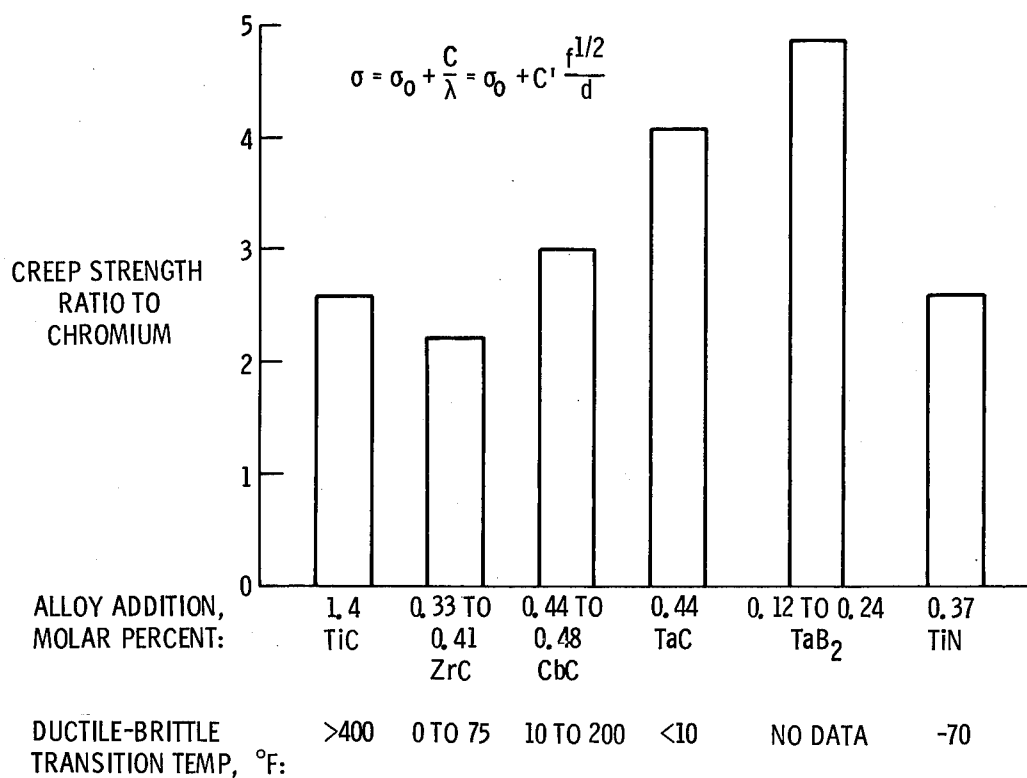


Figure 9-4. - Effects of precipitates on creep strength and ductile-brittle transition temperature of chromium.

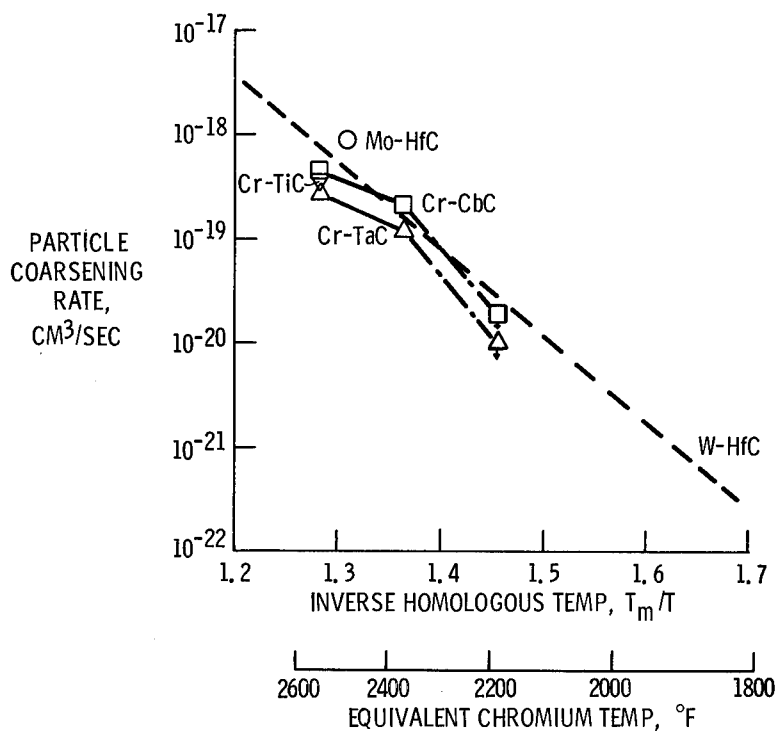


Figure 9-5. - Coarsening rates of carbides in chromium, molybdenum, and tungsten.

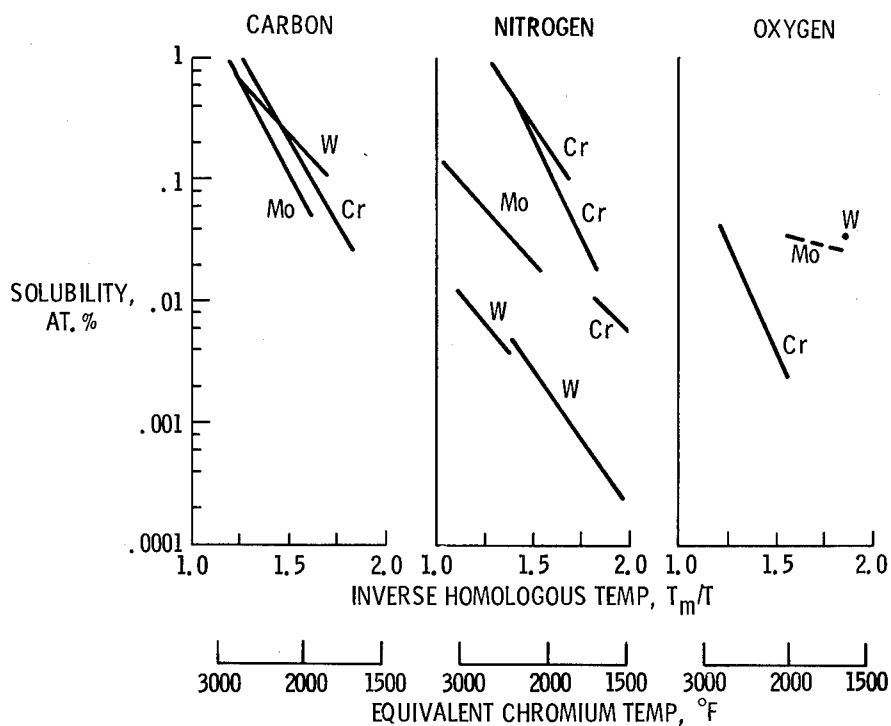


Figure 9-6. - Interstitial solubilities in chromium, molybdenum, and tungsten.



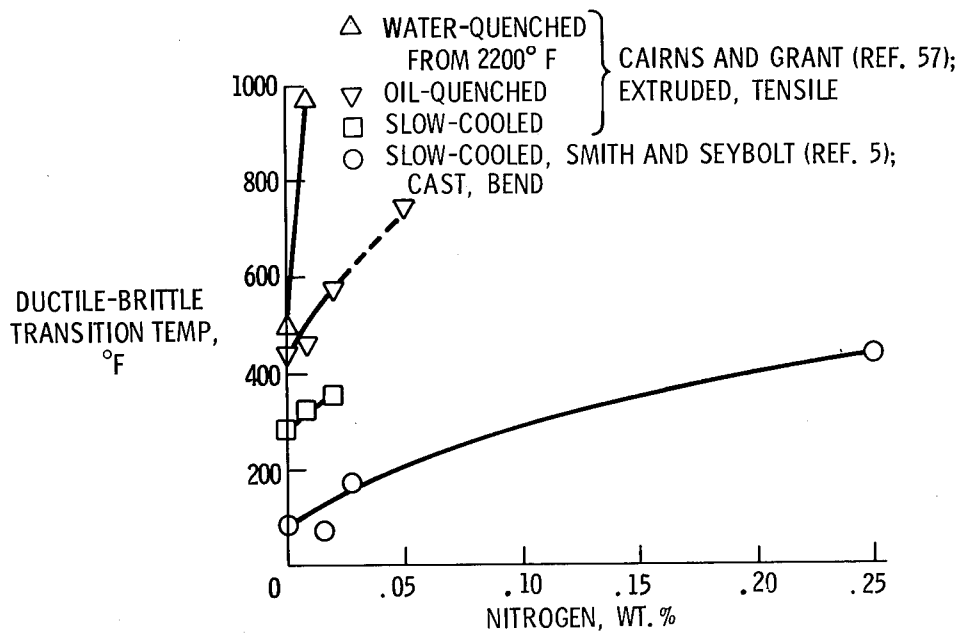


Figure 9-7. - Effects of nitrogen on ductile-brittle transition temperature of chromium.

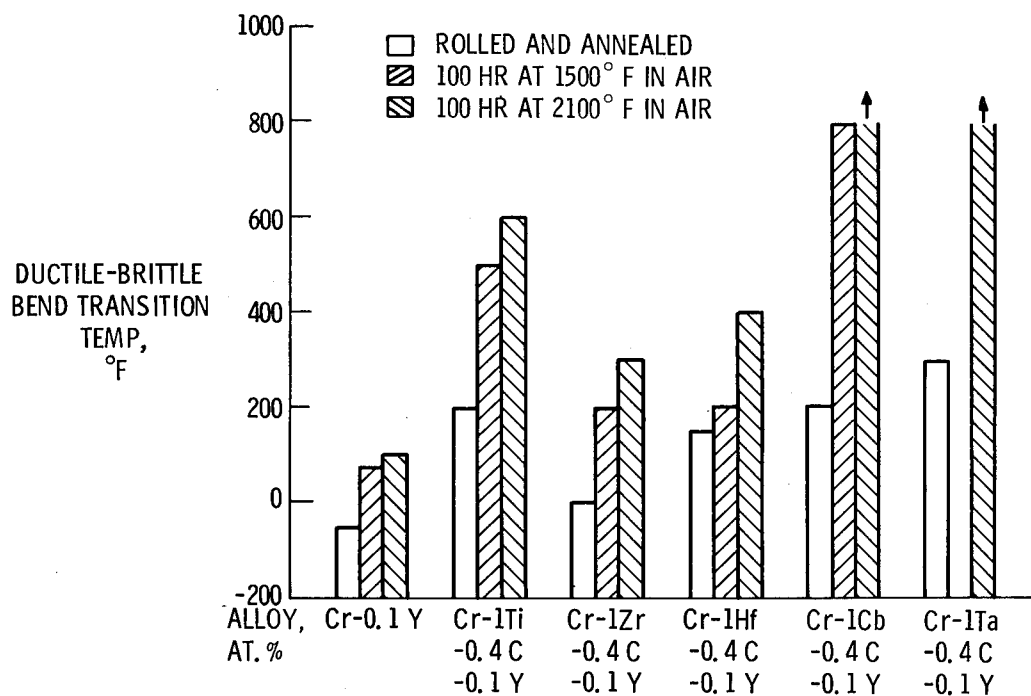


Figure 9-8. - Effects of alloying on oxidation-embrittlement of chromium.

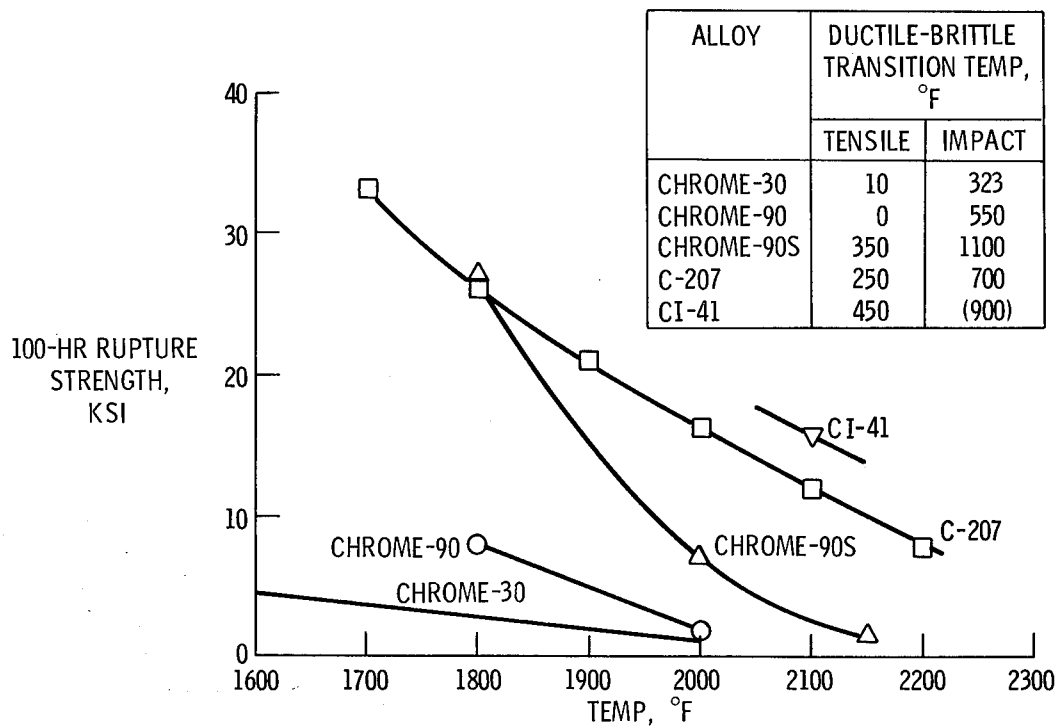


Figure 9-9. - Strength and ductility of United States chromium alloys.

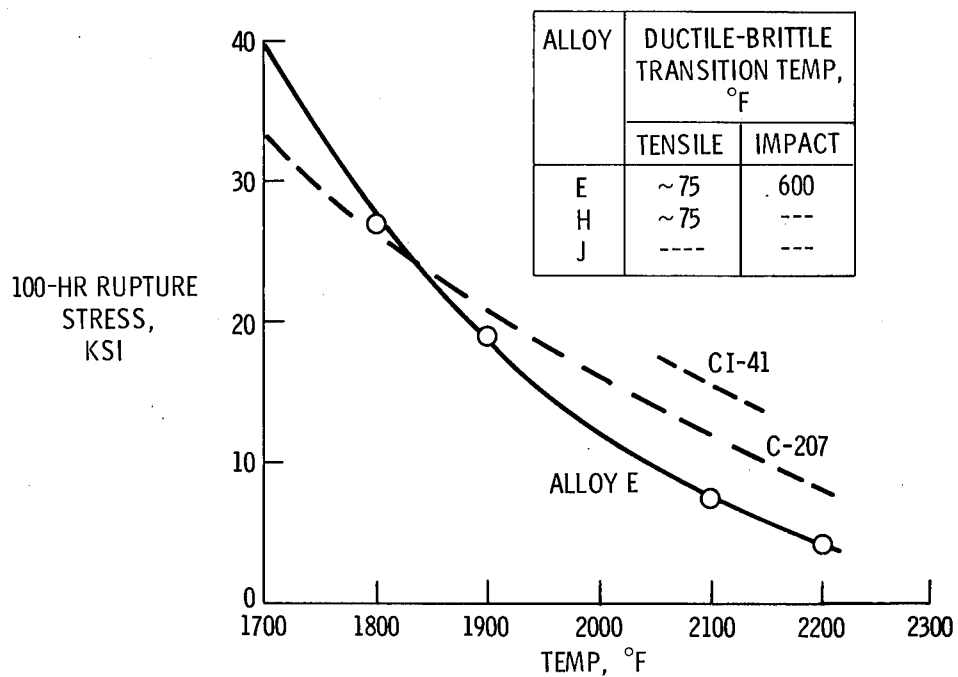


Figure 9-10. - Strength and ductility of Australian chromium alloys.

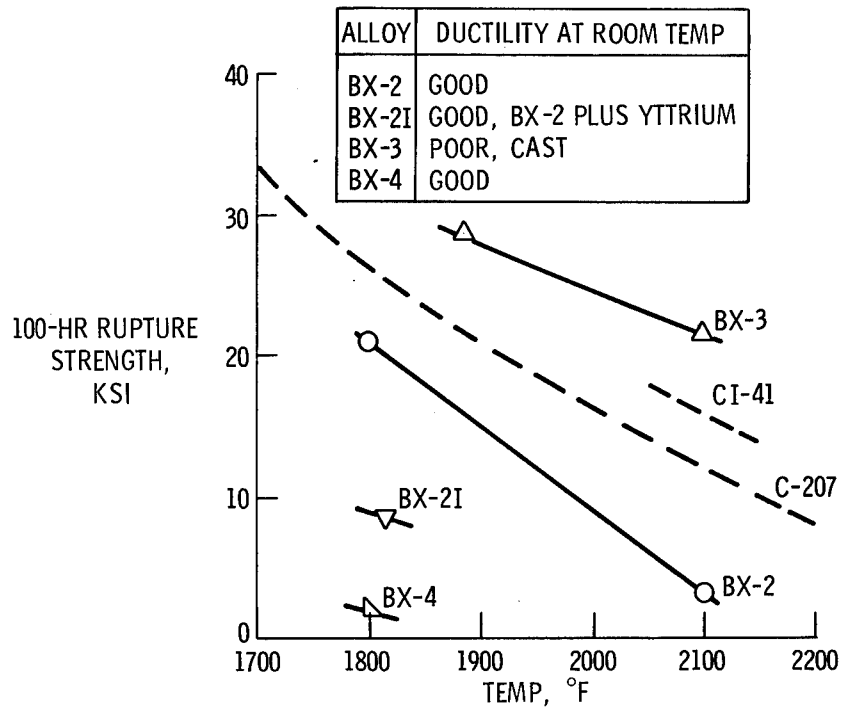


Figure 9-11. - Strength and ductility of Soviet chromium alloys.

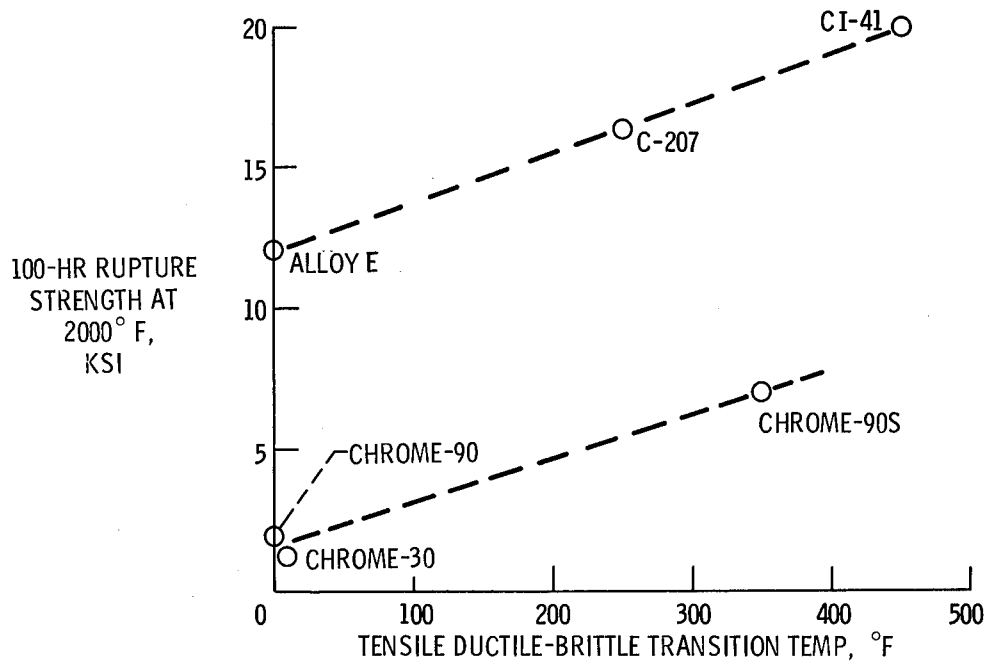


Figure 9-12. - Trade-off between strength and ductility of chromium alloys.

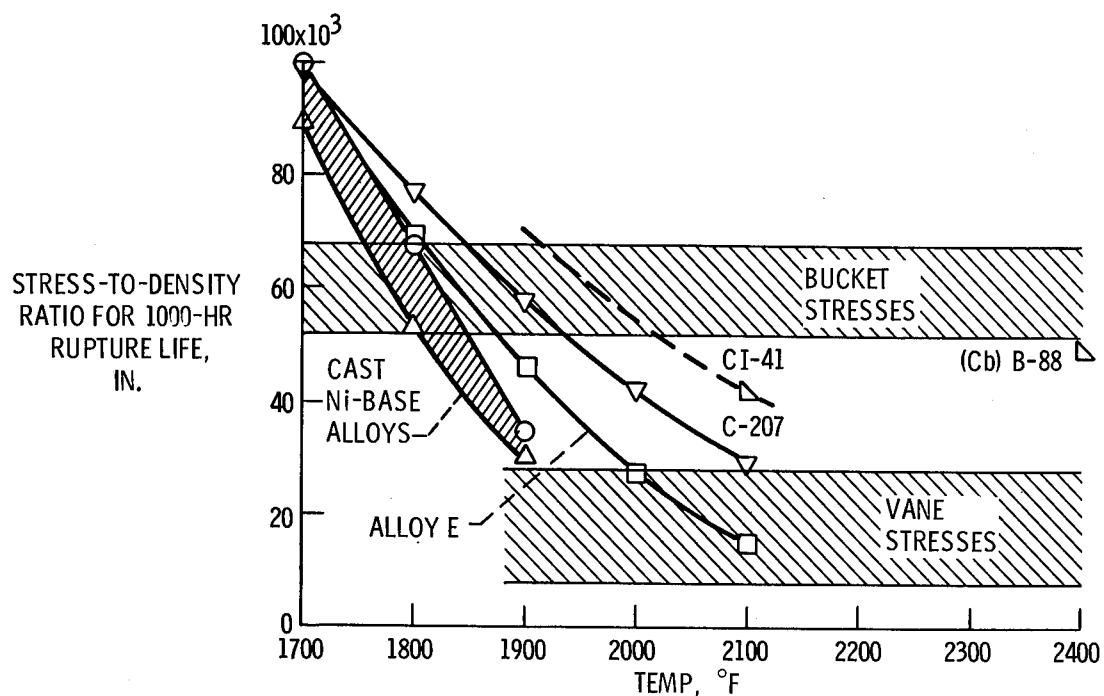


Figure 9-13. - Rupture strength of nickel, chromium, and columbium alloys.

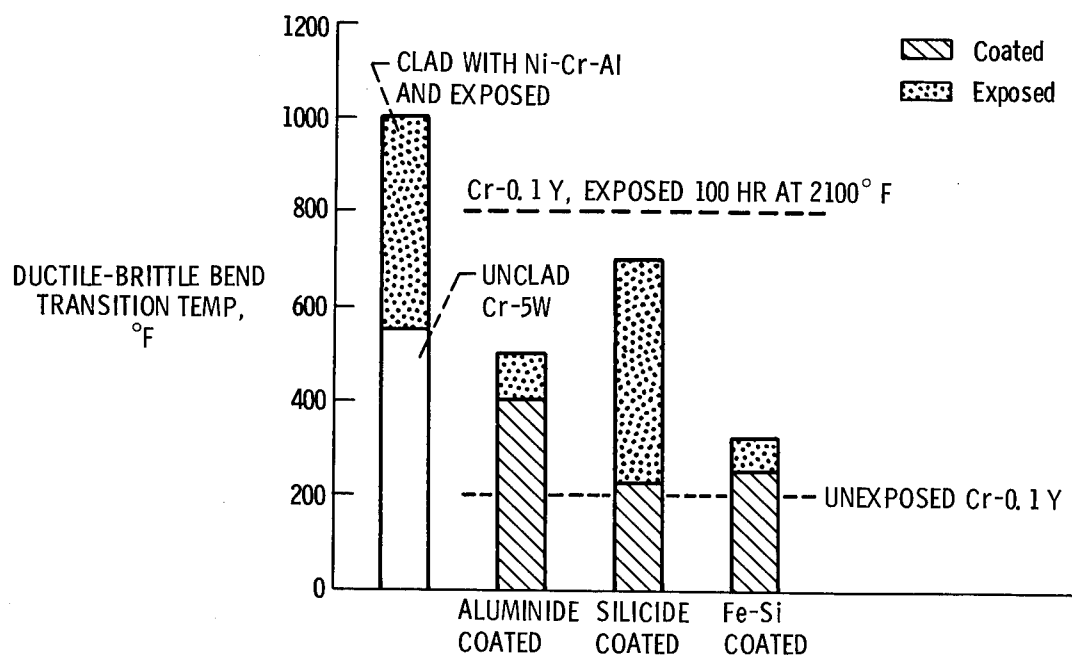


Figure 9-14. - Effects of coatings on ductility of air-exposed chromium.



## 10. CARBIDE STRENGTHENING OF TUNGSTEN AND MOLYBDENUM ALLOYS

Robert W. Hall, Peter L. Raffo, Walter R. Witzke, and William D. Klopp

Arc-melted tungsten alloys strengthened by a finely dispersed hafnium carbide precipitate have exhibited outstanding high-temperature strength. The addition of 4 atom percent rhenium to such alloys significantly improves their low-temperature ductility. The alloy which exhibited optimum properties has the composition (in atom percent) W-4Re-0.35Hf-0.35C. In the swaged condition, this alloy combines a tensile strength of approximately 70 000 psi at 3500° F with a ductile-brittle transition temperature near 200° F.

An exploratory study of similar molybdenum-base alloys strengthened by the hafnium carbide precipitate has been conducted. The mechanical properties of these alloys were highly dependent on the thermomechanical processing schedule used for their fabrication. In the optimum processed condition, the experimental Mo-Hf-C alloys appear to have substantially better high-temperature strength than currently available commercial molybdenum alloys. Achievement of high strength in the Mo-Hf-C alloys is dependent on the use of a high-temperature extrusion operation and subsequent precipitation of the hafnium carbide precipitate during secondary working.

Tungsten- and molybdenum-base alloys are of interest to NASA primarily for such potential applications as heat shields for reentry vehicles, turbines for advanced space power systems, and components of high-temperature nuclear reactors. In addition, in the form of high-strength wires or fibers, they may be used in composite materials for aircraft engines or other high-temperature structures.

Several years ago we identified a series of arc-melted tungsten alloys strengthened by hafnium carbide as having outstanding high-temperature strength (ref. 1). These studies have been continued in order to optimize the compositions of these alloys (ref. 2) and to study the effects of thermomechanical processing on their properties. Recently, we have explored similar Mo-Hf-C alloys (ref. 3). The purpose of this paper is to report on progress in these areas.

### TUNGSTEN ALLOYS

The ternary W-Hf-C alloys which were studied initially had excellent high-

temperature strength but relatively poor low-temperature ductility (fig. 10-1). At 3500° F, the tensile strength of unalloyed tungsten is only about 9000 psi. Typical W-Hf-C alloys containing less than 1 mol percent HfC have strengths of 50 000 to 60 000 psi at this high temperature. Unfortunately, the ductile-brittle transition temperature of these alloys is comparatively high, about 400° F in the swaged condition as compared to 200° F for unalloyed tungsten. Therefore, one of the goals of our continuing tungsten alloy studies has been to improve low-temperature ductility without sacrificing high-temperature strength.

The approaches used were, first, to alloy with small amounts of rhenium to improve ductility and, second, to optimize the thermomechanical processing of these alloys to achieve the best compromise between strength and ductility. Other work at Lewis and elsewhere had shown that additions of rhenium at the 4 to 5 atom percent level significantly increase the low-temperature ductility of unalloyed tungsten (refs. 4 and 5). It was hoped that a similar effect might be realized in the high-strength W-Hf-C alloys. This approach has been moderately successful, as shown in figure 10-2. The addition of 4 percent rhenium to the W-Hf-C alloys significantly improved both high-temperature strength and low-temperature ductility. The quaternary alloy W-4Re-0.35Hf-0.35C (all compositions in atom percent) is believed to be near the optimum composition in the W-Re-Hf-C system, as is shown later. It has been designated tungsten-RHC. This alloy is seven to eight times as strong as unalloyed tungsten at 3500° F, but has essentially the same ductile-brittle transition temperature as the pure metal.

The optimized composition, W-4Re-0.35Hf-0.35C, was arrived at by studying the effects of hafnium and carbon additions to the W-4Re base. Some of the data on which this selection was based are shown in figures 10-3 and 10-4. Recrystallization studies provided an early clue to the optimum hafnium carbide level. Typically, in tungsten alloy development studies, one tries to achieve the highest possible recrystallization temperature. This permits the strengthening effects of cold work to be retained to very high temperatures. Further, since recrystallization and grain growth usually raise the ductile-brittle transition temperature of tungsten alloys, retention of the cold-worked structure also improves low-temperature ductility.

The effect of hafnium carbide content on the recrystallization temperature of the W-4Re base alloy is shown in figure 10-3. Here the temperature for complete recrystallization in 1 hour is shown as a function of HfC content in mol percent. In alloys which had nonstoichiometric proportions of Hf and C, the amount of HfC present was assumed to be governed by the element present at the lower atomic percent level. For example, if chemical analysis showed the alloy to contain 0.4-atom-percent Hf, but only 0.3-atom-percent C, the mol percent HfC is reported to be 0.3.

The recrystallization temperature increases very rapidly with increasing HfC

content, reaching a maximum near 0.4 mol percent HfC. Recrystallization temperatures as high as 4600° F were observed. This large increase in recrystallization temperature with HfC contents less than 0.5 mol percent suggests that the HfC particles must be unusually stable in the tungsten matrix and must be present in such a form that they are very effective in pinning grain boundaries.

The effects of hafnium carbide on the high-temperature tensile strengths of swaged W-Re-Hf-C alloys are shown in figure 10-4. At 2500° and 3000° F, the tensile strength is not very sensitive to HfC content. High strength levels can be achieved over a broad compositional range. However, at 3500° F, strength seems to reach a maximum at the 0.3- to 0.4-mol-percent HfC level. Insufficient data are available at 4000° F to determine if the optimum composition changes at higher temperatures.

In the course of this study of the effect of alloy composition on high-temperature tensile strength, it became very evident that the mechanical properties depended not only on composition but on the entire thermal and mechanical history of the alloys. An attempt was made to optimize the processing and to relate the measured properties to the microstructure developed during fabrication. For this study, it was necessary to use the techniques of transmission electron microscopy since the HfC particles are too small to be resolved with the optical microscope.

Figure 10-5 shows a typical microstructure of a W-Re-Hf-C alloy after testing at 3500° F in the swaged condition. The individual HfC particles are extremely fine, about 150 angstroms in diameter on the average in this specimen. We believe that the high strength of these W-Re-Hf-C alloys is associated with the presence of these very fine carbide particles, which retard the movement of dislocations.

The response of these quaternary W-Re-Hf-C alloys to solution annealing and aging heat treatments was investigated. Heating to 4600° F was required in order to take the HfC particles into solution. A comparison of the high-temperature tensile strengths of the W-RHC alloy in several microstructural conditions is shown in figure 10-6. The properties of unalloyed tungsten are shown for comparison. The W-RHC alloy is considerably stronger in both the as-swaged condition and the solution treated and aged condition than it is in the recrystallized condition. In the as-swaged condition, the strength increment is due primarily to the effects of retained cold work. In the solution annealed and aged condition, the strength advantage over the recrystallized material reflects primarily the more optimum size and distribution of the HfC precipitates. Although the solution annealed material is slightly stronger than the swaged material at high temperatures, it has a much higher ductile-brittle transition temperature. This is probably due primarily to the grain growth that occurs at the very high temperatures needed to take the hafnium carbide particles into solution. Thus, the swaged material exhibits the best combination of



high-temperature strength and low-temperature ductility, and the W-RHC alloy is recommended for use in this structural condition whenever possible.

To summarize the status of our tungsten alloy studies, the W-4Re-0.35Hf-0.35C alloy has been identified as having outstanding high-temperature strength. To the best of our knowledge, this alloy is the strongest known metallic material in the 3000° to 4000° F range. It should be considered primarily for applications where high strength at very high temperatures is required but where low-temperature ductility equivalent to that of unalloyed tungsten is adequate.

## MOLYBDENUM ALLOYS

Recently, we have conducted similar, but less extensive, studies on Mo-Hf-C alloys. The purpose was to determine if the remarkable strengthening and stability of the hafnium carbide precipitate observed in tungsten alloys could also be achieved in a molybdenum matrix. A review of the literature indicated that hafnium carbide had received relatively little investigation as a strengthener for molybdenum alloys, although the carbides of the other Group IV reactive metals, titanium and zirconium, are the basis of strengthening in commercial molybdenum alloys such as TZM and TZC (refs. 6 and 7).

Initially, a screening study of arc-melted and swaged Mo-Hf-C alloys was conducted (ref. 3). Evaluation was by tensile tests covering the range of 1800° to 3000° F. The results are shown in figure 10-7. Note particularly the effectiveness of very small amounts of HfC in increasing high-temperature strength.

Like their tungsten counterparts, the Mo-Hf-C alloys were found to be heat treatable. Their strengths were very sensitive to the thermomechanical processing schedule used to fabricate them. In order to optimize properties during fabrication, we have recently studied the effects of thermomechanical processing on several Mo-Hf-C alloys. The prime process variables studied were the extrusion temperature, the use of a postextrusion solution treatment, and the aging temperature.

The highest strengths were achieved in a Mo-0.6Hf-0.5C alloy. The sensitivity of the high-temperature strength of this alloy to processing is shown in figure 10-8. The highest strength was obtained using process A, which involved extrusion at 4000° F followed only by swaging in the range 2500° to 2000° F, with no intermediate anneals. Considerably lower strength was attained if an aging treatment at 2800° F was inserted between the extrusion and swaging operations.

We believe that extrusion at a very high temperature - in this case 4000° F - has a key effect on the processing of these Mo-Hf-C alloys. At this temperature, the coarse carbides which formed during solidification and cooling of the ingot are taken into solution. If the extrusion is rapidly cooled and swaged without any intermediate

anneals, as in process A, the carbides are most likely precipitated during swaging in the form of extremely fine particles. Admittedly this is somewhat speculative, since we have not yet been able to resolve fine carbides in the swaged structure, even with the electron microscope. If the extruded alloy is given an intermediate anneal, as in process B, the carbide particles are apparently precipitated in a less optimum dispersion.

In the optimum processed condition, the Mo-0.6Hf-0.5C alloy is considerably stronger than currently available commercial molybdenum alloys such as Mo-TZM and TZC (fig. 10-9). For example, at 2500<sup>0</sup> F, the experimental Mo-Hf-C alloy has a tensile strength of over 120 000 psi, while the commercial alloys have strengths ranging from 40 000 to 70 000 psi. The low-temperature ductility of the Mo-Hf-C alloys has not yet been extensively studied; limited data suggest the ductile-brittle transition temperature for as-swaged material will be near or slightly below room temperature.

We believe that these new Mo-Hf-C alloys have significant high-temperature strength advantages and warrant further investigation. They may be of particular interest for such applications as turbines in advanced Rankine or Brayton space power generation systems.

## REFERENCES

1. Rubenstein, L. S.: Effects of Composition and Heat Treatment on High-Temperature Strength of Arc-Melted Tungsten-Hafnium-Carbon Alloys. NASA TN D-4379, 1968.
2. Klopp, William D.; and Witzke, Walter R.: Mechanical Properties of Arc-Melted Tungsten-Rhenium-Hafnium-Carbon Alloys. NASA TN D-5348, 1969.
3. Raffo, Peter L.: Exploratory Study of Mechanical Properties and Heat Treatment of Molybdenum-Hafnium-Carbon Alloys. NASA TN D-5025, 1969.
4. Klopp, William D.; Witzke, Walter R.; and Raffo, Peter L.: Mechanical Properties of Dilute Tungsten-Rhenium Alloys. NASA TN D-3483, 1966.
5. Pugh, J. M.; Amra, L. H.; and Hurd, D. T.: Properties of Tungsten-Rhenium Lamp Wire. Trans. ASM, vol. 55, no. 3, Sept. 1962, pp. 451-461.
6. Semchyshen, M.; and Barr, Robert Q.: Mechanical Properties of Molybdenum and Molybdenum-Base Alloy Sheet. Symposium on Newer Metals. Spec. Tech. Publ. No. 272, ASTM, 1960, pp. 12-35.
7. Gilbert, R. W., Jr.; and Houston, J. V., Jr.: TZM - New Alloy Broadens Applications for Molybdenum. Metal. Progr., vol. 82, no. 5, Nov. 1962, pp. 106-110.

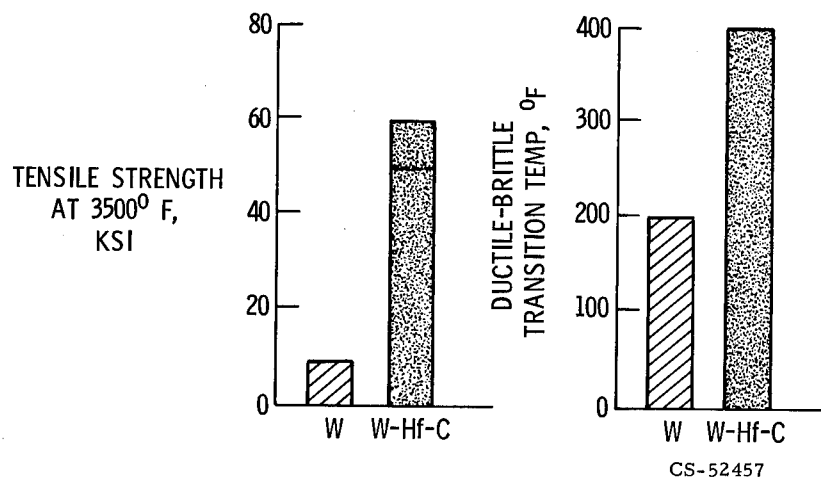


Figure 10-1. - Comparison of strength and ductility of unalloyed tungsten and typical W-Hf-C alloy in swaged condition.

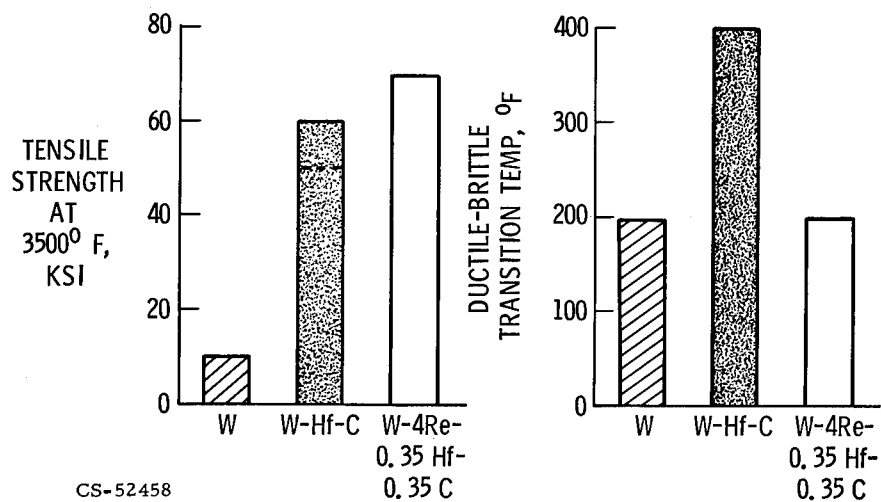


Figure 10-2. - Comparison of mechanical properties of W-RHC alloy with unalloyed tungsten and W-Hf-C alloy in swaged condition.

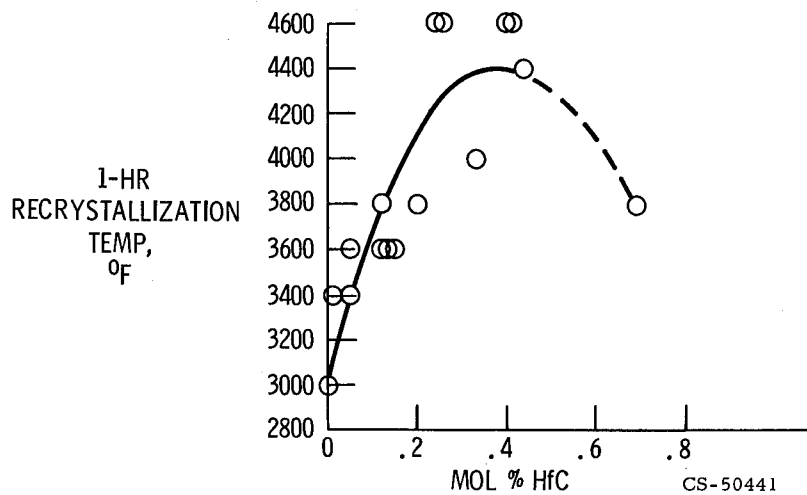


Figure 10-3. - Effect of hafnium carbide content on recrystallization temperature of W-4Re-Hf-C alloys.

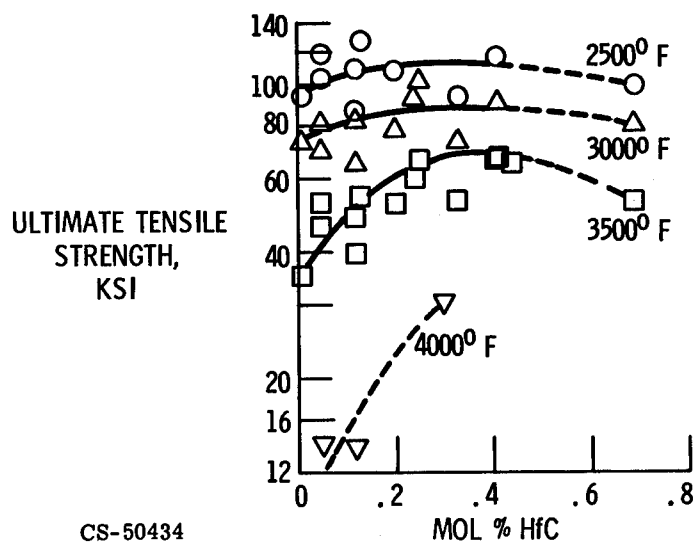


Figure 10-4. - Effect of hafnium carbide content on high-temperature tensile strength of W-4Re-Hf-C alloys.

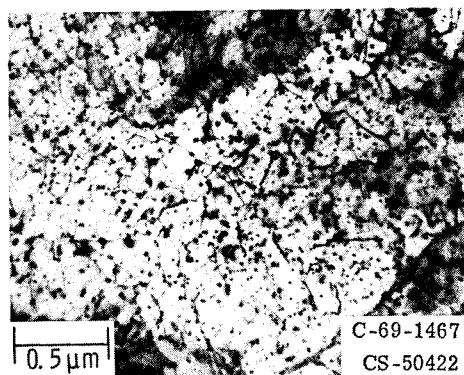


Figure 10-5. - Microstructure of swaged W-4Re-0.23Hf-0.3C alloy after tensile testing at 3500° F.

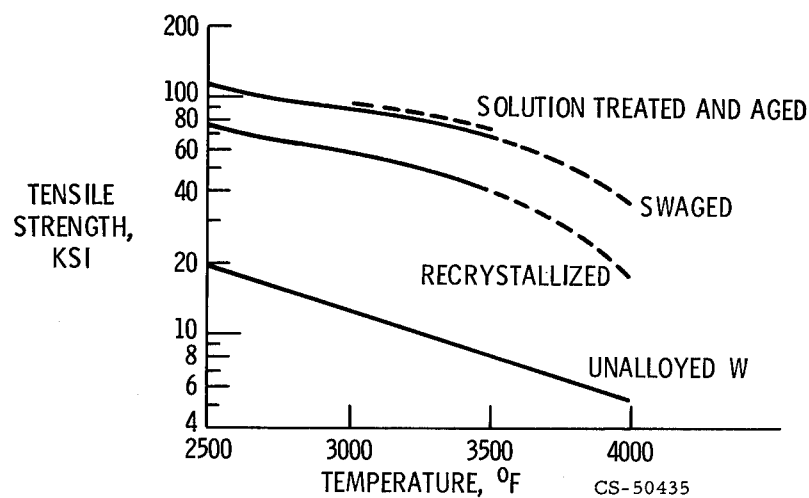


Figure 10-6. - Comparison of tensile strengths of W-4Re-0.35Hf-0.35C in several microstructural conditions.

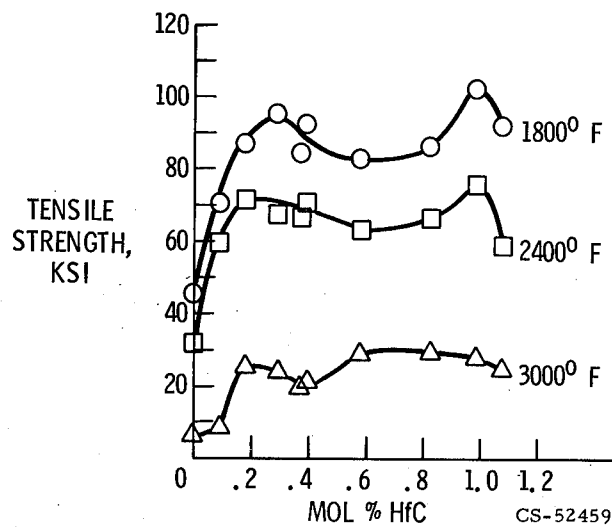


Figure 10-7. - Effect of hafnium carbide content on high-temperature tensile strength of Mo-Hf-C alloys.

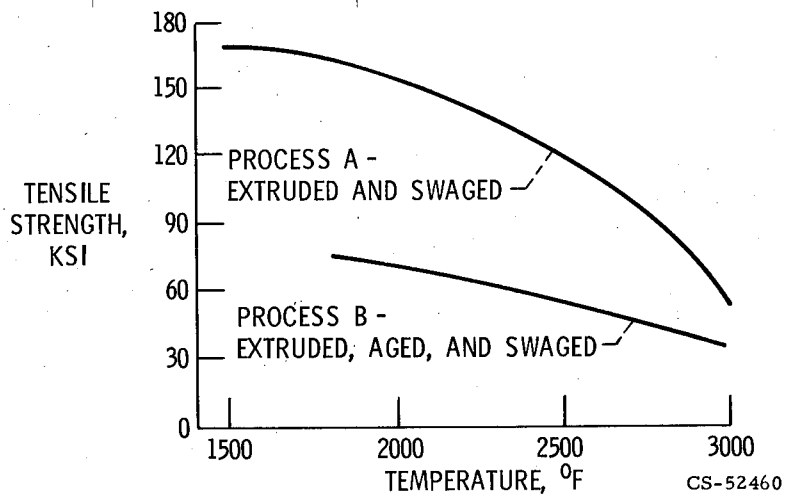


Figure 10-8. - Effect of thermomechanical processing on high-temperature tensile strength of Mo-0.6Hf-0.5C alloy. Extrusion, 4000°F; aging, 1 hour at 2800°F; swaging, 2500° to 2000°F.

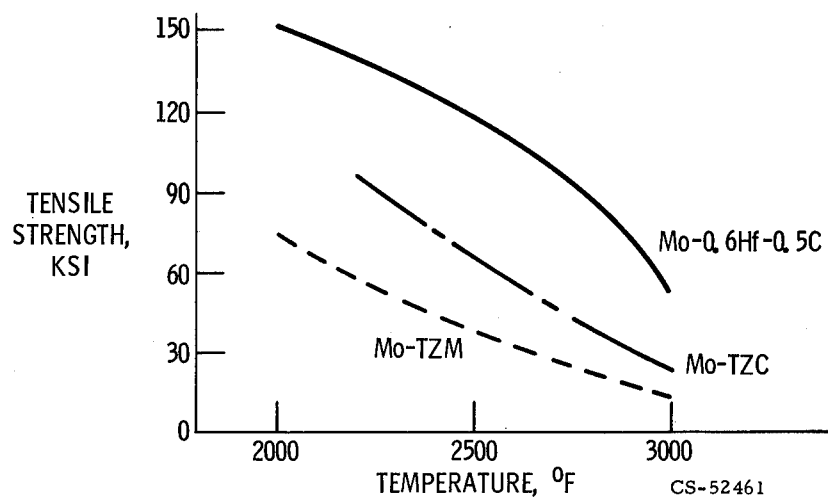


Figure 10-9. - Comparison of high-temperature tensile strengths of experimental Mo-0.6Hf-0.5C alloy and commercial molybdenum alloys.

## 11. MASS SPECTROMETRIC STUDIES OF THE VAPORIZATION OF REFRACTORY CARBIDES AND NITRIDES

Fred J. Kohl and Carl A. Stearns

The use of many refractory materials is limited by their vaporization rates rather than by their melting points. Thus, to realize the full potential of the refractory transition metal compounds for high-temperature applications, the vaporization behavior of these materials must be known and understood.

The Knudsen effusion method has been used in conjunction with a double-focusing mass spectrometer to study the high-temperature vaporization of some refractory carbides and nitrides. The carbide systems of titanium, vanadium, chromium, and yttrium and the nitride system of titanium have been examined. The previously unobserved molecular species  $\text{TiC}_4$ ,  $\text{VC}_4$ ,  $\text{CrC}_2$ ,  $\text{YC}_4$ , and  $\text{TiN}$  have been identified. The dissociation energies of the molecular species have been determined along with other pertinent thermochemical quantities. These properties are of critical importance in testing theories of chemical binding and stability. The experimental results are discussed in terms of their fundamental chemical significance and practical implications.

Modern technology has not yet realized the full potential of some of the most promising high-temperature materials. For example, the transition metal carbides combine the properties of high melting temperature, high strength, and hardness with good electrical and thermal conductivities and chemical stability. However, they have found only a limited number of useful high-temperature applications. Although the lack of ductility of these materials may prevent their use as structural materials in some cases, the unavailability of sufficient and reliable high-temperature properties data is mainly responsible for this situation. If we ever hope to apply the maximum high-temperature potential of such refractory materials as the carbides, nitrides, and borides, we must understand the associated basic thermochemical properties. With such an understanding we should be able to explain, and possibly to predict, high-temperature behavior.

At Lewis the modes of the high-temperature vaporization of refractory carbides and nitrides are being studied. To date the carbide systems of titanium (Ti), vanadium (V), chromium (Cr), and yttrium (Y), plus the nitride system of titanium, have been examined. The purpose of this work has been to obtain experimental thermochemical data which can yield the basic thermodynamic properties of simple



gaseous molecules. These properties are critically important in testing theories of chemical binding and stability. These studies also establish the nature of high-temperature reactions and provide vapor pressure data which are of considerable practical significance. In some cases, vapor pressure or rate of loss of material, rather than melting point, ultimately dictates the major limit of usefulness of materials in high-temperature applications. The refractory carbides and nitrides are examples of materials for which vaporization, rather than melting, may be the most important mode of deterioration.

## APPARATUS

We have developed a unique experimental capability which allows the vaporization of particularly difficult systems to be studied. The attempts of other investigators to study these systems have been incomplete because they were not able to identify and to measure quantitatively all molecular species involved. For the transition and rare-earth metal carbides and nitrides, for example, many experimental problems are encountered because of the extremely small amounts of molecular species which are present and the high temperatures required for appreciable vaporization. Our success can be attributed to adaptation of a Knudsen cell inlet system to a double-focusing mass spectrometer. The Knudsen cell system (ref. 1) is shown schematically in figure 11-1. It was designed and built at Lewis and is the heart of our capability. The solid sample is contained in a tungsten or tantalum crucible, called a Knudsen cell. The cell is heated by electron bombardment. On heating, some of the solid vaporizes, and the composition of the vapor phase is sampled by effusion of the gaseous molecules through the orifice of the cell. The neutral gas molecules pass into the source region of the mass spectrometer. In figure 11-2, a schematic diagram of the mass spectrometer is given. The neutral gas molecules effuse from the Knudsen cell into the source of the mass spectrometer, and are ionized and accelerated down the flight tube. The ions are energy focused in the electric sector and are separated by their mass-to-charge ratios in the magnetic sector. By scanning the magnetic field, the various ions are detected by use of an electron multiplier and electrometer. This apparatus provides us with the ability to study vaporization at temperatures to 3000 K and measure partial pressures in the range from  $10^{-3}$  to  $10^{-10}$  atmosphere. The high sensitivity and good resolution of the double-focusing mass spectrometer allows detection of vaporizing molecular species previously unknown. For example, the titanium nitride molecule has been identified as a product in the vaporization of solid TiN (ref. 1).

The next two figures serve to demonstrate one of the advantages of the apparatus. In figure 11-3 is shown a low resolution mass spectrum in the region of mass-to-charge ratio of 60, where the TiN peak would be expected. Relative intensity is plotted against mass-to-charge ratio. First, note that the only peak evident is the large peak labeled background. If TiN were present, it would be masked by the background. The background peak is due to complex organic molecules from such sources as pump oil, fingerprints, and grease. (These are typical problems which continually plague the mass spectroscopist.) With low resolution, the spectrum in figure 11-3 is all that would be seen because everything of low intensity would be masked by the background. With high resolution, however, the important details become evident, as shown in figure 11-4. The TiN peak is immediately obvious in this high resolution spectrum, in addition to another peak which is due to nickel (Ni). The small Ni peak represents a low-level impurity in the tungsten container or the TiN. The intensity of the TiN peak corresponds to a partial pressure of approximately  $10^{-9}$  atmosphere. The identification of TiN required that the instrument have a resolution sufficient to achieve this separation and a sensitivity capable of measuring a pressure of  $10^{-9}$  atmosphere. Also, to achieve this level of TiN pressure, the apparatus must be capable of raising the sample to a sufficiently high temperature. More detailed results on the TiN system are presented later in this paper. First, let us present the results on the carbide systems, which have thus far received the bulk of our effort.

## SYSTEMS STUDIED

The solid-liquid phase diagram for the titanium-carbon (Ti-C) system (ref. 2) is shown in figure 11-5. The only solid phase existing as a chemical compound is the TiC phase of variable composition. In our studies we have been concerned with the region of excess carbon, that is, the TiC + C boundary in the phase diagram. In a recent vaporization study, Storms (ref. 2) measured the Ti pressure of the Ti-C system at 1900 K as a function of composition. His results are shown in figure 11-6. The compositions studied by Storms correspond to those shown in the phase diagram in figure 11-5. Note that the vapor pressure of Ti is strongly dependent on the composition of the solid phase. For the range from nearly stoichiometric TiC to pure Ti, the Ti partial pressure varies by a factor of more than  $10^4$ . While this information is important in obtaining the activity of Ti as a function of composition, it does not give a complete picture of the vaporization process. To define completely the mode of vaporization of TiC + C, all vaporizing species must be known. The results of our mass spectrometric study are shown in figure 11-7. In addition to Ti, the

carbon species  $C$ ,  $C_2$ ,  $C_3$ ,  $C_4$ ,  $C_5$ , plus  $TiC_2$  and  $TiC_4$ , are significant vaporization products. From the data shown in figure 11-7, certain thermodynamic quantities for gases and solids involved in the thermochemical processes can be deduced. In addition to this fundamental information, certain practical values can be realized from such data. For example, suppose we wish to compute the weight loss of a body fabricated from  $TiC + C$  which is to be operated at, for example, 2500 K in a vacuum. The classical Langmuir equation can be used for this calculation, but we must take into account all vaporizing species and know their partial pressures at the temperature in question. Another practical example of vapor pressure data is the determination of the condensate of a particular vaporization process. The vaporization products from a solid  $TiC + C$  body may condense on an adjacent structure (whose surface properties are critical) and change the character of this surface. From these two examples, it can be seen that the mode of vaporization is a significant factor in designing new materials to have especially desirable properties.

In figure 11-8 are presented the results of our study of the  $YC_2$ -C system. Identification of the  $YC_4$  molecule is an aid to understanding the chemistry involved in this system. Certainly from a classical chemical valency viewpoint, such molecules as  $YC_2$  or  $YC_4$  are unexpected. However, it is not uncommon to find such molecules, or molecules which exhibit apparent valencies different from those in the condensed phase, in high-temperature systems. Exactly this point makes them interesting to the chemist. The reactions which describe the Y-C vaporization process are shown in table 11-I, together with the respective measured heats of reaction. Comparing the heat of vaporization of Y ( $\Delta H_v$ ) from the element (reaction 1) with that from the carbide (reaction 2) gives a comparison of the binding energy of the metal-metal (M-M) and metal-carbon (M-C) bonds in the solids. When the  $\Delta H_v$  values for a series of carbides are compared, an estimate of relative stabilities can be made. From the enthalpies (heats of reaction) associated with reactions 1 and 2, the heat of formation ( $\Delta H_f$ ) of the condensed phase  $YC_2$  can be determined (reaction 3). As a matter of fact, this is the only method for determining this quantity which has been employed up to the present time. When the heats associated with reactions 4 and 5 are combined with suitable auxiliary data, bond energies of the metal dicarbide and tetracarbide molecules can be calculated (reactions 6 and 7).

Our studies of carbide systems have also included vanadium and chromium carbide. In the vanadium system, the major species are V atoms, the carbon polymers, and vanadium dicarbide and tetracarbide. Measurements of  $VC_2$  and  $VC_4$  have allowed us to characterize the vaporization process for this system in a way similar to that previously described for the Y-C system.

In our study of the Cr-C system, Cr, the carbon polymers, and  $\text{CrC}_2$  were the only molecular species detected, and the results are similar to those for the Ti, Y, and V systems.

Thus far, the only nitride system we have studied is the TiN system (ref. 1). While we have been able to identify the TiN molecule in the gas phase, the partial pressure for this species is very low, and for all practical purposes Ti and  $\text{N}_2$  are the only important vaporization products. The chemical reactions pertinent to this system are presented in table 11-II. The heats associated with these reactions compare appropriately with those for other refractory nitride systems (ref. 3) and have contributed to our understanding of these systems. The dissociation energy for TiN (reaction 2) agrees well with the value predicted on the basis of an empirical method (ref. 3) and *ab initio* quantum mechanical calculations (ref. 4). This agreement serves to establish more firmly such calculational methods and allows them to be applied with confidence to yet unstudied nitride systems.

## DISCUSSION

The next two tables serve to summarize this presentation and show the status of our vaporization research on carbide systems. In table 11-III the bond dissociation energies for the oxides (ref. 5) are compared with dicarbides and the dioxides with tetracarbides of some rare-earth, transition metal, and actinide elements. It has been proposed (ref. 6) that the bonding characteristics of the  $\text{C}_2$  or acetylide ion group may be similar in behavior to that of the isoelectronic oxygen (O) atom. This comparison has been reviewed by other investigators (refs. 6 and 7) in some detail with respect to an extensive series of rare-earth and Group IIIA and IVA elements. This comparison is extended herein to some of the refractory carbides. In all cases except chromium, the bond dissociation energies for the metal-oxygen (M-O) bond are stronger than the corresponding metal-carbon (M- $\text{C}_2$ ) bond by approximately 10 to 30 kilocalories. Although the data are not very extensive, a similar trend is apparent in comparing the bond energies for the metal tetracarbides.

On the basis of the consistent trends demonstrated by this empirical comparison of metal-oxides and metal-dicarbides, a prediction can be made concerning the stability of the yet unobserved hafnium (Hf), niobium (Nb), tantalum (Ta), molybdenum (Mo), and tungsten (W) dicarbides and the corresponding metal tetracarbides. The ones which are missing from table 11-III are the hardest to measure. However, on the basis of the presently available data, their properties can perhaps be estimated. Undoubtedly, hafnium dicarbide and tetracarbide and thorium tetracarbide exist as

respectably stable molecules. Although these may be observed only at the highest temperatures and in low concentrations, their existence is important from a chemical viewpoint.

The high physical stability of the gaseous dicarbides and tetracarbides suggests that the metal-dicarbide ( $M-C_2$ ) bond may be of a strong ionic character. An extension of this concept to the solids may partly explain their high melting points and mechanical strength.

In table 11-IV are given the ratios of metal atom to dicarbide and tetracarbide species in the equilibrium vapor compositions for various metal carbides at 2500 K. There is a definite trend in the existence of molecular species as a function of the position of the metal in the periodic table. Although the data are relatively sparse, in all cases, in moving down a column, the existence of the dicarbide species becomes more important. For example, this trend is quite pronounced in columns 1 and 2 where the metal-to-dicarbide ratio goes from 900 to 9 to 1.6 for the Group IIIB metals and from 380 to 16 to 0.7 for the Group IVB metals. The thermodynamic circumstances which dictate these ratios are determined by the vapor pressures of the metal and carbon species and the corresponding relative bond energies for the various molecules, along with the composition and stability of the condensed phase. On the basis of bond energy comparisons and observation of the ratios of metal atom to carbide molecule, it is again concluded that the carbides of W, Ta, and especially Hf will be important species in the mode of vaporization of the respective solids. In general, the vapor composition becomes richer in dicarbide and tetracarbide species as the temperature is increased. Thus, the higher the temperature at which vaporization takes place, the more important the molecular species will become.

## SUMMARY

The vaporization characteristics of metal carbides and nitrides are being investigated by the use of molecular-beam mass spectrometry. In particular, we are interested in determining the composition of the vapor phase, the vapor pressures, and the heats of vaporization of the various atomic and molecular species. These are factors which in some cases determine the usefulness of these materials for high-temperature applications. Also being studied are the heats of reactions which lead to the thermodynamic properties of molecules and solids pertinent to the theories of chemical binding.

Although the mass spectrometric studies described herein are only a small part in the overall characterization of the properties of refractory carbides and nitrides,

additional studies are being conducted in many laboratories to obtain additional experimental data. In the years ahead, such studies undoubtedly will provide the information necessary to make useful these potentially beneficial materials.

## REFERENCES

1. Stearns, Carl A.; and Kohl, Fred J.: The Dissociation Energy of Gaseous Titanium Mononitride. NASA TN D-5027, 1969.
2. Storms, Edmund K.: The Refractory Carbides. Academic Press, 1967.
3. Gingerich, Karl A.: Gaseous Metal Nitrides. III. On the Dissociation Energy of Thorium Mononitride and Predicted Dissociation on Energies of Diatomic Group III-VI Transition-Metal Nitrides. J. Chem. Phys., vol. 49, no. 1, July 1, 1968, pp. 19-24.
4. Carlson, K. Douglas; Claydon, Charles R.; and Moser, Carl: Electronic Structure and Ground-State Properties of Titanium Mononitride. J. Chem. Phys., vol. 46, no. 12, June 15, 1967, pp. 4963-4969.
5. Drowart, J.; and Goldfinger, P.: Investigation of Inorganic Systems at High Temperature by Mass Spectrometry. Angew. Chemie. Int. Ed., vol. 6, no. 7, July 1967, pp. 581-596.
6. Chupka, William A.; Berkowitz, Joseph; Giese, Clayton F.; and Inghram, Mark G.: Thermodynamic Studies of Some Gaseous Metallic Carbides. J. Phys. Chem., vol. 62, no. 5, May 1958, pp. 611-614.
7. DeMaria, G.; Balducci, G.; Capalbi, A.; and Guido, M.: High Temperature Mass Spectrometric Study of the Neodymium-Carbon System. Univ. Rome (AFML-TR-66-323, DDC No. AD-804983), Oct. 1966.

TABLE 11-I. - REACTION ENTHALPIES  
FOR YTTRIUM-CARBON SYSTEM

Reaction	Measured heat of reaction, $\Delta H$ , kcal mole <sup>-1</sup>
1. $Y(s) = Y(g)$	101.5
2. $YC_2(s) = Y(g) + 2C(s)$	123.4
3. $Y(s) + 2C(s) = YC_2(s)$	-22.0
4. $Y(g) + 2C(s) = YC_2(g)$	45.5
5. $YC_2(g) + 2C(s) = YC_4(g)$	44.6
6. $YC_2(g) = Y(g) + C_2(g)$	152.0
7. $YC_4(g) = Y(g) + 2C_2(g)$	304.0

TABLE 11-II. - REACTION ENTHALPIES  
FOR TITANIUM-NITROGEN SYSTEM

Reaction	Measured heat of reaction, $\Delta H$ , kcal mole <sup>-1</sup>
1. $TiN(g) = Ti(g) + 0.5 N_2(g)$	0.8
2. $TiN(g) = Ti(g) + N(g)$	112.6
3. $TiN(s) = Ti(g) + N(g)$	306.7
4. $Ti(s) + 0.5 N_2(g) = TiN(s)$	-80.7

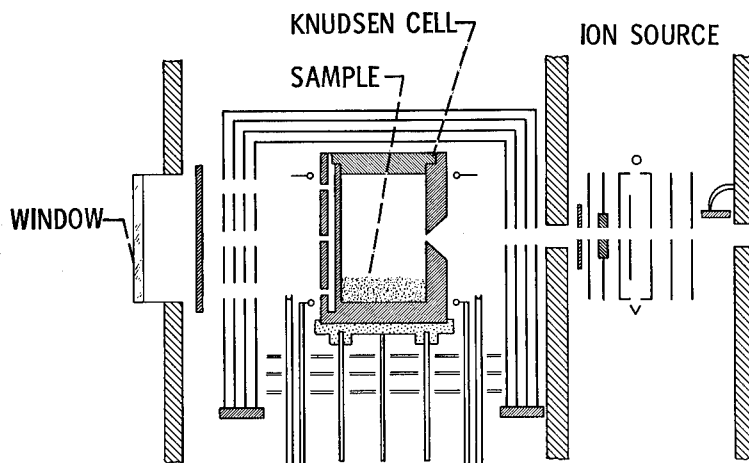
TABLE 11-III. - BOND ENERGIES FOR METAL OXIDES AND  
DICARBIDES, IN KILOCALORIES

	Y	Ti	Zr	Hf	Th	V	Nb	Ta	Cr	Mo	W
M-O	170	158	181	183	198	148	180	194	101	116	155
M-C <sub>2</sub>	152	136	158	---	170	136	---	---	106	---	---
O-M-O	---	313	345	360	388	290	341	343	221	270	296
C <sub>2</sub> -M-C <sub>2</sub>	304	290	---	---	---	285	---	---	---	---	---

TABLE 11-IV. - ABUNDANCE RATIOS OF VAPORIZATION SPECIES  
ABOVE CARBIDES AT 2500 K

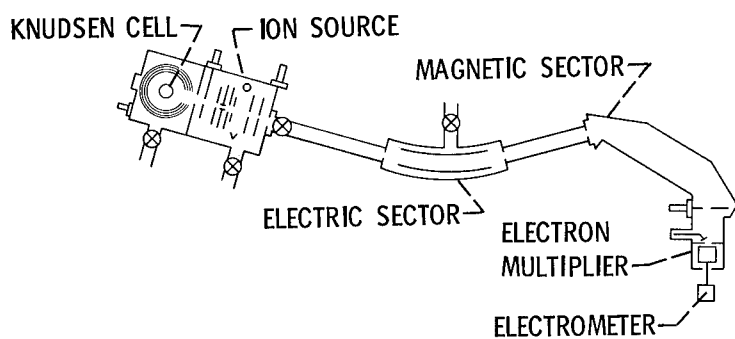
Group IIIB	Group IVB	Group VB	Group VIB
Sc : ScC <sub>2</sub> 900: 1	Ti : TiC <sub>2</sub> : TiC <sub>4</sub> 380: 1 : 6×10 <sup>-4</sup>	V : VC <sub>2</sub> : VC <sub>4</sub> 860: 1 : 2×10 <sup>-3</sup>	Cr : CrC <sub>2</sub> 1.2×10 <sup>6</sup> : 1
Y : YC <sub>2</sub> : YC <sub>4</sub> 9 : 1 : 1.2×10 <sup>-2</sup>	Zr : ZrC <sub>2</sub> 16 : 1	Nb	Mo
La : LaC <sub>2</sub> : LaC <sub>4</sub> 1.6: 1 : 2.5×10 <sup>-2</sup>	Hf	Ta	W
	Th : ThC <sub>2</sub> 0.7: 1		U : UC <sub>2</sub> : UC <sub>4</sub> 4 : 1 : 1.4×10 <sup>-2</sup>





CD-10156  
CS-52330

Figure 11-1. - Knudsen cell assembly and ion source.



CD-10155  
CS-52329

Figure 11-2. - Mass spectrometer and Knudsen cell inlet system.

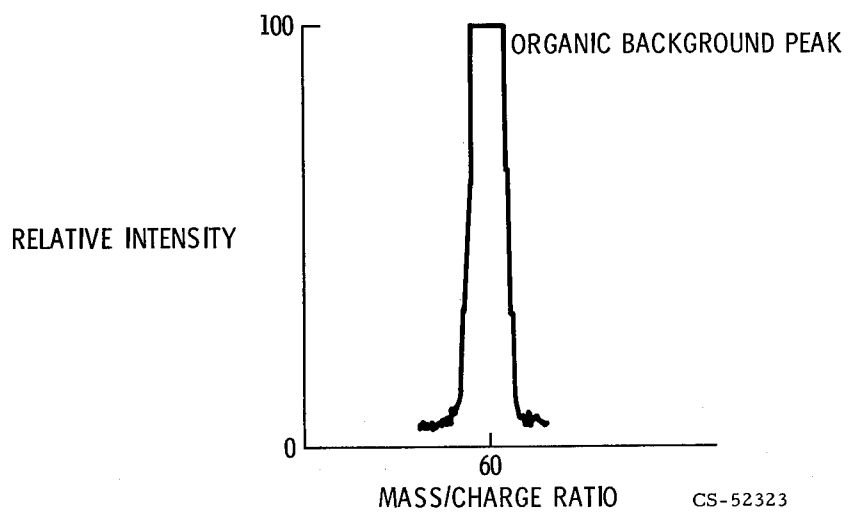


Figure 11-3. - Low resolution mass spectrum.

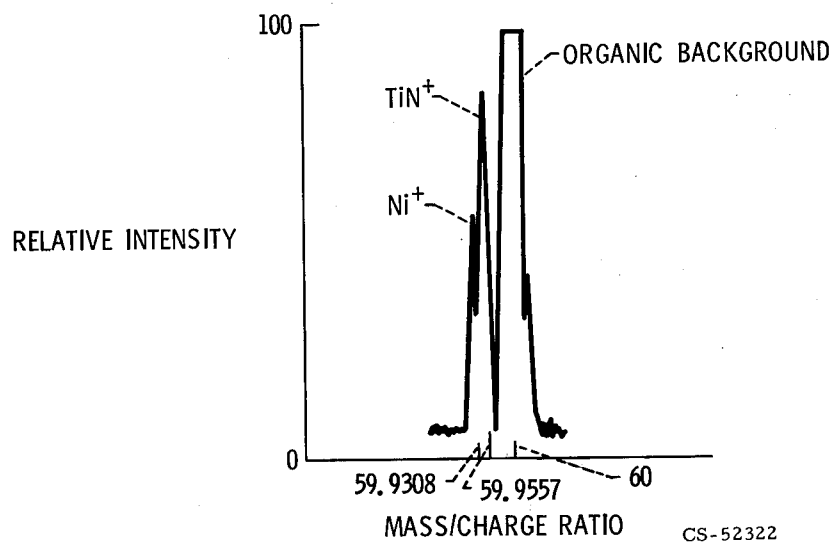


Figure 11-4. - High resolution mass spectrum.

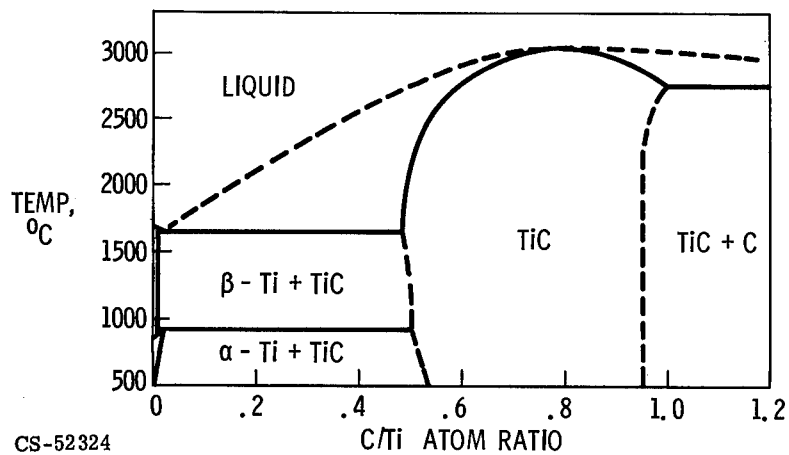


Figure 11-5. - Phase diagram of titanium-carbon system.

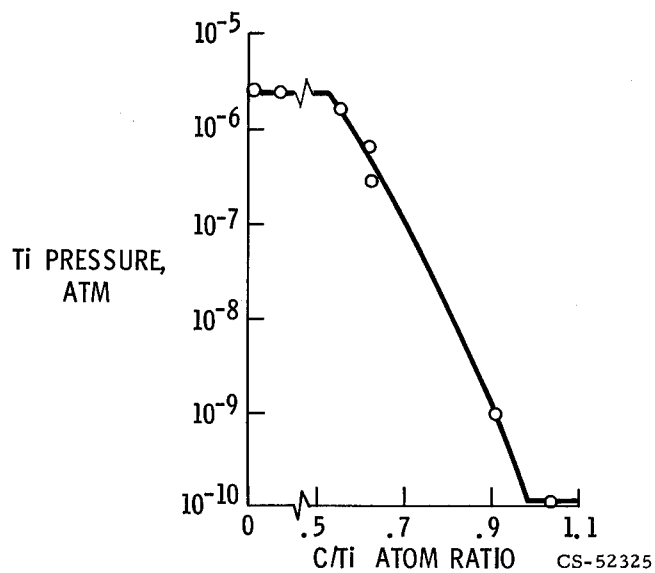
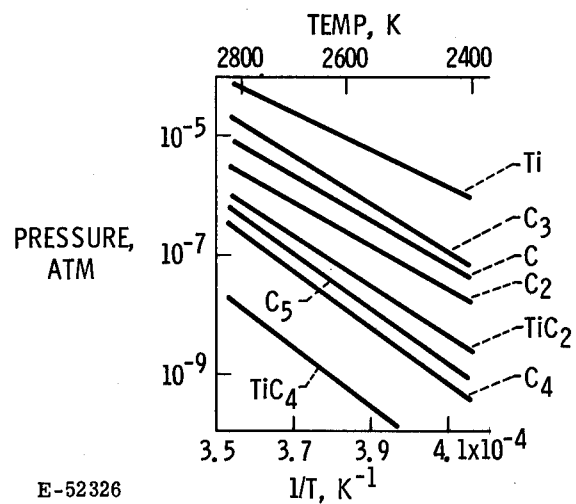
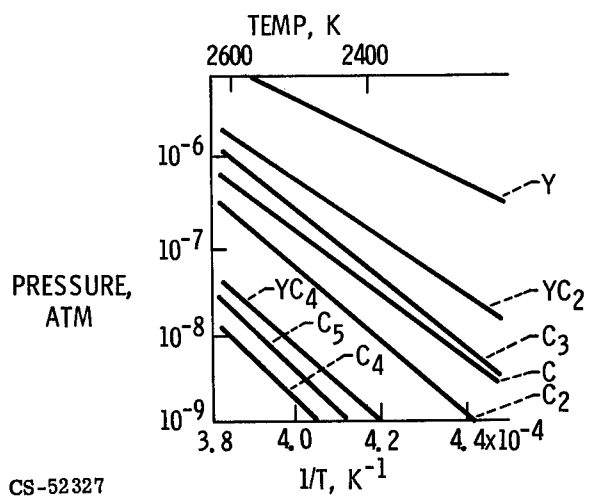


Figure 11-6. - Pressure of Ti(g) over TiC at 1900 K.



E-52326

Figure 11-7. - Vapor pressures for TiC + C system.



CS-52327

Figure 11-8. - Vapor pressures for  $YC_2$ -C system.



## 12. METAL-MATRIX FIBER COMPOSITES FOR HIGH TEMPERATURES

Robert A. Signorelli and John W. Weeton

Composite material research has been stimulated by the desire to use the superior mechanical properties of fibers in structural materials. Metal-matrix fiber composites have the potential to combine the strength of refractory fibers at high temperatures with the superior oxidation resistance and ductility of superalloy matrix materials. Investigations conducted with model systems such as tungsten fibers in copper have indicated that the strength of fibers can be used effectively to increase the strength of the matrix into which they are incorporated. These studies have demonstrated that the strength of fibers can be realized in composites for short-time tensile failure and for long-time rupture failure at elevated temperatures. However, other results have indicated problems to be overcome to achieve high strength with non-ideal or practical combinations of fiber and matrix. The most serious problem was to bond fibers to the matrix effectively while controlling matrix-fiber reaction which otherwise would seriously reduce composite strength.

A program was designed to control matrix-fiber reaction during fabrication and elevated-temperature testing of composites by a combination of the following steps: The matrix alloy composition was selected to reduce the potential for diffusion recrystallization of the fiber, a solid-state sintering fabrication process was developed that used relatively low-temperature consolidation to reduce diffusion, and the fiber diameter was chosen to maximize the retained strength in the unreacted fiber core. Tungsten alloy fiber - superalloy matrix composites fabricated using the approaches evolved in this program demonstrated stress-rupture strengths for rupture in 1000 hours at 2000° F of 37 000 psi. This strength is six times that of conventional nickel superalloys and represents a potential for an increase of 200° F in turbojet engine turbine blade use-temperature. Preliminary oxidation and impact test studies also indicate that the material has merit for potential use as turbine blades.

A great deal of fiber composite research has been conducted in recent years to provide materials with improved strength and rigidity. Fiber composites offer the potential for improvement in material properties because some materials in fiber form are stronger and more rigid than are bulk materials. Figure 12-1 illustrates

examples of the superior properties of fiber materials over bulk metals. The advantage is emphasized by normalizing the data for density variations by dividing the properties of each material by the density of the material. Some fibers, such as S and E glass, are stronger than the metals but not more rigid, while other continuous fibers of boron or carbon are superior in both properties. The very strongest and stiffest fibers are whiskers, with properties above and to the right of the dashed lines in figure 12-1. These dashed lines indicate the values on the abscissa and ordinate scales where the scales are broken to permit the very high whisker values to appear in the same plot. However, all the fibers are very small in diameter: boron filaments are 4 mils in diameter, carbon about 1/3 mil, and whiskers about 1/10 mil - and as such not very useful as structural materials. The superior properties of fibers can be used most effectively when combined with a matrix into engineering materials tailormade for specific applications. Fiber composite research is basically the effort to produce better fibers and to learn how to combine fibers into useful structural materials.

One of the advantages of fiber composites is that the component materials can be selected to meet specific service requirements. Plastic-matrix materials are superior for some applications, and metals for others. Some of the advantages of a metal matrix are higher temperature capability than plastics, increased ductility and toughness, and protection of fibers from oxidation and abrasion. Metals are generally preferred where a stronger, more temperature resistant matrix is required. Metal-matrix composites currently are being developed for service applications to above 2000<sup>0</sup> F, well above the range for plastic-matrix materials.

Metals also provide ductility and toughness where impulse or vibratory loads are a major requirement. The samples shown in figure 12-2 illustrate the ductility advantage of a composite over bulk material. The 40-mil-diameter composite specimen composed of an array of 5-mil-diameter tungsten fibers in a copper matrix was severely deformed without fracture of the tungsten or the composite. However, the 40-mil-diameter tungsten wire fractured when bent much less severely. The superior strength of the smaller diameter wire combined with a ductile matrix has provided a material with both strength and ductility.

A metal matrix can also serve to protect fibers from damage by abrasion and from oxidation at elevated temperatures. The photomicrograph of figure 12-3 shows severe oxidation from high-temperature air exposure of a tungsten fiber in the composite surface, while the fiber buried in the matrix is essentially unaffected. The high-temperature strength of the fiber can be realized because the matrix compensates for the poor oxidation resistance of the fiber.

Fiber composites permit us to use the superior properties of materials avail-

able in fiber form and to provide a combination of the better properties of the components.

## MODEL SYSTEM STUDIES

One of the basic assumptions underlying the effort to develop fiber composites is that the high strength and stiffness of fibers can be used effectively to increase the properties of the matrix into which they are incorporated. A considerable amount of research has been reported (refs. 1 to 13) describing the results of studies conducted to explore fiber composite behavior. The results of these model system studies experimentally established that the strength of fibers could be realized in composites. Since only a brief description of some of these results are presented here, details must be obtained in the references.

Composite specimens of tungsten lamp filament wire and copper were fabricated (ref. 3) as shown in figure 12-4. Wires cut to specimen length were inserted into cylindrical ceramic tubes and a plug of copper placed above the wires. The assembly was placed in a vacuum furnace and the temperature raised above the melting point of copper. The molten copper infiltrated the wire bundle forming a composite rod, which was machined into a test specimen. Specimens with a range of fiber content were prepared and tested in tension. The results of these tests are shown in figure 12-5 in which tensile strength is plotted against fiber content. The strength at 100 percent fiber content is for wires tested individually outside of a composite. The strength at 0 percent fiber content is the strength contribution of the copper matrix when strained about 2 percent in the composite, the fracture strain of the tungsten fibers. The line connects the two end points. The short horizontal portion of the plot at very low fiber contents represents the strength of copper when it failed at over 20 percent strain. The latter occurs for composites when the fiber content is low, such that composite fracture does not occur at fiber-fracture strain. The data of figure 12-5 for the composites follow the line very well, with the strength increasing directly with increasing fiber content. This indicates that the strength of the fibers is being realized in the composite.

The long-length fibers used in the study are more easily used than are short-length fibers. However, some high-strength fibers, such as whiskers, are available only in relatively short lengths. Therefore, specimens were fabricated with short-length, chopped tungsten fibers in copper to determine if short-length fibers also could be used effectively. These specimens were fabricated by a slightly different technique which limited fiber content to 40 volume percent. The short-time tensile data for these specimens are shown in figure 12-6. These data also follow



the line between matrix and fiber strength, indicating that the tensile strength of short-length fibers also can be used effectively in composites.

Many potential high-temperature applications are limited by creep or rupture failure rather than short-time tensile fracture. Therefore, we also evaluated (ref. 10) copper-tungsten composites for long-time elevated-temperature service. The results obtained for 10- and 1000-hour rupture tests are shown in figure 12-7. The plot of composite stress for a range of fiber content indicates that fiber rupture strength also can be realized in composites.

These results and a wealth of additional data have been obtained by many investigators to firmly establish that fiber strength can be used effectively to increase the properties of materials. The field has progressed to very sophisticated structural mechanics treatments to predict composite fracture behavior and to design composites for specific applications. However, much work is needed to progress from the demonstration of potential with model systems to the development of practical composites for engineering applications. The following section reviews some of the results of our work on refractory-metal-fiber-reinforced superalloys.

## REFRACTORY-METAL-FIBER - SUPERALLOY COMPOSITES

Refractory-metal-fiber - superalloy composites might be used in an advanced turbojet engine such as that shown schematically in figure 12-8. Designers want to increase operating temperatures of turbojet engines, but materials limitations prevent this. Material temperatures for the rotating first stage turbine blades might be increased from 1800° F to 2000° to 2400° F if superalloy matrix - fiber composites were successfully developed.

Refractory-metal alloys have the required strength for turbine blades at 2000° F and above but lack oxidation resistance, and some alloys are brittle at room temperature. Nickel and cobalt superalloys have ductility and superior oxidation resistance but are weak at 2000° F. Refractory-metal-fiber - superalloy composites offer the potential to combine the best properties of both components. However, matrix-fiber reaction must be controlled to prevent serious reduction of fiber properties (ref. 14). The tungsten fiber embedded in copper (fig. 12-9) shows no reaction, since this combination is mutually insoluble. That was one of the prime considerations for the selection of those materials for the model system studies. However, when 10 percent nickel is alloyed with the copper and used as a matrix, considerable reaction, which degrades fiber strength, is noted in the fiber; almost complete destruction of the fiber geometry occurs with a nickel matrix.

A research program designed to control matrix-fiber reaction was undertaken (ref. 15) using the following steps:

- (1) Matrix composition selection
- (2) Fabrication process development
- (3) Wire diameter choice

Reactions that occur during specimen fabrication and during elevated-temperature service must be controlled. Matrix compositions shown in table 12-I were selected to reduce the tendency for solute diffusion into the fiber. Both alloys contained large weight percentages of refractory metals, which had been shown in a preceding compatibility study to reduce diffusion-penetration and recrystallization of tungsten fibers. The titanium and aluminum additions were made to form Ni-Ti-Al intermetallic compound, which would reduce the activity of nickel and increase matrix strength.

A fabrication process was developed to control reaction during fabrication of the composite specimens. The process is shown schematically in figure 12-10. Wires, cut to length, were packed into a metal tube, and a slurry of matrix alloy powder was slip cast into the fiber array. The dried slip-casting was sintered at 1500° F for 1 hour in a hydrogen atmosphere. The tube was then evacuated and welded shut with end caps. The encapsulated billet was isostatically hot pressed at 20 000 psi, first at 1500° then at 2000° F. A powder metallurgy approach was selected to take advantage of the lower diffusion rates of solid-state sintering rather than the more damaging liquid-phase methods. Specimens with up to 75-volume-percent fibers were made by the method evolved. The high-volume fiber content possible with this method increased the maximum strength contribution range for the fiber composites compared with other powder methods, which limited fiber contents to 30 to 50 percent. The sintering was conducted in a hydrogen atmosphere at a relatively low temperature to remove surface impurities on the powders and to partially densify the body. Removal of impurities from the powder was thought to reduce the possibility for fiber damage from rapidly diffusing contaminants. The low-temperature sintering and two-step hot pressing were designed to obtain as dense a body as possible before exposing the composite to high temperature because the higher density body would have lower diffusion rates than a porous body.

The final step (fig. 12-11) was to maximize the retained strength in the unreacted fiber core. The depth of penetration of the reaction-affected area was essentially the same for an 8-mil-diameter fiber as for a 20-mil-diameter fiber. By increasing the diameter of the fiber, the percentage of unreacted core was increased. However, the smaller diameter fiber is stronger than the larger, so the two effects have to be balanced. The smaller diameter fiber results in higher

strength material for short-time service, and the larger diameter fiber is better for longer times. A 15-mil-diameter fiber was selected for this study based on its superior strength for 100- and 1000-hour service.

The stress-rupture properties achieved with composites fabricated using these techniques are shown in figure 12-12. Since composites are a new class of materials, the properties of composites shown in figure 12-12 and several that follow are compared with superalloys, the material normally used for turbine blades. The fiber used was 218 tungsten alloy, which is commercial lamp filament wire. The 100-hour and 1000-hour stress-rupture strengths of the composite at 2000° F are about three to four times that of the conventional superalloy included for comparison. The strengths obtained indicated successful control of matrix-fiber reaction. The strength of the composite for 100-hour rupture failure was 90 percent of the strength possible with the fiber used. Only 10 percent of the fiber strength was lost by the reaction that occurred during specimen fabrication and during the 100-hour rupture test at 2000° F.

The 218 tungsten alloy fiber used in the early part of the program was the strongest refractory-metal-alloy fiber available at the time. However, a continuing contractual effort has been conducted to provide stronger fibers for use in composites. Tungsten, tantalum, molybdenum, and columbium alloys have been drawn into wire, and several have properties above those previously available (ref. 16). The rupture strength of wire of one of these alloys is shown in figure 12-13. The tungsten - 2-percent-thoria (W-ThO<sub>2</sub>) alloy wire is considerably stronger in stress rupture at 2000° F than the 218 tungsten wire used in the composites just described.

Composites have been fabricated using the improved wire and the same techniques described for the previous composite. The results obtained (ref. 17) are shown in figure 12-14. Bar graphs of stress over density for rupture in 1000 hours at 2000° F are plotted for conventional superalloys and for three composites. The first composite with 70-volume-percent 218 tungsten alloy wire is over twice as strong as the superalloys. The W-2ThO<sub>2</sub> composite strength is 40 percent higher than the 218 tungsten wire composite and three times as strong as the superalloys. The bar graph with dashed lines represents the strength we expect for composites reinforced with tungsten-hafnium-carbon (W-Hf-C) wire. This tungsten alloy was developed at the Lewis Research Center and is one of the strongest available. This is one of the alloys included in the contractual effort to draw stronger alloys into wire for composite reinforcement. The strength potential shown is based on preliminary data obtained from a limited quantity of wire of this alloy produced in this effort. The strength plotted was calculated using a retention of 80 percent of the fiber strength in the composite. That retention value is similar to those achieved for the other two composites shown. The strength value of the W-Hf-C composite

is about five times that of the superalloys. These high-strength values for composites indicate a potential for use in turbine blades. Figure 12-15 shows the possible turbine blade use-temperature of W-2ThO<sub>2</sub> composites and a typical superalloy based on stress-rupture strength. The fiber composite has a high density compared with the superalloys normally used because of the large tungsten content. Therefore, the strength data were normalized by dividing both by their density. The horizontal band on the figure represents a range of strength-over-density values that might be required for turbine blades for an advanced turbojet engine. The blade use-temperature of the fiber composite is about 200° F above that of the superalloys.

The excellent rupture strength of the fiber composite indicates that the matrix-fiber reaction has been controlled and that the composites have a potential for increased operating temperature of turbine blades. But strength alone is not enough, turbine blades are subjected to impact loads from foreign objects and to a highly erosive, oxidizing gas stream. Therefore, preliminary evaluation of the oxidation resistance and impact strength of the fiber composites has been conducted to further explore their potential for turbine blade use. Figure 12-16 contains some of the miniature specimen Izod pendulum test data collected. Impact energy in inch-pound units is shown for specimens with a range of fiber content, tested at room temperature and at 300° F. There is no clear correlation between pendulum impact data and turbine blade impact requirements. However, the dashed horizontal line represents the pendulum impact data obtained for a brittle superalloy which has been operated as turbine blades in a turbojet engine and survived foreign object impact. The 300° F data, and the higher temperature data not shown, compared very favorably with the superalloy, while the data at room temperature were marginal. A study we are conducting has indicated that impact resistance can be improved. For example, decreasing fiber content to 30 or 40 percent increased the impact strength above the superalloy line. In work not shown in this figure, increased matrix ductility also has increased the values obtained. Efforts to increase room-temperature impact strength will continue, and we are confident that considerable improvement will be achieved; however, the material may be adequate for turbine blades, even with the low impact values obtained. The impact strength is marginal below 300° F, but turbine blades are operated below that temperature only during starting and stopping the engine. The few seconds of operation below 300° F for each start or stop makes the probability for foreign object damage very low. The composite material, room-temperature, impact strength is adequate for normal maintenance operations and may be adequate for most room-temperature, foreign object, impact requirements. For those instances of room-temperature, foreign object impact where the lower composite impact strength would result in

failure, the problem is maintenance cost rather than a safety hazard since the engine normally would be on the ground for a start or stop.

The oxidation resistance of the composite is illustrated in figure 12-17. This photomicrograph shows a cross section from a specimen exposed to a flowing air atmosphere in a furnace at 2000° F. The Inconel alloy tube in which the composite specimen was fabricated had not been removed by machining. The thin cladding and matrix alloy protected the tungsten from the oxidizing environment. Coatings being developed to protect superalloys for operation at 2000° F and above would serve very well for the cladding. Based on rupture strength and impact and oxidation properties, the composites have potential for use as turbine blades. The steps taken to control matrix-fiber reaction have succeeded, and excellent properties at 2000° F have been obtained. However, even higher temperatures and longer service times are needed. Diffusion barriers are one of the approaches being investigated to further reduce matrix-fiber reaction and increase composite properties. The effectiveness of a coating to reduce matrix-fiber reaction is illustrated in the photomicrographs of figure 12-18. Uncoated and coated tungsten wires in a nickel matrix were heated to 2200° F. The uncoated wire is severely reacted, while the metal-oxide-coated wire is unaffected. The problem is to achieve a uniformly good coating. Coatings usually are not adherent in some locations on the wire surface or have porosity in some areas, which causes failure.

Another approach for higher temperature composites is the use of oxide fibers. There is a need for improved candidate oxide fibers, and several studies have been funded to investigate methods to produce oxide fibers. When available, these fibers will be fabricated into composites using techniques similar to those for refractory-metal-alloy fibers.

In summary, the strength of fibers can be realized in metal-matrix composites, and research has demonstrated that a family of materials with excellent properties for engineering applications can be developed. The superior strength of the materials should lead to increased performance in aerospace and other fields.

## REFERENCES

1. Jech, R. W.; McDanel, D. L.; and Weeton, J. W.: Fiber Reinforced Metallic Composites. Composite Materials and Composite Structures. Proceedings of the Sixth Sagamore Ordnance Materials Research Conference. Rep. MET 661-601, Syracuse Univ. Res. Inst., 1959, pp. 116-143.

2. McDanel, D. L.; Jech, R. W.; and Weeton, J. W.: Metals Reinforced with Fibers. *Metal Progr.*, vol. 78, no. 6, Dec. 1960, pp. 118-121.
3. McDanel, David L.; Jech, Robert W.; and Weeton, John W.: Stress-Strain Behavior of Tungsten-Fiber-Reinforced Copper Composites. NASA TN D-1881, 1963.
4. McDanel, D. L.; Jech, R. W.; and Weeton, J. W.: Analysis of Stress-Strain Behavior of Tungsten-Fiber-Reinforced Copper Composites. *Trans. AIME*, vol. 233, no. 4, Apr. 1965, pp. 636-642.
5. Petrsek, Donald W.; and Weeton, John W.: Alloying Effects on Tungsten-Fiber Reinforced Copper-Alloy or High-Temperature-Alloy Matrix Composites. NASA TN D-1568, 1963.
6. Petrsek, Donald W.: Elevated-Temperature Tensile Properties of Alloyed Tungsten Fiber Composites. NASA TN D-3073, 1965.
7. McIntyre, Ruluff D.: Tungsten-Nickel-Copper Ternary Alloys for High-Temperature Applications. NASA TN D-3015, 1965.
8. McDanel, David L.; and Signorelli, Robert A.: Stress-Rupture Properties of Tungsten Wire From 1200<sup>0</sup> to 2500<sup>0</sup> F. NASA TN D-3467, 1966.
9. Petrsek, Donald W.; Signorelli, Robert A.; and Weeton, John W.: Metallurgical and Geometrical Factors Affecting Elevated-Temperature Tensile Properties of Discontinuous-Fiber Composites. NASA TN D-3886, 1967.
10. McDanel, David L.; Signorelli, Robert A.; and Weeton, John W.: Analysis of Stress-Rupture and Creep Properties of Tungsten-Fiber-Reinforced Copper Composites. NASA TN D-4173, 1967.
11. Jech, Robert W.; and Signorelli, Robert A.: The Effect of Interfiber Distance and Temperature on the Critical Aspect Ratio in Composites. NASA TN D-4548, 1968.
12. McIntyre, Ruluff D.: Tensile Properties of Tantalum and Tungsten 10-Fiber Bundles at 1000<sup>0</sup> F (812 K). NASA TN D-4725, 1968.
13. Rubenstein, Lester S.: Effect of Size on Tensile Strength of Fine Polycrystalline Nickel Wires. NASA TN D-4884, 1968.
14. Signorelli, R. A.; Petrsek, D. W.; and Weeton, J. W.: Interfacial Reactions in Metal-Metal and Ceramic-Metal Fiber Composites. *Modern Composite Materials*. Richard Krock and Lawrence Broutman, eds., Addison-Wesley Publ. Co., 1967, pp. 146-171.

15. Petrasek, Donald W.; Signorelli, Robert A.; and Weeton, John W.:  
Refractory-Metal-Fiber - Nickel-Base-Alloy Composites for Use at High  
Temperatures. NASA TN D-4787, 1968.
16. Petrasek, Donald W.; and Signorelli, Robert A.: Stress-Rupture and Tensile  
Properties of Refractory-Metal Wires at 2000<sup>0</sup> and 2200<sup>0</sup> F (1093<sup>0</sup> and  
1204<sup>0</sup> C). NASA TN D-5139, 1969.
17. Petrasek, D. W.; and Signorelli, R. A.: Tungsten Alloy Fiber Reinforced  
Nickel Base Alloy Composites for High Temperature Turbojet Engine Appli-  
cations. Presented at the ASTM Symposium on Composite Testing and De-  
sign, New Orleans, La., Feb. 10-14, 1969.

TABLE 12-I. - MATRIX COMPOSITION

Alloy	Composition, wt %							
	Al	Nb	Cr	Mo	Ta	Ti	W	Ni
1	2	----	15	---	----	2	25	56
2	4.2	1.25	15	4	1.25	3.5	4	66.8

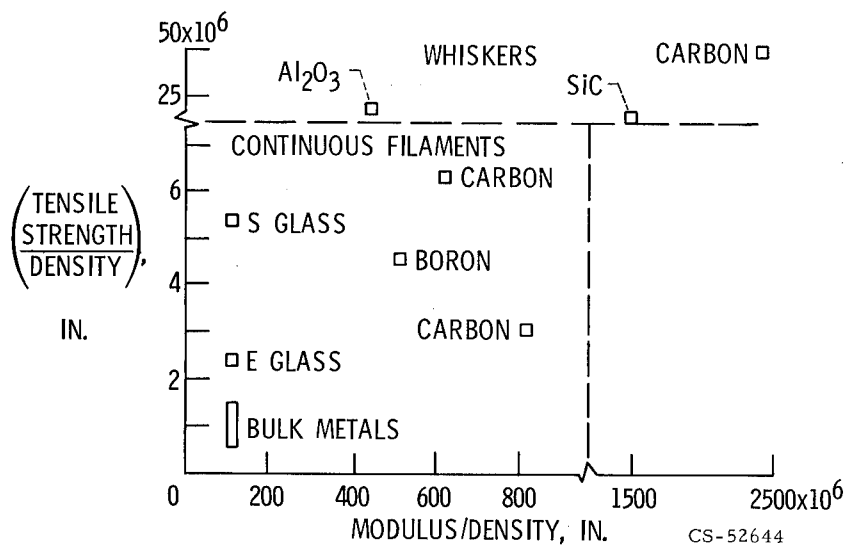
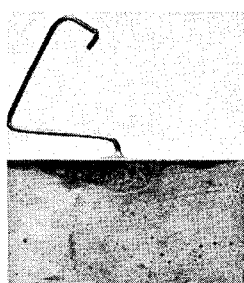
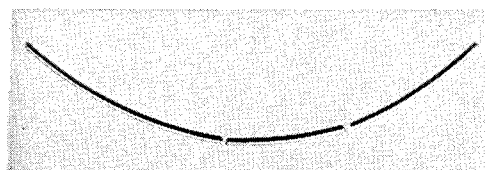


Figure 12-1. - Advantages in strength and rigidity of fibers over bulk metals.



COPPER-TUNGSTEN  
COMPOSITE,  
40 MIL DIAM,  
5 MIL WIRE



TUNGSTEN, 40 MIL DIAM



CS-52477

Figure 12-2. - Apparent bend ductility.



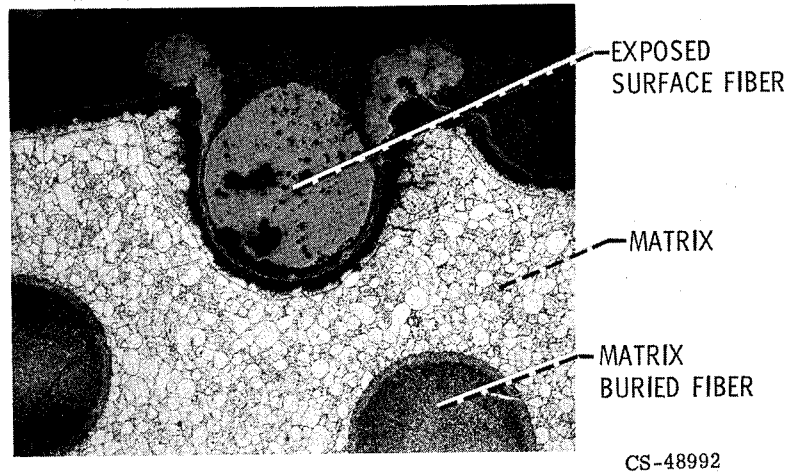


Figure 12-3. - Oxidation protection.

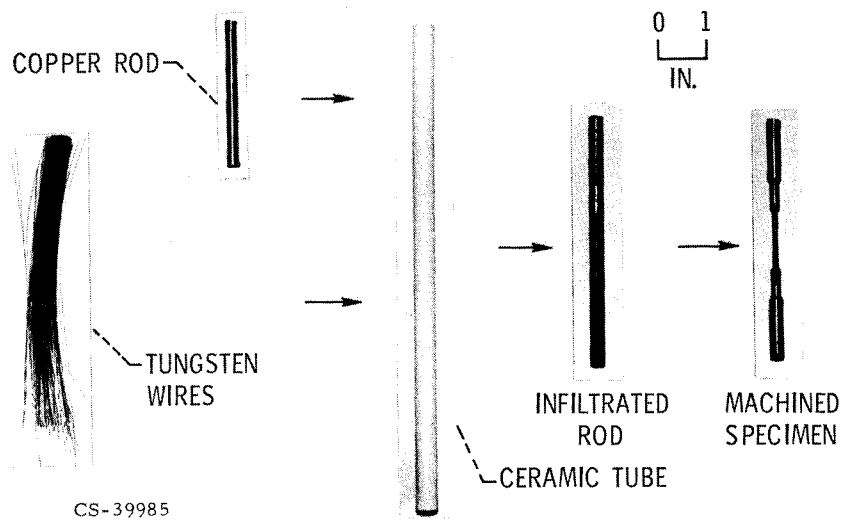


Figure 12-4. - Specimen fabrication - tungsten-fiber-reinforced copper composites.

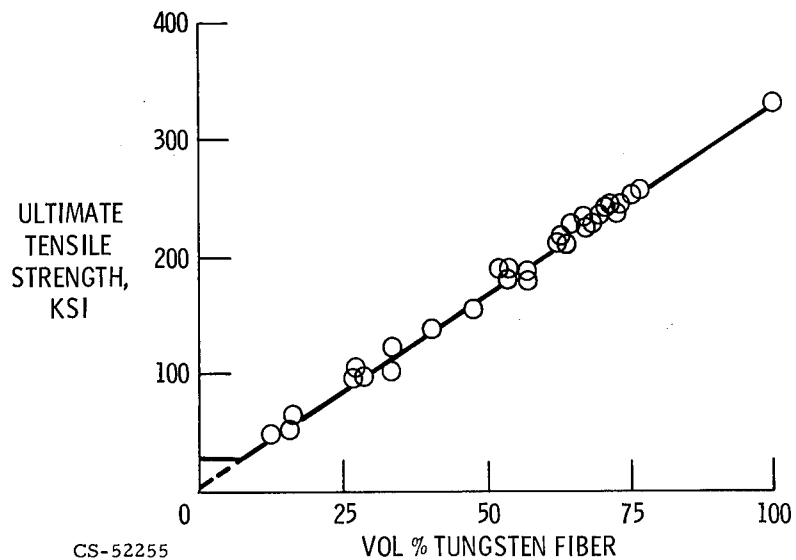


Figure 12-5. - Tensile strength as function of fiber content for continuous tungsten fibers in copper. Fiber diameter, 5 mils.

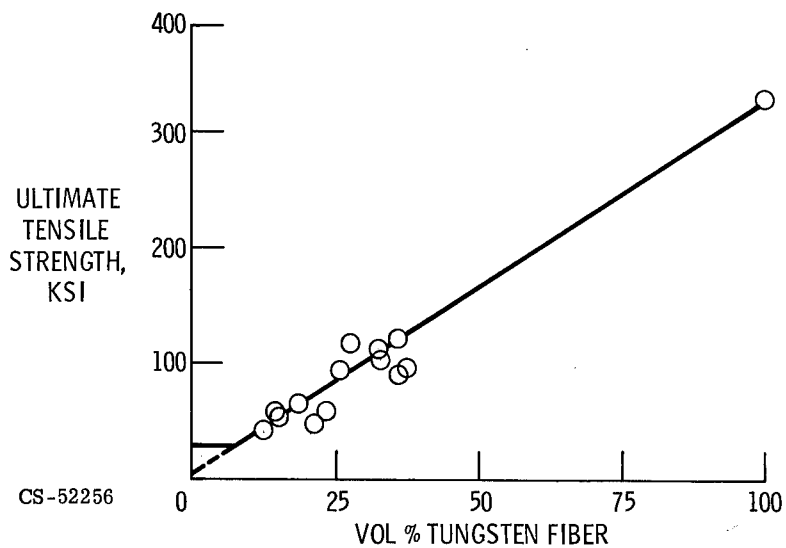


Figure 12-6. - Tensile strength as function of fiber content for discontinuous tungsten fibers in copper. Fiber diameter, 5 mils.

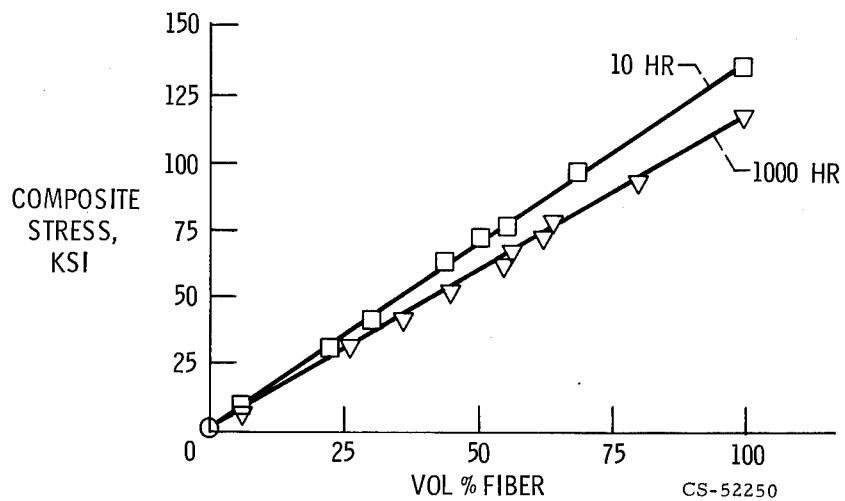


Figure 12-7. - Stress-rupture properties of tungsten-fiber-reinforced copper composites. Temperature, 1500° F.

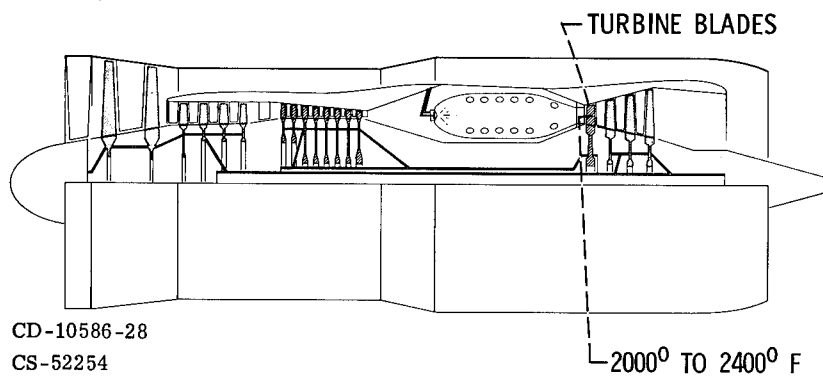


Figure 12-8. - Jet engine.

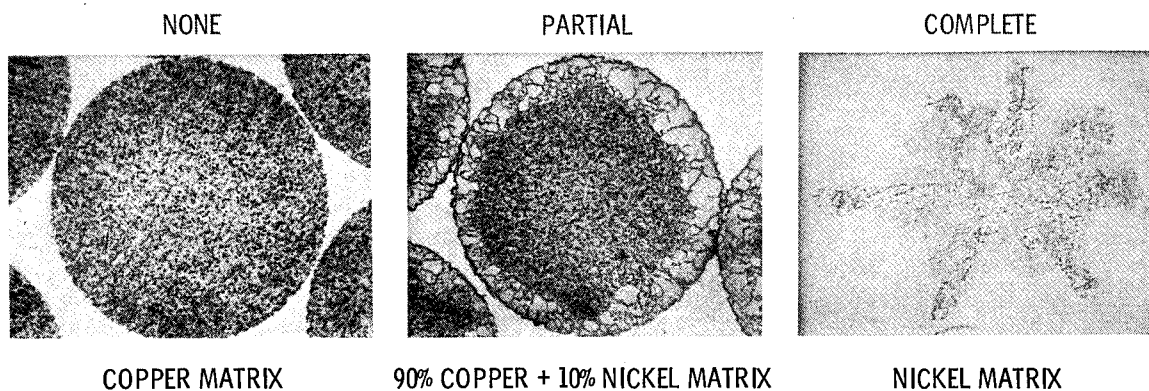


Figure 12-9. - Reaction in composite materials.

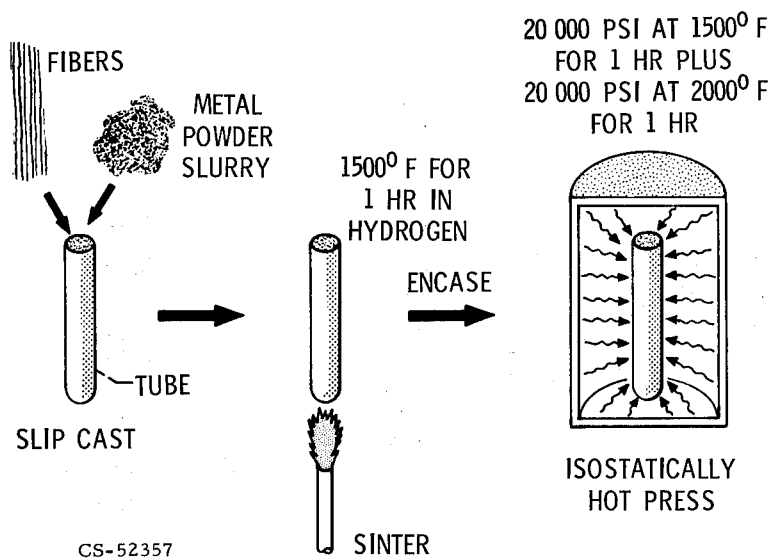
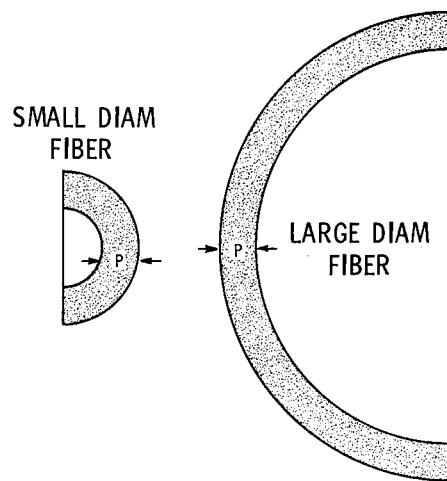


Figure 12-10. - Composite billet fabrication.



CS-44217

Figure 12-11. - Effect of increased diameter on retained fiber strength.

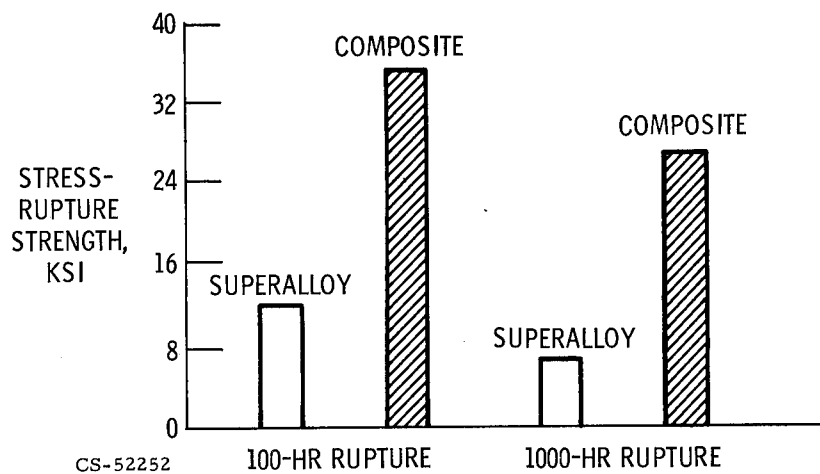


Figure 12-12. - Strength of superalloy composite, 70-volume-percent 218 tungsten wire in nickel superalloy. Temperature, 2000° F.

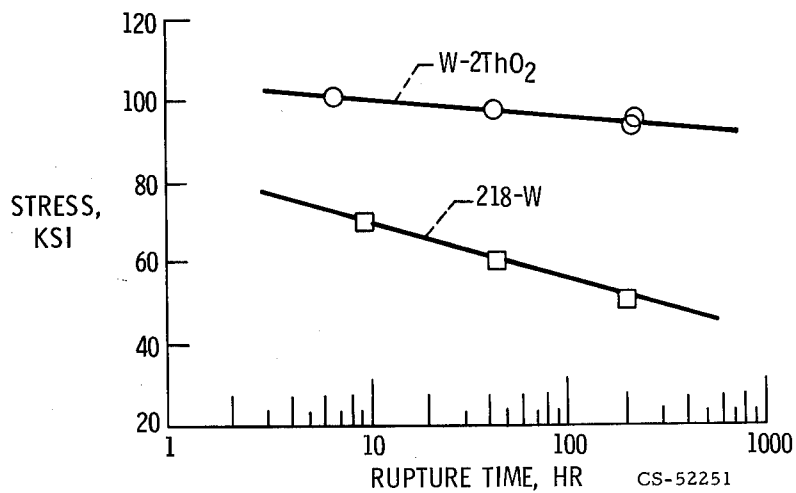


Figure 12-13. - Stress-rupture strength of wire. Wire diameter, 0.015 inch; temperature, 2000° F.

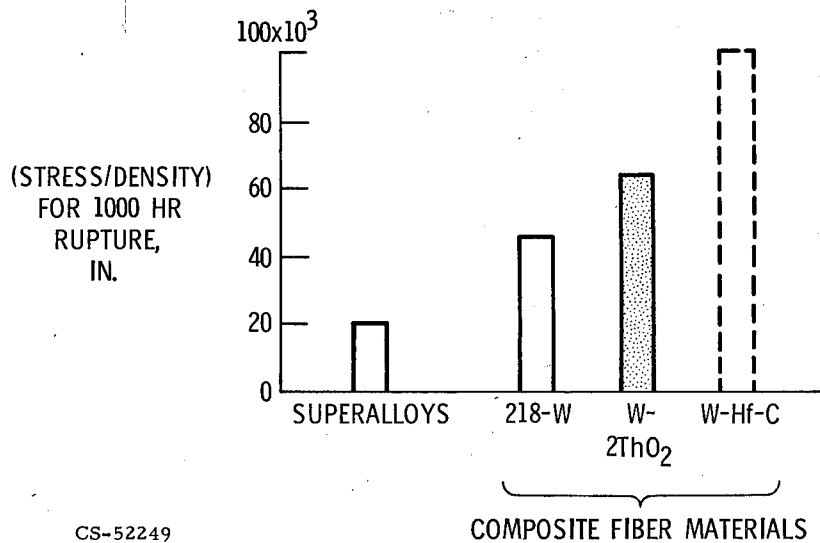


Figure 12-14. - Stress-rupture strength of superalloy composites. Fiber content, 70 volume percent; temperature, 2000° F.

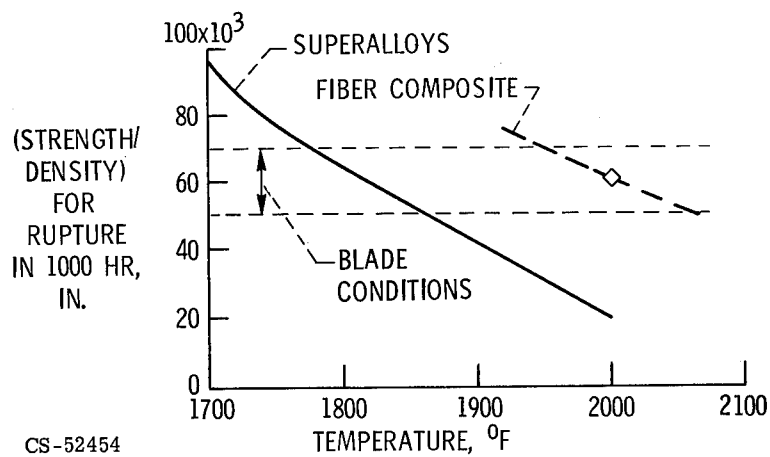


Figure 12-15. - Turbine blade use-temperatures.

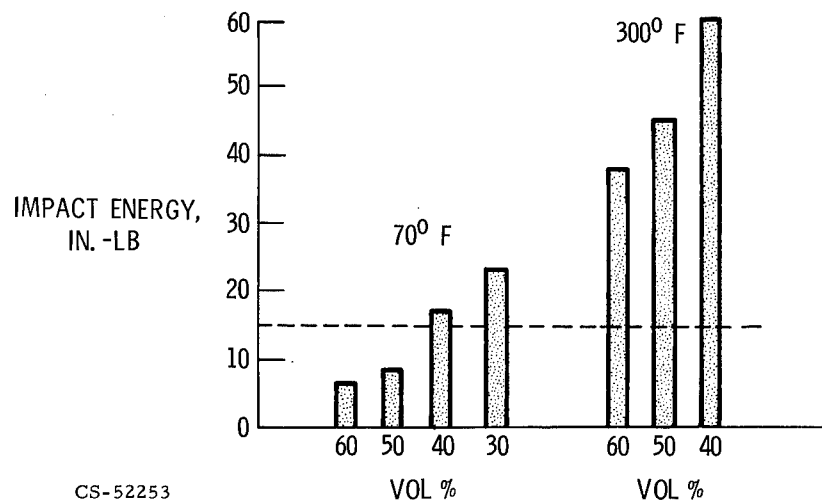


Figure 12-16. - Impact strength of superalloy composite. Miniature specimen Izod pendulum test.

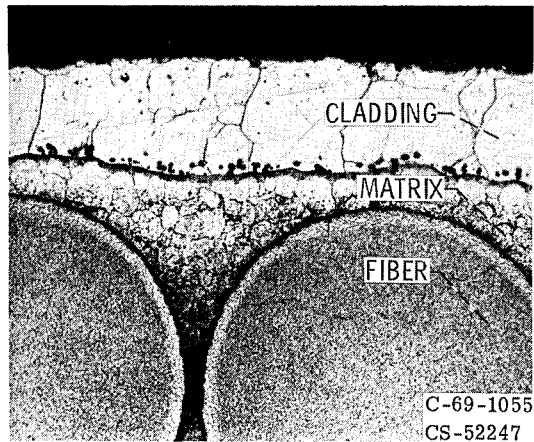


Figure 12-17. - Oxidation resistance of superalloy composites after 50 hours in air at 2000° F. X150.

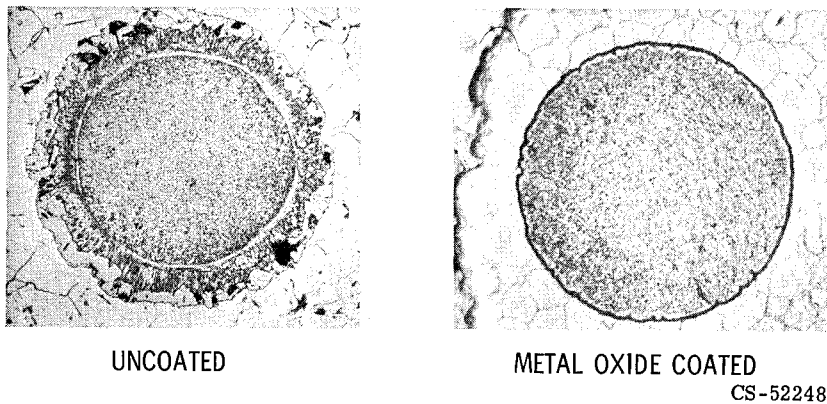


Figure 12-18. - Coating of wire to minimize reaction. Tungsten wire 8 mils in diameter heated at 2200° F for 50 hours in nickel. X250.





### 13. HIGH-TEMPERATURE RESIN-MATRIX COMPOSITES

Tito T. Serafini

A goal of high-temperature-polymer research has been to extend the continuous-use temperature for polymers to at least 600° F. Achievement of this goal has been at the expense of polymer processibility.

Chemical modification and end-capping of polyimide prepolymers are two approaches that are employed to improve the processibility of polyimide polymers for application to components. An amide-modified prepolymer and an ester-modified prepolymer resisted imidization at temperatures to 284° and 250° F, respectively, compared to an unmodified prepolymer which imidized at 230° F. In addition to being more resistive to imidization, it was observed that these modified prepolymers also underwent chain extension without any loss of solubility. The hydrolytic stability of the ester-modified prepolymer was far superior to that of the amide-modified and unmodified prepolymers.

The end-capping approach utilized by TRW, Inc., uses reactive alicyclic rings that are placed on the ends of low-molecular-weight polyimide prepolymers. At elevated temperatures and pressures, the end caps coreact without the release of volatiles. This permits high-quality, void-free composites to be fabricated.

Much of the current interest in fiber-reinforced composites can be attributed to the development of fiber-glass-reinforced plastics during the Second World War. Because fiber glass has a low modulus, fiber-glass-reinforced plastics were primarily used in nonstructural applications. Now that high-performance fibers are currently available, resin-fiber composites are being used as structural materials in a number of aeronautical and aerospace applications.

Some of the current applications are airframes and fan blades, fan duct and vanes, and bearing housings for turbojet engines. Boron-epoxy composites, for example, are being used as airframe structural materials in the F-111 and F-4 aircraft. Graphite-epoxy composites are being used to fabricate a variety of air-breathing engine components. Rolls-Royce is using graphite-epoxy composites to fabricate fan blades, fan duct and vanes, and other components for its RB 211 engine.

All the current applications use epoxy resins as the matrix. Epoxy resins have only limited thermal stability. The continuous-use temperature for epoxies is in the

range of 250° to 300° F. Here at Lewis we are performing research to extend the use of fiber-reinforced plastics into the hotter parts of airbreathing engines by using the so-called high-temperature polymers.

## POLYMER THERMAL STABILITY AND PROCESSIBILITY CONSIDERATIONS

Most organic polymers melt below 400° F or decompose rapidly at temperatures slightly above 400° F. High-temperature polymers are those organic polymers which can withstand continuous exposure in air at temperatures as high as 600° F, and still maintain useful mechanical properties during or after exposure.

The molecular structure of polyethylene is depicted in figure 13-1. Polyethylene, which is composed of simple methylene repeating units, melts in the range of 240° to 275° F. However, its maximum use-temperature is limited to about 150° F.

The key to preparing high-temperature polymers has been to use highly stable structural units in the polymer chain, such as those shown in figure 13-2. The use of aromatic rings and/or heterocyclic rings accounts for the thermo-oxidative stability of high-temperature polymers. These structural units are able to absorb thermal energy and contain a minimum of oxidizable hydrogen atoms. Although these polymers decompose, they decompose at a very slow rate, and they decompose into thermally stable residues which retain structural integrity.

Numerous polymers have been synthesized which are thermally stable at 600° F. Four of the more prominent classes of polymers are polyimides, polyquinoxalines, polybenzothiazoles, and polyimidazopyrrolones. In addition to being noted for their thermal stability, these polymers are all difficult or nearly impossible to process into useful articles. The structural units that are responsible for the thermal stability of those polymers are also responsible for their inherent insolubility and infusibility, commonly referred to as intractability. The most highly developed polymers, and the only ones that have achieved commercial status at this time, are the polyimides. Our in-house and contractually sponsored research efforts are concerned with improving the processibility of polyimide resins. As shown in figure 13-3, aryl polyimides are prepared by reacting on aromatic dianhydride with an aromatic diamine in a suitable solvent. The prepolymer that forms in the first step remains soluble in the solvent. In the second step, water is eliminated, forming the thermally stable imide ring. In this form the polymer is insoluble and infusible. If the second step of the reaction is allowed to proceed in an uncontrolled manner, the polymer is in its intractable condition and cannot be further processed.

Perhaps the significance of the reactions can be more fully appreciated by re-

ferring to a process commonly used to fabricate fiber-reinforced plastics. The process is depicted schematically in figure 13-4. The fiber is drawn through the prepolymer solution, and a monolayer of the fiber is wound onto the takeup drum. The drum is then placed into an oven, and heat is applied to remove most of the solvent. The single layer of impregnated fibers, called the prepreg, is then removed from the drum by slitting the layer longitudinally. This piece of broad goods is then cut into the shapes having the fiber orientation specified by the designer. These layers, or plies, are then placed in a matched metal die and laminated under heat and pressure in a press. The two most critical points in the overall process are the removal of solvent in the oven and the application of heat and pressure in the lamination step. If excessive ring closure occurs when the solvent is removed, the polymer is converted into its infusible form, and the prepreg cannot be further processed.

In the lamination step we want to form the thermally stable ring. However, unless complicated and time-consuming lamination procedures are used, the escaping byproduct, water, and some residual solvent may be trapped, causing voids to form. The presence of these voids seriously degrades both the composite mechanical properties and the thermo-oxidative resistance.

## CHEMICAL MODIFICATION OF PREPOLYMER

Here at Lewis we are currently using the approach of chemically modifying the structure of the prepolymer as a means of controlling the ring-forming reaction (ref. 1). As shown in figure 13-5, our approach was to replace the free hydroxyl groups with other organic groups, depicted by R. The alkoxy and alkyl amino groups were employed to prepare what we call ester-blocked and amide-blocked prepolymers, respectively. These chemically modified prepolymers were found to be more resistant to ring closure than unmodified prepolymers.

The imidization temperatures for three different prepolymers are listed in table 13-I. The prepolymers had been isolated as solids, and their resistance to imidization was studied by using the technique of solid-phase polymerization. The formation of imide rings was monitored by infrared spectroscopy and by observing a decrease in prepolymer solubility. The imidization temperatures listed in the table are those temperatures at which sufficient imidization had occurred to render the prepolymer partially insoluble. The amic, or unmodified, prepolymer had an imidization temperature of 230° F. In contrast, both the ester- and amide-modified prepolymers were more resistant to thermal imidization. The ester- and amide-modified prepolymers had imidization temperatures that were 20 F° and

54 F<sup>0</sup> higher, respectively. These results indicate that by using this approach it should be possible to prevent ring closure during the initial drying of the prepreg.

An unexpected but significant finding, we believe, was that the molecular weight of the modified prepolymers could be increased by using the technique of solid-phase polymerization (table 13-I). The molecular weight of the ester-modified prepolymer experienced a 50-percent increase, and the amide-modified prepolymer underwent approximately a 200-percent increase.

It is well known that, as the molecular weight of a polymer increases, the mechanical properties of the polymer increase. One way to increase the transverse properties of a resin-fiber composite would be to increase the matrix properties. The implication of our results is that it may be possible to improve composite transverse properties by subjecting a prepreg made with a modified prepolymer to a type of solid-phase polymerization.

The variation of prepolymer molecular weight with reaction temperature for the two modified prepolymers is shown in figure 13-6. The molecular weight of the ester-modified prepolymer displayed a gradual increase to 28 000. The molecular weight of the amide-blocked prepolymer leveled off at about 47 000.

Another problem that fabricators encounter using polyimide prepolymer solutions is related to the sensitivity of the prepolymer to hydrolytic degradation. Unless the solutions are stored at approximately 0<sup>0</sup> F and moisture is excluded, the molecular weight of the prepolymer gradually decreases. The hydrolytic stability of the same three prepolymers used in the thermal imidization studies is compared in figure 13-7. There is no great contrast between the hydrolytic stability of the unmodified and amide-modified prepolymers. The amide-modified material was more stable for the first few hours and degraded at a slower rate. The ester-modified prepolymer was completely stable to hydrolysis for over 500 hours.

All the previous results together with ease of prepolymer synthesis need to be considered in selecting the best chemical modification approach. Our current assessment is that the ester-blocked prepolymer represents the best compromise.

## USE OF REACTIVE END-CAPS

In work done under NASA contract NAS 3-7949, TRW, Inc., has discovered a novel polymerization reaction that utilizes reactive alicyclic rings positioned on the ends of low-molecular-weight prepolymers. The end-capped and completely imidized prepolymer is shown schematically in figure 13-8. At 600<sup>0</sup> F and at pressures in the range of 100 to 500 psi, the end-caps coreact, causing chain extension and

cross linking. This final cure occurs with minimal evolution of volatiles and results in nearly void-free composites.

A commercial version of the resin, called P13N, is currently available from TRW. A new resin currently being developed by TRW for NASA that has even greater thermal oxidative stability than P13N will be announced shortly.

In some of our other in-house work, we are currently investigating the use of our approach together with the TRW end-capping approach. The blocked and capped prepolymer should be more resistive to hydrolytic degradation. Chemically modifying the capped prepolymer should also provide a method to control the degree of ring closure of the end-capped prepolymer.

## CONCLUDING REMARKS

During the past decade, scores of high-temperature polymers were synthesized without too much concern for their processibility. The major portion of current research is directed toward improving the processibility of two or three of these polymers. As new polymerization and processing techniques are developed, the true potential of advanced high-temperature resin-fiber composites will be realized.

## REFERENCE

1. Delvigs, Peter; Hsu, Li-Chen; and Serafini, Tito T.: The Synthesis of a Novel Polyimide Precursor. NASA TN D-5184, 1969.

TABLE 13-I. - SOLID-PHASE POLYMERIZATION  
OF POLYIMIDE PREPOLYMERS

Prepolymer	Imidization temperature, °F	Molecular weight	
		Initial	Final
Amic	230	15 000	15 000
Ester	250	19 000	28 000
Amide	284	17 000	48 000

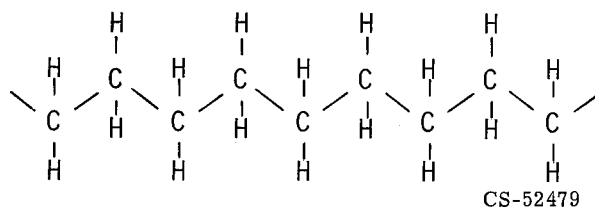
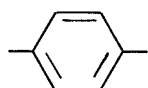
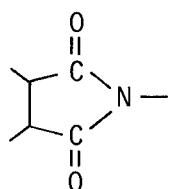


Figure 13-1. - Molecular structure of polyethylene. Repeat unit,  $\text{—CH}_2\text{—}$ ; melting temperature range of polyethylene,  $240^\circ$  to  $275^\circ$  F.



AROMATIC RING



HETEROCYCLIC RING

CS-52480

Figure 13-2. - Thermally stable structural units.

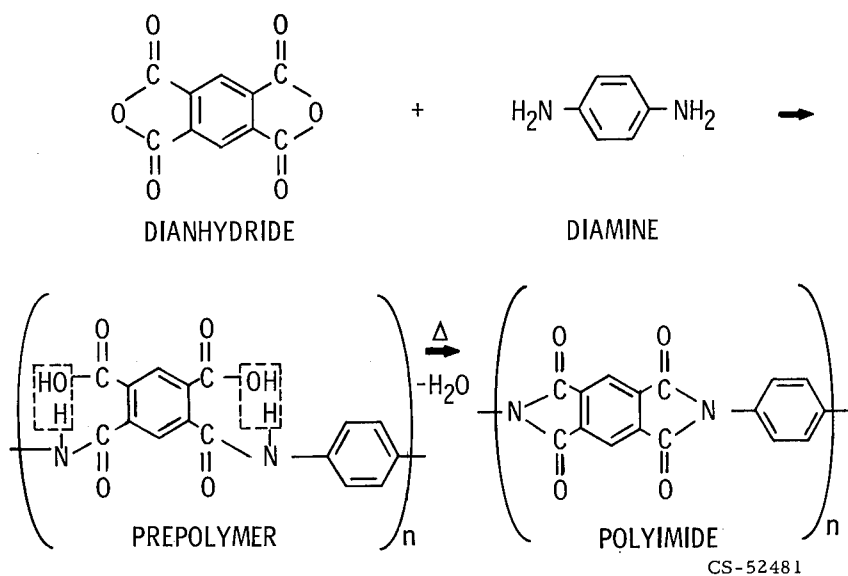


Figure 13-3. - Synthesis of polyimides.

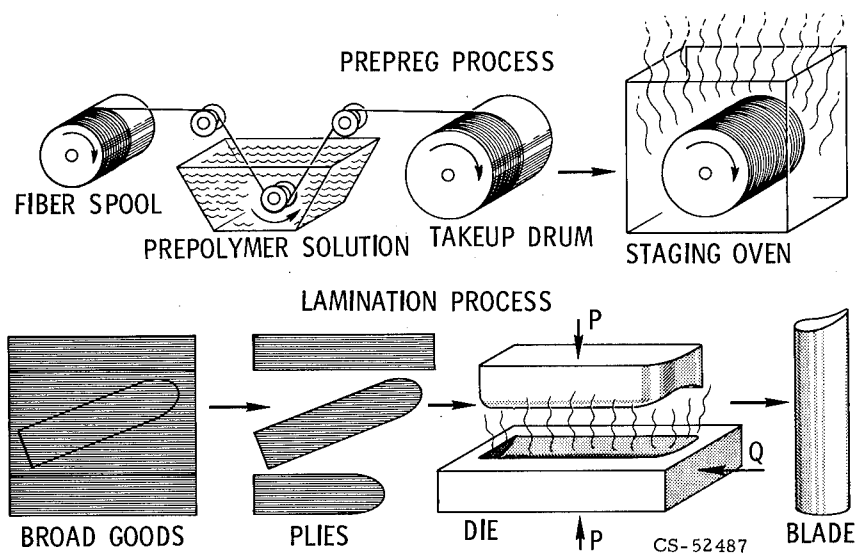
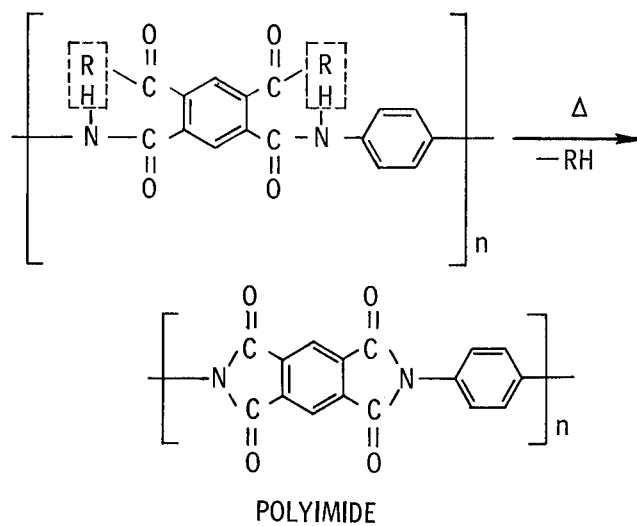


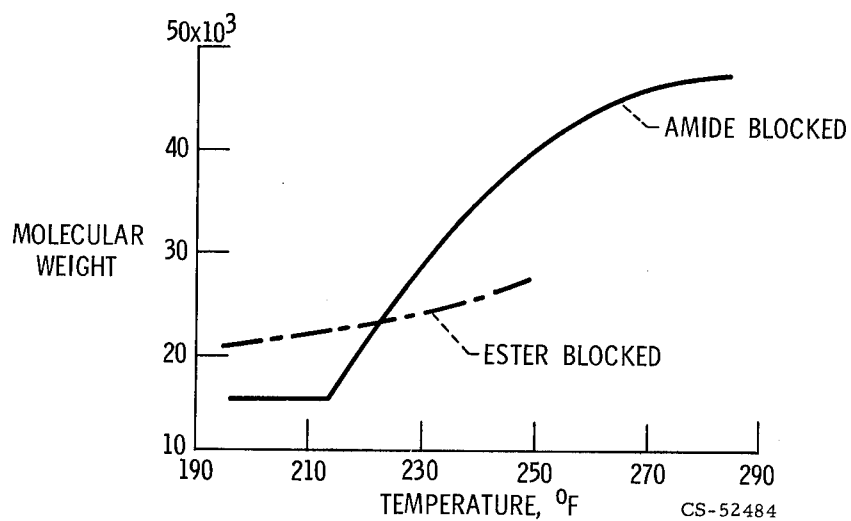
Figure 13-4. - Fabrication of fiber-reinforced plastic composites.





CS-52483

Figure 13-5. - Chemical modification of prepolymer.



CS-52484

Figure 13-6. - Solid-phase polymerization of blocked-polyimide prepolymers.  
Helium atmosphere for 24 hours.

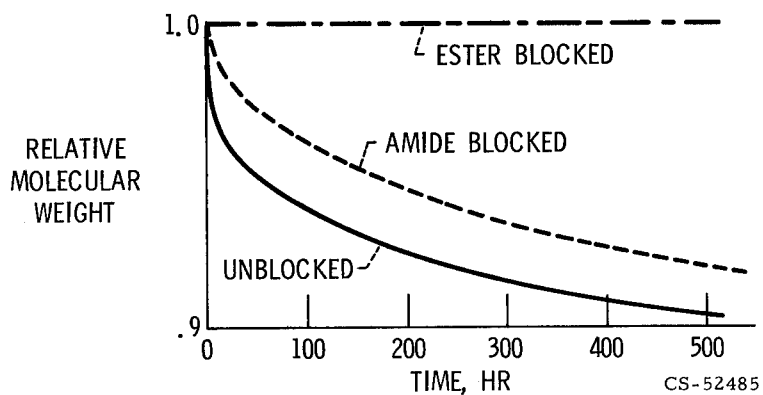


Figure 13-7. - Hydrolytic stability of polyimide prepolymers.  
Aqueous dimethylacetamide at 78° F.

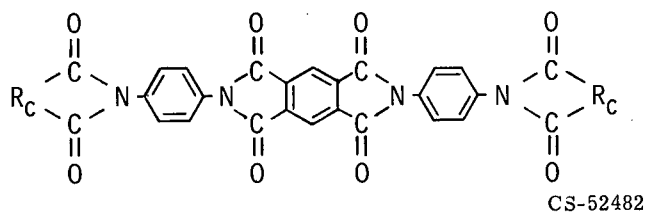


Figure 13-8. - TRW approach to preparing polyimide resins.



## 14. DESIGN AND ANALYSIS OF FIBER COMPOSITE STRUCTURAL COMPONENTS

Christos C. Chamis

Analysis, design, and optimization of structural components made from fiber composites require knowledge of many composite material properties as well as mathematical formalisms which relate the structural response of the component to appropriate properties of its constituents. Selection of the proper combination of constituent materials (fiber and matrix) fiber content, fiber directions, and component thickness to meet certain design requirements leads to the optimum design of the particular structural component. This paper briefly describes our current work in the areas of analysis, design, and optimization with metallic and nonmetallic fiber composites. An example to illustrate the genesis of the mathematical formalisms in relating metallic-composite strength to its constituent materials is described in some detail. The optimization problem of a composite engine blade is defined, and the residual stress in particular composite components is described.

### COMPOSITE SCHEMATIC AND AREAS OF RESEARCH EFFORT

To establish a common reference and to introduce some of the technical jargon pertinent to our subsequent discussion a schematic of a typical composite is shown in figure 14-1. The composite in this figure is made up of several plies (layers) (see fig. 14-2). These plies consist of parallel fibers embedded in a matrix. The plies, then, are stacked in a specified sequence to meet design strength and stiffness requirements. For example, the stacking sequence of the composite in figure 14-1 consists of four plies arranged at  $0^\circ$ ,  $+\theta^\circ$ ,  $-\theta^\circ$ ,  $90^\circ$ , respectively, from the X-axis.

The ply is the basic unit in constructing composites and, in turn, the ply itself consists of fibers embedded in a matrix. It is possible, therefore, to relate composite design properties to corresponding constituent properties. Thereby, we can design fiber-composite structured components when we know the design requirements and the properties of the candidate constituent materials.

Two objectives emerge from our discussion thus far:

(1) Given a fiber composite and its corresponding load system, analyze the composite with respect to its strength and stiffness sufficiency.

(2) Given a set of design requirements and possible candidate constituent materials, design the most efficient fiber composite.

These objectives in our specific areas of interest may be outlined as follows:

(1) Structural mechanics

(a) Predict composite properties

(b) Devise theories for structural and stress analyses

(c) Develop computer programs for (a) and (b)

(d) Analysis of existing test methods and design of new ones

(2) Generation of composite design data

(3) Generation of mathematical formalisms and computer programs for optimum design of compressor and turbine blades

In the area of structural mechanics our work is concerned with the development of analytical tools: to predict the structural behavior of fiber composites from constituent properties, fiber direction, and fabrication process considerations; to carry out the necessary structural and stress analyses; and to develop the appropriate computer programs. The importance of comparing our theoretically predicted results with experimental data leads us to the analysis of existing experimental test methods and the design of new ones as the need arises.

The generation of composite design data is important in several respects. For example, available design data are used in preliminary designs and trade-off studies. As another example appropriate design data can serve as an invaluable tool in identifying problem areas in design and testing. Some specific problem areas that come to mind in this respect are load transfer, edge effects, discontinuities, fiber misalignment, and strain magnification.

Our work in the optimum design of compressor and turbine blades deals primarily with the application of advanced nonmetallic composites to compressor blades and with exploratory studies to use refractory-wire reinforced superalloys in the hot part of the engine.

To obtain a better appreciation of the behavior of these materials under load and what is involved in predicting this behavior, we discuss three examples which illustrate our current work in some depth. The first of these examples deals with the strength prediction of the single ply when subjected to simple and complex loadings. The second defines the composite engine blade optimization problem. And the third example examines the residual stress state in two specific composites.

## SIMPLE AND COMBINED STRENGTH OF THE SINGLE PLY

Closer examination of the ply in figure 14-2 shows that the ply has two principal directions: longitudinal and transverse. It is possible to load the ply by tensile or compressive loads in both the longitudinal and the transverse directions. Or we can load the ply with in-plane shear. Furthermore, the longitudinal load is carried primarily by the fibers, whereas the transverse and shear loads are resisted primarily by the matrix. We conclude, therefore, that five strengths are needed to characterize the ply from the simple strength viewpoint. These strengths are longitudinal tensile, longitudinal compressive, transverse tensile, transverse compressive, and in-plane shear.

The physical variables that influence the ply simple strengths are

- (1) Volume ratio, size, number, and distribution of fibers and voids
- (2) Volume ratio of matrix
- (3) Elastic, thermal, and strength properties of fibers and matrix
- (4) Ply fabrication process variables
- (5) Ply stress state due to applied load.

The group of physical variables (1) to (3) and (5) are directly identified. On the other hand, the group of ply fabrication process variables includes variables such as temperature and pressure at cure, curing cycle time, matrix fiber interaction, and several others. As can be seen the strength of the ply depends on numerous variables. Note, also, that the ply strength depends on the stress state due to the applied load. This is a distinct characteristics of composite materials as compared with conventional structural materials.

Identifying the physical variables which influence the ply simple strength help us construct a suitable mathematical model for predicting the strength. This model may be stated as

$$S_l = F[(k, d, N, A)_{f, v}, k_m, (E, \nu, G, S, \epsilon_p)_{f, m}, S_B, \sigma_R, \sigma_A] \quad (1)$$

where  $S$  is strength,  $(k, d, N, A)$  denote volume ratio, size, number, and distribution, respectively; the subscripts  $l$ ,  $f$ ,  $v$ , and  $m$  stand for ply, fiber, void, and matrix property, respectively;  $(E, \nu, G)$  are the elastic constants (normal modulus, Poisson's ratio, and shear modulus, respectively);  $\epsilon$  and  $\sigma$  denote strain and stress; and the subscripts  $p$ ,  $B$ ,  $R$ , and  $A$  stand for limiting value, bonding, residual, and applied load, respectively.

The first group of physical variables are identified by the first group of symbols in equation (1). The second physical variable is represented by  $k_m$ . All the physical variables of group (3), except the thermal variables, are accounted for by

$(E, \nu, G, S, \text{ and } \epsilon)_{f, m}$ . The fabrication process variables and the thermal variables are grouped in  $S_B$  and  $\sigma_R$ , respectively. The stress state due to the applied load is represented by  $\sigma_A$ . In this way, we have defined the influence of all the physical variables that we are able to identify in a function form. What remains now is to evaluate the function defined in equation (1).

We can relate  $S_R$  explicitly to variables  $(K, d, N, A)_{f, v, k_m}, (E, \nu, G, S, \epsilon_p)_{f, m}$ , and  $\sigma_A$  by making some reasonable assumptions and devising representative mathematical models. However, it is more difficult to relate  $S_l$  to  $S_B$  and  $\sigma_R$  explicitly. One ingenious simple way to bypass this difficulty is to relate  $S_l$  to all variables in the function of equation (1) except  $S_B$  and  $\sigma_R$ . Next, free parameters are introduced in those points in the mathematical derivations where the influence of  $S_B$  and  $\sigma_R$  are most likely to occur. We can think of these free parameters as empirical factors which account for the effects of  $S_B$  and  $\sigma_R$ . Subsequently, these empirical factors are selected so that theoretical predictions and experimental data correlate for that particular fabrication process. Thus, a semiempirical theory can be constructed which is sufficiently general in fiber and matrix types and combinations, but restricted to a particular fabrication process.

The results of such a theory for boron-aluminum composites fabricated by the hot-pressure bonding method are illustrated in figure 14-3. In this figure ply strength is plotted against fiber content in the range 0.4 to 0.75 for zero voids. The type of loading is illustrated by the diagrams, and the leaders point to the corresponding curve. Note that the curve for the longitudinal-compressive strength has a discontinuity. This is so because two different mathematical models are used to predict the longitudinal compressive strength and each model predicts lower strengths in certain fiber content ranges. There are two interesting points in figure 14-3, namely, (1) the longitudinal strengths are about 10 times greater in magnitude than those for transverse and shear, and (2) the transverse and shear strengths are relatively invariant with fiber content in the range shown. In contrast, these strengths are rapidly decreasing functions of fiber content for many fiber nonmetallic-matrix composites.

Analogous strength results for plies with 5 percent void content are shown in figure 14-4. Comparison of corresponding curves in figures 14-3 and 14-4 shows a 20-percent drop in the longitudinal compressive strength and about a 30-percent drop in the transverse and shear for the plies with the 5-percent void content. The important point here is that the presence of voids (porosity) in metallic-matrix composites is detrimental to their strength.

Thus far this discussion has been limited to plies under simple loading. But the ply is a member in a composite (fig. 14-1). So even a simple load on the composite will produce a complex stress state in the ply. In this case the strength suf-

efficiency of the ply is predicted by the so-called combined-stress strength criterion. For a specific boron-aluminum composite the envelope generated by one such a criterion is illustrated in figure 14-5.

Here the ply failure envelope of a boron-aluminum composite is at 50-percent fiber content, zero voids, and no shear. This envelope separates the safe and the unsafe regions. The transverse strength is plotted against longitudinal strength. And the transverse strength scale is 1/10 that of the longitudinal. Note also, that the envelope consists of four quadrants. Each quadrant is associated with a unique class of stress state as noted by the diagrams. The arrows on these diagrams are drawn proportional to some scale to the actual magnitude for the specific point on the envelope indicated by the leader. The envelope intercepts correspond to strength values in figure 14-3 at 50-percent fiber content. The addition of shear stress will be represented by contours which tend to shrink the envelope towards the origin. Obviously analogous plots can be made for plies of other fiber contents or fiber-void combinations. Thus, we can characterize the ply strength starting from constituent properties.

Analogous theories can be developed to predict the thermal and elastic properties of plies from constituent material properties and fabrication process considerations. These factors have been incorporated in a computer program which has been applied extensively and quite successfully in our work with nonmetallic composites. This computer program is an important part of our studies for the optimum design of compressor blades made from advanced nonmetallic composites.

Presently, the computer program is being modified and expanded to predict elastic, thermal, and strength properties of the refractory-wire reinforced superalloy composites. This is in connection with our exploratory studies in using superalloy composites for turbine blades. This leads us to the second example of our current work, that is, definition of the turbine blade optimization problem.

## DEFINITION OF THE TURBINE BLADE OPTIMIZATION PROBLEM

The physical parameters entering the turbine blade optimization problem are illustrated in figure 14-6. In this figure we see the blade topology (blade geometric configuration); the various load conditions to which the blade is subjected; the constraints (limiting conditions), which the blade must meet if it is to perform safely and efficiently; the design variables, those quantities we can manipulate; and our design goal, which is a minimum-weight blade.

Again, we need to convert the physical description of the optimization problem (fig. 14-6) into a corresponding mathematical model. This is done as follows:



Given

$$\begin{aligned} & \left[ a_i, i = 1(1)N_{PP} \right], \quad \left[ P_i, i = 1(1)N_{LC} \right], \quad \left[ D_i, i = 1(1)N_{DV} \right], \\ & \left[ B_i, i = 1(1)N_{BV} \right], \quad \left[ G_i, i = 1(1)N_C \right], \quad W \end{aligned}$$

a set of rules

$$B_i = B_i(\vec{D})$$

$$G_i = G_i(\vec{D})$$

$$W = W(\vec{D})$$

and efficient optimization algorithms, find  $\vec{D}^*$

$$\ni W(\vec{D}^*) \rightarrow \text{Minimum}$$

and

$$\ni G_i(\vec{D}^*) \geq 0$$

Here, we have replaced the blade topology and other preassigned parameters with the symbol  $a$ . The load conditions are represented by  $P$ . The design variables are represented by  $D$ , the constraints by  $G$ , and the objective function (design goal) by  $W$ . The symbol  $B$  denotes the behavior variables, that is, those variables which measure the structural response of the blade in its load environment. Stresses, strains, displacements, temperature distribution through the blade, and the various frequencies constitute the behavior variables. The set of rules simply means mathematical formalisms or equations. The arrow ( $\rightarrow$ ) over the letter  $D$  indicates that  $D$  is a vector containing ( $N_{DV}$ ) elements. Efficient optimization algorithms are computational procedures (recipes) which carry out the optimization process efficiently. The symbol  $\ni$  means "such that." According to these equations, we can state the turbine blade optimization problem having given the

- (1) blade topology
- (2) load conditions
- (3) design variables
- (4) behavior variables

- (5) constraints
- (6) objective function
- (7) appropriate mathematical relations
- (8) efficient computational procedures.

We can then find that combination of design variables such that the objective function has its minimum value and such that none of the constraints is violated.

With respect to our turbine blade exploratory studies, we are now in the process of establishing the required set of rules (e.g., relate  $\bar{B}$  to  $\bar{D}$ , etc.) and are considering selection of optimization algorithms.

In addition to designing fiber composites to perform satisfactorily under applied load, the designer has to ascertain the composite's strength sufficiency with respect to residual stresses which results from the fabrication process. This leads us to the third example of our current work, that is, examination of the residual stress state in two specific composites.

## RESIDUAL STRESSES

There are two types of composite residual stresses, namely, micro- and macroresidual stresses (refer to fig. 14-1).

(1) Microresidual stresses are present in the constituents within the ply. They arise primarily from the differences in the thermal coefficients of expansion between fiber and matrix. In a semiempirical theory these are accounted for by the correlation factors. Polymerization shrinkage stresses are also accounted for by the correlation factors.

(2) Macroresidual stresses are approximately constant throughout the ply. They arise from the differences in the longitudinal and transverse thermal coefficients of expansion of the ply. The macroresidual stresses can be predicted from laminate analysis. Table 14-I illustrates the analysis results of two proposed compressor-blade design configurations made from a high-temperature polymer matrix material. The type of fiber and fiber content are noted in the table. The first configuration in table 14-I was proposed for its high torsional stiffness. If a blade from this configuration is fabricated, the plies in the blade will have through cracks after cure. An analysis of the macroresidual stress state shows why the plies will crack. As can be seen from the table the ply-transverse residual stresses exceed the ply-transverse strength. The second configuration will not crack after fabrication. In this configuration, the ply transverse residual stresses do not exceed the corresponding ply strength. However, the margin of safety is very small. In addition, the second blade configuration results in lower torsional stiffness as

compared with the first. This leads us to the conclusion that the blade has to be optimized with respect to both applied load and residual stress. One important factor to be kept in mind about residual stresses is that they are a function of temperature. Their effects diminish with increases in compressor operating temperature up to the blade cure temperature.

### CONCLUDING REMARKS

1. A computer program has been developed for the analysis of multilayered fiber composites. This program is essentially the state of the art of the field. Input data are available to analyze practically all of the available nonmetallic composites and some metallic composites. The input data library will be updated as new composite systems become available.

2. The optimization problem of engine blades has been formulated and results are expected in the near future.

3. The computer program determines the macroresidual stresses in composites as a byproduct.

TABLE 14-I. - ANALYSIS OF PROPOSED BLADES

[Ply transverse strength, 8000 psi; graphite-polyimide composite, fiber content, 0.50; curing temperature, 600° F.]

Blade	Number of plies, percent	Angle, deg	Ply transverse residual stress, psi	Blade torsional stiffness, lb-in./in.
I	32	±45	10 400	9500
	16	±22.5	9 600	
	52	0	9 300	
II	32	±30	6 600	7100
	16	±15	5 600	
	52	0	5 300	

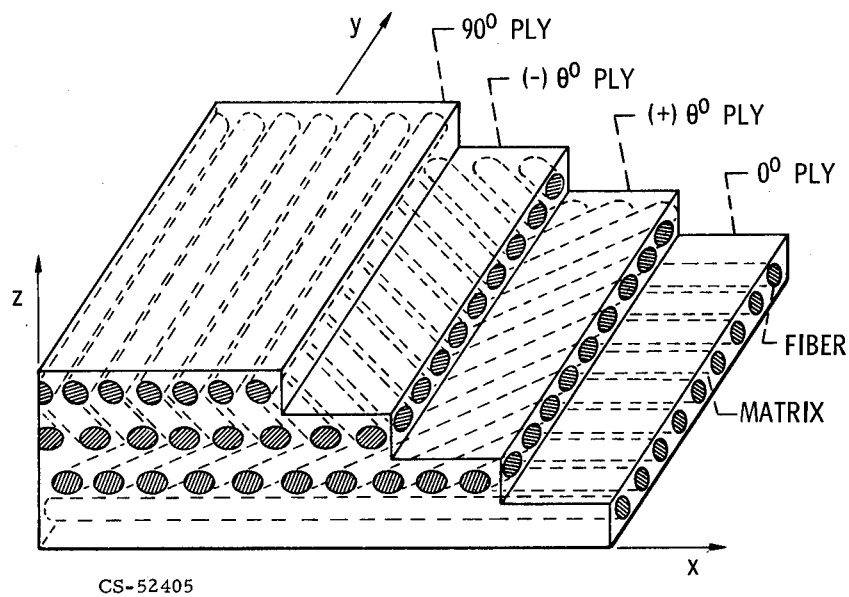


Figure 14-1. - Fiber composite.

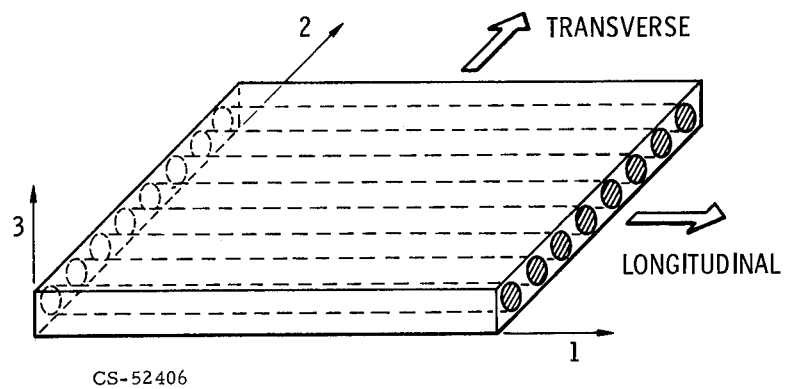


Figure 14-2. - Single ply.

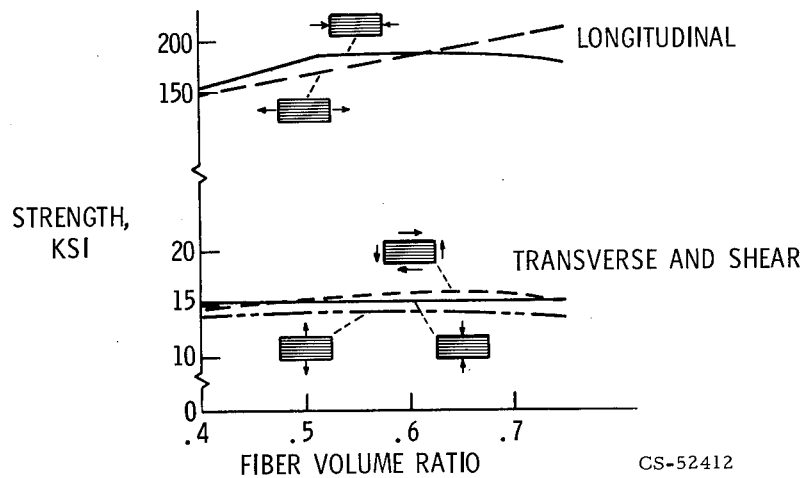


Figure 14-3. - Boron-aluminum ply strengths. Fiber content, 50 percent, and zero voids.

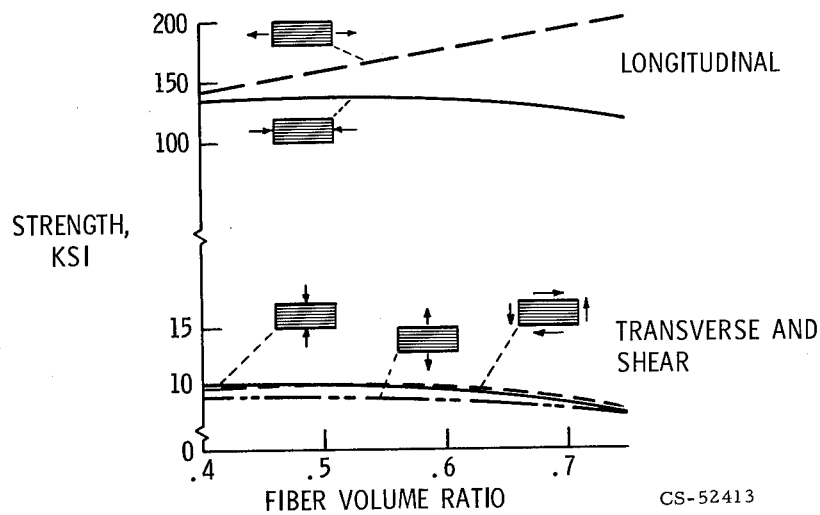


Figure 14-4. - Boron-aluminum ply strengths. Fiber content, 50 percent; 5 percent voids by volume.

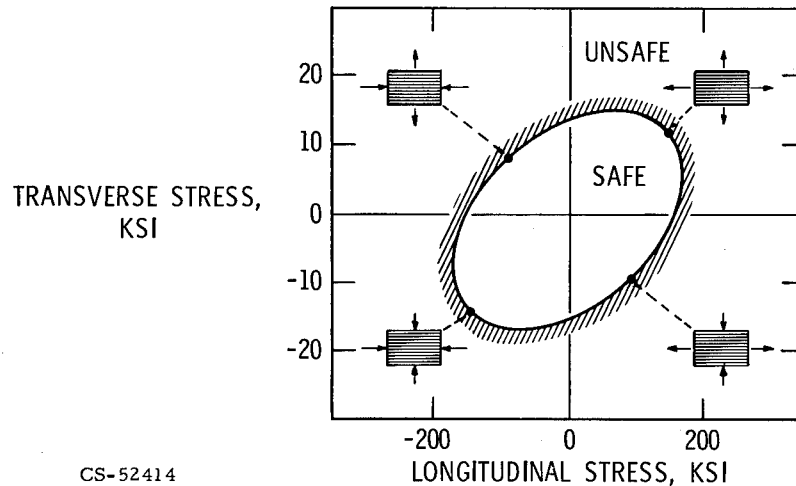
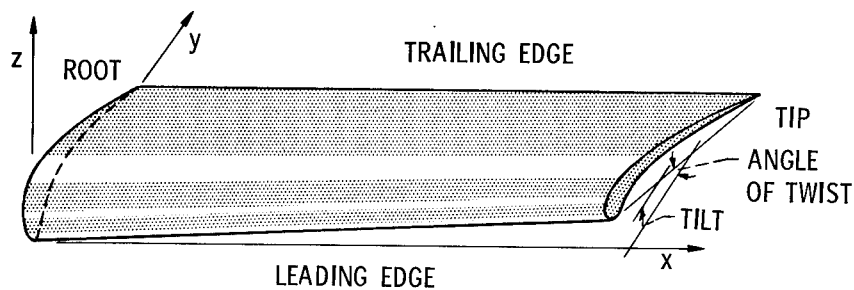


Figure 14-5. - Ply failure envelope. Boron-aluminum composite; fiber content, 50 percent, and zero voids.



BLADE TOPOLOGY		
LOADS	CONSTRAINTS	DESIGN VARIABLES
CENTRIFUGAL	MATERIAL STRENGTH	FIBER AND MATRIX TYPES
GAS PRESSURE	RESONANT FREQUENCIES	FIBER CONTENT
DYNAMIC	UNTWIST AND TIP DE-	NO. OF PLYS
ENVIRONMENTAL	FLECTIONS	PLY ORIENTATIONS
	FLUTTER SPEED	
DESIGN GOAL: MINIMUM BLADE WEIGHT		

CS-52404

Figure 14-6. - Definition of turbine blade optimization problem.

## 15. RADIATION-INDUCED PREPARATION OF PURE METALS FROM SOLUTION

Warren H. Philipp and Robert A. Lad

A new method has been developed at Lewis for the preparation of pure metals and compounds. It involves the bombardment of metal salt solutions with high-energy electrons (0.5 to 2 MeV). This bombardment promotes chemical reactions which cause the precipitation of the desired metal or compounds.

Ten metals have been prepared from aqueous solutions by this method: They are cobalt, nickel, copper, zinc, palladium, cadmium, tin, antimony, thallium, and lead. The yields range from 3.5 to 126 grams per kilowatt hour of beam power. Furthermore, preferential deposition is easily accomplished by proper selection of conditions. For example, 99.998 percent copper was prepared from an acidic equimolar solution of copper and nickel salts.

Also studied were the applications of this method to the production of mirrors, coatings, catalysts, radiographs, and anhydrous compounds.

Many of the papers at this conference are examples of the response to technology's demand for new materials such as superalloys and plastics. Development of these new materials has also created a demand for high-purity metals and compounds. Most of the research for producing these high-purity materials has been centered on the refinement of established procedures. Procedures of this kind are being used at Lewis to prepare high-purity refractory nitrides. In addition, we have developed a new approach to the preparation of pure metals and compounds (refs. 1 and 2).

This new method involves the bombardment of solutions of metal salts with high-energy electrons in the range of 0.5 to 2 MeV. The electron bombardment promotes chemical reactions which result in the deposition of metals or compounds. The solvent for the metal salts can be either water or an organic liquid. Most of our work to date has been with aqueous systems, and therefore the major part of this discussion is about these experiments.

No attempt has been made as yet to optimize the method in terms of cost or convenience. Our main concern has been to understand the process and to explore some of its applications.



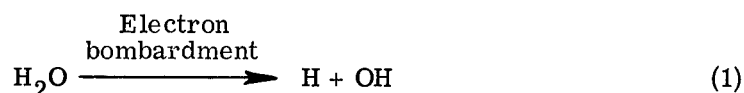
## PROCEDURE

Figure 15-1 illustrates the experimental equipment. The glass vessel shown has a titanium foil window on top. The foil is 50 micrometers thick. The solution can be cooled by immersion of the vessel in a refrigerated bath.

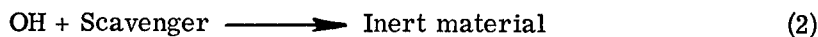
The solution is stirred by the bubbling of helium; the gas is introduced through a glass frit at the bottom and removed through a gas outlet, as shown. Stirring is necessary because the electrons penetrate only a short distance. The 2-MeV electrons from our Dynamitron (linear) accelerator penetrate to a depth of 1 centimeter. The beam is 4 centimeters in diameter. Thus, the reaction takes place in the zone indicated in figure 15-1. The reaction product forms in this zone and settles to the bottom of the vessel. New material is continually brought to the reaction zone by the stirring.

## MECHANISM

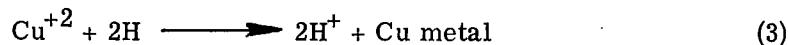
The reaction that is basic to the process is the reduction of a metal ion by a hydrogen atom. The following reaction shows how the hydrogen atoms (H) are generated:



When a water molecule is struck by an energetic electron, the water is dissociated to hydrogen atoms and hydroxyl (OH) radicals. The hydrogen atom is a reducing agent, while the OH radical is an oxidizing agent. Because the two species are formed in equal quantities, pure water bombarded in this way is neither oxidizing nor reducing. However, an excess of hydrogen atoms can be created by removing the OH radicals as fast as they are formed with a scavenger

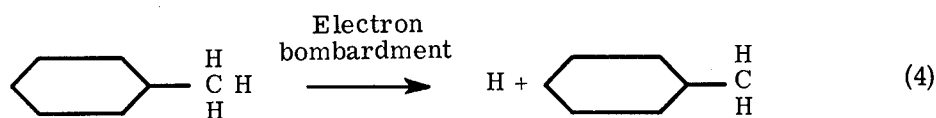


The alcohols, such as methanol, ethanol, and isopropanol, are very effective OH radical scavengers. They react to form products which do not interfere with the reduction reaction. Thus, if a small amount of alcohol is added to the aqueous solution of a metal salt, say copper sulphate, the hydrogen atoms, which persist longer than the OH radicals, can reduce the copper ion to copper metal

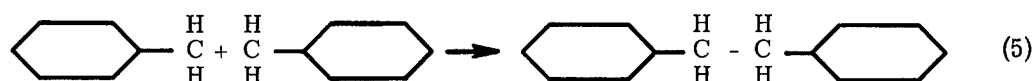


This copper precipitates out as a powder which can then be isolated by filtration.

The bombardment of some organic solvents can also result in the formation of hydrogen atoms and oxidizing radicals



Thus, metal ions can also be reduced if they are dissolved in the appropriate organic solvent. In general, a scavenger is not needed in the organic systems because the oxidizing radicals formed tend to react with each other



The obvious advantage to the organic system is the absence of water, which would react with many metals or compounds.

## ADVANTAGES OF NEW METHOD

Our radiochemical method offers three advantages over other methods for the production of metals and other materials. These advantages are: (1) low temperature, (2) easily isolated product, and (3) wide choice of solvent.

In reference to the low temperature, the reaction takes place at room temperature, and if necessary the operation can be carried out at even lower temperatures. The low temperature eliminates reactions with the container which in high-temperature methods lead to the contamination of the product. In the radiochemical method, any reasonable container material can be used because electrons do not generate any radioactivity problems. Another important attribute of room-temperature operation is that the reduction can be done in the complete absence of oxygen or nitrogen by degassing the solution and stirring with an inert gas.

The second beneficial characteristic of our new process is that the product is easily isolated. All other reaction products are soluble, so that filtration and washing are all that is necessary. And these can be done in an inert atmosphere, if desired.

The third advantage of the radiochemical method is the wide choice of solvents. The only restriction is that a true solution is obtained. We can design a solvent to produce the desired effect either by choosing a particular solvent material, re-

gulating the pH, or adjusting the chemical activity of the metal ion through the use of the appropriate metal salt. By manipulations of this sort, one can vary the particle size of the metal product and provide for better separation of particular metal impurities.

The first two beneficial characteristics are also common to the electrochemical method. However, electrochemical separation is limited by the availability of solutions that conduct electricity.

## APPLICATIONS

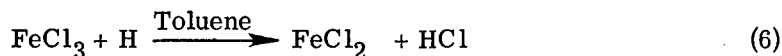
The first application of our new method was the preparation of a number of metals from aqueous solution. These results are summarized in the periodic table shown in figure 15-2. The 10 elements crosshatched in figure 15-2 have been prepared; they are cobalt, nickel, copper, zinc, palladium, cadmium, tin, antimony, thallium, and lead. Although we have not made the metals shown in the dotted boxes in figure 15-2, our experience indicates that they can also be made from aqueous solution; these are iron, gallium, germanium, arsenic, ruthenium, rhodium, silver, indium, osmium, iridium, platinum, gold, mercury, and bismuth. The characteristics of either the metal salts or the metal would make preparation of the others from water solution highly improbable. However, we anticipate that a large number can be made in organic solvent systems.

Table 15-1 gives a comparison of the metal yields obtained in the water system. As mentioned before, we have not attempted to optimize the conditions; the figures are merely order-of-magnitude yields and are intended to give only a rough comparison between the various metals. The solutions used were dilute, about 0.1 molar. The yields are given in grams of product per kilowatt hour. A kilowatt hour of beam input in our experiment corresponds to a beam current of 0.5 milli-ampere for 2 million volt electrons. As seen in table 15-I, 41 grams of antimony per kilowatt hour were produced (from an aqueous antimony trichloride solution), while a cadmium salt (acetate) solution yielded 38 grams of cadmium. The yields varied from 3.5 grams for zinc to 126 grams for lead.

Our research next centered around the question of how effective our method could separate a particular metal from other metallic ions in solution. We found that preferential deposition is easily accomplished by proper selection of the solution system. Table 15-II lists two examples. Very high concentrations of the contaminant or impurity ion were used. The starting material for the copper-nickel experiment was an equimolar mixture. When the acidified solution was irradiated, copper was quantitatively deposited, leaving the nickel in solution. The precipitated

copper contained only 20 parts per million of nickel. This is purer than electrolytic copper. A 50-50 mixture of cadmium and zinc (table 15-II) was used because zinc-free cadmium is normally quite difficult to obtain. Irradiation of the alkaline solution produced cadmium. The zinc present in the cadmium was below the X-ray fluorescence limit of detection (<100 ppm). Obviously, successive passes through the process (redissolution of the metal and redeposition) should result in even greater separations. And, of course, purification would normally be started with a much purer material, certainly not one only 50 percent pure.

As yet, we have not looked into the organic solvent systems in detail. However, we have examined the possible use of organic solvent systems to produce completely anhydrous compounds. The compound we chose to make was ferrous chloride. Pure anhydrous ferrous chloride is very difficult, if not impossible, to make by conventional chemical means: it always contains some ferric chloride and water. The reaction we used is



The reduction of ferric chloride in toluene solution stops at ferrous chloride, which is insoluble and precipitates out as the pure compound. The hydrogen atom in reaction (6) results from the electron bombardment of the toluene (reaction (4)); as mentioned before, the organic radicals that are formed react with each other to form unreactive larger molecules.

Another application of the radiochemical method arises from the fact that the particle size of the powder product can be varied by the proper choice of solvent. In fact, metal films can be deposited by using conditions which favor the formation of extremely small particles in the colloid range. One of these conditions is the use of salts which are very weak electrolytes.

We have had some successes with this type of application. We have made films of nickel and lead on glass. They formed tightly adherent mirrors which could be mechanically polished. We have also deposited nickel on silica powder and on porous substrates. The catalytic activity of the nickel deposited on a porous substrate compares very well with the activity of Raney nickel, which is much harder to handle and is harder to bring into contact with reactants than is the porous substrate preparation.

While working with the deposition of nickel films, we also discovered that metals can be prepared by a series of steps which include irradiation of nickel hypophosphite in the dry state. X-rays as well as electrons can be used for this irradiation.

We can take porous paper, such as filter paper, and deposit in it (either by

dipping or brushing) a solution of nickel hypophosphite. The paper is dried and irradiated. Then the paper is dipped in a developing solution. We have made several radiographs using the sensitized paper instead of the usual photographic film. Two such radiographs are shown in figure 15-3. The first picture in figure 15-3 was produced with a metal screen interposed between the X-ray source and the sensitized filter paper. The flaws in the screen are easily seen on the radiograph. The second picture in figure 15-3 was taken with various thicknesses of filter paper interposed, and shows the tonal gradation possible. (Nickel deposits of this type are catalytically active.)

The process involved is very much like the ordinary photographic process with silver halides. The exposure to radiation causes the formation of some sort of metal precursor which acts as a nucleus for the deposition of nickel in the developing solution. The density of the image is dependent on the radiation dose, and thus tonal gradations result, as shown in the figure.

The interesting feature of the nickel hypophosphite system is that it is not sensitive to visible light; thus, all these operations can be performed without the use of a darkroom. Other interesting features are the rapid development (~1 min) and the low cost of nickel as compared with silver.

## SUMMARY

A radiochemical method for the reduction of metal ions in solution has been described. The solvent may be either water or an organic solvent, depending on the desired product. The method can be used for the preparation of pure metals and compounds. It produces powdered metals, as well as metal films. Finally, a modification of the process can be used to produce nickel images in radiography.

## REFERENCES

1. Philipp, Warren H.; and Marsik, Stanley J.: Radiation-Induced Reduction of Divalent Copper Salts in Solution. NASA TN D-4451, 1968.
2. Philipp, Warren H.; and Marsik, Stanley J.: Radiation-Induced Reduction of Ammoniacal Nickel(II) Sulfate to Metallic Nickel. NASA TN D-5213, 1969.

TABLE 15-I. -  
PREPARATION OF  
METAL POWDERS

Metal	Yield, g/kW-hr
Lead	126
Palladium	96
Thallium	60
Copper	53
Antimony	41
Cadmium	38
Tin	23
Nickel	19
Cobalt	6.6
Zinc	3.5

TABLE 15-II. - METAL SEPARATIONS

Starting material	Product
50 Percent Cu - 50 percent Ni	Cu (20 ppm Ni)
50 Percent Cd - 50 percent Zn	Cd (<100 ppm Zn)

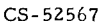
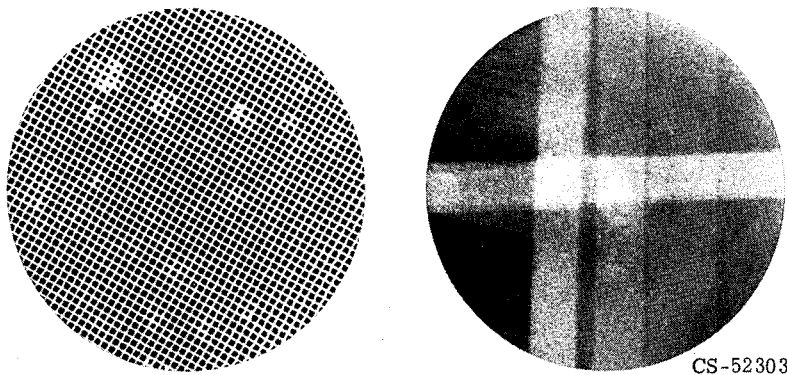


Figure 15-1. - Reaction vessel.

CS-52302

Figure 15-2. - Preparation of metals.



CS-52303

Figure 15-3. - Nickel images.





## 16. AN APPROACH TO A UNIVERSAL SPECTROCHEMICAL ANALYSIS

William A. Gordon

A procedure is described for performing chemical analysis with an emission spectrometer without the need for standards. Random compositions of 20 metallic elements can be quantitatively determined from microgram sample weights. The procedure improves the utility of the emission spectrometer for support of materials research.

Samples are prepared for analysis by dissolving them and depositing a fraction of the solution containing 10 micrograms of metal on a carbon electrode. The electrodes are specially prepared to contain 4 milligrams of silver chloride in the carbon matrix. The deposited solution is dried on the electrode, which results in an intimate mixture of the sample residue with a 400-fold amount of silver chloride. A stable, direct-current arc in argon, developed for use in this procedure, is used to vaporize the silver chloride sample mixture and to excite atomic emissions from metal constituents. The silver chloride serves to enhance atomic emissions and also to provide a constant excitation environment for the metals in the sample.

The light emitted from the arc plasma is detected by the spectrometer. The absolute microgram amounts of metal are derived from the spectrometer readout. Percentage compositions in the unknown samples are calculated from these data.

This procedure, combined with automation of the arcing sequences and data reduction, yields recorded emission data from a dissolved sample in about 4 minutes. Successful application has been made to a variety of analytical problems including analysis of extracted phases from superalloys, analysis of surface films, and analysis of corrosion residues.

The use of emission spectroscopy in chemical analysis involves first the production of atomic emission from elements in a sample of unknown composition, and then detection of that emission with a spectrometer. The emission can be excited by numerous energy sources which produce high temperatures, such as arcs, sparks, flames, and lasers. The spectrometer serves to measure spectral light intensities quantitatively. From these intensities, concentrations of elements in the sample under analysis can be determined.

Although the emission spectrometer is a well-established tool for performing

chemical analysis, it is not, unfortunately, a black box in which samples simply are placed in one end and the analytical results are derived immediately out of the other. Between the two ends, the technique suffers from some problems and limitations.

One of the limitations that has plagued the analyst is broadly referred to as matrix effect. In this broad context, matrix effect refers to the fact that the light intensities emitted by the elements in the unknown sample are not simply dependent on the concentrations of elements but are also dependent on the matrix composition of that sample. A discussion of the many and complex causes of matrix effect is not within the scope of this presentation. Rather, it is only important to indicate that the influence of sample composition on emitted line intensities complicates the separation of concentration-dependent relations from composition-dependent relations.

The traditional way around matrix effect is simply to calibrate it out by comparing emissions from the unknown sample with those from a series of standard samples. The comparison standards must not only have known concentrations of the elements to be determined, but must also be of the same physical form as the unknown samples.

Figure 16-1 illustrates matrix effect in superalloys. For this comparison, two alloys are shown, one containing 66 percent cobalt and the other containing 37 percent cobalt and 37 percent nickel. These alloys also contain known concentrations of zirconium, tungsten, chromium, iron, and titanium as minor constituents and in varying amounts. Spectrometer counts are plotted as a function of the known Ti concentrations in the two alloy series. For a given concentration of Ti in the alloys, the spectrometer response is higher in the alloy containing a matrix of 66 percent cobalt. Because of this matrix effect, the plot for one alloy series cannot be used to determine quantitatively Ti concentrations in the other. Therefore, two series of standards would be required for these Ti determinations. The unavailability of standard samples and the effort required to synthesize them is a limitation of spectrochemical analysis. Multiplying this limitation by the standard samples that would be required for chemical analysis of the variety of materials discussed at this conference should give an appreciation for the magnitude of the problem in a materials research laboratory. Matrix effect is of continuing concern in materials research because of the need to analyze a wide variety of compositions and because new compositions are continually introduced as others are phased out.

In this presentation, a single spectrochemical procedure is described that can be used to determine major and minor metal constituents of virtually any alloy composition or base metal. The procedure is also useful for analyzing miscellaneous samples derived from various research programs and which can weigh as

little as 10 micrograms. Some examples of applications are given at the end of this presentation.

## APPROACH

In seeking an approach to the problem of matrix effect, one needs to look no further than the excitation source, where the sample is vaporized and atomic spectra are excited. What goes on at the source will almost exclusively determine the precision, accuracy, and degree of matrix effect in the final analytical results. No amount of instrumentation, regardless of how sophisticated it may be, can in itself solve the problem of matrix effect.

The chemical form of the sample is an important consideration in the vaporization of samples. The procedure described herein includes three steps in preparing samples for vaporization. These procedural steps are designed to eliminate the effects of sample composition on the vaporization and excitation of the samples. First, the physical and metallurgical history of the sample is eliminated by dissolving the sample in halide acids (HCl, HF). Second, all metal elements are transformed to a common chemical form by drying a portion of the acid solution to form a metal halide residue. Third, a common excitation environment is provided for all residues by diluting them in a common matrix. With these procedures, matrix effects can be suppressed, and for analytical purposes, can be eliminated.

The concept of diluting the sample in a common matrix is a useful ploy in spectrochemical analysis and is basic to this procedure. This approach is illustrated in figure 16-2. The strategy is to dilute a small amount of the unknown sample in a relatively large amount of some pure material. In this procedure, silver chloride (AgCl) is used as the diluent because it also serves to enhance spectral emissions from the elements. The spectrographic sample that is finally analyzed consists of 99.75 percent AgCl. Therefore, the light emissions are governed by the preponderance of AgCl vapor, with the atoms from the unknown sample playing only a minor role in the process. The actual amounts of unknown sample and AgCl contained in the mixture are 10 micrograms and 4 milligrams, respectively.

The usefulness of this dilution procedure depends on detecting very small amounts of metals because the sample is already diluted by a factor of 400. The relations between percentage compositions in the unknown sample and in the AgCl are shown in table 16-I. For example, a pure metal would be present in the AgCl at a concentration of 2500 parts per million, and an element present at 0.1 percent in the unknown sample would be present at 2.5 parts per million in the AgCl. Also shown in table 16-I are the absolute amounts of the unknown sample present in the

AgCl. The sample weight is always 10 micrograms, and various elements in the sample weigh at least about 0.01 microgram. Thus, the spectrometer response is a measure of element weight present in the unknown sample over the range from 0.01 to 10 micrograms. Therefore, the more appropriate way of expressing quantities in this procedure is in absolute amounts of metals. The microgram amount of metals determined is subsequently converted to percentage compositions. The precision and accuracy of the percentage compositions is directly related to the precision and accuracy of the measurement of these small quantities of metals.

Much of the effort in the development of this procedure was concerned with the development of an excitation system that would provide the necessary detection sensitivity and also good precision. This work was started with an ordinary direct-current arc of a type that has been a workhorse in emission spectroscopy for trace analysis, but is notoriously imprecise. For this method, the arc is operated under closely controlled conditions in an argon atmosphere. Optimizing conditions such as argon pressure, electrode spacing, and arc current allows detection of about 1 nanogram of most of the common elements, and in the presence of 4 milligrams of AgCl. To determine these quantities with precision, several improvements were necessary in arc excitation. One of the improvements that was made was the elimination of arc wander, or flicker, that is characteristic of a free-running arc in static rare-gas atmospheres. This problem was solved by departing from the use of the customary graphite cathode and substituting a tantalum-tipped graphite cathode. This special cathode effectively eliminates arc wander and results in a more constant light output from the arc. This result is illustrated in figure 16-3, which shows photometric traces of the arc light as viewed through the narrow spectrometer slit. The top trace was made using a graphite cathode, and the effect of arc wander is shown by the vertical variations of the trace. The lower trace shows the constant light intensity that results from the use of a Ta-tipped cathode. These cathodes are easily prepared in about 5 minutes, and each is used for about 100 sample arcings. There is no serious spectral interference from the Ta spectrum. Even the most intense spectral lines of Ta are only faintly detected.

This stable and sensitive arc source was combined with the common-matrix approach and developed into a procedure for analyzing samples without the need for standard samples. The excitation of spectra with the stable arc and the recording and processing of data are automated to provide a versatile tool for analysis. The overall procedure is illustrated in figure 16-4.

## PROCEDURE

The sample is first dissolved in acids. Generally, hydrofluoric or hydrochloric acid is used with additions of nitric acid as necessary to effect the dissolution. This solution is diluted to contain 10 micrograms of sample per 10 microliters of solution. Next, a precise 10-microliter fraction is taken and added to a pointed carbon electrode which has been previously prepared to contain 4 milligrams of AgCl in the porous carbon tip. The addition of the AgCl is done in a two-step doping of silver nitrate solution followed by addition of hydrochloric acid solution. The concentrations of the two solutions are such that exactly 4 milligrams of AgCl are precipitated in the carbon electrode. With the addition of the sample fraction to this electrode followed by drying at 90° C, an intimate mixing of the sample residue and the AgCl is achieved.

A group of electrodes prepared in this way is loaded into a gas-tight chamber and arced in a completely automated sequence. The emitted light is received by the spectrometer, and the spectral intensities of 20 programmed elements are recorded on perforated paper tape. The recorded data are processed by a central computer to derive the percentage compositions of the sample residues.

These procedures are rapid and simple, requiring only about 40 minutes for 10 samples, after the samples are dissolved, through recording of spectral data.

The main steps of data processing are illustrated in figure 16-5 in simplified form. The spectrometer counts are converted to micrograms of each of the 20 programmed elements by means of computer-fitted calibration data for each of the elements. In deriving the microgram quantities, the program corrects automatically for the spectral interference of each programmed element on every other programmed element. This is done by solution of simultaneous equations that are produced from data accumulated in the calibration process.

From the micrograms determined for each element, percentages of elements in the sample are calculated. This calculation is done by one of two relations shown in figure 16-5. The percentages are calculated by relation (1) relative to the 10 micrograms sample weight. Alternatively, percentages can be calculated relative to the sum of micrograms of elements determined. This latter method is useful for applications where the sample weight is not known, such as in the analysis of surface films.

## APPLICATIONS

Some typical results of alloy analyses are summarized in table 16-II. The

three alloys shown are National Bureau of Standards samples which were selected because they were the most compositionally complex standards available. Comparison of the certified percentages with determined percentages provides a measure of the accuracy of this procedure. In general, the determined percentages are in reasonable agreement with the certified percentages. Although the results are not as accurate as wet chemical determinations in a single laboratory, they are within the range of results that could be expected from analyses in several different laboratories. In some instances, such as chromium in the S-816 alloy, the systematic difference in percentages greatly exceeds the precision of the measurement. In this case, the results for Cr were repeatable to within about 2 units in the second decimal place, or about 4 parts in 100. The difference in percentages is about 36 parts in 100. The cause of such discrepancies is unknown. It is possible that the certified analyses do not accurately represent the composition of the particular samples that were analyzed.

The results on these alloys include errors caused by the excitation process, by data reduction, and also short-term (a few days) drift in the electronic and photometric systems. One of the unsolved problems in this procedure is the control of long-term (weeks or months) instrumental drifts. Solution of this problem is important so that frequent element calibrations or calibration checks will not be necessary.

In addition to its application to metal alloys, the common-matrix procedure can be applied to miscellaneous samples which otherwise might be difficult to analyze because of requirements for low detection limits or because of small sample size. Some examples of these applications are shown in figure 16-6. In example (a), the problem was to analyze a small metal chip on the magnetic oil plug of a NASA aircraft. The chip was of a cast iron composition similar to the piston ring material. In example (b), the analysis of surface deposits on furnace sight glasses typifies analysis of metal surface films of many varieties. For samples of this type, an acid drop was deposited on the metal film, allowed to react for a few seconds, and then recovered with a micropipette and deposited on the electrode. The analysis of extracted phases from superalloys (example (c)) involved only a few milligrams of material on filter paper. This material was removed, weighed, and dissolved in acids. The surfaces of metal fibers (example (d)) were analyzed by a slightly modified procedure. A short length of metal wire was placed in a cupped graphite electrode along with 4 milligrams of AgCl powder. In the process of vaporizing the AgCl, a small amount of material was removed from the surface of the fiber, and the quantity of elements was determined. For metal fibers, the amount of metal removed was only a few micrograms. The amount of metal removed was measured by weighing the metal fiber before and after arcing. From the micro-

grams of metals determined, and the total amount of material removed, concentrations of elements at the metal surface can be detected. By adding more AgCl and repeating the arcings several times, estimates of concentration gradients of metals near the wire surface can be made. In example (c), the determination of trace elements in ashed blood serum was done in cooperation with medical researchers of the University of Colorado Medical School. Finally, in example (f), the determination of metal constituents in hot-salt corrosion residues provided information on the extent of corrosion.

These and other applications of this procedure are under continuing development as an effort is made to make the emission spectrometer a more universally applicable tool for chemical analysis.



TABLE 16-I. - RELATION OF METAL CONTENT IN  
SPECTROGRAPHIC SAMPLE

Metal content in unknown sample, percent	Metal content in AgCl, ppm	Absolute amount of unknown sample in AgCl, $\mu\text{g}$
100	2500	10
10	250	1
1	25	0.1
0.1	2.5	0.01

TABLE 16-II. - ANALYSIS RESULTS ON NBS STANDARDS

Standard	Element	Certified percentages	Determined percentages
NBS 153 (Co-Mo-W steel)	Co	8.45	8.05
	Cr	4.14	3.91
	Fe	73.9	75.6
	Mn	.22	.11
	Mo	8.38	8.03
	Ni	.107	.10
	V	2.04	1.85
	W	1.58	1.32
NBS 61A (ferro-vanadium)	Cr	0.68	0.55
	Fe	41.0	42.4
	Mn	1.78	1.56
	V	50.2	49.6
NBS 168 (S-816)	Co	41.2	41.9
	Cr	20.33	21.7
	Fe	3.43	3.45
	Mn	1.50	1.32
	Mo	3.95	3.76
	Nb	2.95	2.79
	Ni	20.25	19.2
	Ta	.95	1.21
	W	3.95	3.95

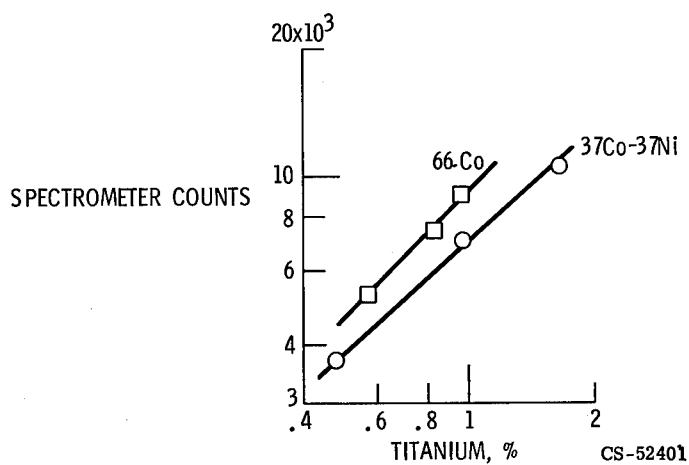


Figure 16-1. - Example of matrix effect with superalloys.

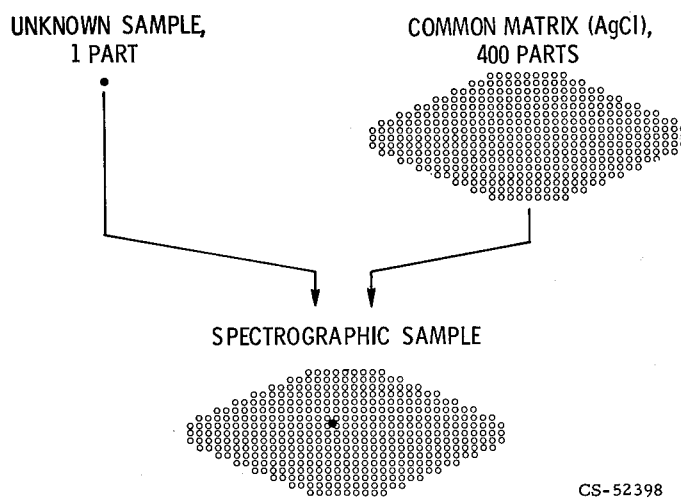


Figure 16-2. - Sample composition in common-matrix procedure.

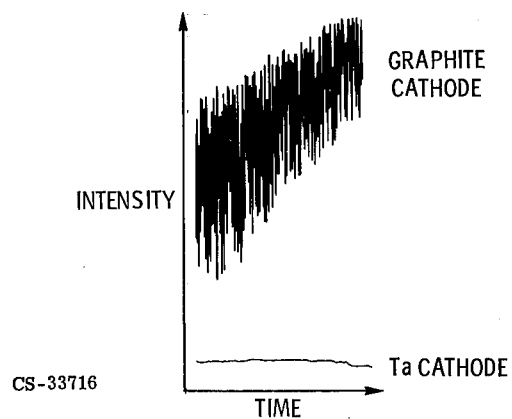


Figure 16-3. - Photometric stability of 30-ampere argon arc.

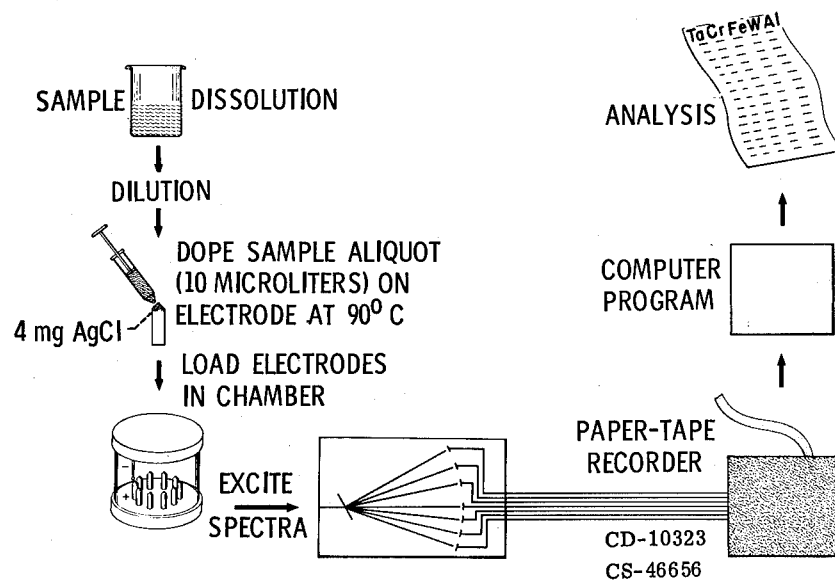


Figure 16-4. - Schematic illustration of procedure for common-matrix spectrochemical analysis.

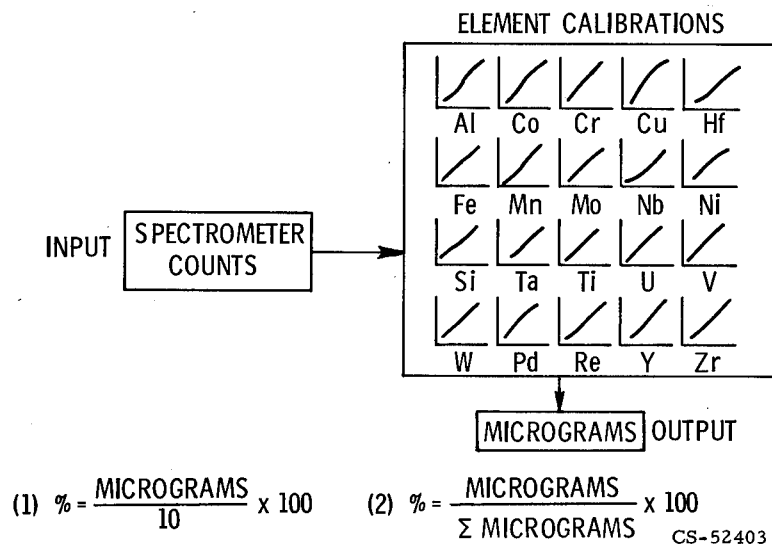
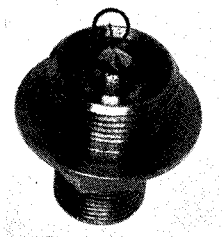
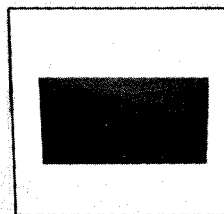


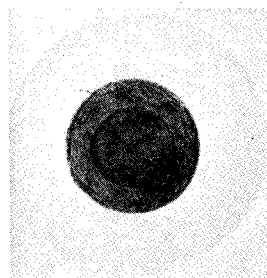
Figure 16-5. - Simplified schematic of data computer processing.



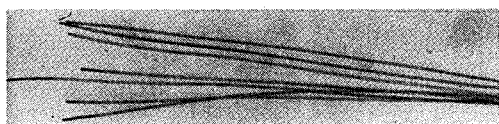
(a) Metal splinter on aircraft oil plug.



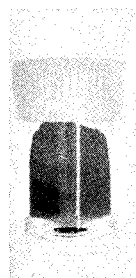
(b) Deposits on furnace sight glasses.



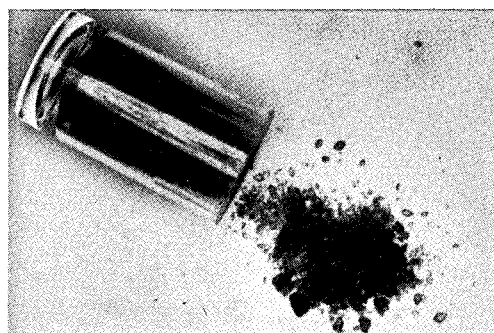
(c) Filtered phases from superalloys.



(d) Surface analysis of metal fibers.



(e) Trace metals in ashed blood serum.



(f) Residues from hot-salt corrosion experiments.

CS-52395

CS-52561

Figure 16-6. - Miscellaneous samples to which common-matrix procedure can be applied.



## 17. HOT-SALT STRESS-CORROSION OF TITANIUM ALLOYS

Hugh R. Gray

Laboratory investigations have demonstrated that titanium alloys exhibit embrittlement and cracking after exposure to halides while being stressed in the temperature range 500° to 900° F. This phenomenon has been termed hot-salt stress-corrosion. No service failures have yet been reported which could conclusively be attributed to this problem. However, there is continuing concern on the part of engine designers that such failures may occur. The rationalization for the lack of service failures is not clear, nor is the exact mechanism of embrittlement observed in the laboratory fully understood. Both of these aspects are under investigation at the Lewis Research Center.

A survey of engine manufacturers indicated that many titanium components in jet engines are operating at temperature and stress conditions where laboratory stress-corrosion tests indicate potential cracking problems. Field surveys conducted at engine overhaul depots to quantitatively measure salt concentrations on compressor airfoils demonstrated that salt deposits were accumulated during flight in excess of the minimum amounts reported to cause cracking in laboratory tests.

Hot-salt stress-corrosion tests conducted in a dynamic air facility which simulated the environmental conditions in a compressor have demonstrated that high velocity airflow does not eliminate hot-salt stress-corrosion. Specimen surface preparation was found to exhibit a dramatic influence on susceptibility to hot-salt stress-corrosion.

Mechanical tests and chemical analyses aimed at revealing the fundamental mechanism of hot-salt stress-corrosion have confirmed that hydrogen is generated during the corrosion process and causes embrittlement.

Laboratory investigations have shown that titanium alloys are susceptible to cracking after exposure to salt while being stressed in the temperature range 500° to 900° F. This phenomenon has been termed hot-salt stress-corrosion. Since jet aircraft frequently operate in salt-air environments, there is concern on the part of engine designers that this problem may severely limit the potential use of titanium alloys in aircraft. However, no service failures have yet been reported which could conclusively be attributed to this problem. The rationalization for the lack of service failures is not clear, nor is the exact mechanism of embrittlement

observed in the laboratory fully understood. We are investigating both of these aspects at the Lewis Research Center. Some of the reasons postulated for the lack of service failures are as follows:

- (1) Compressor components may not be operating at stress and temperature levels where stress-corrosion occurs in laboratory tests.
- (2) Engine components may not be exposed to sufficient salt during normal flying conditions.
- (3) High velocity airflow may sweep away salt and damaging gaseous corrosion products.
- (4) Cyclic operating conditions of engines may inhibit corrosion reactions.

The results of our investigations for three of these aspects are presented in the first part of this paper. The aspect of cyclic operating conditions is currently in the initial stages of investigation and is not considered here. The second part of this paper is concerned with our concurrent research program dealing with the fundamental mechanism of hot-salt stress-corrosion of titanium alloys.

To set the stage for subsequent discussion, figure 17-1 illustrates a typical titanium alloy hot-salt stress-corrosion threshold curve separating regions of cracking from no-cracking. As evident from the figure, the threshold curve severely limits the potential use of titanium alloy components with respect to typical design limitations such as creep or yield strength.

Threshold curves actually determined in various investigations reported in the literature for the commonly used Ti-6Al-4V alloy are presented in figure 17-2. As evident from these 100-hour threshold curves, wide variations exist among investigators. Several aspects of experimental procedure - namely, material heat treatment, specimen type, surface condition, salt concentration, and mechanical testing techniques - as well as the criteria employed to define a threshold curve probably contribute to these reported variations. Some investigators defined their threshold on the basis of residual mechanical properties determined by a variety of testing conditions, while others were concerned only with cracks or corrosion products. The significance of both experimental procedure and the criteria used for defining a threshold curve are demonstrated in subsequent portions of this paper.

## ENGINE EXPERIENCE

A letter survey of engine manufacturers (private communication) was conducted to determine the operating conditions of titanium alloy components in current engines and the design conditions of developmental engines. The maximum temperature and stress conditions of the Ti-6Al-4V alloy components in current engines are

illustrated by the data points in figure 17-3. The scatter band represents the various literature threshold curves presented in the previous figure. It is evident that almost all of the reported engine components are operating at stress and temperature levels above the most pessimistic of the reported laboratory threshold curves. Similarly, many Ti-6Al-4V alloy components are being designed for use in developmental engines at operating conditions above the minimum laboratory exposure conditions which have been reported to cause cracking (see fig. 17-4). In summary, titanium alloy engine components are currently operating and are being designed to operate at stress and temperature levels where laboratory tests indicate potential hot-salt stress-corrosion problems. Hence, the postulate that engine components are operating at "safe" conditions is invalid in many cases, at least insofar as laboratory test data regarding titanium hot-salt stress-corrosion is concerned.

## SALT DEPOSITION DURING FLIGHT

A field survey (ref. 1) was conducted at engine overhaul depots to determine actual salt concentrations deposited on compressor airfoils after exposure to a variety of flight conditions. Photographs of salt deposits on a compressor airfoil are presented in figure 17-5. The light areas near the root of the concave side of the blade and along the leading edge of the convex side are deposits of salt. Actual cubic crystals of salt were also observed as shown in figure 17-6. Quantitative measurements of salt deposits were also obtained for a variety of flying conditions. Mild exposure conditions, such as occur during transoceanic flight, resulted in average salt concentrations of 0.01 to 0.1 milligram per square inch over the entire airfoil surface, as can be seen in figure 17-7. Concentrations of up to 1 milligram per square inch were measured after severe operating conditions, such as pilot training in the Caribbean (see fig. 17-8). It is important to note that localized concentrations 10 times greater than these average values were measured in many instances. This field survey demonstrated that salt does deposit on airfoils during normal flight conditions and that these salt deposits may persist even after flying through rainstorms. These measured salt concentrations are in excess of the minimum amounts (0.03 mg/in.<sup>2</sup>) that have been reported to cause cracking in the laboratory.

## SIMULATED COMPRESSOR ENVIRONMENT

In order to investigate the postulate that high velocity airflows may sweep away



damaging gaseous corrosion products, three rigs were constructed to simulate the dynamic air environment encountered in compressors of jet engines (ref. 2). Tubular specimens of the type illustrated in figure 17-9 were used in this investigation. The dynamic air apparatus is illustrated schematically in figure 17-10. Service air was dried to a dewpoint of  $-120^{\circ}$  F and heated to a maximum temperature of  $900^{\circ}$  F. The air was rehumidified if the influence of dewpoint was under investigation, and salt-water fog was injected into the airstream before it passed through the stressed tubular specimen. Air velocities of 1100 feet per second (Mach 0.7) at pressures of 30 to 60 psia have been used in our investigations. Two modes of operation have been used. Specimens were either precoated with salt and then exposed to salt-free air during the 100-hour exposure period, or salt-laden air was continuously passed through the specimen for the entire 100-hour test period. The desired concentration of salt in air was maintained to simulate environmental conditions at coastal airports during normal flying weather (4 parts per billion) or during storms (40 parts per billion).

Typical salt deposits that occurred on the bore of these specimens are illustrated in figure 17-11. Uniformly dispersed, submicron size crystals of salt were reproducibly achieved to any desired concentration level. Specimens were precoated to concentrations of about 0.2 milligram per square inch for all subsequently discussed tests.

Before discussing the results of tests conducted in this dynamic air apparatus, it is necessary to define the criteria used in this investigation for establishing the threshold for hot-salt stress-corrosion. As mentioned previously, investigations have used various schemes for defining their threshold - namely, residual mechanical ductility, stress rupture, crack observation, and/or the presence of corrosion products. The criterion used in this investigation was residual ductility after a 100-hour exposure period. Ductility was determined by a room temperature tensile test at a slow, constant crosshead speed of 0.005 inch per minute. The significance of these test conditions is discussed later. Specifically, if the elongation of an exposed specimen was less than 15 percent and the reduction in area was less than 25 percent, compared to as-received values of 19 and 33 percent, respectively, then the specimen was declared embrittled and the stress and temperature exposure conditions were considered to be above the threshold curve. If both of these criteria were not met, then the specimen was considered not to be embrittled, and the exposure conditions fall below the threshold curve.

The 8Al-1Mo-1V was selected for the initial phases of our investigation because the literature indicated that it was one of the most susceptible alloys.

A threshold curve determined by the embrittlement procedure described is more sensitive than any other criterion, as is evident from figure 17-12. The

embrittlement threshold curve occurs at lower stress levels than a crack threshold curve over the entire temperature range of investigation. The increased sensitivity of the embrittlement technique is especially apparent at 800° F where embrittlement was determined at an exposure stress of about 5 ksi, while stress-corrosion cracks were not observed until the exposure stress exceeded 50 ksi. Another type of threshold, brittle stress rupture, is also presented for comparative purposes. A sensitive technique for determining the onset of hot-salt stress-corrosion, such as the embrittlement threshold technique, is especially important in any investigation where the influence of environmental variations is being studied.

The influence of air velocity was determined by comparing results of tests conducted with as-machined specimens in static air laboratory furnaces and in our dynamic air rigs at a velocity of 1100 feet per second at 30 psia. As is evident from figure 17-13, embrittlement was determined at slightly higher exposure stresses in the dynamic air environment at 600° and 700° F. No differences were determined at 800° F. It appears that a dynamic airstream similar to that encountered in a compressor may decrease hot-salt stress-corrosion slightly, but it does not eliminate the problem.

Little attention has been paid to the potential influence of various types of surface conditions in literature studies of hot-salt stress-corrosion. However, the effect of specimen surface preparation was found to be the most important variable encountered in this investigation. The dramatic influence of two types of surface conditions on embrittlement thresholds is illustrated in figure 17-14. For specimens exposed to the dynamic air environment described previously, the embrittlement threshold curve for specimens in the as-machined condition occurred at substantially higher stress levels than for chemically milled specimens at both 600° and 700° F. No difference was apparent at 800° F. It must be pointed out that these as-machined tubular specimens had a residual compressively stressed surface layer on the bore. Chemical milling techniques resulted in the removal of this residually stressed surface material. The chemical milling techniques used in this investigation did not result in any measurable absorption of hydrogen by the specimens. Both the chemically milled and as-machined surface conditions actually simulate commonly encountered industrial conditions - that is, a shot-peened surface and a chemically machined or stress-relieved surface. It is important to note that other types of machining operations - for example, grinding the outside diameter of a tensile specimen could result in residual tensile stresses on the surface of the specimen. In those instances, the threshold curve could be expected to occur at lower stress levels than if the same specimens were in the stress-relieved condition. It is also interesting to note that there was no beneficial effect of long-time preoxidation at 800° F, regardless of the mode of surface preparation.

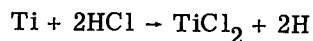
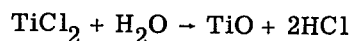
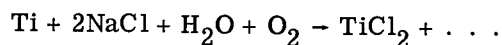
We are continuing to investigate both the effects of surface condition and environments on a number of titanium alloys.

## FUNDAMENTAL ASPECTS

Up until now the paper has dealt with the portion of our investigation aimed at rationalizing the postulates for the lack of service failures. It appears that none of these postulates are valid. As mentioned previously, the influence of cyclic operating conditions on the susceptibility of titanium alloys to hot-salt stress-corrosion is currently under investigation. This portion of the paper deals with the results of our investigations into the fundamental aspects of the embrittling mechanism (refs. 3 and 4).

The effect of salt-exposure on the ductility of the Ti-8Al-1Mo-1V alloy is illustrated in figure 17-15, where electron fractographs of the fracture surfaces of unsalted and salted specimens are presented. Concurrent with this marked change in the mode of fracture from a dimple to a cleavage pattern was a decrease in elongation from the as-received value of 19 to 5 percent.

Several investigators have suggested that hydrogen may be responsible for this embrittlement. The feasibility for the generation of hydrogen is indicated in the following reactions:



The four basic ingredients in the corrosion process (titanium, halides, moisture, and oxygen) may form  $\text{TiCl}_2$  together with other corrosion products whose identity is not conclusively resolved. In a moist atmosphere HCl is formed which then attacks the bare titanium surface and results in the generation of hydrogen. The last two reactions may be autocatalytic in a moist environment.

If hydrogen is responsible for hot-salt stress-corrosion, then it may be diffusible and material ductility would be a function of strain rate and temperature. To determine the validity of this postulate, tensile tests were conducted over a range of strain rates and temperatures after exposure conducive to hot-salt stress-corrosion (800° F; 96 hr; 50 ksi). The effect of tensile testing speed is shown in

figure 17-16 where elongation is plotted as a function of crosshead speed at room temperature. At a fast crosshead speed of 0.5 inch per minute, the elongation of salted material is unchanged from that of unsalted material. However, at a constant, slow strain rate of 0.005 inch per minute, the elongation of the salted material is substantially less than that of the unsalted (e.g., 5 against 19 percent). It should be pointed out that a commonly used tensile test technique, which involves a tenfold increase in the strain rate when the yield stress is reached, is not as sensitive a test as the procedure discussed previously.

The influence of tensile testing temperature is presented in figure 17-17 for constant crosshead speeds of 0.005 and 0.05 inch per minute. Embrittlement was most pronounced in the vicinity of room temperature. For a constant strain rate, ductility was recovered as the test temperature was raised. For the slower strain rate (0.005 in./min), full ductility was observed in the vicinity of 300° F. If hydrogen were responsible for the observed mechanical behavior, then total hydrogen concentration would be expected to influence the position and width of both the strain-rate and temperature minima.

The observed strain-rate and temperature sensitivity confirmed that a diffusable species is controlling the embrittling process. In an effort to positively identify the species, vacuum fusion chemical analyses were conducted on samples taken from areas close to the fracture surfaces of specimens in various conditions. As shown in table 17-I, the hydrogen content of specimens subjected to a hot-salt stress-corrosion exposure increased to as much as 126 ppm, as compared to the as-received value of 70 ppm. Hydrogen contents up to 255 ppm were measured after a severe exposure condition (brittle stress rupture). It should be noted that these analyses represent the average hydrogen concentration of a fairly large sample (0.1 g). Local concentrations at internal interfaces and crack tips may be substantially in excess of these average values. A vacuum annealing treatment at 1200° F for 24 hours reduced the hydrogen concentration to about 7 ppm. Together with the measured decrease in hydrogen concentration after vacuum annealing, full recovery of ductility was observed for salted specimens that had been vacuum annealed after exposure. For example, an elongation of 19 percent was measured on specimens after salt exposure followed by vacuum annealing as compared to only 5 percent after salt exposure without subsequent annealing (see fig. 17-18). This full reversibility of the embrittling process could occur only if a diffusable species were controlling the mechanism and if no permanent damage, such as cracks, had occurred during the hot-salt stress-corrosion exposure period. Metallographic examination confirmed that the specimens were crack free, as was expected because the exposure conditions (800° F; 96 hr; 50 ksi) were chosen at

levels slightly below the crack threshold curve for this Ti-8Al-1Mo-1V alloy (see fig. 17-12).

These mechanical tests and chemical analyses have confirmed that hydrogen is generated during the hot-salt stress-corrosion process and is absorbed by the titanium alloy. Thus, it can be concluded that hydrogen is responsible for the observed embrittlement in subsequent mechanical tests. We are continuing with research aimed at identifying the actual embrittling role of hydrogen particularly at higher temperatures.

## REFERENCES

1. Ashbrook, Richard L.: A Survey of Salt Deposits in Compressors of Flight Gas Turbine Engines. NASA TN D-4999, 1969.
2. Gray, Hugh R.; and Johnston, James R.: Hot-Salt Stress-Corrosion of a Titanium Alloy Under A Simulated Turbine-Engine Compressor Environment. NASA TN D-5510, 1969.
3. Gray, Hugh R.: Hot-Salt Stress-Corrosion of Titanium Alloys: Generation of Hydrogen and Its Embrittling Effect. NASA TN D-5000, 1969.
4. Gray, H. R.: Hot Salt Stress Corrosion of a Titanium Alloy: Generation of Hydrogen and Its Embrittling Effect. Corrosion, vol. 25, no. 8, Aug. 1969, pp. 337-341.

TABLE 17-I. - HYDROGEN ANALYSES<sup>a</sup>

Specimen condition	Hydrogen content, ppm by wt
As-received <sup>b</sup>	70
As-received	55 to 89
Salted <sup>c</sup> and exposed <sup>d</sup>	100 to 126
Salted and stress rupture <sup>e</sup>	189 to 255
Salted, exposed, and vacuum annealed <sup>f</sup>	6 to 8

<sup>a</sup>Analyses obtained in regions near fracture surfaces.

<sup>b</sup>Vendor's analysis.

<sup>c</sup>0.2 mg/in.<sup>2</sup> (0.03 mg/cm<sup>2</sup>).

<sup>d</sup>800° F (425° C) at 50 000 psi (350 MN/m<sup>2</sup>) for 100 hr.

<sup>e</sup>800° F (425° C) at 80 000 psi (550 MN/m<sup>2</sup>) for 285 hr.

<sup>f</sup>1200° F (650° C) at <10<sup>-3</sup> torr for 24 hr.

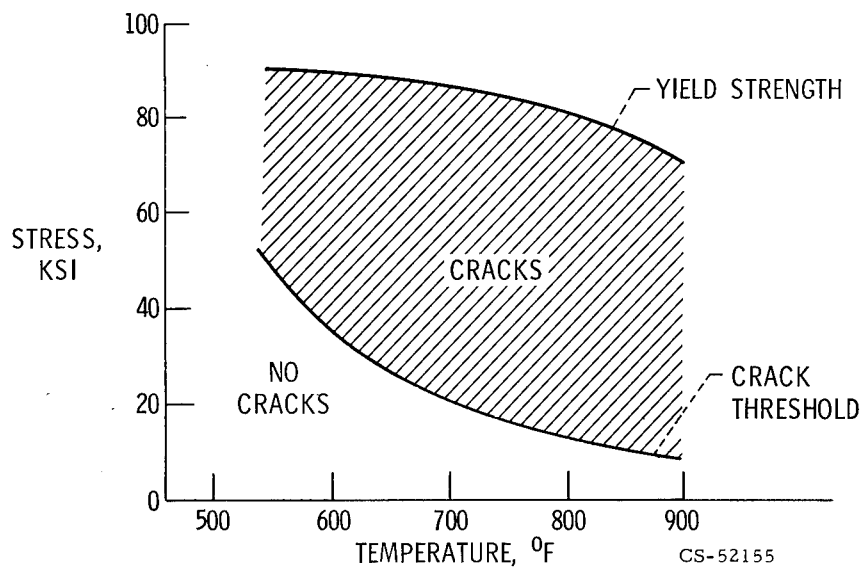


Figure 17-1. - Typical titanium alloy threshold curve.

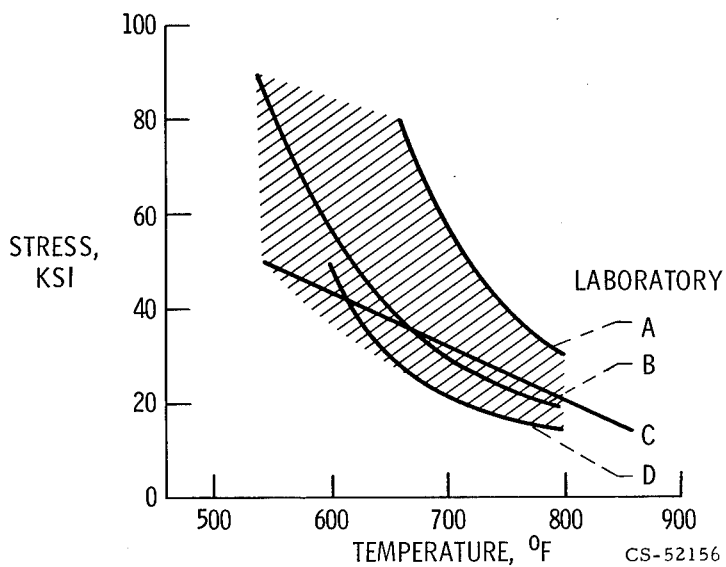


Figure 17-2. - 100-Hour thresholds for Ti-6Al-4V alloy.

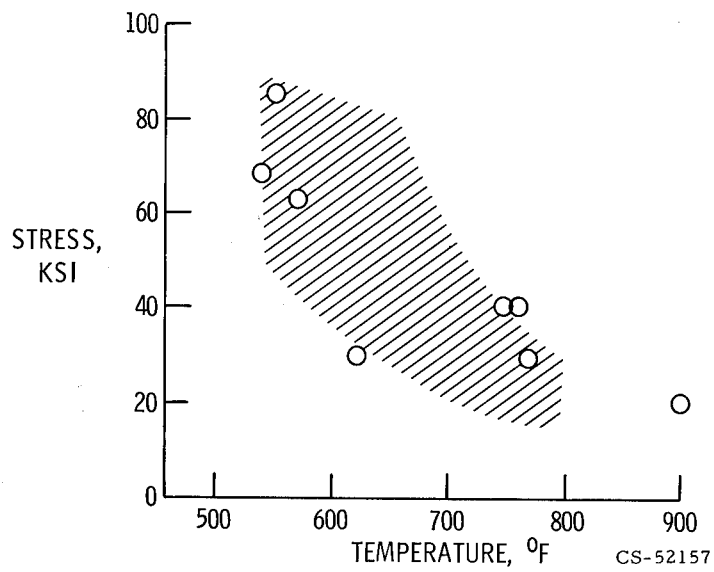


Figure 17-3. - Operating conditions of current Ti-6Al-4V alloy engine components.

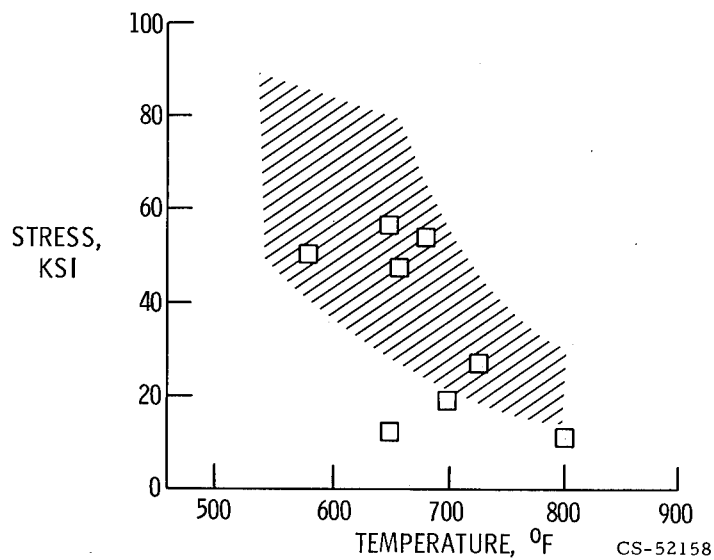
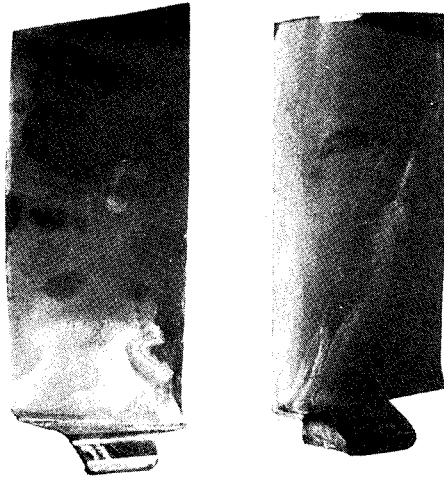


Figure 17-4. - Operating conditions of developmental Ti-6Al-4V alloy engine components.



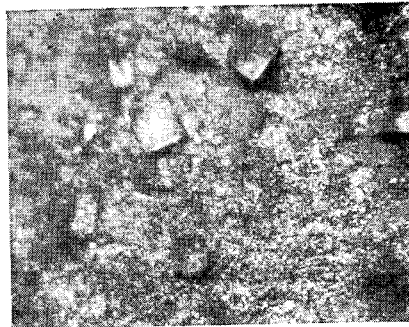


CONCAVE

CONVEX

CS-45512

Figure 17-5. - Salt deposits on compressor blade.



0.010"

CS-45509

Figure 17-6. - Salt crystals on compressor blade.

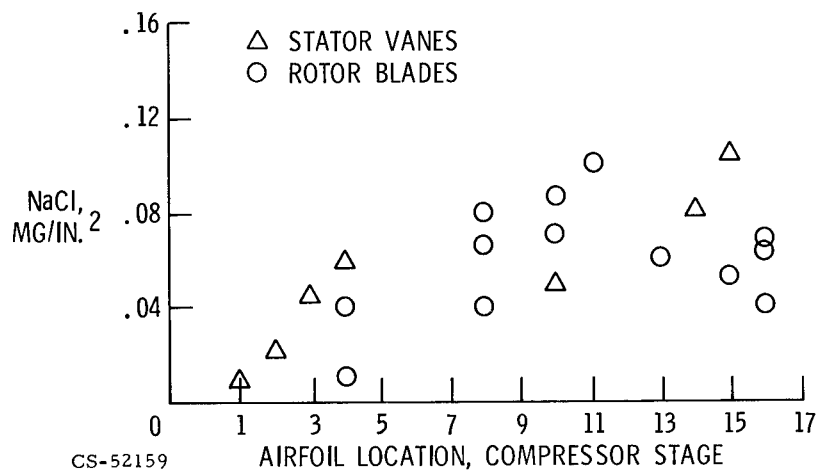


Figure 17-7. - Salt concentrations after mild operating conditions (such as transoceanic flight).

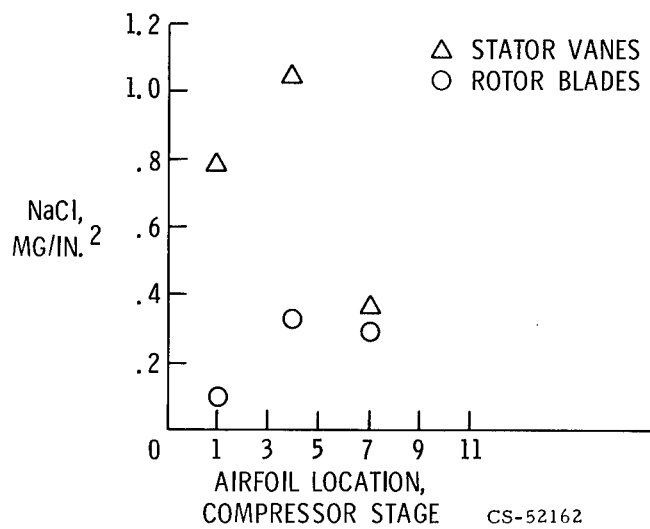
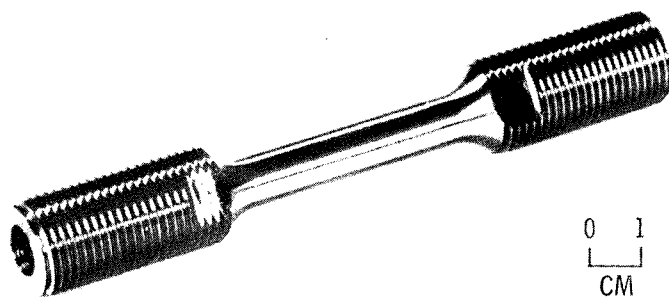


Figure 17-8. - Salt concentrations after severe operating conditions (such as pilot training in Caribbean).



0 1  
CM

CS-47266

Figure 17-9. - Hollow specimen for this investigation.

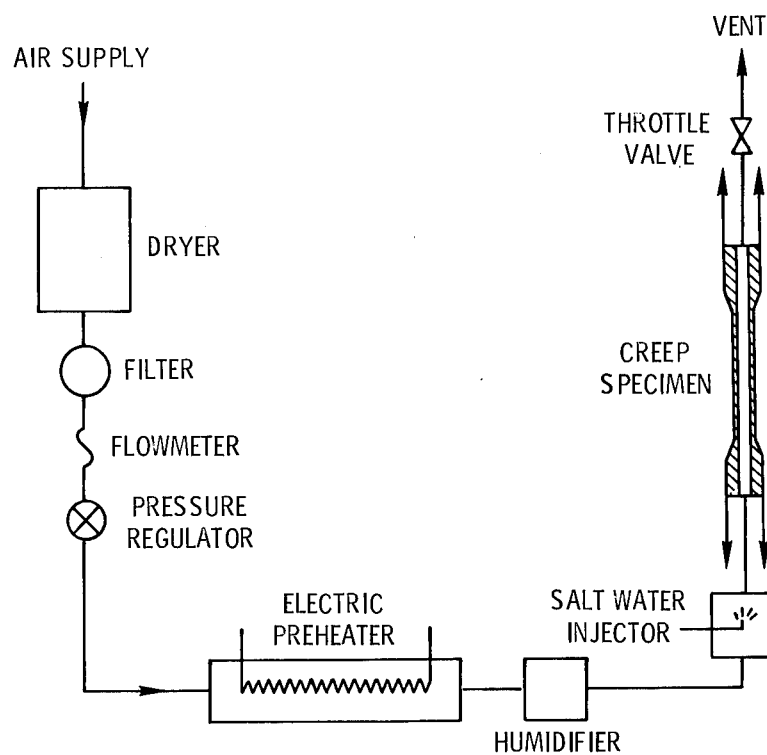
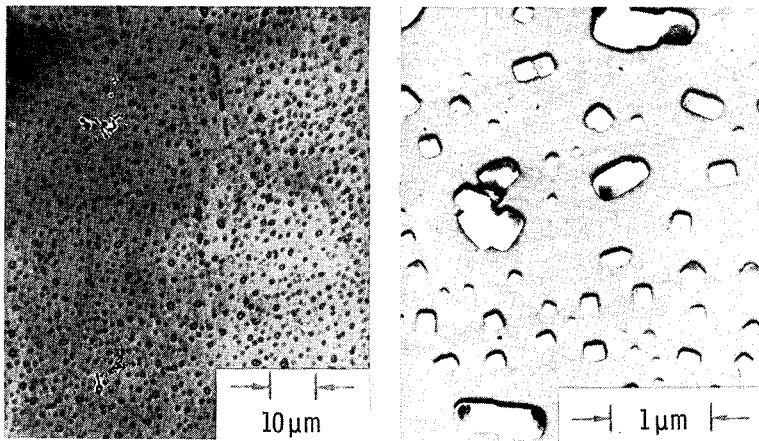


Figure 17-10. - Titanium hot-salt stress-corrosion apparatus.



C-68-3781  
CS-52163

Figure 17-11. - Salt deposits on titanium alloy specimens.

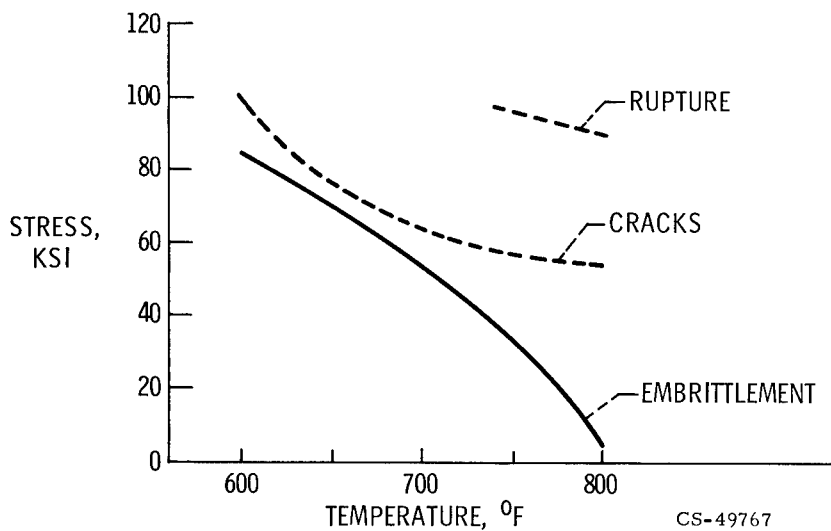


Figure 17-12. - 100-Hour threshold curves for Ti-8Al-1Mo-1V alloy.

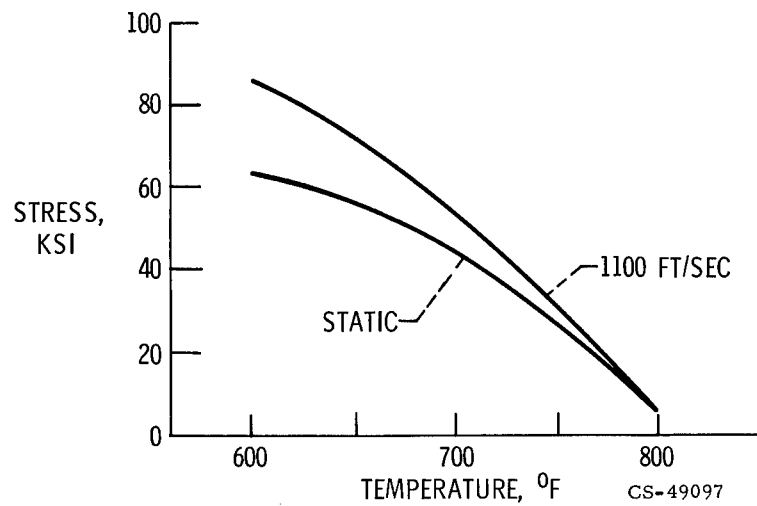


Figure 17-13. - Effect of air velocity. 100-Hour threshold for Ti-8Al-1Mo-1V alloy.

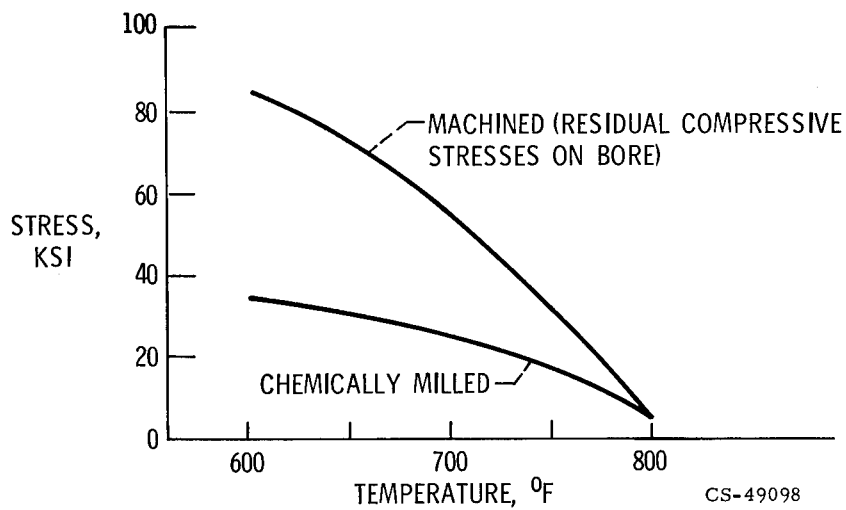


Figure 17-14. - Effect of specimen surface condition. 100-Hour threshold for Ti-8Al-1Mo-1V alloy.

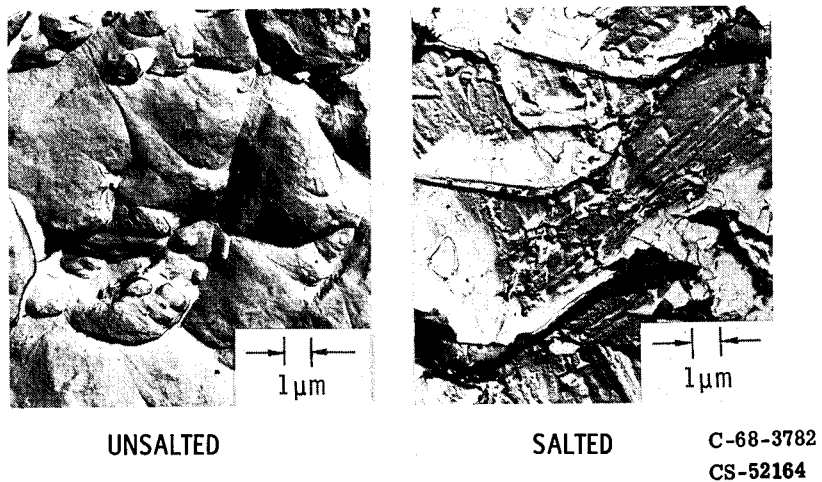


Figure 17-15. - Effect of salt exposure on fracture surface.

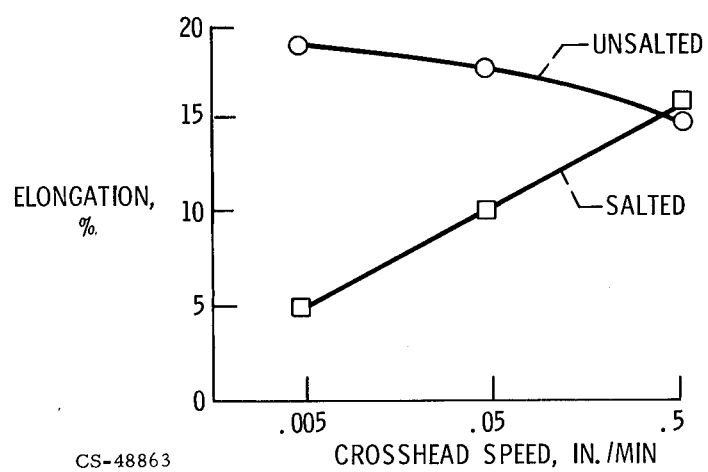


Figure 17-16. - Effect of tensile testing speed on ductility. Tensile test at 72° F.

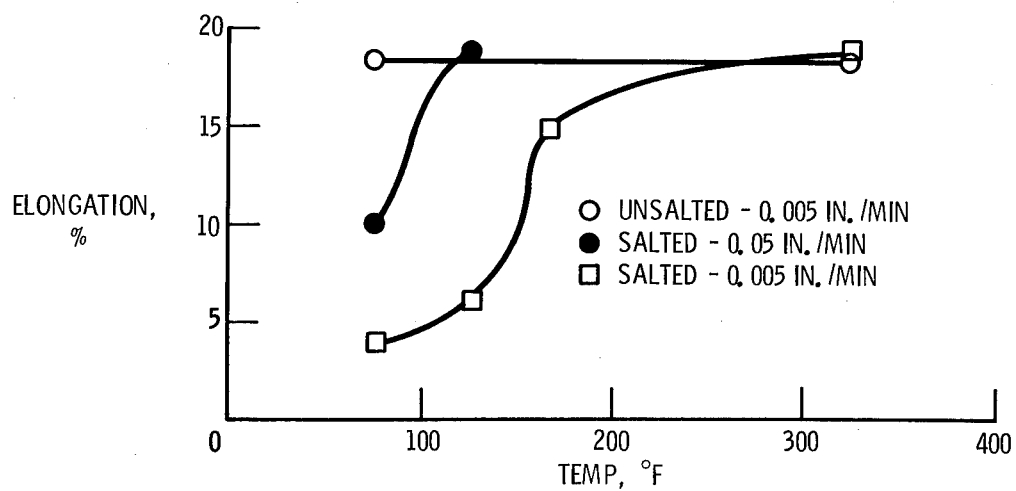


Figure 17-17. - Effect of tensile testing temperature on ductility.

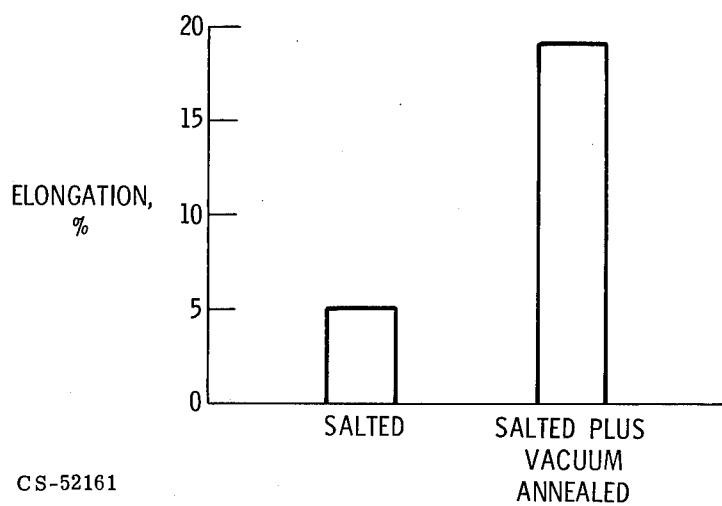


Figure 17-18. - Effect of vacuum annealing on ductility.

## 18. SOME TENSILE AND ELECTRICAL RESISTANCE PROPERTIES OF PALLADIUM-HYDROGEN AND TITANIUM-HYDROGEN SYSTEMS

Robert J. Smith and Dumas A. Otterson

The variation in electrical resistivity with hydrogen-palladium ratio is related to the crystallographic structure and to the mode by which the hydrogen electron is added to the s- and d-bands of the palladium. The conclusions reached allow the prediction of the tensile properties. The  $\alpha$ -phase, which is characterized by an unfilled d-band, has a high cohesive energy, while the  $\beta$ -phase, for which the d-band is filled, has a low cohesive energy. The tensile properties in the region where both phases exist obey a simple mixture rule. Like palladium, titanium is a transition metal having unfilled s- and d-bands. The mechanical behavior of the titanium-hydrogen system should, therefore, also be examined from this point of view. Initial work in preparation of titanium-hydrogen compositions in wire form by electrolytic deposition of hydrogen has served to emphasize the tendency for hydrogen segregation and also the need for property data for the compositions high in hydrogen.

Metallurgists are concerned about the effects of less than a few hundred parts per million of hydrogen on the mechanical properties of some transition metals. Physicists and chemists are also interested in metal-hydrogen systems. However, we are interested in the whole range of attainable hydrogen concentrations. In general, metal-hydrogen systems involve those metals which have at least two incomplete outer electron bands or states. For the transition metals, these are the neighboring s- and d-states.

Simple representations of these states are given in figures 18-1(a) and (b). In a way, these models are similar to the old shell model of the atom. The letters s, p, and d represent the energy levels for a given shell. When more than one atom is present, the outer energy levels become delocalized and tend to spread from one atom to the next and form a band. In this case, we are concerned with the outer s- and d-bands.

For the model in figure 18-1(a), a nontransition metal is represented by silver. Its 4d-states are filled with 10 electrons per atom. It has one 5s or conduction electron per atom.



However, transition metals have 10 or less electrons per atom to be shared between the s- and d-bands. Since the s- and d-bands overlap in energy, these electrons are easily shared. The transition metals are represented by palladium (fig. 18-1(b)). It has 10 outer electrons for its 4d- and 5s-bands. There are  $10 - x$  electrons in the 4d-band and  $x$  electrons in the 5s-band. This incomplete d-band is responsible for transition metals having higher electrical resistivities and higher cohesive energies than the nontransition metals. The need to fill the d-band appears to be a prime reason that hydrogen may easily enter the transition metal lattice. In general, the hydrogen electron becomes associated with the d-band.

The d-band is quite sensitive to changes in its electron concentration and changes in the lattice configuration. These changes can be seen in the electrical resistivity and many other properties including mechanical properties of the transition metals. It is for these reasons we studied the palladium-hydrogen system and are now studying the titanium-hydrogen system.

Our resistivity work with the palladium-hydrogen system is presented. Also presented is how the resistivity work helped us to partially understand the changes observed in the yield and ultimate tensile strengths of this system. Finally, a description is given of some of our current work on the titanium-hydrogen system.

In the palladium-hydrogen system, the composition can vary from pure palladium to PdH. Figure 18-2 shows the variation in lattice parameter with composition. (The lattice parameter is given in Å and is plotted against the hydrogen-palladium atom ratio.) In the  $\alpha$ -phase, which is a solid solution, the lattice parameter varies continuously from 3.890 to 3.895 Å for ratios up to 0.2. At 0.02, the  $\beta$ -phase appears with a lattice constant of approximately 4.025 Å. These two phases,  $\alpha$  and  $\beta$ , coexist up to a ratio of 0.6. The dashed line represents an averaging of the two observed lattice parameters in this mixed phase region. It should be pointed out that two and only two lattice parameters exist in this mixed phase region - that is, 3.895 and 4.025 Å. The averaging is just an artifact used in developing a theory which is discussed later. The  $\alpha$ -phase disappears near a ratio of 0.6. For ratios between 0.6 and 1.0, there is only the  $\beta$ -phase with a lattice parameter of 4.025 Å.

Figure 18-3 shows the atomic configurations in the  $\alpha$ - and  $\beta$ -phases. Since both structures are face centered cubic, just one face is used to illustrate the point. As hydrogen is added to palladium in the  $\alpha$ -phase, it fills interstitial cube edge sites at random to form a solid solution, and the lattice expands as a whole. The  $\beta$ -phase has a sodium chloride (NaCl) structure as shown on the right. The structure, as shown, has vacant hydrogen sites. The number of these vacant sites decreases to zero as PdH is approached. No change occurs in the lattice parameter of the  $\beta$ -phase as hydrogen fills the vacant sites.

At Lewis, a theory has been developed which accounts for the variation in electrical resistivity with hydrogen content. It is generally known that the electrical resistivity of a metal is lowest when the lattice is most perfect. Defects, which disturb the perfect periodicity, interfere with the motion of the conduction electrons; that is, these defects scatter the conduction electrons. This scattering causes the resistivity to increase. So, for the palladium-hydrogen system, the resistivity is lowest in the two perfect lattice regions - pure palladium and PdH. The curve between the two extremes rises to some maximum. The shape of this curve is determined by the electronic structure of the palladium-hydrogen system.

Now, when a hydrogen atom is added to the palladium lattice, it can do one of two things. It can contribute its electron to the unfilled d-band of the palladium, or, if the d-band has been filled by previous hydrogen electrons, it can contribute its electron to the unfilled s-band. When the electron is added to the d-band, its presence is felt by all the palladium atoms around it - the electron is shared by all of them and the lattice expands as a result of the d-band filling. The net result is that the d-band effectively screens the hydrogen from the conduction electrons; that is, the hydrogen ion scatters the conduction electrons only a little. As the d-band becomes filled, the electrons from additional hydrogen ions go increasingly into the s-band. The screening associated with the s-band is small. This permits these additional hydrogen ions to become effective scatterers, and the resistivity increases more rapidly. Another way to consider this screening is to look at figure 18-3. In regions of very low hydrogen concentration, the dominant and regular array is the palladium lattice. This, coupled with the covalent bonding of the hydrogen ion to the palladium, presents only a slight distortion of the periodic potential to the conduction electron. This slight distortion gives the small increase in resistivity.

However, once the hydrogen lattice starts to form, a new potential appears. The periodicity of this new potential is interrupted by vacancies in the hydrogen lattice. In this case, both hydrogen ions and hydrogen vacancies scatter - but in different ways. These various scattering sites cause the resistivity to increase more rapidly.

In figure 18-4, the resistivity as a function of hydrogen concentration at 273 K is given. For increasing hydrogen content, the resistivity rises. There is a slight break at 0.02 and a point of inflection near 0.6. The resistivity goes through a maximum near 0.75 and then decreases as the ratio approaches 1.0. As hydrogen is added to pure palladium, the increase in the resistivity is due to the increasing lattice parameter. When the hydrogen population reaches 0.02, the hydrogen ions are then close enough together - on the average - so that the second phase,  $\beta$ , appears. From here on, the lattice does not continuously expand as a whole, but rather relative amounts of  $\alpha$ - and  $\beta$ -phases change. The resistivity curve in the

mixed phase region curves away from the concentration axis. This is due to the screening effect. Without this screening effect, we would have expected the curve to be concave toward the concentration axis.

The theory developed at Lewis to account for the variation of electrical resistivity with hydrogen content involves the screening effect. It was based on data obtained at 4.2 K. In figure 18-5, the theory is shown by the solid lines and the data are indicated by the circles. The theory is divided into two parts - from 0 to 0.6 and from 0.6 to 1.0. In the first part the screening effect (i.e., the initial slow rate of rise of resistivity in the mixed phase region) is more pronounced here than at 273 K. This is because thermal vibrations tend to mask the screening effect at 273 K. It is in this region that we assumed a linear lattice expansion as the hydrogen-palladium atom ratio went from 0 to 0.6. We made this assumption to simplify the development of the theory.

In the second part of the theory, the region of pure  $\beta$ -phase, the hydrogen ions scatter in two ways: first, as the screened ions which have contributed their electrons to the d-band; and second, as essentially unscreened ions which have contributed their electrons to the s-band. By taking these two scattering processes together in the proper fashion and considering the formation of the hydrogen lattice, we get the theoretical curve on the right. The theory involves d-band filling. We assume the d-band is totally filled at a ratio of 0.6 (this value was used in the theory to fit the curves). The value of 0.6 is consistent with that deduced from magnetic susceptibility measurements made elsewhere.

To summarize at this point, an understanding has been developed of how the hydrogen atom interacts with the palladium lattice. This understanding has enabled us to account for the variation of resistivity as hydrogen is added to palladium.

The mechanical data are given in figures 18-6 and 18-7. Figure 18-6 shows the variation of the yield stress with composition. The crosshead speed used was 0.1 inch per minute. The yield stress rises and finally reaches a constant value at the ratio of 0.6, which is where the d-band is filled and a single phase region is reached. For ratios between 0 and 0.6, typical solution strengthening behavior is seen. The hydrogen, as it is added, gives rise to centers which impede the motion of dislocations, and the yield strength rises. The lack of any great change as the  $\beta$ -phase appears at 0.02 indicates that the  $\beta$ -phase regions contribute to strengthening in much the same way as do the hydrogen sites in the  $\alpha$ -phase. The leveling off in yield stress at 0.6 occurs when the fracture becomes completely brittle at 44 ksi.

Figure 18-7 shows the ultimate strength and elongation. The ultimate strength rises to a maximum near a ratio of 0.02. When the  $\beta$ -phase appears, the ultimate strength begins to decrease. It then falls to a constant value of brittle failure for

the  $\beta$ -phase at 44 ksi. It is at 44 ksi that the yield and ultimate strengths coincide. The elongation is similar in character to the ultimate strength.

The decrease in the ultimate strength, as the  $\beta$ -phase appears, can be understood if one considers the electronic structure of the  $\beta$ -phase and, also, if one recognizes that ultimate tensile strength is dependent on crack propagation. The critical stress for the propagation of a crack is dependent on Young's modulus and the surface energy. Both of these are proportional to the cohesive energy.

Now, the cohesive energy of transition metals is strongly dependent on the existence of the unfilled d-band. As the d-band is filled, the cohesive energy falls. Therefore, we would expect that the  $\beta$ -phase with its filled d-band is weaker than the  $\alpha$ -phase which has an unfilled d-band. The fact that the ultimate strength is constant from 0.6 to 1.0 indicates that the contribution of hydrogen to the s-band has little effect on strength.

The variation of ultimate strength, in the two-phase region, is then dictated by the amount of  $\beta$ -phase present and the stress required to propagate a crack, rather than by the yield strength as it is in the pure  $\alpha$ -phase (i. e., for ratios up to 0.02). In this system, it appears that the ultimate strength can be estimated from the number of holes remaining in the d-band, just as it was possible to predict electrical resistivity from this quantity. This simple dependence may be peculiar to this system, because both phases have the same crystal structure.

There is still much to be done here. For example, the strain rate effects have not been examined. Also, we do not totally understand why the  $\beta$ -phase appears when it does. However, we have turned to the titanium-hydrogen system because we feel that this approach may contribute some understanding to a material that is very important for aerospace applications.

There have been many mechanisms proposed for hydrogen embrittlement in titanium. A short but perhaps representative list is as follows:

- (1) Weak second phase in bulk
- (2) Weak surface hydride
- (3) Weak phase boundary
- (4) Hydrogen formation in voids
- (5) Hydrogen reaction with interstitial oxygen or nitrogen
- (6) Surface tension lowering
- (7) Cohesive energy lowering

First there is the formation of a weak second phase in the bulk, perhaps  $\text{TiH}_2$ . This phase could be the region in which cracks are initiated. Second, the brittle phase - a hydride - can form on the surface and give rise to surface cracks. The formation of phases with weak boundaries can also give rise to cracking. The next two mechanisms suggest reaction of hydrogen either with itself, to form molecular hydrogen

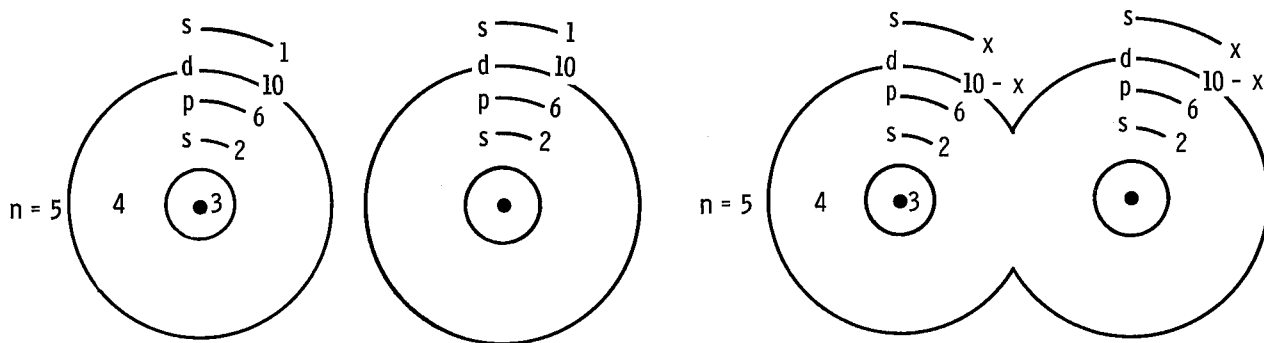
in voids, or with oxygen or nitrogen which are present as interstitial impurities. In either case, formation of molecular species could increase local stresses. The sixth item suggests that hydrogen entering a surface crack could reduce the energy required to make a new surface and thereby cause crack propagation at a lower stress. Finally, from our experience with palladium, the entry of hydrogen into the lattice at the tip of the crack can cause a lowering of cohesive energy due to d-band filling.

More information is needed before we can decide which one of these mechanisms are important. Some obvious unknowns are the strength properties of the various titanium-hydrogen phases and the mobility of hydrogen in the various lattices. Both of these depend on the details of the interaction of the hydrogen with the titanium lattice. Therefore, we should study the large hydrogen to titanium ratios as bulk specimens rather than as precipitates in a titanium lattice.

Palladium and titanium are similar in that they are both transition metals with unfilled s- and d-bands. Also, they both absorb hydrogen to high concentrations - titanium takes up twice as much hydrogen as palladium. However, the titanium-hydrogen system is more complex in that three phases exist at room temperature - one of these is hexagonal rather than face centered cubic.

Now, in order to study the properties as a function of composition, it must first be possible to prepare specimens. An interesting and perhaps important fact was discovered when preparing 10-mil wire specimens by electrolytic deposition of hydrogen. Figure 18-8 shows the curve for plotting the hydrogen to titanium atom ratio against the loading time in days. This experiment was run at a current density of 8 milliamperes per square centimeter. This process makes available a large number of hydrogen atoms to be absorbed by the titanium. The hydrogen content was determined with a mass spectrograph. The limit being reached is far below  $\text{TiH}_2$ . The interesting fact is that the composition is far from uniform. The surface layer of the 10-mil wire is  $\text{TiH}_2$  to a depth of less than 1 mil. Below this depth is pure titanium. We conclude that  $\text{TiH}_2$  is easily formed and quite stable. Also, it is apparently a good barrier to the diffusion of hydrogen. These findings would lend credence to the proposal that  $\text{TiH}_2$  formed on the surface could give rise to cracks. It also implies that localization of hydrogen as  $\text{TiH}_2$  at very low overall concentrations is possible. We expect to obtain a better bulk distribution of hydrogen by using thinner specimens and lower charging rates.

In conclusion, our work with the palladium-hydrogen system has been described. We have been able to relate the electrical resistivity and mechanical behavior to the mode by which hydrogen interacts with the electronic structure of the palladium lattice. Finally, we have described the beginnings of our work with titanium where nonuniformity in hydrogen content has been observed during electrolytic loading.



(a) Nontransition metal, silver. Low resistivity;  
low cohesive energy.

(b) Transition metal, palladium. High resistivity;  
high cohesive energy.

Figure 18-1. - Electronic states for nontransition and transition metals.

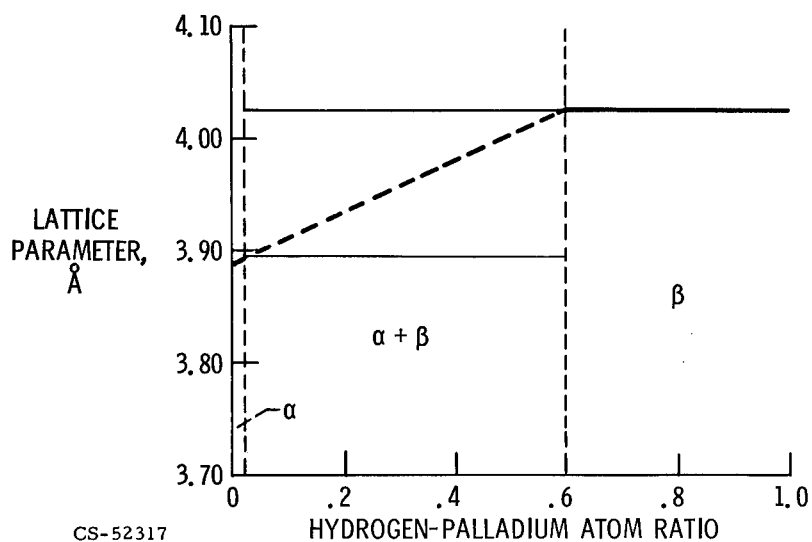


Figure 18-2. - Lattice parameter for palladium-hydrogen system.

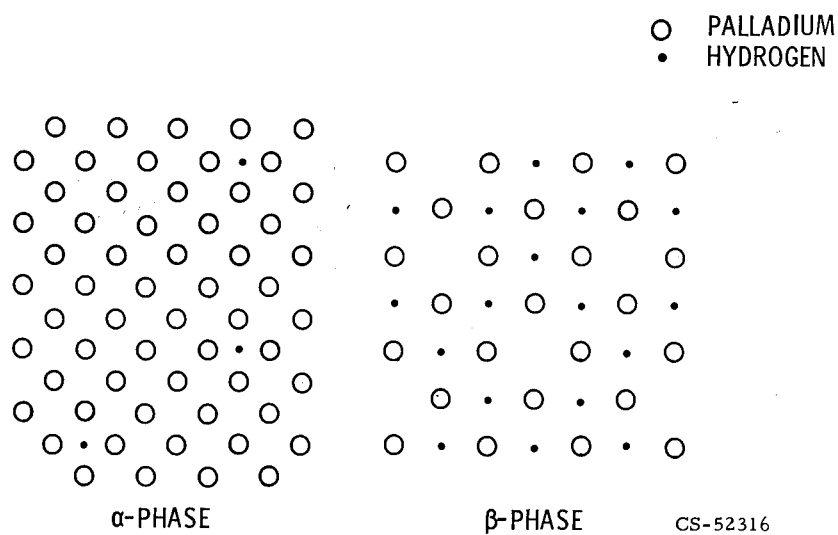


Figure 18-3. - Atom configuration in  $\alpha$ - and  $\beta$ -phases.

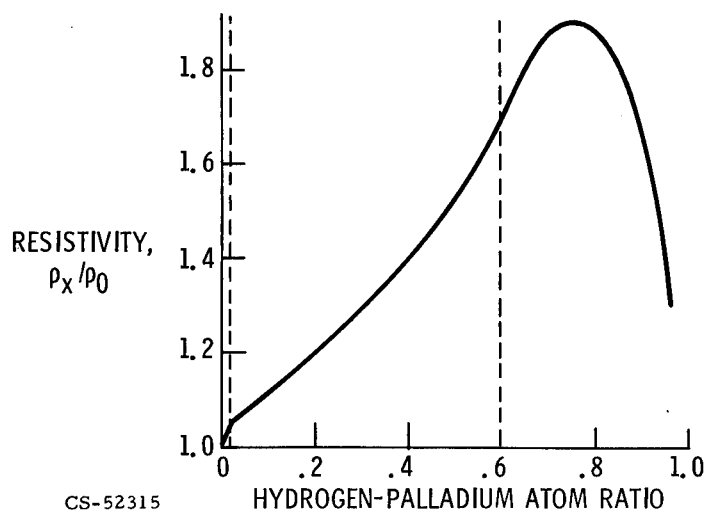


Figure 18-4. - Electrical resistivity for palladium-hydrogen system at 273 K.

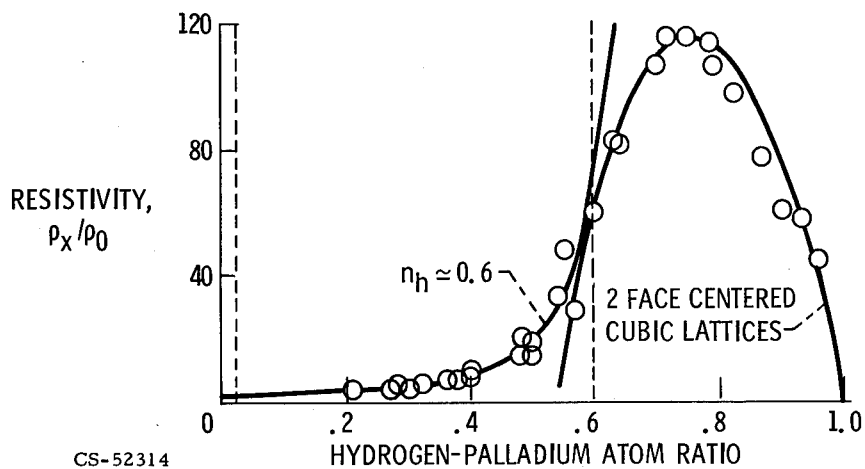


Figure 18-5. - Electrical resistivity for palladium-hydrogen system at 4.2 K.

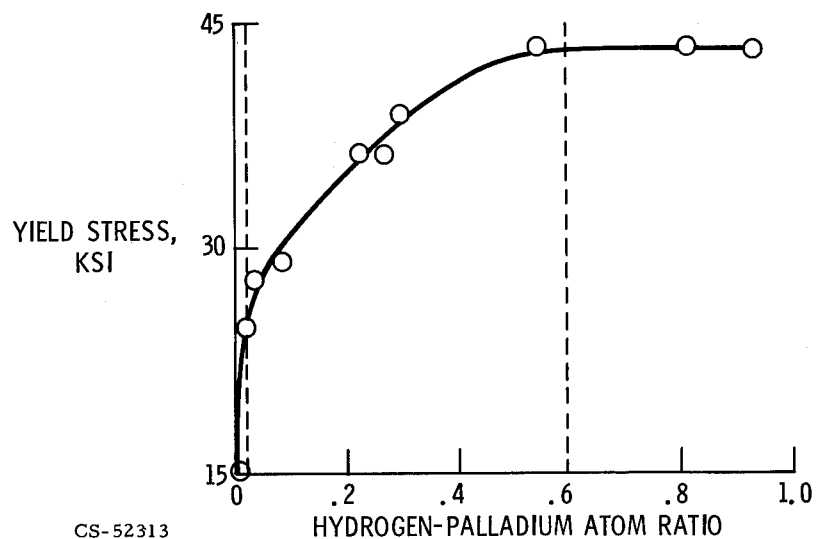


Figure 18-6. - Yield stress for palladium-hydrogen system.



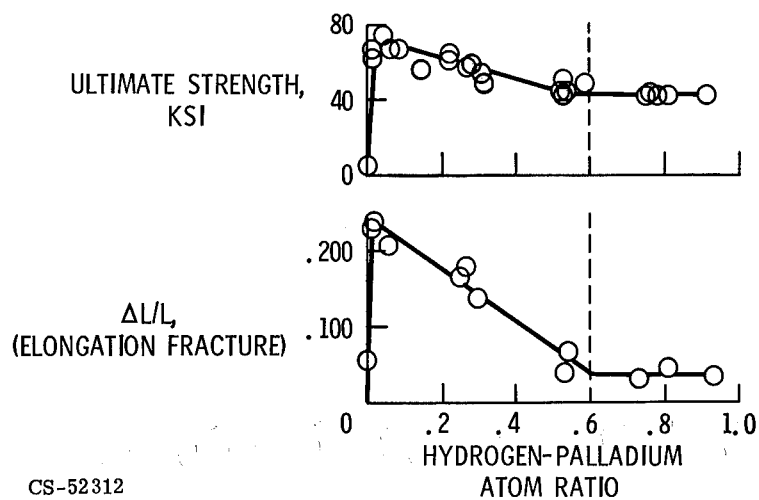


Figure 18-7. - Ultimate tensile properties of palladium-hydrogen.

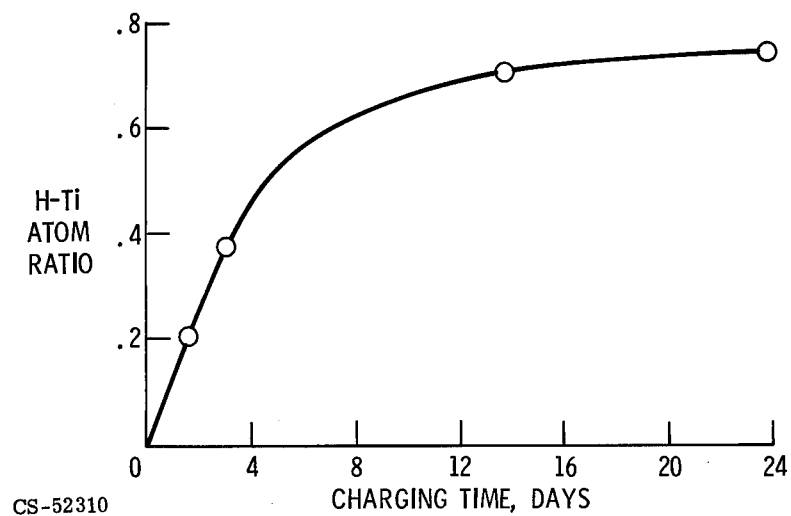


Figure 18-8. - Electrolytic charging of titanium.

## 19. EFFECT OF ENVIRONMENT ON EROSION-CORROSION PROCESSES

Hubert B. Probst

The present corrosion problem associated with the use of superalloys in aircraft gas turbine engines is described. The evolution of this problem is also considered. The problem is more serious today than in the years past: The higher strengths of today's alloys allow higher operating temperatures; however, the corrosion resistance of such alloys has not kept pace with their strength capabilities.

In studying the corrosion behavior of complex alloys, their intrinsic behavior must be understood, as well as the effects of extrinsic environmental features. The NASA burner rig, a facility capable of simulating some of the severe features of the engine environment, is described. It is shown that some engine conditions, simulated in the burner rig, have such a strong effect on corrosion behavior that the ranking of alloys changes from that based on simpler laboratory tests.

Examples of specific effects of such environmental variables as thermal cycling, gas velocity, and gas composition on corrosion resistance are presented. Thermal cycling, particularly the frequency of cycling, has a strong influence on corrosion resistance. The effect of high gas velocity may be a combination of erosion and accelerated vaporization of protective scales.

The importance of corrosion resistance and its dependence on environmental factors should receive greater attention in alloy development programs. Although specialized facilities are required to duplicate some features of the engine environment, simple laboratory tests can be conducted in such a manner that the results are more meaningful in evaluating alloy performance in an engine.

Classical gaseous corrosion studies are usually concerned primarily with the intrinsic behavior of the material per se; that is, variables inherent to the material itself and their effect upon corrosion resistance are the subject of the usual gaseous corrosion or oxidation study. A typical example is the evaluation of the oxidation resistance of a binary alloy system as a function of composition. Such studies can be enlightening as to the specific effects of individual alloying elements. However, it must be realized that such studies are rarely conducted under experimental conditions that are even close to those of any ultimate application. Thus, the effects of the real environment on corrosion resistance must come under consideration when a material is considered for a specific application.

The more drastic the departure from simple laboratory tests to the ultimate application, the more concern we should have for the environmental effects. In the case of the demanding environment of the turbine in an aircraft gas turbine engine, a knowledge of the effects of environmental parameters on corrosion resistance is particularly important. Some of these environmental features in the turbine are so severe that it is not unlikely that these extrinsic factors might completely override any intrinsic variables in determining the capability of an alloy to survive in the engine environment.

This paper is concerned with the high-temperature corrosive environment in the turbine portion of the engine. Its purpose is twofold: First, it will attempt to describe the erosion-corrosion problem as it exists today and as it presents a barrier to the development of advanced engines. Second, by the use of a few examples, this paper will try to illustrate and emphasize the importance of environmental factors on the problem.

## EROSION-CORROSION PROBLEM

### Description

Basically, the corrosion that occurs in a gas turbine engine is the result of reactions occurring at high temperatures between one or more components in the gaseous atmosphere and one or more elements in the alloy. Corrosion constitutes a problem inasmuch as these reactions can reduce the overall load-carrying ability by progressive consumption of the part or degrade mechanical properties by alterations of the composition of the remaining alloy.

The reactions that occur may range from the formation of simple oxides of the least noble elements in the alloy to more complex reactions involving other components in the gas in addition to oxygen, with the resultant formation of multiphase complex scales. The process may be further complicated by solid-state reactions among individual phases in the scale or by reactions between scale components and liquid salts that might condense on the surface of the part. The entire process can be further complicated and accelerated by the mechanical erosion of scales by abrasive particles entrained in the gas stream.

### Evolution

The present corrosion problem is the result of an evolutionary process that has

occurred in the development of superalloys and their application in gas turbine engines. This evolution for nickel-base alloys is illustrated in figure 19-1. Here, the strength and corrosion capabilities of nickel-base alloys as they were developed through the years are plotted. The corrosion limit is plotted as a band since the corrosion capabilities of any one alloy are dependent on test conditions. The early alloy, Nimonic 80-A, is a nickel alloy containing 20-weight-percent chromium. With this high chromium content it possesses good corrosion resistance to the 1900° to 2000° F range. However, the low strength of this alloy sets a limit of just slightly over 1400° F on its high-temperature use. Thus, its low strength precluded a corrosion problem by limiting its upper use-temperature. In the years that followed, the major emphasis in the development of alloys was higher strength. In the nickel-base alloys, strength improvement (and consequently higher use-temperatures) was sought by compositional changes, such as increased aluminum and titanium as strong  $\gamma'(\text{Ni}_3\text{Al})$  formers and increased cobalt and refractory metals as solid solution strengtheners. Such compositional changes usually were accommodated by lowering chromium contents. Thus, as figure 19-1 illustrates, higher use-temperatures were realized but at the expense of corrosion resistance. This evolutionary process has continued until today we have high-strength alloys of low chromium content, such as alloy VI-A. In such alloys, the use-temperature of the bare alloy is set by corrosion limitations rather than strength limitations. Thus, corrosion resistance is now a barrier to the full utilization of the strength that has been developed.

The same type of evolutionary process occurred in the development of cobalt-base superalloys; however, corrosion resistance as a barrier occurred and was recognized at an earlier point in time.

## MATERIALS APPROACHES

The present need then is for hot engine components that can survive the high-temperature engine environment from both strength and corrosion viewpoints. The major approach currently taken by engine designers is to cope with the problem by cooling, that is, to provide cooling air internally to turbine blades and vanes in order to hold their temperatures down. Cooling is effective but costly. Cooling air is bled from the compressor and therefore it not available for combustion, thus overall engine efficiency is lowered.

The more direct approach is to provide improved materials more capable of surviving the engine environment. Efforts to provide better materials usually fall

into one of three categories: improved alloys, improved coatings, or improved oxidation-resistant nonmetallics.

As pointed out earlier, past efforts to improve alloys have often concentrated too much on mechanical property improvement, with insufficient concern for corrosion resistance. With this in mind, current and near future efforts should also include basic attempts to understand the corrosion processes of current alloys and thereby seek to enhance corrosion resistance and guide the development of new alloys.

Aluminide coatings have performed an admirable job in allowing use-temperatures and lifetimes of superalloy components to be increased. However, much remains to be done in improving lifetimes and reliability of coated parts as well as in gaining better understanding of the protective and degradation mechanisms of coatings.

The third area, nonmetallics, is one that holds much promise from the corrosion viewpoint but whose chances of success might be judged small because of mechanical shortcomings. The philosophy is to start with corrosion-resistant nonmetallics such as oxides, intermetallics, or refractory compounds and attempt to lessen or circumvent their mechanical shortcomings of brittleness and catastrophic fracture. This is admittedly a long-shot approach. However, the chances of improving alloys and coatings to the required levels of corrosion resistance might approach similar odds. The payoff offered by improved superalloys and coatings is inherently limited by the melting temperatures of the alloys. Although eliminating or circumventing the brittleness problem of nonmetallics is no small task, the potential payoff in terms of weight, cost, and ultimate temperature capabilities is so great that it cannot be ignored.

## LABORATORY TESTS VERSUS ENGINE ENVIRONMENT

In order to emphasize the importance of environment let us draw a contrast between two extremes, the usual laboratory oxidation test (in which environmental factors are not paramount) and the severe environment in a gas turbine.

Figure 19-2 depicts schematically the pertinent features of the usual oxidation test. In this test a small sample is suspended from an analytical balance into a furnace. The atmosphere of the furnace is usually room-temperature air of unknown and uncontrolled humidity and contamination levels. Bottled oxygen or gas mixtures of known oxygen partial pressures are also used. The test is usually conducted under isothermal conditions; that is, no effort is made to subject the sample to thermal cycling.

The data provided by such a test are some functional relation between the mea-

sured weight change per unit surface area and the exposure time, as illustrated in figure 19-2. From determinations of the exponent  $n$  and the rate constant  $k$ , information is gained as to the reaction kinetics and possible mechanisms.

In such a test the effect of many variables on oxidation resistance can be studied (e.g., sample composition, prior heat treatment, sample geometry, and surface preparation). However, all such variables are intrinsic to the sample itself, and with the obvious exceptions of temperature and straightforward gas composition changes, environmental features are usually not studied in such a test.

Such tests can give a lot of information regarding the behavior of the material per se. But even when this is the expressed purpose, the weight change results can be misleading if their limitations are not realized. The weight change measured is the resultant net value of any weight gain and any weight loss. Weight gain, of course, is due to the sample taking gas components into solution and the formation of definite surface-layer scales. Weight loss, on the other hand, can occur as a result of subtle factors such as vaporization of alloy or scale components and cracking of the scale with subsequent flaking or spalling. Thus, for example, a given alloy might be judged oxidation resistant because it shows a low value of absolute weight gain when in reality the actual weight gain may have been high but offset by scale vaporization.

Since in most corrosion problems we are concerned more with the true consumption rate of the alloy or the depth to which its load-carrying ability has been altered, the most meaningful measurement is a thickness change. This is probably best made by a metallographic section, although there are inherent difficulties in establishing the original thickness and any thickness changes with sufficient accuracy. In addition to thickness of metal consumed, this technique can also provide other valuable information, such as depth of alloy depletion zone, depth of internal oxidation, depth of surface cracks, and thickness of various scale layers.

Of course, weight change is the easiest measurement to make. It can provide useful information if its limitations are realized and if supplemental data are also gathered to assist interpretation.

By way of contrast to the simple isothermal oxidation test, table 19-I lists some of the environmental conditions present in a gas turbine. Instead of the relatively simple gas composition of the furnace test, the engine atmosphere is made up of combustion products and can contain a variety of contaminants. These contaminants may come from either the jet propulsion fuel (sulfur and possibly vanadium) or the local environment in which the engine happens to be running (salt and water vapor). This complex atmosphere will result in faster corrosion than normally measured in laboratory furnaces.

The usual start-stop operation of an engine introduces an all-important cyclic

aspect to the problem. The cyclic variation of both temperature and stress can lead to thermal-fatigue cracking of alloys and/or spalling of protective scales with or without cracking of the underlying alloy. Both effects will accelerate corrosion rates.

The high-velocity gas stream in an engine, possibly containing particles of sand (ingested) or carbon (from engine combustion cans) can intensify corrosion by erosion and possibly by enhanced vaporization of protective scales.

The high pressure in an engine can also contribute to faster corrosion by accelerating the condensation of salts from the atmosphere, leading to fluxing of protective scales.

This contrast between a simple laboratory test and the engine environment is large and points up the necessity for evaluating the behavior of an alloy under conditions that at least approximate the ultimate use. However, full-scale engine testing is prohibitively expensive, except for alloys that have utmost potential of success as judged by simpler tests. Thus, tests are required at many points along the spectrum between the simple isothermal test and the ultimate engine test.

## NASA BURNER RIG

In an attempt to simulate some features of the engine environment, a so-called burner-rig facility has been designed and assembled here at Lewis. Similar facilities are used by other investigators; however, this one is unique in that it is capable of producing hot gases at velocities to approximately Mach 1 (ref. 1).

The burner rig is shown schematically in figure 19-3. It consists of a burner capable of operating on either natural gas or jet propulsion fuel and generating gas temperatures to 2800° F. A 2-inch-diameter water-cooled nozzle through which the hot gases expand produces gas velocities to approximately Mach 1. A cooling air jet supplies room-temperature air, also at Mach 1 velocity. A control thermocouple and exhaust ducts are provided. The usual sample is 4 inches long by 1 inch wide by 1/4 inch thick with a taper and a 0.030-inch radius on one edge to simulate the leading edge of an airfoil. The slot and channel shown on the sample in figure 19-3 are for gripping.

Eight samples can be tested at once in a rotating fixture in the exit path of the burner nozzle. Material temperatures to 2200° F can be achieved. The entire assembly of specimens can be dropped out of the hot gas stream and cooled rapidly. The usual cycle of operation is 1 hour at temperature followed by a 3-minute cool.

The usual data collected from the operation of such a test facility are weight change as a function of exposure time. However, it is also possible to obtain the

more meaningful surface recession rates, as was illustrated in reference 1, through the use of inert pin inserts in the burner-rig samples. Information on thermal cracking and the appearance of surface scales can also be obtained.

As sophisticated as this facility is in simulating engine gas chemistry and velocity, in the configuration shown in figure 19-3, it cannot simulate a most important parameter of the engine environment - stress. This deficiency is common to most such facilities in use throughout the country. The effect of stress in an engine environment on the corrosion resistance of superalloys is virtually unknown. However, as described in another paper of this conference by David Spera, a NASA burner rig has been combined with a tensile machine so that stress may be applied to samples positioned in the hot gas stream of the burner rig. This combined facility is currently used for basic studies related to the prediction of thermal-fatigue life. However, such facilities could also provide valuable information as to the effect of stress on corrosion resistance.

## COMPARISON OF ALLOYS

When superalloys are evaluated for corrosion resistance in the burner rig, it is indeed found that the severe environmental features are of such importance that the behavior and ranking of alloys are altered from those of the simple furnace test. This is illustrated in figure 19-4 (ref. 1). Here the weight change for four nickel-base alloys and two cobalt-base alloys (X-40 and Mar-M-509A) are recorded after 50-hour tests at 2000<sup>0</sup> F. In the upper portion of the figure, the results obtained in static-air isothermal tests are given. All alloys show weight gain: the two cobalt alloys show the poorest performance; and thoriated nickel chromium (TD-NiCr) appears to be the most corrosion resistant. This latter judgement may not be completely valid, as the true behavior of TD-NiCr may be masked by vaporizing scale, as will be shown shortly.

Behavior of these same alloys in the cyclic and high-gas-velocity environment of the burner rig is completely altered as shown in the lower portion of figure 19-4. Now all alloys lose weight, due primarily to scale spalling, and the best performer appears to be IN-100.

This comparison again illustrates the point that we cannot rely on simple testing alone to evaluate superalloys for engine service. Some effort must be made to introduce important environmental features of the engine.



## ENVIRONMENTAL EFFECTS

Three environmental features of the gas turbine which might be expected to play an important role in erosion-corrosion resistance are thermal cycling, gas velocity, and gas composition. Each of these features is considered separately and selected data presented to illustrate their importance.

### Thermal Cycling

The strong effect of thermal cycling on oxidation behavior is illustrated for the cobalt-base alloy WI-52 in figure 19-5 (based on unpublished data by Daniel L. Deadmore of Lewis). Weight change is plotted as a function of exposure time at 2000° F for several modes of furnace testing. Under isothermal conditions, the behavior of the alloy is as expected: a decreasing oxidation rate with increasing exposure time, indicating that the surface scale layer is offering some degree of protection.

Two curves are shown for cyclic testing; that is, instead of following weight change continuously, the samples were removed from the furnace at various intervals (20 hr and 1 hr), allowed to cool, and weighed. Under cyclic conditions, oxidation behavior is totally altered. Now a progressively more severe weight loss due to scale spalling is recorded. On each cooling cycle, some portion of the previously formed scale spalls from the surface because of both thermal stresses and, as suggested by Carl E. Lowell of Lewis, stresses resulting from a phase transformation in the scale. Upon reexposure to high temperature, oxidation occurs at an accelerated rate because some of the protective scale is now gone and the surface region of the underlying alloy is altered in composition. This attack under cyclic conditions becomes more severe as the frequency of the cycling is increased.

This example illustrates a phenomenon so severe for this particular alloy that it can be evaluated and studied in depth by simple furnace testing without high gas velocities or severe cycling rates. Also, because of the severity of spalling in this case, the simple weight change measurement can allow a fairly accurate appraisal of the oxidation behavior.

### Gas Velocity

An indication of the effect of gas velocity is illustrated in table 19-II (ref. 1). Weight loss values are recorded for identical specimens of a nickel-base alloy,

TD-NiCr, and a cobalt-base alloy, WI-52, after 100 hours of cyclic operation in the burner rig at 2000° F. Data were obtained under two velocity conditions: Mach 0.7 and Mach 1.

WI-52 is such a poor alloy under burner-rig conditions that there is no significant effect of gas velocity in the range investigated. On the other hand, TD-NiCr does show a strong response to gas velocity, with corrosion seemingly more severe at the higher velocity of Mach 1.

The explanation of this effect on TD-NiCr is not completely straightforward. It would seem reasonable that it might be explained by the more severe erosive action of the higher velocity gas. However, it may also be related to the loss of a protective scale by accelerated vaporization.

Chromia ( $\text{Cr}_2\text{O}_3$ ), a component of the scale on most superalloys, can vaporize at these high temperatures. Figure 19-6 illustrates the effect of the vaporization of  $\text{Cr}_2\text{O}_3$ .

Before discussing figure 19-6 in detail, it is necessary to point out a very important intrinsic aspect of the oxidation of TD-NiCr. It has been found by Carl E. Lowell of Lewis that the scales that form on TD-NiCr can be altered by surface preparation of the sample. A polished surface of TD-NiCr oxidizes to a thin layer of  $\text{Cr}_2\text{O}_3$  immediately adjacent to the alloy covered by layers of the spinel  $\text{NiCr}_2\text{O}_4$  and NiO. In contrast to this, a TD-NiCr sample prepared by surface grinding oxidizes to a scale consisting nearly exclusively of  $\text{Cr}_2\text{O}_3$ .

Now returning to figure 19-6, the behavior of a polished sample at 2200° F shows a continuous weight gain. However, the behavior of a ground sample is quite different. After experiencing an initial weight gain, a continuous linear weight loss occurs, indicative of no protective scale. In the case of the ground sample,  $\text{Cr}_2\text{O}_3$  vaporizes as fast as it forms, while the overlying NiO and  $\text{NiCr}_2\text{O}_4$  of the polished sample inhibit the loss of  $\text{Cr}_2\text{O}_3$ .

It is not known which of these two surface preparations actually offers the superior oxidation resistance. This determination will be made by more detailed measurements of thickness change. However, initial thickness-change measurements suggest that the ground surface, even with its evaporative loss of  $\text{Cr}_2\text{O}_3$ , might result in a lower rate of metal loss.

This evaporative loss of  $\text{Cr}_2\text{O}_3$  then may be an important factor in the velocity effect noted for TD-NiCr and may also be influential in the observed oxidation behavior of other high-chromium-content superalloys.

## Gas Composition

Table 19-III (based on ref. 1 and unpublished data by William A. Sanders of Lewis) illustrates the strong effect spurious components of the gas stream can have on corrosion resistance. The effect illustrated is the well-known catastrophic attack which can result from the combination of sea salt ingested in the engine and the sulfur contained in jet propulsion fuel.

When IN-100 is burner-rig tested using low-sulfur natural gas fuel with no intentional contaminants added, the expected thermal effect on weight change is observed. As shown in table 19-III, IN-100 loses 110 milligrams in 50 hours at 2000° and only 10 milligrams at 1800° F. A further reduction in temperature would be expected to result in only minute weight changes. In contrast to this expected behavior, table 19-III shows that a temperature reduction to 1650° F accompanied by sulfur and sea-salt gas contamination leads to the comparatively enormous weight loss of 8000 milligrams.

This catastrophic attack has become known as "sulfidation" or "hot corrosion" and can be a particularly severe problem for aircraft operating in marine environments such as from aircraft carriers or coastal airfields. This attack is generally believed to be due to the formation and condensation of  $\text{Na}_2\text{SO}_4$  which can flux protective scales and lead to exceedingly high corrosion rates. This particular form of corrosion is receiving attention today in both alloy and coating development efforts as well as in basic mechanistic studies.

## CONCLUDING REMARKS

A few examples have been given to illustrate and emphasize the many and varied factors that can affect corrosion resistance.

It is a fact that today we are up against a corrosion barrier. In the field of alloy development, this means that more attention should be given to corrosion resistance; our alloy development efforts should not be guided exclusively by mechanical properties requirements. We can no longer leave the protection of the alloys solely to the coater. The ultimate and nonreplaceable evaluation is the actual engine test; however, we need knowledge at many points short of an engine test: both basic knowledge, obtainable in relatively simple experimental procedures, and the more applied knowledge which requires specialized equipment for simulation of engine conditions.

It is absolutely necessary to simulate engine conditions. However, even simple laboratory tests, such as the classical oxidation test, can be conducted so as to

provide data that are more meaningful to actual alloy performance. For example, even simple tests can introduce the effects of cycling and surface preparation.

Efforts on all fronts, alloy development, coatings, basic corrosion studies, and advanced testing and evaluation, are required if we are to overcome the corrosion barrier.

#### REFERENCE

1. Johnston, James R.; and Ashbrook, Richard L.: Oxidation and Thermal Fatigue Cracking of Nickel- and Cobalt-Base Alloys in a High Velocity Gas Stream. NASA TN D-5376, 1969.

TABLE 19-I. - CORROSION IN GAS TURBINE ENGINE

Condition	Result
Oxidizing gas: Combustion products Sulfur, vanadium, salt, water	Accelerated corrosion
Cyclic temperature and stress	Spalling, thermal fatigue
High gas velocity (entrained particles of sand and/or carbon)	Erosion and vaporization
High pressure	Condensed salts and fluxing of protective scales

TABLE 19-II. - EFFECT OF GAS  
VELOCITY

Alloy	Weight loss after 100 hours at 2000° F, mg	
	Mach 0.7	Mach 1
TD-NiCr	840	1 400
WI-52	22 100	23 700

TABLE 19-III. - EFFECT OF GAS COMPOSITION

[IN-100, 50 hr, standard burner-rig cycle.]

	Natural gas		JP-5
Sulfur content	5 ppm		4000 ppm (max.)
Salt content	None		5 ppm
Temperature, °F	2000	1800	1650
Weight loss, mg	110	10	8000

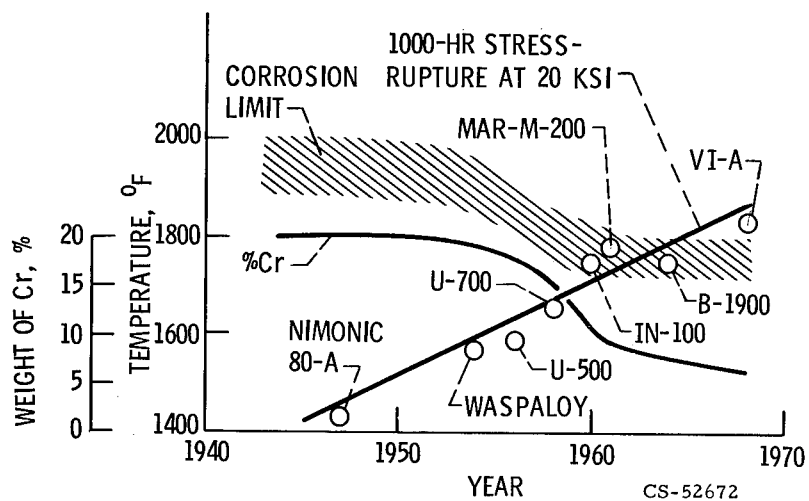


Figure 19-1. - Evolution of corrosion barrier. Nickel-base alloys.

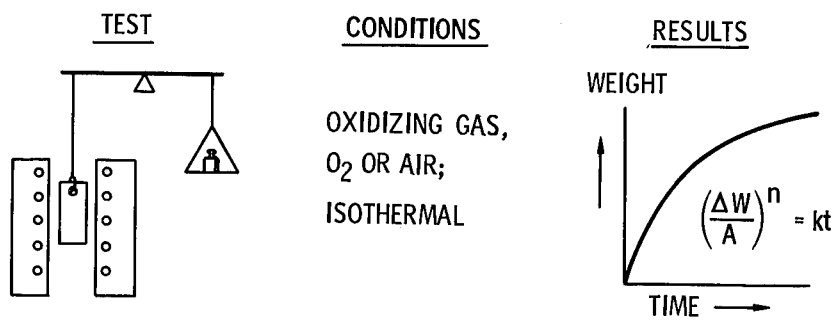


Figure 19-2. - Features of usual oxidation study.

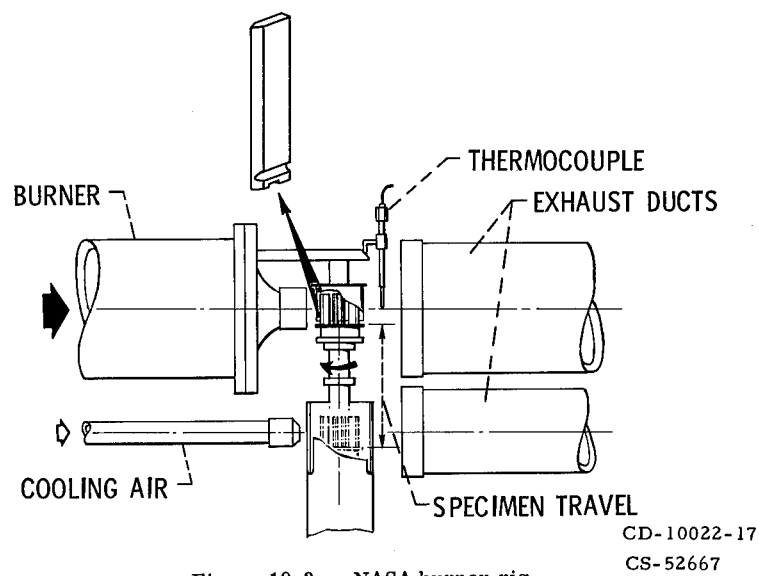


Figure 19-3. - NASA burner rig.

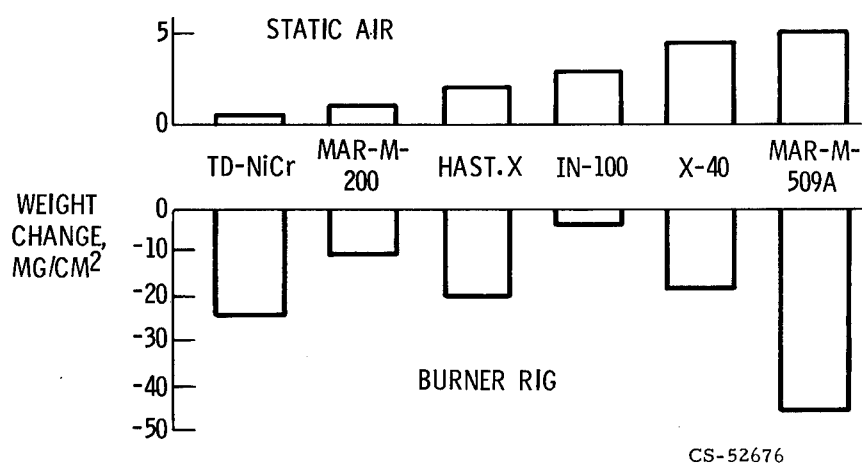


Figure 19-4. - Effect of testing method on ranking of alloys. Test conditions: 50 hours at 2000° F.

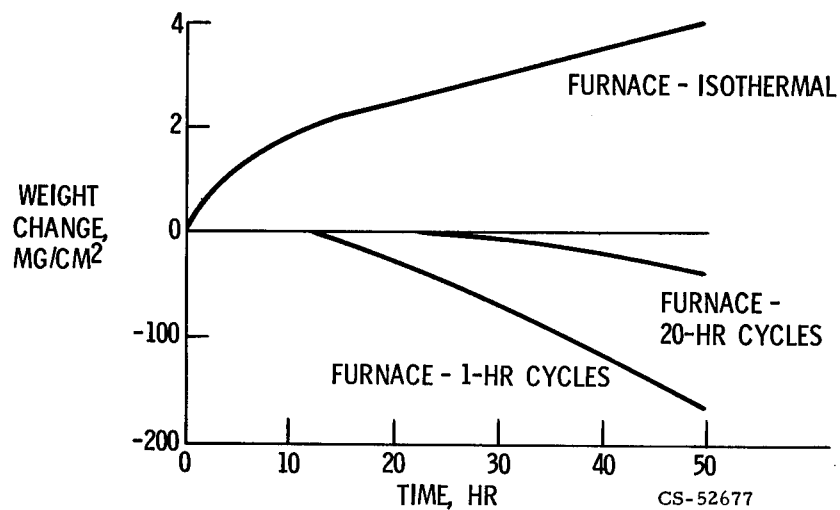


Figure 19-5. - Effect of thermal cycling on WI-52 at 2000° F.

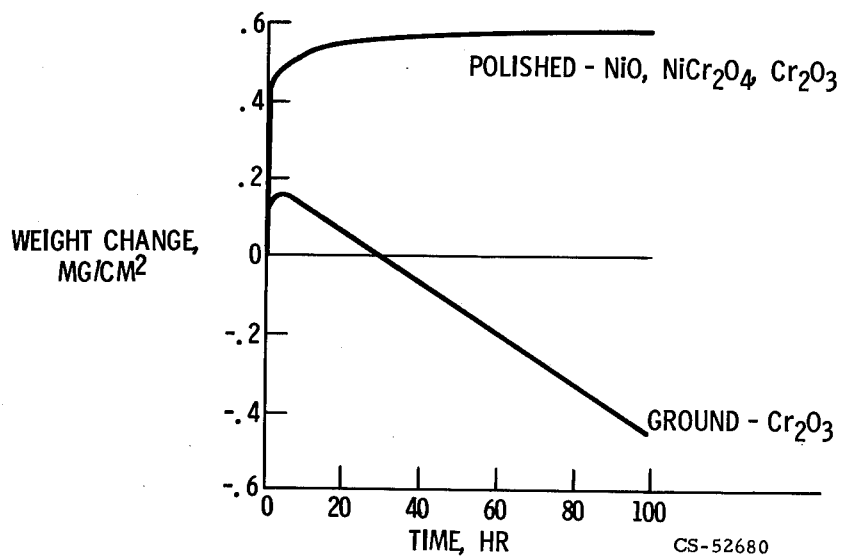


Figure 19-6. - Effect of  $\text{Cr}_2\text{O}_3$  vaporization from thoriated nickel chromium. Isothermal furnace test at 2200° F.





## 20. OXIDATION OF WI-52, A COBALT-BASE SUPERALLOY

Carl E. Lowell

The oxidation of WI-52 was studied by combining weight gain, high temperature X-ray diffraction, and high temperature microscopy experiments. All experiments were carried out at 1800° F in static air. The weight gain data followed a parabolic curve, implying a simple diffusion controlled reaction. High temperature X-ray diffraction, however, revealed a complex oxide growth pattern. The strongest phase initially was CoO with  $\text{Cr}_2\text{O}_3$  and  $\text{Co}_4\text{Cb}_2\text{O}_9$  as minor phases. As the oxidation progressed, the CoO and  $\text{Cr}_2\text{O}_3$  reacted to form a spinel,  $\text{CoCr}_2\text{O}_4$ . At the end of 100 hours,  $\text{CoCr}_2\text{O}_4$  was by far the major oxide. High temperature microscopy showed complex oxide morphology changes. Initially, the grain boundary carbides,  $(\text{Cb}, \text{W})\text{C}$ , oxidized rapidly. As this reaction slowed, the matrix oxidized uniformly, giving the color appearance of a thickening interference film. Finally, a nodular oxide nucleated in the middle of the matrix. This oxide spread laterally and in thickness until it covered all but the grain boundary oxide. Combining the results of all experiments led to a three-stage model of oxidation. The first was the oxidation of the grain boundary  $\text{CbC}$  and the nearby matrix to form  $\text{Co}_4\text{Cb}_2\text{O}_9$ . The succeeding matrix oxidation consisted of CoO formation with  $\text{Cr}_2\text{O}_3$  formed between the CoO and the metal. The final stage was the reaction of CoO and  $\text{Cr}_2\text{O}_3$  to form  $\text{CoCr}_2\text{O}_4$  and its subsequent growth over all of the surface except for parts of the grain boundary oxide.

The preceding paper shows that the use of superalloys in jet engines is currently limited by a lack of oxidation resistance at operating temperatures hoped for in future designs. One approach to an oxidation resistance improvement of these alloys is through an understanding of their oxidation processes. This paper is an attempt at such an understanding. The oxidation of a superalloy is, however, a complex process which cannot rely on the use of a single experimental technique, such as the weight change experiments described in the previous paper. This work is a synthesis of the results obtained from several techniques to form a comprehensive view of the oxidation of a superalloy.

The first technique whose results are described is the standard oxidation test - weight change experiments. This technique is used to determine an overall rate of oxidation. To supplement this information with a knowledge of what oxides are being formed and their changes in relative abundance with time, high temperature X-ray

diffraction is employed. High temperature microscopy is used to obtain information concerning the change of morphology of the oxide with time. Finally, these results are combined with a conventional post mortem analysis by room temperature X-ray diffraction and metallography.

This paper presents the results of the use of this approach on WI-52. This cobalt-base alloy is currently used in jet engines at temperatures lower than those dictated by its strength potential.

## MATERIALS AND PREPARATION

The following shows the nominal composition of WI-52:

Co	Cr	W	Cb	Fe	C	Si	N
63.0	21.0	11.0	2.0	2.0	0.45	0.25	0.25

While individual heats show slight variations, all samples in this work came from the same heat, thus making comparisons more reliable. The important elements from an oxidation standpoint are the first four, which are the major oxide formers (Co, Cr, W, and Cb).

Figure 20-1 is the microstructure of as-cast WI-52. The matrix phase is basically a solid solution of Cr, W, Fe, and probably Mn and Si in Co. At the grain boundaries are two kinds of carbides. Most of the carbides are needlelike (Cb,W)C. The rest are irregularly shaped particles of  $\text{Cr}_6\text{C}$ .

All samples were prepared by cutting to size followed by polishing to a 0.5 diamond finish to remove surface roughness and stress. No heat treatment was given to the samples prior to oxidation.

## PROCEDURE AND RESULTS

### Weight Gain

Figure 20-2 shows the results of the weight gain experiment, which was outlined in Dr. Probst's paper. The data are obtained by suspending the sample from a balance into a hot furnace and recording its change in weight as a function of time. In this case the weight change per unit area was squared and plotted against time. This is a commonly used technique to determine whether or not the data fit a para-

bola. It is commonly assumed that if the weight change is parabolic then the oxidation process is simply a diffusion controlled layer growth. Although our data do fit such a parabola, the following shows that the usual conclusions do not apply.

### High Temperature X-Ray Diffraction

If, instead of suspending the sample in a furnace from the end of a balance, we heat the sample while it is positioned in an X-ray diffractometer, we get the results shown in figure 20-3. Here the relative X-ray intensity of phases in the oxide is plotted as a function of time. These data were taken from X-ray diffractometer scans made at frequent intervals while the sample oxidized. The major phase was CoO initially. Also present are  $\text{Cr}_2\text{O}_3$ ,  $\text{Co}_4\text{Cb}_2\text{O}_9$ , and some spinel,  $\text{CoCr}_2\text{O}_4$ . With time the CoO and  $\text{Cr}_2\text{O}_3$  react to form  $\text{CoCr}_2\text{O}_4$  causing a marked lessening of the amounts of the simple oxides. The spinel intensity continues to increase at the expense of the other oxides until the end of the test (100 hr).

### High Temperature Microscopy

Figure 20-4 shows the layout of the high temperature microscope. The sample is heated on a strip of platinum through which current is passed. Normal incident illumination is provided by a xenon lamp. The quartz plate prevents volatiles from the sample from coating the lens. The beam splitter allows focusing while the time lapse camera is in operation. This equipment is used to photograph the changing morphology of the surface of an oxidizing sample. In the sequence shown, the time scale has been reduced by adjusting both the frame interval and the temperature. As oxidation begins, we first see the reaction of the grain boundary carbides with the matrix and oxygen to form  $\text{Co}_4\text{Cb}_2\text{O}_9$  (see fig. 20-5(a)). Next, the matrix begins to oxidize to CoO with probably  $\text{Cr}_2\text{O}_3$  underneath (fig. 20-5(b)). A change in color is noted due to interference film thickening as the oxide layer grows. Also  $\text{Cr}_2\text{O}_3$  is formed over the  $\text{Cr}_6\text{C}$  at the grain boundaries. Now, in the middle of the CoO layer nodules of  $\text{CoCr}_2\text{O}_4$ , the reaction product of CoO and  $\text{Cr}_2\text{O}_3$ , begin to form (fig. 20-5(c)). These nodules start the final stage of the process which is their growth upwards and laterally until they cover all but the areas of  $\text{Cr}_2\text{O}_3$  which formed over the  $\text{Cr}_6\text{C}$  and the  $\text{Co}_4\text{Cb}_2\text{O}_9$  which formed over the (W,Cb)Co (fig. 20-5(d)).

## Post Mortem Analysis

After oxidation the samples were scraped for room temperature X-ray diffraction and sectioned for metallography. Room temperature diffraction confirmed the high temperature diffraction data as to the oxides present. Figure 20-6 is the microstructure of WI-52 after oxidation for 100 hours at 1800<sup>0</sup> F. The surface oxide appears to be single phase,  $\text{CoCr}_2\text{O}_4$ , and continuous but of varying thickness. Notice the rather extensive subscale corrosion along grain boundaries caused by the oxidation of the grain boundary carbides.

## Synthesis

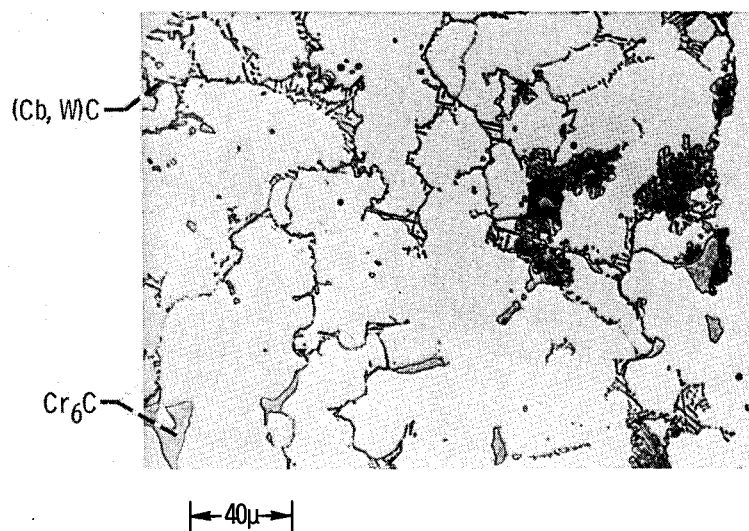
Combining all of the previous sources of information gives the model for the oxidation of WI-52 shown in figure 20-7. The top line represents the unoxidized metal as it reaches temperature. The dark vertical lines represent the (W,Cb)C, the triangle represents  $\text{Cr}_6\text{C}$ , and the shaded area represents the cobalt solid solution. As oxidation starts on the second line, the (Cb,W)C have begun to oxidize to  $\text{Co}_4\text{Cb}_2\text{O}_9$  with the evolution of CO gas. The fact that one of the products of this reaction is a gas undoubtedly helps keep open a path for oxygen down the grain boundaries. This results in the subscale oxidation shown earlier. As the grain boundary attack slows, the matrix begins to oxidize to form a thin film of CoO overlaying  $\text{Cr}_2\text{O}_3$ . However, over the small  $\text{Cr}_6\text{C}$  particles only  $\text{Cr}_2\text{O}_3$  forms. Shortly after the CoO film formation, the CoO begins to react with the underlying  $\text{Cr}_2\text{O}_3$  to form  $\text{CoCr}_2\text{O}_4$ . The final stage shown on the bottom line shows how the  $\text{CoCr}_2\text{O}_4$  has grown both in thickness and laterally to almost completely cover the surface. Note that the oxides over the carbides are the last to be covered and therefore the thinnest  $\text{CoCr}_2\text{O}_4$  layers are at that point.

## CONCLUDING REMARKS

As a result of this investigation, we have gained an understanding of the intrinsic oxidation of WI-52. This understanding alone does not, however, solve the oxidation problems of this material for use in engines where thermal cycling, high gas velocity, and sulphidation are complicating effects. These factors were clearly defined by Dr. Probst in his paper. This work, however, can be used for finding directions in which to proceed for improvement of oxidation resistance. It may also be used to predict the effect of variables such as stress and microstructural changes on the ox-

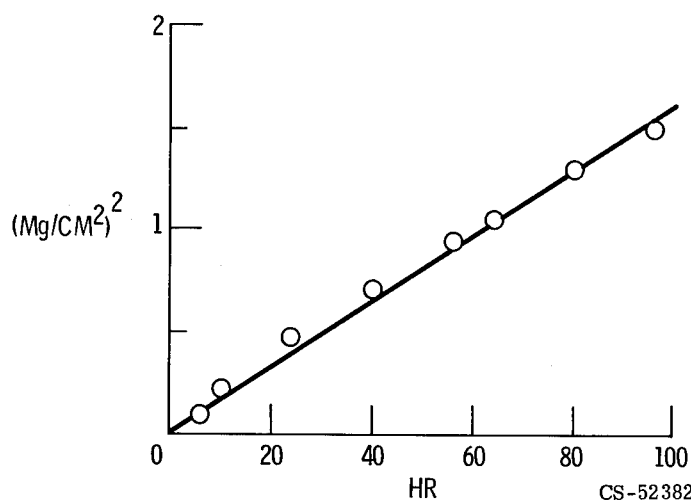
dation process. For example, the microstructure might be altered to minimize subscale penetration of the oxide. Another possibility might be the use of surface stress to promote  $\text{Cr}_2\text{O}_3$  formation and inhibit  $\text{CoCr}_2\text{O}_4$ . This could be useful inasmuch as  $\text{Cr}_2\text{O}_3$  scales are more stable during thermal cycling than spinel scales.

Even though we cannot solve all the problems associated with the corrosion of this alloy, we have established a base of information on which to build.



CS-52378

Figure 20-1. - Microstructure of as-cast WI-52. X500.



CS-52382

Figure 20-2. - Parabolic weight gain of WI-52 in air (1800° F).

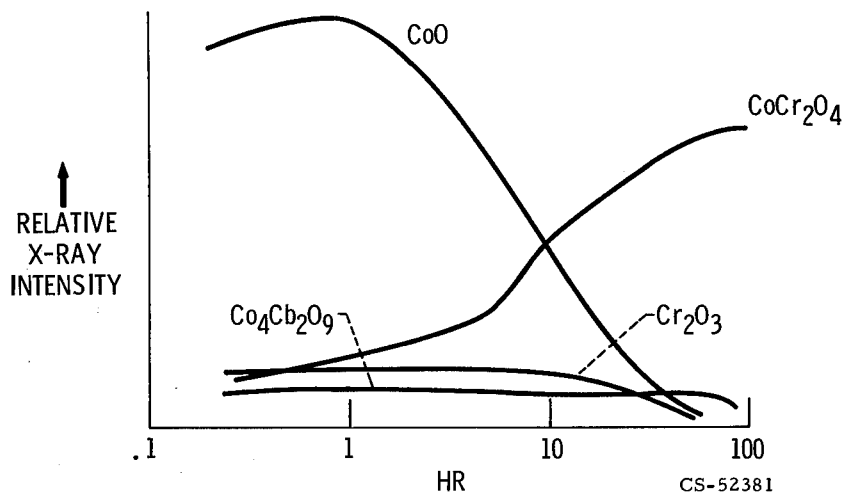


Figure 20-3. - Composition changes in oxide layer on WI-52 (1800° F).

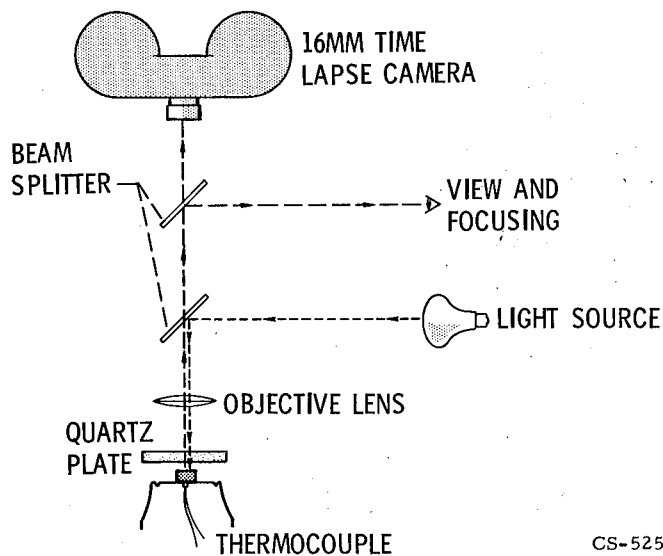
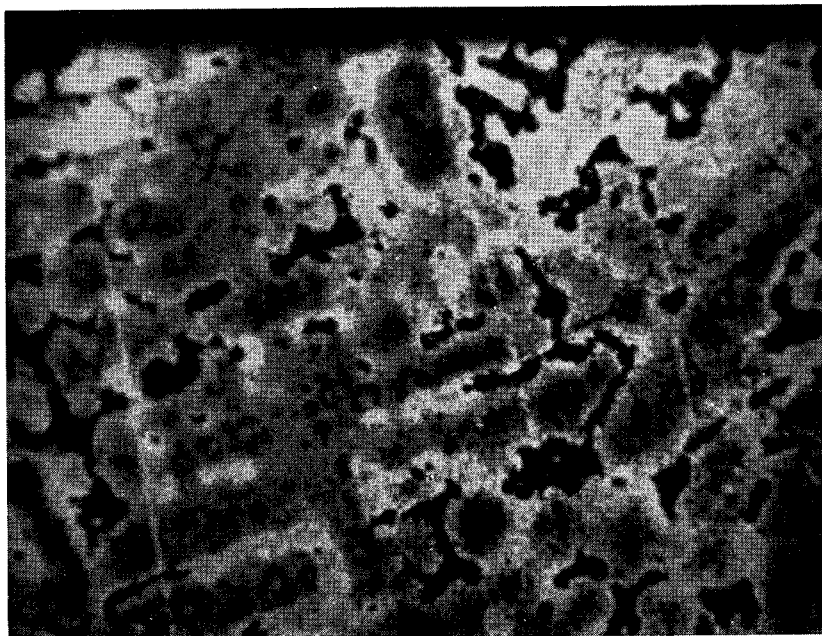
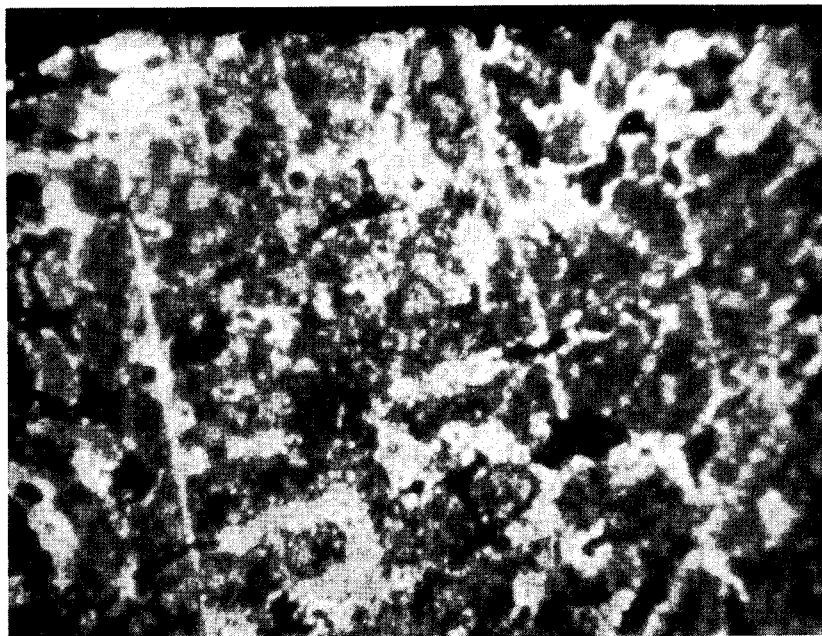


Figure 20-4. - High temperature microscope.



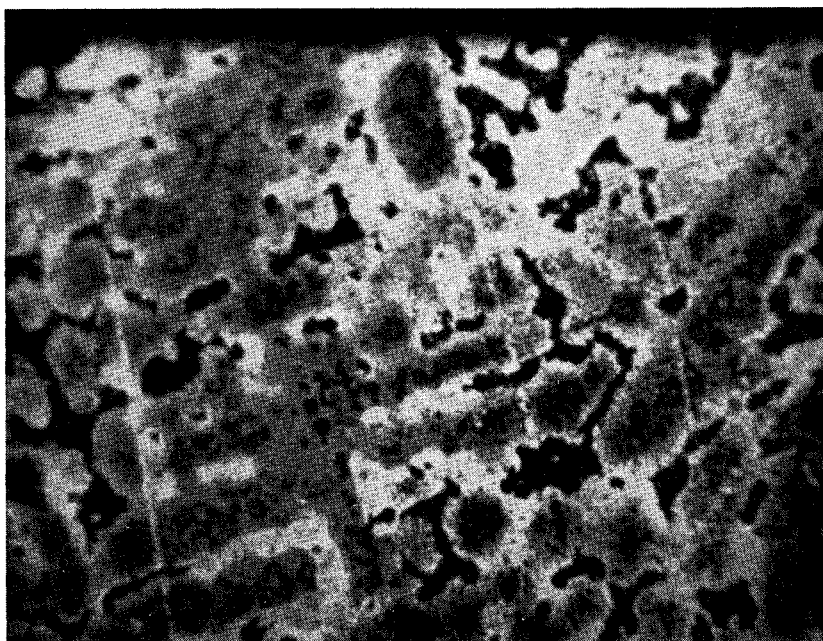


(a) Oxidation of (Cs, W)C to  $\text{Co}_4\text{Cb}_2\text{O}_9$ .

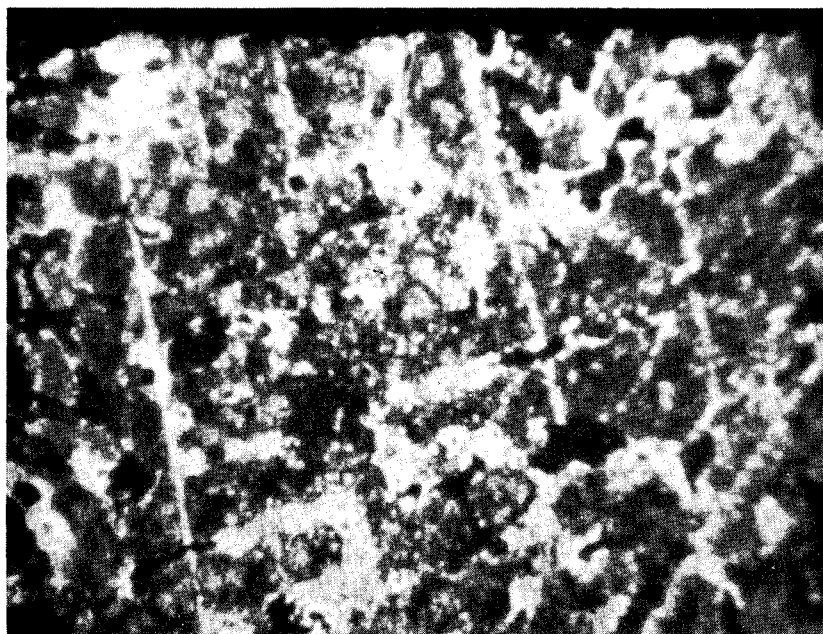


(b) Oxidation of matrix to  $\text{CoO}$  and  $\text{Cr}_2\text{O}_3$ .

Figure 20-5. - High temperature microscopy of oxidizing WI-52.

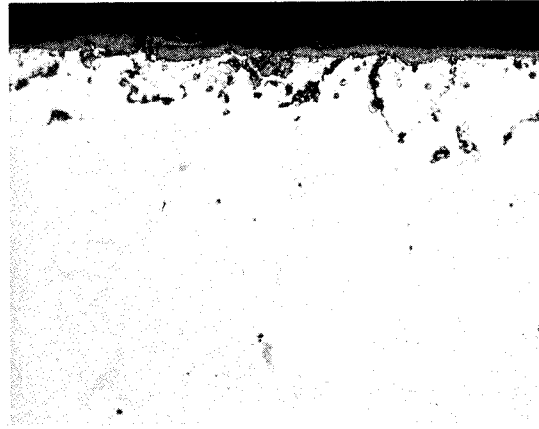


(c) Initiation of  $\text{CoCr}_2\text{O}_4$  formation.



(d) Growth of  $\text{CoCr}_2\text{O}_4$ .

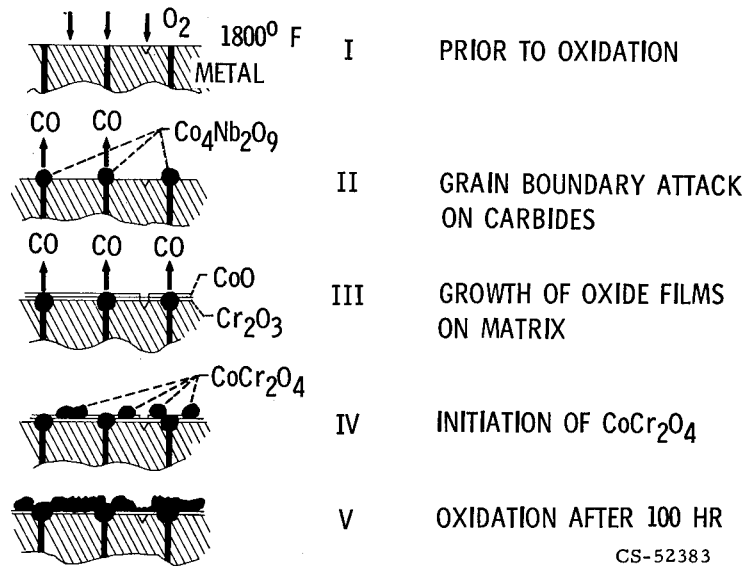
Figure 20-5. - Concluded.



→ | 20μ | ←

CS-52379

Figure 20-6. - Structure of corrosion zone on WI-52  
(100 hr; 1800° F). X750.



CS-52383

Figure 20-7. - Sequential oxidation of WI-52.

## 21. PROTECTIVE COATINGS FOR SUPERALLOYS

Salvatore J. Grisaffe

Protective coatings offer one means of improving the oxidation resistance of superalloys. The useful time-temperature limits of selected commercial aluminide coatings were more closely defined by evaluation in the Lewis Mach 1 burner rigs. Coating lives decrease rapidly at temperatures above 1900° F. A principal factor in reduced life was the oxide spalling that occurred on thermal cycling. Loss of the protective aluminum oxide scale by spalling depleted the coating of aluminum. Less protective surface oxides then formed and rapid oxidation attack occurred. Such studies indicate several potential ways of improving aluminide coatings. One of these involves doping the aluminide with additional elements to promote improved resistance to oxide spalling.

In order to achieve protection at temperatures beyond those possible with aluminide coatings, alternate coating concepts are under investigation. One such approach combines the excellent oxidation resistance (up to 2200° F) of low-strength heater alloys with the high-strength of oxidation prone superalloys. Cyclic laboratory furnace tests have shown that such systems offer considerable potential. For example, a Fe-Cr-Al-Y cladding on the cobalt alloy WI-52 showed a net weight loss after 380 hours at 2000° F as compared with 30 hours for a commercial aluminide coating. This is an improvement of more than a factor of 12. Further evaluation of such promising systems is planned using the Mach 1 burner rig.

Protective coatings are important to NASA for many aerospace applications. Thermal barrier coatings greatly extended the life of the X-15 rocket engine. These coatings prevented the development of hot spots on the regeneratively cooled nozzle which sometimes resulted in burn-through. The descent engine of the Apollo 11 incorporated a coated niobium alloy nozzle extension skirt. This coating prevented oxidation during ground testing and actual mission operations. As system temperatures are increased to improve performance, the number of aerospace applications requiring coatings is increasing rapidly. For this reason, we are conducting research and development on a wide variety of coatings to meet such needs. Coatings for refractory metals, chromium alloys, dispersion-strengthened materials, and superalloys are all under study. This paper will limit its coverage to the development of coatings for nickel- and cobalt-base superalloys.

The trend in superalloy development in recent years has been to increase high-temperature strength at the expense of oxidation resistance. One way of protecting these strong, new alloys is by physically separating them from the oxidizing environment. This can be done by covering their surface with a protective coating. This paper summarizes Lewis efforts to understand and improve conventional aluminide coatings for superalloys, along with concurrent work on the development of advanced protection systems.

## ALUMINIDE COATINGS FOR SUPERALLOYS

Figure 21-1 shows a schematic cross section of an aluminide coated superalloy. By enriching the superalloy surface with aluminum (sometimes small amounts of chromium, titanium, or silicon are also added), a layer of intermetallic aluminide is formed. This is predominantly NiAl for nickel alloys and CoAl for cobalt alloys. Since aluminum is the main element added, the aluminide composition is mainly dependent on the starting composition of the superalloy base material. When this aluminide is exposed to an oxidizing environment, a thin, adherent, and protective layer of aluminum oxide ( $\text{Al}_2\text{O}_3$ ) rapidly forms on its surface. Aluminum oxide is a good diffusion barrier to both oxygen and metal cations from the substrate and coating, and it forms the basis of this successful protection system. The coating is merely a reservoir to rebuild the oxide if it is damaged.

Beneath the coating is a reaction-diffusion zone formed during coating deposition by interdiffusion. At high temperatures, continued interdiffusion can cause problems. Substrate elements diffusing into the coating can decrease its protective ability. In addition, the diffusion of coating-elements into the substrate can affect its strength and stability. One type of metallurgical instability that can be caused by coating elements diffusing into the superalloy substrate is shown in figure 21-2. This is a cross section of the interdiffusion zone beneath a chromium-rich aluminide coating on the nickel alloy B-1900 (ref. 1). The composition of this alloy, one of the stronger nickel alloys, has been carefully adjusted to prevent the precipitation of embrittling phases during long, high-temperature service. After 100 hours at  $1850^\circ\text{F}$  ( $\sim 1020^\circ\text{C}$ ), however, coating-element interdiffusion has caused the precipitation of unwanted sigma-phase needles in the interdiffusion zone. Such phases can have an adverse effect on mechanical properties of the superalloy. Thus, the coating chemistry must also be controlled to achieve optimum protection and minimize the formation of such unwanted phases.

Some coating suppliers have been quite successful in achieving this balance. Aluminide coatings are being widely used to protect aircraft gas turbine engine

parts from oxidation. Some typical cobalt alloy WI-52 stator vanes that have been aluminized are shown in figure 21-3. In most current engines, such parts operate at temperatures no more than 1600° to 1700° F (870 to 925° C). However, the time-temperature limits of such coatings are not well defined.

As part of the Lewis effort to support high-temperature engine development, one of the first goals was to characterize the useful upper temperature limits of commercial coatings. A number of commercial coatings were evaluated in Mach 1 burner rigs. Rapid weight loss or gross visual deterioration criteria were used to establish failure times. Some of the approximate lives of coatings in this facility, along with comparative values for uncoated superalloys, are summarized in figure 21-4. This figure relates temperature and life. The shaded areas are representative of lives of bare cobalt and nickel alloys. These data show that the nickel alloys are generally more oxidation resistant than the cobalt alloys. There are, of course, exceptions that depend on specific alloy composition. Summaries of coating life data are represented by lines here for the sake of simplicity. Again, coated nickel alloys generally have longer lives than the coated cobalt alloys. For example, at 1900° F (1035° C), a cobalt alloy such as WI-52 suffers severe oxidation in only 10 hours, but, with a commercial aluminide coating, the life was increased to over 300 hours. A nickel alloy such as IN-100 had a life of about 50 hours at 2000° F (1092° C), and when coated this alloy had a life of around 300 hours. As figure 21-4 shows, life decreases rapidly with increasing temperature. The present coatings do not have long service potential at temperatures above 1800° F. To achieve longer lives between overhauls and the higher operating temperatures required for advanced aircraft engines, improved coatings are definitely needed.

Unfortunately, it is difficult to know just how to improve commercial aluminide coatings. Frequently, information on both coating composition and processing techniques are held proprietary by the coating vendors. Furthermore, there has been little systematic study of the factors that lead to degradation and eventual failure of these coatings during service. An understanding of such factors is needed if a rational coating improvement program is to be formulated.

To achieve insight into the deposition of aluminide coatings on both nickel and cobalt alloys, studies are being conducted at Lewis in which temperature, time, activator, and starting compositions are being varied using a pack cementation coating approach.

To achieve insight into coating degradation during service, a detailed study of these experimental coatings, as well as commercial coatings, is being conducted. As an example of this work, a discussion of the performance of one of the best commercial coatings on cobalt alloy WI-52 is presented. Because the coating compos-

ition is proprietary, it is not described here. This system's oxidation resistance has been evaluated at temperatures up to 2100<sup>0</sup> F in both cyclic furnace and burner rig tests. We have examined coating performance by both weight change and metallographic measurements. This combination allows the gain or loss of weight to be correlated with coating loss, oxide scale location, and microstructural changes. Since coating failure was being determined, tests were stopped before alloy surface recession became extensive. To follow the oxide scaling and coating-superalloy interdiffusion behavior, we are using both X-ray diffraction and electron microprobe analyses. Although this study is not yet complete, some of the results obtained to date are presented in the following paragraphs.

The initial tests were conducted in high-temperature furnaces. In these tests, the frequency of cycling specimens in and out of the furnace exerted a major influence on coating life as shown in figure 21-5.

In figure 21-5, weight change is plotted versus air exposure time at 2000<sup>0</sup> F (1092<sup>0</sup> C). When 20-hour cycles were used, the coating exhibited relatively good performance - a life of nearly 200 hours at 2000<sup>0</sup> F (1092<sup>0</sup> C). Such long time cycles are frequently used in oxidation testing to minimize the manpower and time involved with removing and re-inserting specimens into a furnace. However, when 1-hour cycles were used to duplicate the cycle frequency used in the burner rigs and to more closely simulate high-speed aircraft engine cycles, the coating life was drastically decreased. These data suggest that for this aluminide coating on WI-52, coating failure is due primarily to the spallation of the protective aluminum oxide scale rather than to a time-sensitive diffusion-controlled process.

Since the surface aluminum oxide apparently spalls on each cool down, the coating reservoir must supply aluminum to rebuild this scale. Eventually, all the aluminum is consumed and the coating fails. The changes in the coating microstructure that accompany this degradation are shown in figure 21-6.

Figure 21-6 shows metallographic cross sections of aluminide coated WI-52 at various stages of degradation. The top micrograph shows the as-coated condition. Here, the coating thickness is between 2 and 3 mils. After cyclic exposure, (lower left), the CoAl layer thickness has decreased as compared with its original value (indicated by the bracket drawn at the right). Finally, when no more CoAl is left to supply aluminum to rebuild the protective oxide scale, the coating system fails (lower right). The scale then consists of the same oxides observed on unprotected WI-52.

Tests of aluminide coated WI-52 were also conducted in the Mach 1 burner rig. For this alloy and coating system, the results achieved in the 1-hour cyclic furnace tests compared favorably with those of the burner rig tests as shown in figure 21-7. This figure presents weight change versus time at 2000<sup>0</sup> F (1092<sup>0</sup> C).

The curves for the furnace and the burner rig are not very different. Similar behavior has been observed for some aluminide coated nickel alloys. Where spalling of the surface oxide is the critical factor in coating failure, it appears that simple cyclic furnace tests can be used to gain considerable insight into system performance. Confirmation by the more costly burner rig testing is required, however.

Tests on aluminide coated WI-52 in the Mach 1 burner rigs were conducted at 1900°, 2000°, and 2100° F (1035°, 1092°, and 1145° C). The lives of the aluminide coating at these temperatures are shown in figure 21-8. There is a linear relation between the log of the coating life and temperature. At 1900° F (1035° C), life was about 300 hours, at 2000° F (1092° C) it was 60 hours, and at 2100° F (1145° C) it was only 12 hours. For each 100° F (~55° C) increase in temperature, the life decreases by an order of five. While this line shows long extrapolated lives around 1700° F (925° C), it also shows that such coatings need improvement if they are to be used at higher temperatures.

The results of this and other concurrent studies have suggested several routes to improve the performance of simple aluminide coatings: improve oxide adherence, modify coating microstructure and develop improved deposition techniques. Clearly, from all the previous data, increasing the adherence of the oxide scale to minimize spalling should be a primary goal. This is currently being studied by examining the effect of small chemistry changes on the oxidation and scale spalling tendencies of bulk NiAl. Modification of coating microstructure by the incorporation of inert particles is being also studied. Such modification may eliminate the columnar grains sometimes found in aluminide coatings. The presence of columnar grain boundaries, perpendicular to the surface, provides short-circuit oxidation paths to the substrate. Alternate deposition techniques are also being sought which offer better control over aluminum deposition and interdiffusion. Aluminide coated nickel alloy specimens, coated by fused salt metallizing, an electrolytic process with inherently good control, are currently being evaluated.

## MULTICOMPONENT PROTECTION SYSTEMS

The work described so far has dealt with relatively simple aluminide coatings. To provide oxidation protection at temperatures significantly above the operating limits for these simple aluminides, it appears that coatings of more complex chemistry may be required. For example, alloys such as FeCrAlY and NiCrAl have been used as heating elements because of their excellent oxidation resistance at temperatures up to at least 2200° F (~1200° C). Such alloys are much too weak for structural application in aircraft engines at high temperatures. However, they



might be useful in the form of coatings or claddings on stronger, but less oxidation resistant superalloys. Unfortunately, currently used commercial coating processes do not permit controlled deposition of such multielement coatings.

In order to evaluate the feasibility of using these highly oxidation resistant iron and nickel-base alloys for coatings, we have been conducting a program in which the desired alloy, in thin foil form, is hot-gas pressure bonded to the surface of typical superalloys. Claddings of FeCrAlY, NiCrAl, and Ni30Cr have been applied to IN-100, WI-52, and, to a lesser extent, TD-Ni and TD-NiCr (thoria dispersion-strengthened materials). Other techniques of depositing such coatings which may be more amenable to coating complex airfoil shapes are also being explored. All these clad-superalloy combinations have been in cyclic furnace tests, and the results are very encouraging (ref. 2).

For the purpose of continuity and brevity, only one cladding, (Fe25Cr4Al1Y) on WI-52, will be discussed in this paper. One-hour cyclic furnace test results for this system are shown in figure 21-9 as a weight change versus time plot. Figure 21-9 also shows comparative data for uncoated and aluminide coated WI-52. Clearly, the clad WI-52 has the best oxidation resistance. If the clad and coated systems are arbitrarily compared at the point where their weight change curves cross from weight gain to weight loss, the FeCrAlY cladding shows about a factor of 12 improvement (380 hr for the FeCrAlY cladding and 30 hr for the coating). Because of this good performance and that of other systems studied, burner rig tests will be conducted on a number of clad superalloys and dispersion strengthened materials in the near future.

In such systems, where two alloys of different composition are in intimate contact, however, there is always the possibility of extensive interdiffusion. Figure 21-10 (ref. 2) shows the microstructures of the as-bonded FeCrAlY/WI-52 system and the same system after 200 hours at 2000° F (1092° C). The as-bonded specimen shows that enough interdiffusion occurred during bonding so that the cladding was metallurgically bonded to the WI-52. After 200 hours at 2000° F (1092° C), no gross interdiffusion is visible. However, some second-phase formation is evident (light globular areas) in both the cladding and in the WI-52. Furthermore, some voids are present near the cladding-superalloy interface. Both of these factors show that interdiffusion is a potential problem for long service. The use of diffusion barriers may be required to allow such systems to reach their full potential.

## CONCLUDING REMARKS

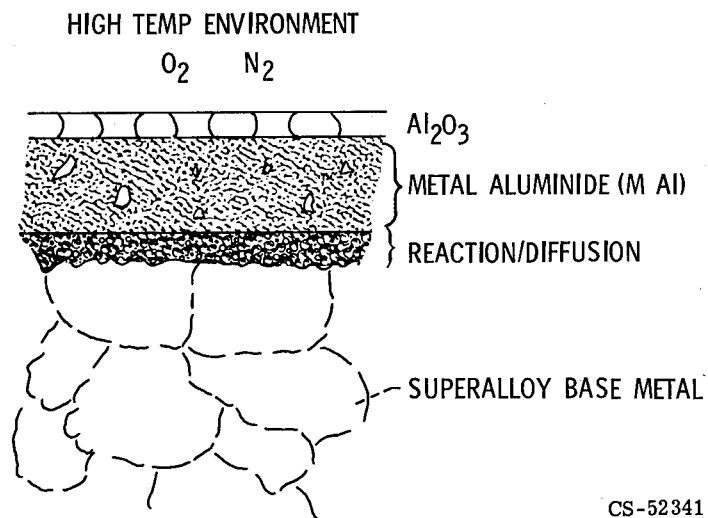
This paper has attempted to provide a description of the current state-of-the-

art in aluminide coatings for superalloys as well as information on some of the routes being followed at the Lewis Research Center to achieve improved aluminide coatings.

From the limited data available at this time, it is probable that metallic coatings capable of providing long resistance to oxidation at temperatures up to about 2000<sup>0</sup> F (1092<sup>0</sup> C) can be developed. Interdiffusion between the coating and the substrate appears to set the upper use-temperature limit for such metallic coatings. For higher temperature service, more inherently oxidation resistant alloys or greatly different types of coatings will be required.

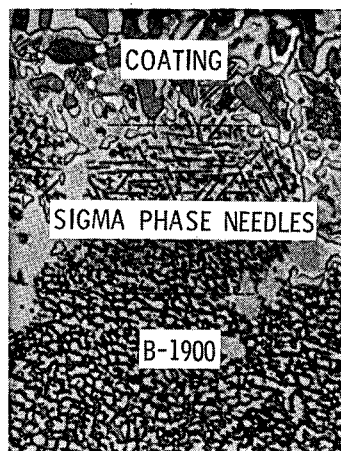
## REFERENCES

1. Moore, V. S.; Brentnall, W. D.; and Stetson, A. R.: Evaluation of Coatings for Cobalt and Nickel Base Superalloys. Vol. 1. Rep. RDR-1474-2, Solar Div., International Harvester (NASA CR-72359), Jan. 31, 1969.
2. Gedwill, Michael A.: An Evaluation of Three Oxidation-Resistant Alloy Claddings for IN-100 and WI-52 Superalloys. NASA TN D-5483, 1969.



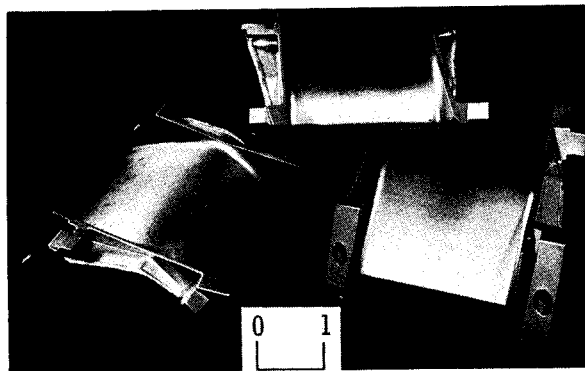
CS-52341

Figure 21-1. - Schematic cross section of aluminide coating on superalloy.



CS-51478

Figure 21-2. - Superalloy instability caused by coating interdiffusion. Sigma phase precipitation beneath aluminide coating on B-1900 after 100 hours at 1850° F. X1400.



IN.

CS-51474

Figure 21-3. - Aluminide coated WI-52 turbine vanes.

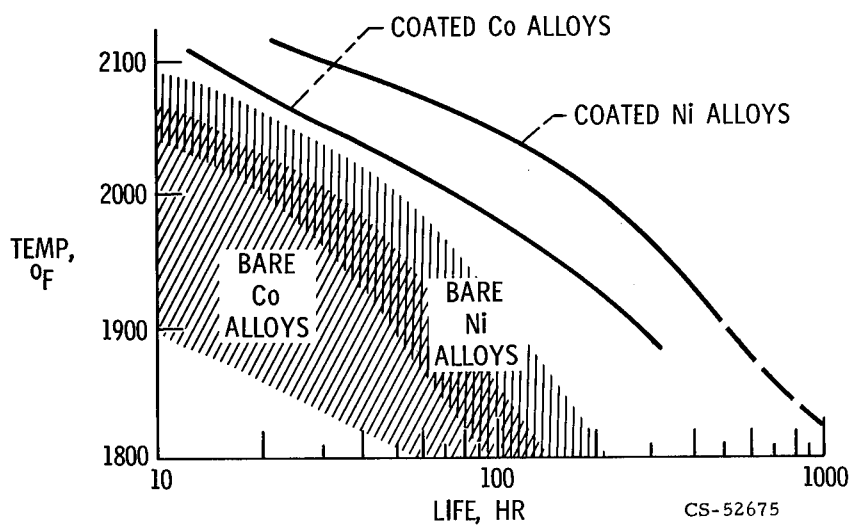


Figure 21-4. - Temperature-life summary of uncoated and coated superalloys tested in Mach 1 burner rig.

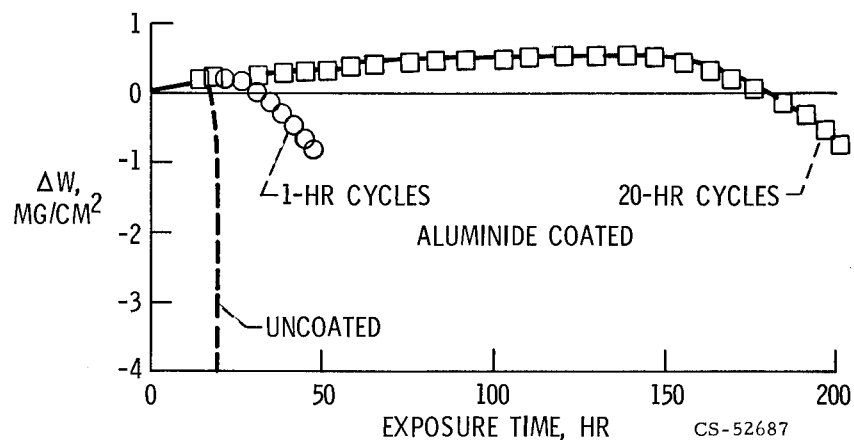


Figure 21-5. - Cycle frequency effect on weight change of aluminide coated WI-52 that was furnace tested at 2000° F.

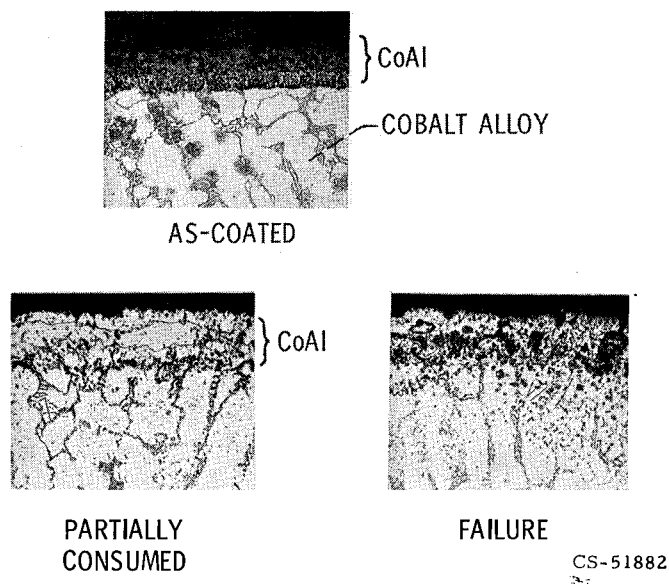


Figure 21-6. - Typical microstructure changes accompanying aluminum depletion of aluminide coated WI-52. X250.

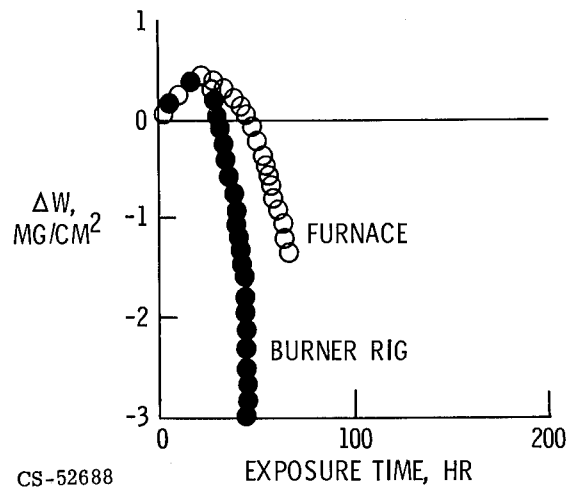


Figure 21-7. - Comparison of furnace and burner rig weight change data for aluminized WI-52 tested at 2000° F using 1-hour cycles.

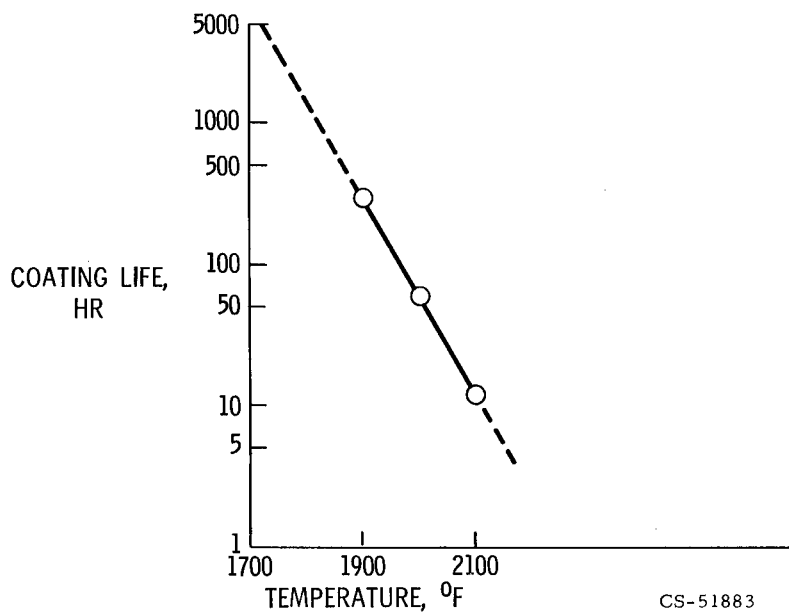


Figure 21-8. - Relation between temperature and Mach 1 burner rig life for aluminide coated WI-52 tested in 1 hour cycles.

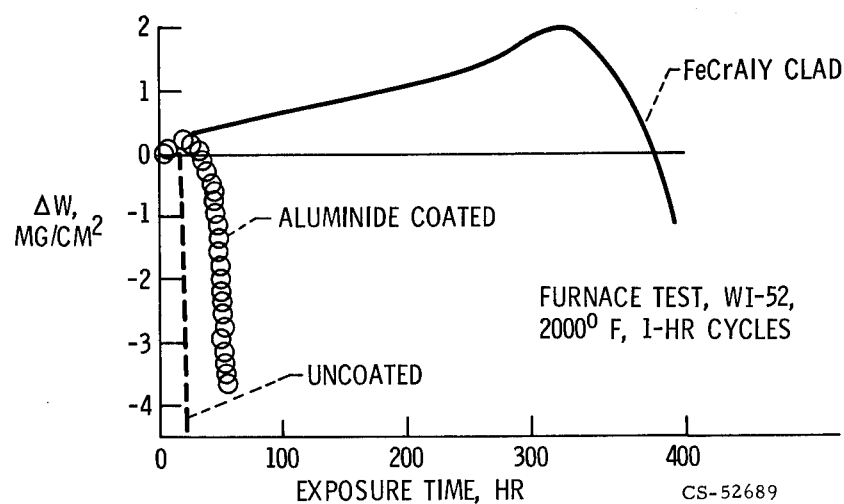


Figure 21-9. - Comparison of weight change behavior for aluminide coated WI-52 and FeCrAlY clad WI-52 tested using 1-hour cycles.

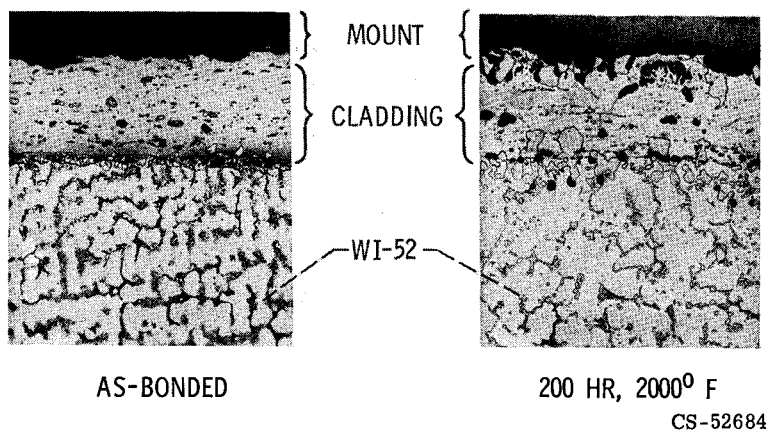


Figure 21-10. - Cross-sectional microstructures of as-bonded and oxidized FeCrAlY clad WI-52. X250.

## 22. MATERIALS PROBLEMS IN AUTOMOTIVE EXHAUST REACTORS FOR POLLUTION CONTROL

Robert E. Oldrieve and Neal T. Saunders

Major contributors to air pollution from automobile engines include hydrocarbons (HC) and carbon monoxide (CO). Automobile exhaust reactors (afterburners) have shown good potential for reducing these pollutants by oxidizing the HC and CO to water vapor and carbon dioxide. From the oxidation process, the exhaust reactors reach temperatures from about 1600° to 1900° F under normal driving conditions. This high-temperature oxidizing environment in combination with other corrosive constituents in the exhaust gas such as lead present a severe environment for reactor materials.

Recently, in cooperation with the National Air Pollution and Control Administration, the NASA Lewis Research Center has initiated programs directed toward development of materials for use in automobile exhaust reactors. Both metallic and ceramic materials are being considered. The current status of the materials development planned as well as the status of other development work in this area are described. In addition, factors affecting materials selection for use in the reactors are reviewed.

Most of the previous presentation in this conference have described types of research for developing new materials or improving specific properties of current materials. In addition to this materials research, NASA-Lewis is involved in the application of materials for specific hardware systems. In this area NASA-Lewis has been asked by the National Air Pollution and Control Administration of the Department of Health, Education, and Welfare to evaluate materials and requirements and initiate programs as may be needed to provide materials for thermal reactors for automobile pollution control. Our initial evaluation of the problem is described in this paper.

### POLLUTION REQUIREMENTS

The contribution of the automobile to the current air pollution problem has been much discussed. Each automobile on the road today exhausts about 1/4 to 1/2 ton of



pollutants per year. On a quantitative basis, pollution levels are tabulated in table 22-I. Shown are the actual levels as a proportion of total gases exhausted from an individual automobile for the year 1956 before Federal requirements were imposed. In most states the levels tabulated (1500 ppm by weight hydrocarbons, 4 percent carbon monoxide, and 1500 ppm nitrogen oxides) existed until the 1963 model year (ref. 1). Also tabulated are the Federal requirements for maximum allowable pollution levels for the year 1968 and the current 1970 model year. The table also includes the expected Federal requirements for the years 1975 and 1980.

Pollution control modifications for 1970 model automobiles have met the Federal requirements for 200 ppm hydrocarbons and 0.75 percent carbon monoxide but have not made an appreciable reduction in the quantity of nitrogen oxides exhausted. Nitrogen oxides should have to be reduced by a factor of nearly 10 to meet the Federal requirements projected for 1975. Most of the improvements made to meet the current 1970 requirements have resulted primarily from relatively minor changes in engine hardware and operating conditions. For example, leaning of the fuel-air mixture and retarding the spark advance have been particularly helpful in achieving the limits imposed on carbon monoxide and hydrocarbons. But the automobile manufacturers are about reaching the limit on gains which can be made by these relatively minor changes. It appears that supplemental devices will be necessary to provide further substantial reductions in the types and quantity of pollutants in future model years.

One such device is a (catalytic) converter to treat nitrogen oxides. However, it is currently reported (refs. 2 and 3) that such converters are expensive and cannot be made to be effective beyond 15 000 miles of operation. Neither do such converters treat carbon monoxide and hydrocarbon pollutants. To provide a partial solution to limitation of nitrogen oxide and to provide for treatment of carbon monoxide and hydrocarbons as well, a device called a thermal reactor is one of the most promising systems being investigated (ref. 3).

## THERMAL REACTORS

The pollutants exhausted from an automobile are created by the combustion process in the cylinders of an internal combustion engine. The conditions for the production of nitrogen oxide and the other major identified pollutants (HC and CO) are mutually exclusive and in opposition to one another. Nearly complete combustion at high temperatures produces an abundance of nitrogen oxide. At lower temperatures, however, less complete combustion (aided by thermal quenching at the cylinder walls)

produces a preponderance of carbon monoxide and unburned hydrocarbons. The thermal reactor concept involves completion of the combustion processes without further production of nitrogen oxide.

A typical thermal reactor installation is shown in figure 22-1. A reaction chamber replaces the commonplace cast-iron manifold of the engine. In the section view, air is injected into the hot exhaust gases as they leave the exhaust port and before they enter the simple combustion chamber (which is shown in longitudinal section in fig. 22-2). In figure 22-2, the hot exhaust gases and injected air are shown entering the inner can of the thermal reactor through the four exhaust ports on one side of a V-8 engine. At cruise conditions (of about 40 to 60 miles/hr) the exhaust gas enters at about  $1400^{\circ}\text{F}$  where it is mixed with the injected air such that the carbon monoxide is oxidized to produce carbon dioxide, and the hydrocarbons are burned to produce water vapor. The reactions in the chamber increase the temperature of the mixture to about  $1700^{\circ}\text{F}$  at cruise conditions and from  $1800^{\circ}\text{F}$  to  $1900^{\circ}\text{F}$  at wide open throttle. The hot exhaust products then pass through the annulus between the inner and outer can to be exhausted through a conventional exhaust pipe system.

The materials problems for this application are largely caused by the high-temperature oxidizing conditions. As discussed in the previous papers in this conference, even a superalloy might not survive for long when exposed to the conditions produced in the core of a thermal reactor.

Proper design of a thermal reaction chamber requires a balance between

- (1) Minimum temperature - required to initiate the reaction
- (2) Maximum temperature - required to complete the reactions and limited by the capability of the materials
- (3) Residence time - required to complete the reaction
- (4) Air injection - and the controls required to satisfy other factors
- (5) Mixing - as required to achieve effective combustion
- (6) Chemical and thermodynamic considerations.

The effectiveness of a thermal reactor depends on each of these factors properly combined to provide efficient combustion of an intermittent (nonsteady flow) gas-air mixture under all conditions of automobile engine operation. Since this paper deals with the selection of core materials for this application, the maximum temperature is of greatest concern. For example, air cooling the core could reduce maximum materials temperatures but that all other design factors would be affected accordingly. These design considerations are being studied by other groups at Lewis. But at this time, we must accept the high temperatures in making materials selection. The temperatures quoted are for a thermal reactor on an engine operated at conditions which minimize production of nitrogen oxide. However, if means are

found by others to allow higher  $\text{NO}_x$  production in the engine, the correspondingly hotter exhaust temperature would be expected to result in about the same net reactor core temperatures. Materials requirements would not be expected to change.

## EFFECTIVENESS OF THERMAL REACTORS

Thermal reactors have been shown to be extremely effective in reducing pollution levels from automobile exhaust pipes. Some of the results obtained by the Automotive Emissions Division of the DuPont Petroleum Laboratories are shown in figure 22-3. (Because our automobile engine test facility is just beginning to yield information, we are indebted to the automobile manufacturers, other government agencies, and especially to DuPont for making available materials performance data used in this presentation.) DuPont installed a pair of reactors on an automobile which was operated following the Modified Automobile Manufacturers Association City Driving Schedule for 100 000 miles. Figure 22-3(a) shows hydrocarbon emission in ppm plotted against miles of operation. The arrow points to the 300-ppm value obtained on the engine before reactors were installed. Superimposed on both figures 22-3(a) and (b) are dashed horizontal lines which show 1975 and 1980 projected Federal regulation values. The reduction in hydrocarbons using the reactors is dramatic. Nearly a ten-fold reduction was found for the average of about 30 sampling runs made during the test. The average with reactors is reported to be 27 ppm or just above the projected 1980 Federal requirements. In figure 22-3(b) a reduction in carbon monoxide is seen to be from 2 percent without reactors to about 0.5 percent with reactors installed for the first 50 000 miles. The 0.5-percent value rises to about -0.6 percent carbon monoxide with longer operating times. Thus, substantial reductions were made in carbon monoxide and hydrocarbons. However, there is still need for improvement to meet the 1980 Federal requirements. And in most areas of research and development, the job becomes more difficult the closer you come to meeting the requirements. Thus, additional reactor design effort is required before thermal reactors are fully acceptable for use.

The 100 000-mile test provided reactor durability under only one set of conditions which did not include the severest test of materials. The test was primarily an emissions test. Emissions levels were obtained at the low speeds specified in the Federal test procedure because these conditions produce the greatest pollution in an automobile without thermal reactors installed. This test engine was subjected to only about 30 cold starts whereas the average automobile is subjected

to at least 10 000 cold starts during its lifetime and at least 10 000 other cycles where the engine does not completely cool.

In practice all types of drivers must be considered including the little old lady who drives to church on Sunday and the lead-footed hot rodder who runs with the throttle full-on and full-off. From the materials viewpoint, the hot rodder appears to create the greatest problems. Reactors on his engine will see assured high temperatures from wide-open throttle operation and possible thermal fatigue from rapid thermal cycling. We are also concerned about lugging operations (e.g., pulling a heavy load), motoring operations (e.g., downhill runs), and high temperatures from extended idling or associated with high-speed operation (e.g., valve overlap can cause excessive fuel to the reactor as does intermittent spark ignition or missing and, at the extreme, cessation of the spark from failed plugs, pulled or failed wires, etc., which constitutes the spark-out condition mentioned later).

Thus, the state of technology is that feasibility has been demonstrated but additional design work and testing under all types of conditions is necessary before thermal reactors will be fully accepted for use. In addition, better materials must be found to overcome various types of reactor failures that have been observed. These failure modes include burn-through holes due to severe erosion-corrosion; swelling of the cores due to creep; and cracking attributed to mechanical or thermal stresses.

Because the problems encountered are somewhat related to our experience in jet engine components, the National Air Pollution Control Administration asked the NASA Lewis Research Center to take responsibility for guiding materials testing and development as required for this application. Although we are just in the beginning stages of our program, we would like to indicate some of our current thinking on the problem of materials selection.

## MATERIALS SELECTION

For the selection of materials the four main factors which result from the conditions previously discussed are as follows:

- (1) High combustion temperatures
  - (a) 1700° to 1900° F in ordinary operation
  - (b) Greater than 2300° F possible upon spark-out operation (This is particularly hard on conventional metals.)
- (2) Long cyclic lifetime
  - (a) 50 000 to 100 000 miles lifetime desired - equivalent to 2000 to 4000

- hours of average driving (Such durability requires good creep resistance of the core materials.)
- (b) 10 000 to 20 000 engine on-off cycles (This could lead to thermal fatigue failures.)
- (3) Severe corrosion conditions
  - (a) High temperature oxidation (This requires materials with good oxidation resistance.)
  - (b) Chemical attack from lead to sulfur in the fuel (These contribute to fluxing of protective oxide on metals and require good sulfidation resistance, respectively.)
  - (c) Erosion from particulates in the exhaust (These particulates can have velocities of the order of 600 ft/sec.)
- (4) Low cost
  - (a) Less than \$50 per installation
  - (b) Easy fabrication and assembly (This would allow mass production.)

## METALS

Finding materials to meet all of these goals is difficult; none of the materials available today meet all of them. Thus we are trying to determine the trade-offs necessary to best meet the needs of the application. To illustrate the possible trade-offs table 22-II lists four classifications of alloys being investigated. In this table is given a typical alloy in each class, with its trade name designation, major constituents, approximate cost, and approximate 1800° F tensile strength. Other alloys are equal to or better than these selected alloys in each class; however, these are presented because of the availability of the pertinent data. It can be observed from the table that, as nickel content is increased from the nickel-free Fe-Cr-Al's to the high-nickel Hastelloy-X, cost increases from about 60 cents per pound to more than 3 dollars per pound and tensile strength increases from less than 2000 psi to about 18 000 psi at 1800° F.

Trade-off properties can be considered by reference to figure 22-4 which presents oxidation resistance for these alloys exposed as test coupons held directly in the flow of exhaust gases from an automobile engine burning typical commercially available fuel (with tetraethyl lead, as the antiknock agent). Weight loss is plotted against test time for specimens at the indicated temperatures exposed for times to 400 hours. An oxidation-resistant alloy will generally gain or lose little weight and will not deviate greatly from the horizontal zero coordinate until failure ensues (as was noted and further qualified in previously presented papers in this

conference). The data shown in figure 22-4 (from ref. 3) indicate that the low-cost Fe-Cr-Al alloy has good oxidation resistance. But the strength of most Fe-Cr-Al alloys is probably too low for use in this application. (Further data on Fe-Cr-Al alloys was presented by S. J. Grisaffe.) The more expensive Hastelloy-X also does well in engine oxidation and has much better strength at these high temperatures. But use of Hastelloy-X for this application would consume large quantities of strategic nickel, and its high cost would probably make the cost of reactors prohibitive.

As a trade-off of cost for strength, the intermediate classes of alloys listed in table 22-II are considered. The data of figure 22-4, however, show that such alloys are nearly consumed (as indicated by 300 to 400 mg (in.<sup>2</sup>) loss) in the 400-hour test (4000 hr is desired). However, there is a way out for the alloys which oxidize too quickly. As shown in figure 22-5 coatings can be very effective. This plot shows results from aluminized Incoloy-800 specimens which were subjected to the same engine exhaust exposure test. The increase in oxidation resistance of the coated material is dramatic when compared with the uncoated material which had been exposed at a 100° F lower test temperature. The coated Incoloy-800 performed as well as both the Fe-Cr-Al alloy and Hastelloy-X in this test.

Although coated alloys appear attractive, coatings do complicate the solution because they increase the materials cost to offset the otherwise clear-cut advantage of these trade-off alloys. Coating may have to be applied after fabrication, which would make inspection more costly and difficult. And, as with all of the materials being considered, the coated materials have not been subjected to the most severe operating conditions.

Thus, better materials must be developed for this application. We are most interested in the Fe-Cr-Al class of alloys because of their low cost and good oxidation resistance. But methods must be developed to increase the high temperature strength of these alloys. In addition we will continue to evaluate coatings for other materials which have sufficient strength and reasonable cost.

## CERAMICS

Because of the high temperatures that can be encountered under spark-out conditions, we also look to ceramics for a solution. Most metals will not be able to withstand these severe conditions (as illustrated in fig. 22-6). The figure shows a 4-inch end of a metal-core reactor which had been subjected to the greater than 2300° F spark-out condition. The high temperatures result from the addition of unburned gasoline to the fuel-air mixture which enters the reactor.

For these high temperature conditions, several features of ceramics must be considered. Some of the newer ceramics offer considerable promise in meeting our main criteria. They are generally made using raw materials with a cost much less than 25 cents per pound. They maintain good oxidation resistance and have good strength at temperatures well above the temperatures a metal can survive. But the disadvantages of ceramics are well known (and have been discussed by H. B. Probst earlier). Brittleness is their foremost shortcoming. However, brittleness can be overcome for many applications, with the expenditure of considerable time, money, and effort. For example, ceramic materials are now being seriously evaluated for use in heat exchangers for gas turbine truck engines. To use ceramic cores for reactors adds additional considerations of possible greater thermal shock and the chemical attack by lead in automobile engine fuel. Many ceramics which appear to be favorable from other considerations are degraded in the presence of lead oxide.

Both brittleness and lead attack must be overcome before ceramics can be seriously considered for our application.

## SUMMARY

The following points summarize our evaluation of this application:

1. Thermal reactors look promising for the reduction of automobile pollution levels in the near future.
2. Both metals and ceramics are promising candidates for use in the high-temperature cores of thermal reactors. Since each has its own limitations we will evaluate both metallic and ceramic reactors.
3. Better reactor design are needed to
  - a. Improve gas mixing
  - b. Reduce thermal stresses on metallic core materials
  - c. Minimize mechanical and thermal shock in reactors with ceramic cores
  - d. Make such a device as compact as possible.
4. Since none of the currently available materials have all of the attributes desired, better low-cost materials are needed.

Thus, Lewis is starting both in-house and contracted programs to extensively test available materials and coatings for thermal reactors on test engines. Simultaneously we will seek improvement of reactor design and the development of improved materials.

## REFERENCES

1. Report by the Panel on Electrically Powered Vehicle: The Automobile and Air Pollution - A Program for Progress, Parts I - II. U. S. Dept. Commerce, Oct. and Dec. 1967. U. S. Govt. Printing Office, No. 0-278-482 and 0-280-842.
2. Anon.: Air & Water News, Nov. 25, 1968, and Jan. 27, 1969.
3. Cantwell, E. N.; et al.: A Progress Report on The Development of Exhaust Manifold Reactors. Paper 690139, SAE, Jan. 1969.

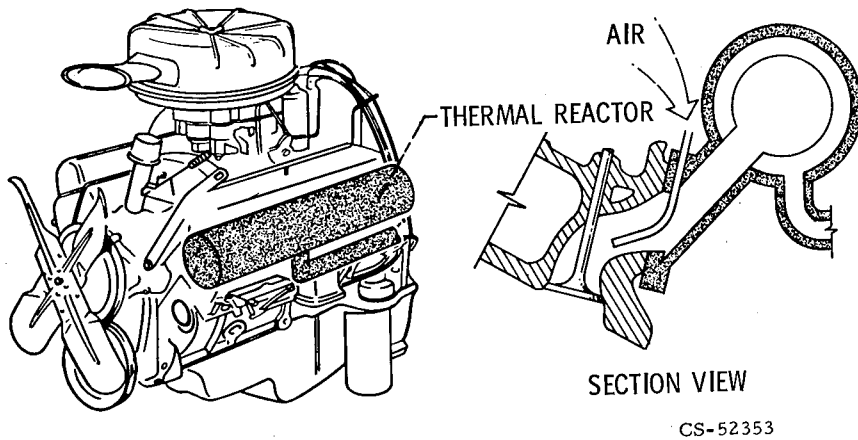


TABLE 22-I. - AUTO POLLUTION LEVELS

Year	Hydro-carbons, ppm	Carbon monoxide, percent	Nitrogen oxides, ppm
1956 (Actual)	~1500	~4	~1500
1968 (Federal requirements)	<275	<1 $\frac{1}{2}$	-----
1970 (Federal requirements)	<200	<3/4	-----
1975 (Estimate)	<50	<1/2	<175
1980 (Estimate)	<25	<1/4	-----

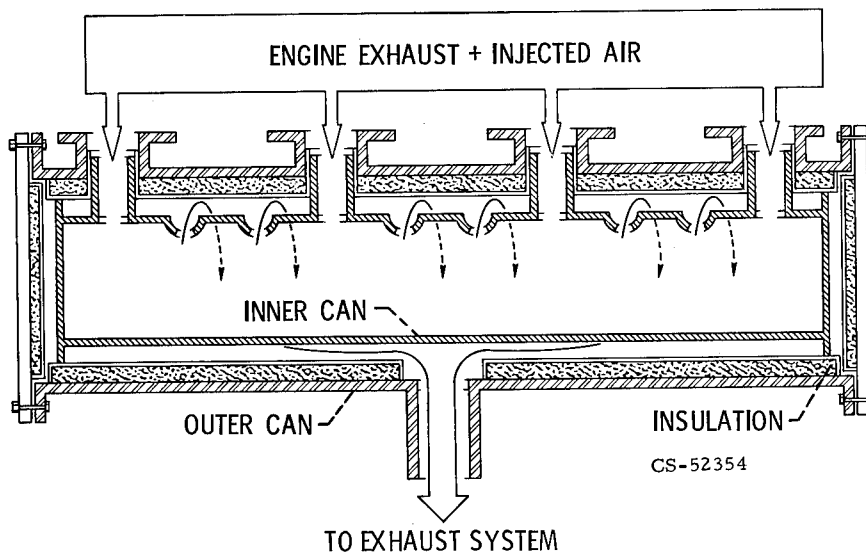
TABLE 22-II. - POTENTIAL REACTOR MATERIALS

Alloy class	Representative alloy					Approximate cost per pound, \$	Tensile strength at 1800° F, psi
	Name	Fe	Ni	Cr	Other		
Fe-Cr-Al steel	Alchrome-D	79	--	15	5Al	0.60	<2 000
Austenitic stainless steel	AISI 310	55	20	25	----	1.15	8 000
Fe-Ni-Cr alloy	Incoloy-800	48	32	20	----	1.30	<10 000
Superalloy	Hastelloy-X	20	47	22	9Mo	>3.00	18 000



CS-52353

Figure 22-1. - Thermal reactor installation on engine.



CS-52354

Figure 22-2. - Thermal reactor longitudinal section.

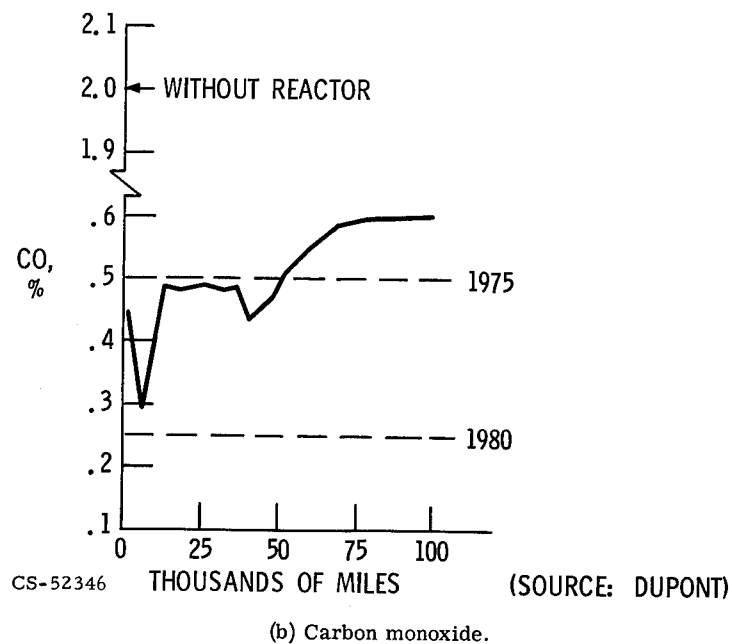
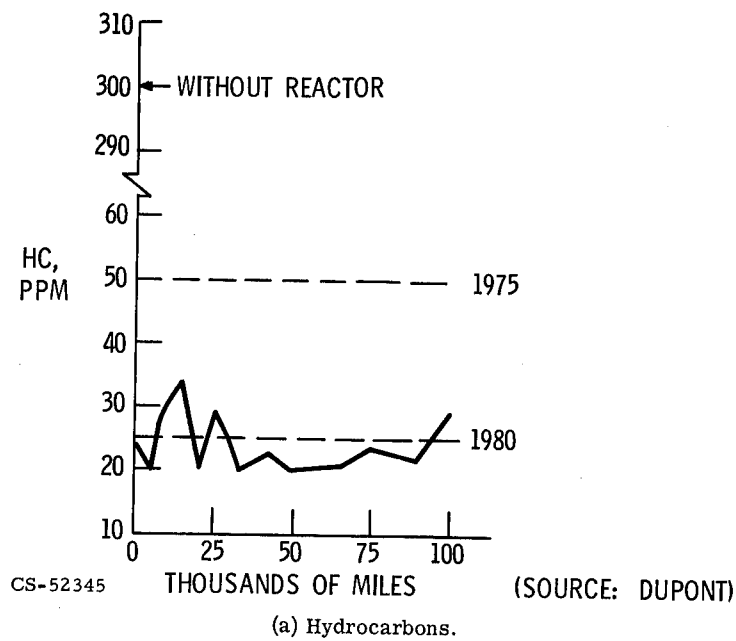


Figure 22-3. - Effectiveness of thermal reactors.

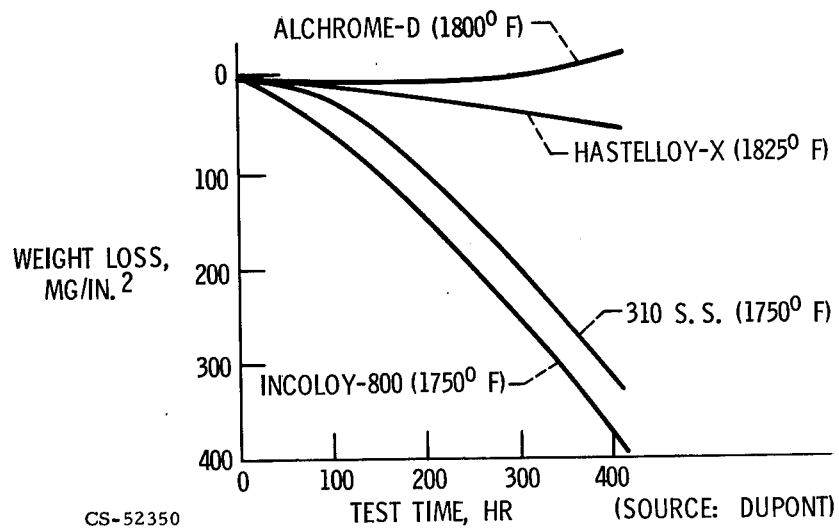


Figure 22-4. - Oxidation resistance in engine exhaust environment.

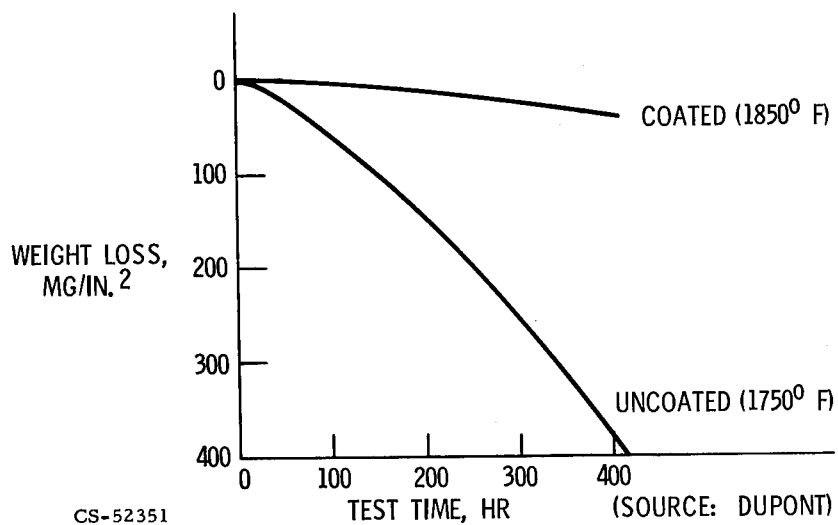
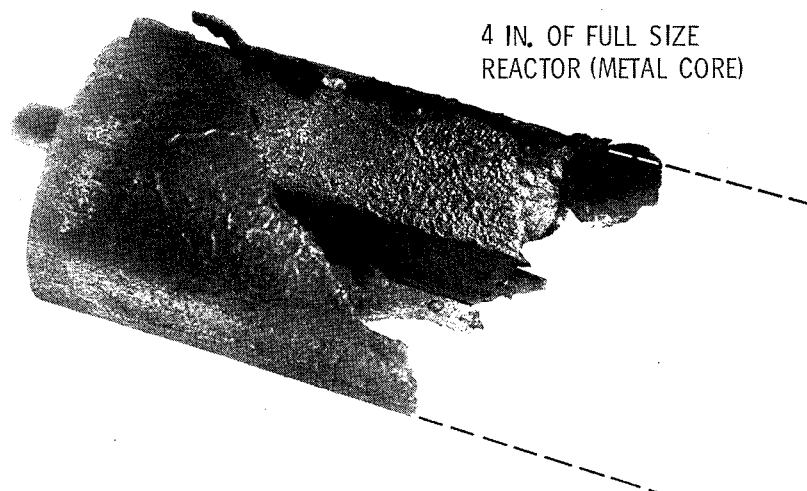


Figure 22-5. - Coating effectiveness in engine exhaust environment for Incoloy-800.



CS-52691

SOURCE DUPONT

Figure 22-6. - Reactor failure under spark-out conditions.